

UNIVERSITY OF SOUTHAMPTON
FACULTY OF PHYSICAL SCIENCES AND ENGINEERING
Department of Physics & Astronomy

Disc Winds Matter: Modelling Accretion and Outflow on All Scales

by
James Matthews

A thesis submitted for the degree of Doctor of Philosophy

June 2016

“Here, on the edge of what we know, in contact with the ocean of the unknown, shines the mystery and the beauty of the world.

And it’s breathtaking.”

Seven Brief Lessons on Physics, Carlo Rovelli

“Good enough for government work.”

Christian Knigge

UNIVERSITY OF SOUTHAMPTON

ABSTRACT

FACULTY OF PHYSICAL SCIENCES AND ENGINEERING

Department of Physics & Astronomy

Doctor of Philosophy

DISC WINDS MATTER: MODELLING ACCRETION AND OUTFLOW ON ALL SCALES

by James Matthews

Outflows are ubiquitous in accreting systems across 10 orders of magnitude in mass, and there is good evidence that mass-loaded winds are launched from the accretion discs of quasars and cataclysmic variables (CVs). Perhaps the most spectacular evidence for accretion disc winds is the blue-shifted, broad absorption lines (BALs) in UV resonance lines, seen in CVs and the BAL quasars. As well as imprinting absorption features, disc winds may affect the line and continuum emission from accreting objects. They thus offer a natural way to *unify* much of the phenomenology of CVs and active galactic nuclei (AGN).

In this thesis, I use a state-of-the-art Monte Carlo radiative transfer (MCRT) code, PYTHON, to conduct a series of simulations designed to test simple biconical disc wind models. I outline the MCRT techniques used, before describing a series of code validation exercises. Having tested my methods thoroughly, I explore whether the winds that are responsible for the UV BALs in high-state CVs could also have an effect on the optical spectrum. I find that the wind produces strong emission in the Balmer series, He II 4686 Å and a series of He I lines. The model shows the observed trends with inclination and in some cases produces sufficient recombination continuum emission to fill in the Balmer photoabsorption edge intrinsic to disc atmospheres. The results suggest that disc winds could have a significant impact on the optical spectra of high-state CVs.

The next step was to apply the techniques to quasar winds in a test of disc wind unification models. In previous efforts, the outflow tended to become ‘over-ionized’, and BAL features were only present if the X-ray luminosity was limited to around 10^{43} erg s $^{-1}$. The outflow also failed to produce significant line emission. Motivated by these problems, I introduce a simple treatment of clumping and find that it allows BAL features to form in the rest-frame UV at more realistic X-ray luminosities. The fiducial model shows good agreement with AGN X-ray properties and the wind produces strong line emission. Despite these successes, the model cannot reproduce all emission lines seen in quasar spectra with the correct equivalent width (EW) ratios, and I find the emission line EWs have a strong dependence on inclination.

Informed by the quasar wind modelling, I examine the emission line EW distributions of quasars in the context of geometric unification. I find that the observed distributions are not consistent with a model in which an equatorial BAL outflow rises from a foreshortened accretion disc. I discuss this finding in the context of other observational orientation indicators. Finally, I summarise my findings and suggest avenues for future work. Overall, the work presented here suggests that *disc winds matter*. They not only act as a spectral ‘filter’ for the underlying accretion continuum, but may actually dominate the emergent spectrum from accreting objects. As a result, unveiling their driving mechanisms, mass-loss rates and ionization structure is an important goal for the astronomical community.

Contents

Abstract	iv
List of Figures	xi
List of Tables	xv
Declaration of Authorship	xvii
Acknowledgements	xix
Abbreviations	xxi
Physical Constants	xxiii
1 Introduction	1
1.1 The Physics of Accretion	3
1.1.1 Spherical Accretion and The Eddington Limit	4
1.1.2 Accretion Discs	6
1.1.2.1 Steady-state Accretion Discs: the α -prescription	6
1.1.3 Boundary Layers, Black Hole Spin and the ISCO	8
1.1.4 The Emergent Spectrum	12
1.2 Accreting Compact Binaries	12
1.2.1 Roche Lobe-Overflow	13
1.2.2 Cataclysmic Variables	16
1.2.2.1 Dwarf Novae and the Disc-instability Model	16
1.2.2.2 Nova-like Variables	17
1.2.3 Low Mass X-ray Binaries	21
1.3 Quasars and Active Galactic Nuclei	21
1.3.1 AGN Unification and the Dusty Torus	22
1.3.2 X-ray Properties of AGN	24
1.3.2.1 The Soft X-ray Excess	27
1.3.3 The Broad Line Region: Connection to Winds and Unification . .	28
1.4 The Current Understanding of the Disc Continuum	28
1.4.1 The Spectral Shape of CV Discs	28
1.4.2 The Big Blue Bump in AGN	30
1.4.2.1 The Accretion Disc Size Problem	30
1.4.2.2 Fitting AGN Spectra and the 1000 Å Break	30
1.5 The Universality of Accretion	31
1.5.1 The RMS-flux relation	31
1.5.2 Accretion states and disc-jet coupling	32
1.5.3 A Global Picture	33

2 Accretion Disc Winds	35
2.1 Observational Evidence	35
2.1.1 Cataclysmic Variables	36
2.1.2 X-ray Binaries	39
2.1.3 AGN and Quasars	40
2.1.3.1 Broad Absorption Line Quasars	40
2.1.3.2 Warm Absorbers	44
2.1.3.3 Ultra-fast Outflows	45
2.1.4 Stellar Winds	47
2.1.4.1 Clumping in Stellar Winds	48
2.1.5 Outflow Physics	48
2.2 Driving Mechanisms	48
2.2.1 Thermal Winds	49
2.2.2 Radiatively Driven Winds	50
2.2.3 Line-driven Winds	50
2.2.4 Magnetic Winds	52
2.3 Accretion Disc Wind Models	53
2.3.1 MCGV95: A Line-driven Wind Model for AGN	53
2.3.2 De Kool & Begelman: A Radiatively Driven, Magnetically Confined Wind	54
2.3.3 Elvis 2000: A Structure for Quasars	55
2.3.4 Proga et al.: Line-driven Hydrodynamic Models for AGN and CVs	56
2.4 A Kinematic Prescription for a Biconical Wind	58
2.5 The big picture: AGN Feedback	60
2.5.1 Observational evidence for feedback	62
2.5.2 Alternative Explanations	65
3 Monte Carlo Radiative Transfer and Ionization	67
3.1 Fundamentals of Radiative Transfer	68
3.1.1 Spectral Line Formation	69
3.1.2 Local Thermodynamic Equilibrium	69
3.1.2.1 Dilute Approximation	70
3.1.3 The Two Level Atom	71
3.1.3.1 Einstein coefficients	71
3.1.4 The Sobolev Approximation	72
3.1.4.1 Two-level Atom with Escape Probabilities	74
3.1.5 Monte Carlo Approaches	74
3.2 PYTHON: A Monte Carlo Ionization and Radiative Transfer Code	75
3.2.1 Basics	75
3.2.2 Radiation Packets	77
3.2.3 Radiative Transfer Procedure	78
3.2.3.1 Continuum Opacities	78
3.2.3.2 Doppler Shifts	80
3.2.3.3 Choosing Packet Directions	80
3.3 Macro-atoms	81
3.3.1 Transition Probabilities	82
3.3.2 Rate equations	83
3.3.2.1 Collision Strengths	85
3.3.3 Macro-atom estimators	86
3.3.3.1 Bound-free estimators	86

3.3.3.2	Bound-bound estimators	87
3.3.3.3	Other heating and cooling estimators	88
3.3.4	<i>k</i> -packets	89
3.3.5	Putting it All Together	89
3.3.6	Ionization Fractions and Level Populations	89
3.3.7	Numerical Issues and Population Inversions	92
3.4	A hybrid line transfer scheme: including simple-atoms	92
3.4.1	Line Transfer	93
3.4.2	Heating and Cooling Estimators	94
3.4.2.1	Radiation Field Estimators, Ionization and Excitation . .	94
3.5	Heating And Cooling Balance	97
3.5.1	Convergence	97
3.6	Spectral Cycles	98
3.6.1	Macro-atom Emissivity Calculation	99
3.7	Atomic Data	101
3.7.1	Macro-atom Level and Line Data	101
3.7.2	Photoionization Cross-sections	102
3.8	Code Validation	103
3.8.1	Testing Against CLOUDY	103
3.8.2	Macro-atom Testing Against TARDIS and Theory	105
3.8.3	Testing Line Transfer Modes	109
3.9	Code Maintenance and Version Control	111
3.9.1	Parallelisation	111
4	The Impact of Accretion Disc Winds on the Optical Spectra of Cataclysmic Variables	115
4.1	Introduction	115
4.1.1	Sources and Sinks of Radiation	117
4.1.1.1	Accretion disc	117
4.1.1.2	White Dwarf	118
4.1.1.3	Boundary Layer	118
4.1.1.4	Secondary Star	119
4.2	A Benchmark Disc Wind Model	119
4.2.1	Physical Structure and Ionization State	121
4.2.2	Synthetic Spectra	121
4.3	A Revised Model Optimized for Optical Wavelengths	125
4.3.1	Synthetic Spectra	126
4.3.2	Continuum Shape and the Balmer Jump	129
4.3.3	Line Profile Shapes: Producing Single-Peaked Emission	131
4.3.4	Sensitivity to Model Parameters	133
4.3.5	Comparison to RW Tri	133
4.3.6	A Note on Collision Strengths	135
4.4	Conclusions	136
5	Testing Quasar Unification: Radiative Transfer In Clumpy Winds	139
5.1	Introduction	139
5.2	A Clumpy Biconical Disk Wind Model for Quasars	140
5.2.1	Photon Sources	141
5.2.2	A Simple Approximation for Clumping	142
5.2.3	The Simulation Grid	144

5.3	Results and Analysis from a Fiducial Model	146
5.3.1	Physical Conditions and Ionization State	146
5.3.2	Synthetic Spectra: Comparison to Observations	150
5.3.2.1	Broad Absorption Lines ('BALQSO-like' angles)	150
5.3.2.2	Broad Emission Lines ('quasar-like' angles)	152
5.3.3	X-ray Properties	155
5.3.4	LoBALs and Ionization Stratification	156
5.4	Discussion	158
5.4.1	Parameter Sensitivity	158
5.4.2	Inclination Trends: FWHM and EW	158
5.4.2.1	FWHM and Black Hole Mass Estimates	161
5.5	Summary And Conclusions	163
6	Quasar Emission Lines as Probes of Orientation and Unification	165
6.1	Introduction	165
6.2	Data Sample	167
6.3	The Angular Distribution of Emission from an Accretion Disc	171
6.3.1	Standard Thin Disc Models	171
6.3.2	Including GR and Opacity Effects	172
6.4	Predicted EW Distributions Compared to Observations	174
6.4.1	Fitting the Quasar Distribution	174
6.4.2	Comparing non-BAL and LoBAL Distributions: Sample A	175
6.5	Discussion	181
6.5.1	Eigenvector 1	181
6.5.2	Polarisation	183
6.5.3	The Effect of Obscuration	186
6.5.4	Line Anisotropy	187
6.6	Conclusions	189
7	Conclusions and Future Work	193
7.1	Suggestions for Future Work	196
7.1.1	CVs as Accretion and Outflow Laboratories	196
7.1.2	Improving the Treatment of Clumping	197
7.1.3	Improving Atomic Models	198
7.1.4	Using Radiative Transfer to Make Reverberation and Microlensing Predictions	199
7.1.5	Placing BAL Quasars on the Eigenvector 1 Parameter Space	199
7.2	Closing Remarks	200
Bibliography		203

List of Figures

1.1	The temperature profile of an accretion disc for three different classes of compact object.	9
1.2	Angular velocity as a function of radius in an accretion disc around a rotating compact object.	10
1.3	The radius of the ISCO, R_{ISCO} , and the horizon, R_H , is as a function of the BH spin parameter, a_*	11
1.4	Accretion disc SEDs for three different compact objects.	11
1.5	A comparison between an accretion disc spectrum computed with black-body and stellar atmosphere spectra.	13
1.6	Artists impression of an LMXB and CV.	14
1.7	The Roche potential in a binary system	15
1.8	A year in the life of SS Cyg.	17
1.9	Spectra of SS Cyg during an outburst cycle	18
1.10	UV spectrum of RW Tri in and out of eclipse.	19
1.11	Optical spectra of three nova-like variables.	20
1.12	Template spectra, from the AGN atlas, for four common types of AGN. .	23
1.13	A unified scheme for AGN.	25
1.14	Broadband SEDs for different AGN SEDs	26
1.15	Occam's quasar	29
1.16	Hardness-intensity diagrams for three types of accreting objects.	33
2.1	A diagram showing how P-Cygni profiles form.	36
2.2	UV spectrum of the DN TW Vir during outburst.	37
2.3	UV spectrum of Z Cam, compared to a synthetic spectrum from MCRT simulations.	37
2.4	The effect of a disc wind on a double-peaked line profile.	38
2.5	A cartoon illustrating the expected geometry of soft-state LMXB winds. .	39
2.6	Hardness-intensity diagram for four dipping LMXBs.	40
2.7	Some example non-BAL, HiBAL and LoBAL spectra.	41
2.8	X-ray spectrum of PDS 456 fitted with a P-Cygni profile.	46
2.9	UV spectrum of one of the O4 supergiant ζ Puppis.	47
2.10	Cartoon showing the geometry of the MCGV95 model.	54
2.11	A cartoon showing the components in the De Kool & Begelman model. .	55
2.12	A schematic showing the main features of the Elvis model.	56
2.13	Density snapshot of the PK04 model.	57
2.14	A schematic showing the geometry and kinematics of the SV93 model .	59
2.15	The SV93 velocity law for various values of the acceleration exponent, α . .	61
2.16	The $M_{BH} - \sigma_*$ correlation.	63
2.17	The $M_{BH} - M_{bulge}$ correlation.	63

2.18	<i>Chandra</i> X-ray images showing two examples of X-ray cavities.	64
2.19	Results of Gaussian line profile fitting to integral field spectroscopy of Mrk 231.	65
3.1	A schematic showing a ray obliquely incident on a surface of area dA . The labeled quantities are used in the definition of specific intensity.	68
3.2	A flowchart showing the basic operation of PYTHON.	76
3.3	The process of choosing a scattering location in a cell.	79
3.4	The decision tree traversed by an energy packet in macro-atom mode.	90
3.5	An example of a modeled spectrum in PYTHON compared to the recorded MC spectrum, from an individual cell in an AGN model.	96
3.6	The average temperature and fraction of converged cells in a typical CV model, shown as a function of the number of ionization cycles completed.	98
3.7	A comparison of synthetic spectra produced in extract and live or die modes.	100
3.8	The effect of extrapolated cross-sections on the soft X-ray spectrum	103
3.9	Relative ion fractions for Hydrogen in CLOUDY, PYTHON in standard mode and PYTHON in hybrid mode.	105
3.10	As figure 3.9, but for Helium.	106
3.11	As figure 3.9, but for Carbon.	106
3.12	As figure 3.9, but for Nitrogen.	107
3.13	As figure 3.9, but for Oxygen.	107
3.14	As figure 3.9, but for the first 11 ionization stages of Iron.	108
3.15	Balmer decrements in PYTHON compared to Seaton (1959), and He level populations compared to TARDIS.	109
3.16	Comparison between TARDIS and PYTHON synthetic spectra from a simple 1D supernova model.	110
3.17	A comparison between weight reduction and line transfer mode.	111
3.18	Github commit history for PYTHON from 2013-2016.	112
3.19	Total runtime per cycle for an AGN run as a function of the number of processors.	113
4.1	Cartoon illustrating the geometry and kinematics of the benchmark CV wind model.	116
4.2	The spectral energy distribution of the accretion disc and white dwarf used in the ionization cycles for the CV modelling.	118
4.3	The physical properties of the wind in the benchmark CV model.	120
4.4	UV and optical synthetic spectra from the benchmark CV model	122
4.5	Optical synthetic spectra from the benchmark CV model divided by the continuum.	124
4.6	Total packet-binned spectra across all viewing angles from the benchmark CV model.	125
4.7	UV and optical synthetic spectra from CV model B	127
4.8	Optical synthetic spectra from CV model B divided by the continuum.	130
4.9	Total packet-binned spectra across all viewing angles from CV model B.	131
4.10	H α line profiles from CV models A, B and X	132
4.11	In and out of eclipse spectra from model B compared to the high inclination NL RW Tri	134

5.1	A cartoon showing the geometry and some key parameters of the biconical quasar wind model.	141
5.2	The input spectrum used for the quasar modelling.	142
5.3	Some typical length scales for the fiducial model.	145
5.4	Contour plots showing the logarithm of some important physical properties of the quasar outflow.	147
5.5	The electron density in the fiducial model on linear axes.	148
5.6	Synthetic spectra at four viewing angles for the fiducial quasar model.	151
5.7	A schematic showing the broad classes of sightline in the fiducial model.	152
5.8	Synthetic spectra at two viewing angles compared to the non-BAL SDSS quasar composite.	153
5.9	X-ray properties of the clumped quasar model compared to H13 and samples from the literature.	155
5.10	C IV, Mg II, Al III and Fe II line profiles for wind viewing angles.	157
5.11	Equivalent widths and BALnicities of some important lines for the quasar wind grid.	159
5.12	EW_{RW} as a function of inclination in the fiducial model.	160
5.13	f_{FWHM} as a function of inclination from the fiducial model.	162
6.1	BH mass and Eddington fraction measurements for samples A and B.	168
6.2	Histograms of equivalent widths for three emission lines from the two different samples.	169
6.3	Angular variation of continuum luminosity from AGNSPEC and classical thin disc models.	173
6.4	Theoretical EW distributions from the numerical experiment described in section 6.4.1.	176
6.5	The EW[O III] distribution of quasars in the R11 sample and the best fit model.	177
6.6	χ^2 as a function of maximum angle.	178
6.7	The geometry of the toy model used to carry out the Monte Carlo simulations.	178
6.8	Heat map showing the results of the MC simulation described in section 6.4.2.	180
6.9	Eigenvector 1 for LoBAL and non-BAL quasars.	182
6.10	LoBAL fraction compared to global LoBAL fraction in Eigenvector 1 space.	184
6.11	Histograms of polarisation percentages for BAL quasars from Schmidt et al. (1999) together with the Marin et al. (2014) AGN sample.	185
6.12	Cumulative distribution functions of the histograms shown in Fig. 6.11	185
6.13	The line angular emissivity function from a Keplerian disc as a function of inclination angle.	189
6.14	The azimuthally-averaged line angular emissivity function from a Keplerian disc as a function of inclination angle.	190
7.1	Ion fractions as a function of ionization parameter when Carbon is treated as a simple-atom and macro-atom.	198
7.2	Velocity-resolved transfer function for H α from the fiducial quasar model.	200

List of Tables

1.1	Approximate values of compactness and accretion efficiency for four different compact objects.	4
4.1	Model parameters for the CV wind models	119
5.1	The grid points used in the parameter search for quasar wind models . . .	146
5.2	Model parameters for the fiducial quasar model.	148
5.3	Some derived spectral properties of the fiducial model compared to observations.	154
6.1	The values of the Keplerian velocity, v_k , thermal velocity, v_{th} , and ratio of disc scale height to radius, H/R , for four models.	189

Declaration of Authorship

I, James Matthews, declare that this thesis titled, ‘Disc Winds Matter: Modelling Accretion and Outflow on All Scales’ and the work presented in it are my own. I confirm that:

- This work was done wholly or mainly while in candidature for a research degree at this University.
- Where any part of this thesis has previously been submitted for a degree or any other qualification at this University or any other institution, this has been clearly stated.
- Where I have consulted the published work of others, this is always clearly attributed.
- Where I have quoted from the work of others, the source is always given. With the exception of such quotations, this thesis is entirely my own work.
- I have acknowledged all main sources of help.
- Where the thesis is based on work done by myself jointly with others, I have made clear exactly what was done by others and what I have contributed myself.

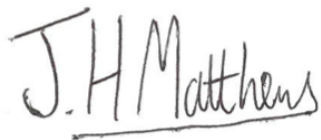
The first two chapters of this thesis provide a general introduction to the field, and thus are based on the relevant literature. Where a figure is not produced by me, I have acknowledged this clearly with a credit to the relevant publication. Chapter 3 contains a description of the methods used. This is partly a description of the radiative transfer code PYTHON, which was originally developed by Knox Long and Christian Knigge ([Long & Knigge 2002](#)), but also includes substantial detail on the ‘macro-atom’ technique, which was proposed by Leon Lucy and incorporated into PYTHON by Stuart Sim for a study on young-stellar objects ([Sim et al. 2005](#)). Although I have put significant effort into testing, fixing and developing this scheme, I did not write the original code to deal with macro-atoms in PYTHON.

Chapter 4, 5 and 6 were studies I led under the guidance of my supervisor. For these chapters I conducted all simulations and data analysis, produced all the figures and wrote the text. A publication based on chapter 6 is in preparation, and chapters 4 and 5 are based on the following papers:

- Chapter 4: Matthews J. H., Knigge C., Long K. S., Sim S. A., Higginbottom N., ‘The impact of accretion disc winds on the optical spectra of cataclysmic variables’, 2015, MNRAS, 450, 3331.
- Chapter 5: Matthews J. H., Knigge C., Long K. S., Sim S. A., Higginbottom N., Mangham S. W., ‘Testing quasar unification: radiative transfer in clumpy winds’, 2016, MNRAS, 458, 293.

The following additional publications are not included in this thesis, although some of the work presented here did contribute towards the respective results

- Higginbottom N., Knigge C., Long K. S., Sim S. A., Matthews J. H., ‘A simple disc wind model for broad absorption line quasars’, 2013, MNRAS, 436, 2.3
- Higginbottom, N., Proga D., Knigge C., Long K. S., Matthews J. H., Sim S. A., ‘Line-driven Disk Winds in Active Galactic Nuclei: The Critical Importance of Ionization’ and Radiative Transfer, 2014, ApJ, 789, 1.
- Shankar F., Calderone G., Knigge C., Matthews J. H., et al., ‘The Optical–UV Emissivity of Quasars: Dependence on Black Hole Mass and Radio Loudness’, 2016, ApJ Letters, 818, 1.

A handwritten signature in black ink, appearing to read "J.H. Matthews". The signature is written in a cursive style with a horizontal line underneath it.

Signed:

Date: 25/05/2016

Acknowledgements

First and foremost, I would like to thank Christian Knigge, for being such an enthusiastic, helpful and stimulating supervisor throughout my PhD. Christian, I *always* left our meetings more positive than before – that speaks volumes – and I greatly enjoyed our conversations about science and Explosions in the Sky. I am also extremely grateful to Knox Long for all his assistance, writing the majority of the code and sharing some of his astronomy knowledge with me, and Stuart Sim for being immensely helpful throughout, especially when it comes to radiative transfer. I would also like to thank Nick Higginbottom for hours upon hours of assistance and friendship, and Sam Mangham for his help and input nearer the end of my PhD. To all of the above people; thank you for being part of a collaboration that does some great science, but also knew when to discuss a disastrous code bug with a knowing smile and ironic joke. I would also like to thank Daniel Proga, Omer Blaes, Ivan Hubeny, Shane Davis, Mike Brotherton, Mike DiPompeo, Frederic Marin, Daniel Capellupo, Dirk Grupe, Simo Scaringi, Adam Foster, Randall Smith, Chris Done, Anna Pala, Boris Gaensicke, Patrick Woudt and countless others for useful correspondence or stimulating scientific conversations. I am also very grateful to my masters supervisor Rosanne Di Stefano for inspiring me to continue doing research beyond my year in Boston.

Apart from those who I worked with, I am grateful to everyone who helped make Southampton a happy place to be over 3+ years. There are too many to name, but I will indulge a few. To Cat, thank you for being generally lovely, being so patient with me and having great taste in comedy. To Sam Connolly, you have been an ever-present and someone who I can always rely on for good beer, music and knowing looks. Sadie Jones, you were there when I needed you most for a cwtch or wanted to hear you pronounce year or ear. To Rob, Aarran, Juan, Georgios and Poppy, thanks for being true friends throughout the process. Big thanks to everyone else in the department for making it a super cool place to work, my office mates Mari, Judith, Stew and CFro, and my housemates Rich, Stu, Ollie, Sophie and Szymon. Thanks also goes to all the staff for being so friendly and approachable, particularly Poshak, Diego and Seb who have all helped me at various points through the PhD, and to Phil Charles for his sage advice since the early days.

There are also many people, outside of Southampton, who I must thank. Most of all, Mum, Dad, Beth and Nick, and the rest of my family – you have always supported me

throughout my studies and just been all round lovely people. Cheers to Nick, Jack and the Hannahs for being great mates and helping me avoid Lemony Snickets. Thank you Josh, James and Alex, and our now manager John, for allowing me to play music that I love in Waking Aida. Eschaton and Full Heal were both released during my PhD, and in many ways they are each a thesis within themselves.

This work was supported by the Science and Technology Facilities Council via a 3.5 year PhD studentship. This work made use of the Sloan Digital Sky Survey. Funding for the Sloan Digital Sky Survey has been provided by the Alfred P. Sloan Foundation, the U.S. Department of Energy Office of Science, and the Participating Institutions. I acknowledge the use of the IRIDIS High Performance Computing Facility, and associated support services at the University of Southampton, in the completion of this work. Figures were produced using the `matplotlib` plotting library.

Abbreviations

AGN	Active galactic nuclei/nucleus
ADAF	Advection dominated accretion flow
BAL	Broad absorption line
BALQSO	Broad absorption line quasar
BBB	Big blue bump
BEL	Broad emission line
BH	Black hole
BI	Balnicity index
BL	Boundary Layer
BLR	Broad line region
CDF	Cumulative distribution function
CGS	Centimetre-gram-second
CV	Cataclysmic variable
DN(e)	Dwarf nova(e)
EW	Equivalent width
HERG	High excitation radio galaxy
HMXB	High-mass X-ray binary
HSE	Hydrostatic Equilibrium
IP	Intermediate polar
IR	Infra-red
ISCO	Innermost stable circular orbit
LHS	Left-hand side
LINER	Low ionization nuclear emission-line region
LMXB	Low-mass X-ray binary
LTE	Local thermodynamic equilibrium
MCRT	Monte Carlo radiative transfer

MRI	Magneto-Rotational Instability
NAL	Narrow absorption line
NEL	Narrow emission line
NLR	Narrow line region
NL	Nova-like variable
NS	Neutron Star
QSO	Quasa-stellar object / Quasar
RL	Radio-loud
RHS	Right-hand side
RIAF	Radiatively inefficient accretion flow
RLOF	Roche lobe overflow
SA	Sobolev approximation
SED	Spectral energy distribution
SFR	Star formation rate
sSFR	Specific star formation rate
SMBH	Supermassive black hole
SXSS	Soft X-ray excess
UFO	Ultra-fast outflow
UV	Ultraviolet
WA	Warm absorber
WD	White dwarf
WHIM	Warm, highly ionized medium
XRB	X-ray binary
YSO	Young stellar object

Physical Constants

Speed of light	$c = 2.997\ 924\ 58 \times 10^{10} \text{ cm s}^{-1}$
Boltzmann constant	$k = 1.380\ 658 \times 10^{-16} \text{ erg K}^{-1}$
Gravitational constant	$G = 6.672\ 599 \times 10^{-8} \text{ cm}^3 \text{ g}^{-1} \text{ s}^{-2}$
Solar mass	$M_{\odot} = 1.988\ 550 \times 10^{33} \text{ g}$
Solar radius	$L_{\odot} = 6.957\ 000 \times 10^{10} \text{ cm}$
Thomson cross-section	$\sigma_T = 6.652\ 458 \times 10^{-25} \text{ cm}^2$
Planck constant	$h = 6.626\ 076 \times 10^{-27} \text{ cm}^2 \text{ g s}^{-1}$
Stefan-Boltzmann constant	$\sigma = 5.670\ 367 \times 10^{-5} \text{ erg cm}^{-2} \text{ K}^{-4} \text{ s}^{-1}$
Parsec	$pc = 3.085\ 678 \times 10^{18} \text{ cm}$
Proton mass	$m_p = 1.672\ 621 \times 10^{-24} \text{ g}$
Electron mass	$m_e = 9.109\ 390 \times 10^{-28} \text{ g}$
Electron volt	$eV = 1.602\ 177 \times 10^{-12} \text{ erg}$
Electron charge	$q_e = 4.803\ 207 \times 10^{-10} \text{ esu}$
π	$= 3.141\ 593$
e	$= 2.718\ 282$

All constants are given to 6 decimal places, except for the speed of light which is exact. Throughout this thesis I use the centimetre-gram-second (CGS) system of units unless otherwise stated.

Dedicated to my family.

Chapter 1

Introduction

“And now you’re asking, I don’t know where to begin”

Mike Vennart, Silent/Transparent

The release of gravitational potential energy as mass falls towards a compact object is the most efficient energetic process in the universe, even more efficient than nuclear fusion. This *accretion* process is thought to power the huge radiative engines at the centres of many galaxies – accreting supermassive black holes known as active galactic nuclei (AGN). As the matter falls into the potential well of the black hole, it often forms an accretion disc. This disc is an efficient radiator of the gravitational potential energy released and can sometimes outshine the entire stellar population of the galaxy, appearing as a quasi-stellar object (QSO) or *quasar*. As well as powering AGN, accretion discs are present in X-ray binaries (XRBs), young-stellar objects (YSOs) and cataclysmic variables (CVs). Accretion is a universal process; broadly speaking, the physics is similar regardless of whether matter is falling on to a $\sim 1 M_{\odot}$ neutron star or white dwarf, or a $\sim 10^{10} M_{\odot}$ black hole.

Outflows are ubiquitous in accreting systems. We see collimated radio jets in AGN (Hazard et al. 1963; Potash & Wardle 1980; Perley et al. 1984; Marscher 2006) and XRBs (Belloni 2010), and there is even evidence of radio emission in CVs (Benz et al. 1983; Körding et al. 2008; Coppejans et al. 2015). These radio jets tend to appear in specific accretion states (Fender 2001; Fender et al. 2004; Körding et al. 2008), implying an intrinsic connection to the accretion process. Even more intriguing, less collimated,

mass-loaded outflows or *winds* are observed in XRBs in soft accretion states, possibly emanating from the accretion disc (Ponti et al. 2012). Evidence for disc winds is widespread across the mass range, but perhaps the most spectacular indication is the blue-shifted, broad absorption lines (BALs) in the rest-frame ultraviolet (UV) seen in high-state CVs (Heap et al. 1978; Greenstein & Oke 1982; Cordova & Mason 1982) and in the so-called broad absorption line quasars (BALQSOs) that make up 20% – 40% of quasars (Weymann et al. 1991; Knigge et al. 2008; Allen et al. 2011). BALs and ‘P-Cygni’ profiles (Struve 1935; Rottenberg 1952) are also seen in stellar winds (e.g. Cassinelli 1979) and sometimes even in the optical spectra of CVs (Patterson et al. 1996; Ringwald & Naylor 1998; Kafka & Honeycutt 2004). Broad, blue-shifted absorption is also observed in the Fe K α line in some AGN (Reeves et al. 2003; Pounds & Reeves 2009; Tombesi et al. 2010) – these are known as ultra-fast outflows or UFOs.

The astrophysical significance of AGN disc winds extends, quite literally, far beyond the accretion environment. They offer a potential mechanism by which the central accretion engine can interact with the host galaxy and interstellar medium via a ‘feedback’ mechanism (King 2003; Fabian 2012). Feedback is required in models of galaxy evolution (Springel et al. 2005) and may explain the famous ‘ $M_{BH} - \sigma_*$ ’ (Silk & Rees 1998; Häring & Rix 2004) and ‘ $M_{BH} - M_{bulge}$ ’ (Magorrian et al. 1998) relations. Winds also offer a natural way to *unify* much of the diverse phenomenology of AGN, CVs and XRBs. This principle of unification can be applied along more than one ‘axis’ of parameter space. For example, there exist elegant models that attempt to explain *all* of the behaviour of quasars with only a central black hole, a jet, an accretion disc, and an associated outflow, just by varying the viewing angle (Elvis 2000). Similarly elegantly, it has been shown that much of the behaviour of XRBs is directly analogous to AGN (McHardy et al. 2006), and models of outflows in CVs have been successfully ‘scaled-up’ and applied to quasars and AGN (e.g. Higginbottom et al. 2013).

Despite their importance and ubiquity, there are still many unanswered questions relating to the true impact of winds and their underlying physical origins. Here, I aim to address some of these questions and take steps towards building a more holistic picture of the impact of winds on the spectral appearance and accretion physics of disc systems. This thesis is structured as follows. In the remainder of this chapter, I will outline the background accretion theory and highlight the successes and failures of accretion disc models when compared to observations, as well as describing the different classes

of accreting objects in more detail. In chapter 2, I dedicate some time to specifically discussing the theory of, and observational evidence for, accretion disc winds. In chapter 3, I outline the Monte Carlo radiative transfer and photoionization methods I have used in order to investigate the impact of disc winds on the spectra of accreting systems. The next three chapters are based on two publications and one paper in preparation, in which I discuss the impact of disc winds on the spectra of CVs (Chapter 4), and test disc wind quasar unification models (Chapters 5 and 6). In chapter 7, I summarise my findings and their astrophysical significance, and discuss potential avenues for future work.

1.1 The Physics of Accretion

The basic phenomenon of accretion – matter falling into a gravitational potential well – is ubiquitous in astrophysics. The energy, ΔE , released by a parcel of mass, Δm , falling from infinity onto an object of mass M and radius R_* is given by

$$\Delta E = \frac{GM\Delta m}{R_*}, \quad (1.1)$$

meaning that the power generated by mass accreting at a rate \dot{M} onto this object is given by

$$L_{\text{acc}} = \frac{GM\dot{M}}{R_*}. \quad (1.2)$$

We can also characterise the efficiency of any energetic process by relating the energy released to the rest mass energy of the parcel of mass, such that

$$\Delta E = \eta\Delta mc^2, \quad (1.3)$$

where η is the radiative efficiency. Similarly, in terms of luminosity, L ,

$$L = \eta\dot{M}c^2. \quad (1.4)$$

Nuclear fusion is one of the more efficient energetic processes in the universe, with an efficiency of $\eta = 0.007$. If we rearrange the above equations in terms of η , we find

$$\eta = \frac{G}{c^2} \frac{M}{R_*}. \quad (1.5)$$

Object	$M(M_\odot)$	$R_*(R_\odot)$	$M/R_*(M_\odot/R_\odot)$	η
White Dwarf	0.8	0.01	79.4	1.6×10^{-4}
Neutron Star	1.4	1.4×10^{-5}	10^5	0.2
Black Hole	10	4.2×10^{-6}	2.4×10^5	0.5
SMBH	10^9	4244	2.4×10^5	0.5

TABLE 1.1: Approximate values of compactness and accretion efficiency for four different compact objects with typical parameters. Here, R_* for black holes is set to the event horizon for a Schwarzschild black hole, whereas values of $\eta \sim 0.1$ in discs are more realistic due to the presence of an innermost stable orbit (see section 1.1.3). SMBH stands for supermassive black hole.

In other words, the efficiency of accretion is directly related to the *compactness*, M/R_* , of the central object. Values of compactness and the associated radiative efficiencies for four different compact objects are shown in table 1.1. The compactness for black holes was calculated using the Schwarzschild radius,

$$r_S = \frac{2GM}{c^2}, \quad (1.6)$$

which defines the event horizon of a non-rotating black hole. It is also pertinent to define the gravitational radius, $r_G = 1/2 r_S$, which can be useful as a characteristic scale for any compact object of mass M .

1.1.1 Spherical Accretion and The Eddington Limit

The simplest geometry one might propose for accretion would be one in which a central mass accretes matter in a spherically symmetric manner. The process of spherical accretion has come to be known as Bondi-Hoyle-Lyttleton accretion ([Hoyle & Lyttleton 1939](#); [Bondi & Hoyle 1944](#)). In particular, [Bondi \(1952\)](#) studied spherically symmetric accretion onto a point mass and derived the Bondi radius,

$$r_B = \frac{GM}{c_S^2}, \quad (1.7)$$

where $c_S = c_S(r_B)$ is the sound speed as a function of radius. The Bondi radius represents a critical point inside which the material is supersonic and will accrete on the free-fall timescale, τ_{ff} . For a cloud of uniform density, ρ_0 , this is given by

$$\tau_{\text{ff}} = \sqrt{\frac{3\pi}{32G\rho_0}}. \quad (1.8)$$

When this timescale is long enough, the accreting matter can radiate away its potential energy, generating a luminosity L . This radiation will exert a force on the electrons at radius r in the cloud, given by

$$F_{\text{rad}} = \frac{L\sigma_T}{4\pi r^2 c}, \quad (1.9)$$

where $\sigma_T = 6.65 \times 10^{-25} \text{ cm}^2$ is the Thomson cross-section. If this outward radiation force dominates over the inward pull of gravity, the material will no longer fall inwards. Consider radiation pressure acting on ionized hydrogen, for which the gravitational force is approximately given by $F_G \approx GMm_p/r^2$. Combining this expression with equation 1.9 gives a natural maximum accretion luminosity, known as the *Eddington limit*, of

$$L_{\text{Edd}} = \frac{4\pi GMm_p c}{\sigma_T}, \quad (1.10)$$

with an associated Eddington accretion rate of

$$\dot{M}_{\text{Edd}} = \frac{L_{\text{Edd}}}{\eta c^2}. \quad (1.11)$$

The Eddington limit depends on a number of assumptions, namely that the accretion flow is steady, spherically symmetric, ionized, and that its opacities are dominated by electron scattering. Clearly, there are many astrophysical situations where one or more of these assumptions do not hold. For example, the recent outburst of V404 Cyg showed wildly variable luminosities on short timescales (see, e.g., [Kuulkers et al. 2015](#); [Motta et al. 2015](#), among many, many Astronomer's Telegrams), and in any binary or disc dominated system the assumption of spherical symmetry will break down. Nevertheless, the Eddington limit provides a good order of magnitude estimate of the maximum luminosity of an accreting object, and also provides a useful way of parameterising accretion rates, as it scales linearly with mass. It can also be used to characterise the *state* of an accretion flow. In general, sources above $\sim 0.1 L_{\text{Edd}}$ find themselves in a ‘soft’ or thin-disc state (see section 1.1.2.1), whereas for much lower Eddington fractions, sources are expected to harbour geometrically thick, advection-dominated accretion flows (ADAFs; [Narayan & Yi 1994, 1995](#)) or, more generally, radiatively inefficient accretion flows (RIAFs). It is also clear that, near the Eddington limit, radiation pressure must play a major role in determining the disc morphology (see section 2.2.2).

1.1.2 Accretion Discs

In many astrophysical situations – for example, in binary systems and gas clouds orbiting black holes (BHs) – any accreting matter will possess some net angular momentum. If the medium is dense enough, collisions between particles will be frequent, but the total angular momentum vector of two colliding particles will always be conserved. This provides a mechanism for a gas cloud to relax to its minimum energy state – an accretion disc.

As well as losing gravitational potential energy as it falls towards the central mass, a parcel of matter must also lose its angular momentum. Crucially, accretion discs provide a way for this to happen. If the disc overall maintains the same total angular momentum, it follows that angular momentum must be transported outwards within the disc. The mechanism for transporting angular momentum outwards is unknown, and this is one of the biggest weaknesses of current accretion disc theory. Traditional molecular viscosity is insufficient in this regard ([Pringle 1981](#)). The reasons for this are readily apparent when we consider that molecular viscosity operates over the Debye length, λ_D , and at the sound speed, c_s . At density ρ , this results in a viscous force density ($\sim \rho \lambda_D c_s v_\phi / R^2$) that is much lower than the inertial force density ($\sim \rho v_\phi^2 / R$) – in other words, the Reynolds number is much greater than 1. The consequence is that molecular viscosity is dynamically unimportant in accretion flows.

An alternative mechanism for angular momentum transport is therefore necessary. The most commonly invoked candidate is the magnetorotational instability (MRI; [Balbus & Hawley 1991](#)), in which accretion discs are subject to a strong shearing instability even when the magnetic field is weak. Angular momentum could also be lost via a magnetohydrodynamic outflow ([Blandford & Payne 1982](#)) or transported by spiral shock waves ([Ju et al. 2016](#)), although in the former case the disc would actually be dark if a wind extracted all the angular momentum (e.g. [Spruit 1996](#); [Knigge 1999](#)). Given the uncertainty about the transport mechanism, it is convenient to simply parameterise the unknown physics in an *effective viscosity*.

1.1.2.1 Steady-state Accretion Discs: the α -prescription

The so-called α -disc model developed by [Shakura & Sunyaev \(1973\)](#), hereafter SS73) and [Lynden-Bell \(1969\)](#) is a simple approximation for how energy and angular momentum

are transported in an accretion disc and provides useful insights into the disc's expected observational appearance. The starting point for this model is a parameterisation of the viscosity, ν' , using the simple form

$$\nu' = \alpha c_s H, \quad (1.12)$$

where H is the scale height of the disc, α is a parameter ≤ 1 , and c_s is the sound speed. Viscous torques then allow the conversion of orbital kinetic energy into heat, which can be radiated away. If we make one further assumption, that the accretion rate is constant throughout the disc, we can write down a mass continuity equation valid at any radius, given by

$$\dot{M} \equiv 2\pi R v_R \Sigma = \text{constant}, \quad (1.13)$$

where Σ is the surface density at that radius and v_R is the radial ‘drift’ velocity towards the compact object. The angular momentum equation then becomes

$$\nu' \Sigma = \frac{\dot{M}}{3\pi} \left[1 - \left(\frac{R_*}{R} \right)^{1/2} \right]. \quad (1.14)$$

The viscous torques throughout the disc cause a local loss of mechanical energy, allowing us to derive (see, e.g. Frank et al. 1992) a rate of viscous dissipation, per unit area, given by

$$D(R) = \frac{1}{2} \nu' \Sigma (R \Omega')^2. \quad (1.15)$$

Here, $D(R)$ is proportional to the derivative of the angular velocity, $\Omega' = d\Omega/dR$. By combining equations 1.15 and 1.14, we can show that the viscous dissipation rate is

$$D(R) = \frac{GM\dot{M}}{8\pi R^3} \left[1 - \left(\frac{R_*}{R} \right)^{1/2} \right], \quad (1.16)$$

where we have also set the angular velocity to the Keplerian velocity. This expression is independent of viscosity – which is fortunate, because we do not know what value of α to use in equation 1.12. This result comes about because of the implicit assumption that the viscosity regulates the mass accretion rate so as to achieve a steady state.

We can now integrate across both sides of the whole disc to obtain the disc luminosity,

$$L_{\text{disc}} = 2 \int_{R_*}^{\infty} D(R) 2\pi R dR = \frac{GM\dot{M}}{2R_*} = \frac{1}{2} L_{\text{acc}}. \quad (1.17)$$

This result can also be shown by considering the difference in gravitational binding energy of gas in Keplerian rotation at $R = R_*$ and $R = \infty$. From equation 1.16, an effective temperature distribution can be derived by setting

$$\sigma T_{\text{eff}}^4(R) = D(R), \quad (1.18)$$

which then gives

$$T_{\text{eff}}(R) = T_* \left[1 - \left(\frac{R_*}{R} \right)^{1/2} \right]^{1/4}, \quad (1.19)$$

where

$$T_* = \left(\frac{3GM\dot{M}}{8\pi R_*^3 \sigma} \right)^{1/4}. \quad (1.20)$$

When $R \gg R_*$ this simplifies to

$$T_{\text{eff}}(R) = T_* (R/R_*)^{-3/4}. \quad (1.21)$$

Now we have not only derived the total luminosity of an accretion disc, but also the effective temperature profile which will govern the shape of the emergent SED. This temperature profile is shown in Fig. 1.1 for three different compact objects, assuming an Eddington fraction of 0.2.

1.1.3 Boundary Layers, Black Hole Spin and the ISCO

In equation 1.17, we found that $L_{\text{disc}} = 1/2 L_{\text{acc}}$. One might then ask: where does the rest of the luminosity go? Alternatively, what happens to the kinetic energy the material has at the inner disc edge? The answer is dependent on the compact object in question. In an accreting WD, the rotating matter must eventually deposit itself on the surface of the WD. This is illustrated in Fig. 1.2, which shows the angular velocity as a function of radius in a disc around a compact object rotating with angular velocity Ω_* . The boundary layer (BL) is the region to the left of the dotted line, inside the maximum of Ω , the angular velocity. The luminosity of the boundary layer is (Frank et al. 1992)

$$L_{BL} = \frac{1}{2} \frac{G M \dot{M}}{R} \left[1 - \left(\frac{\Omega_*}{\Omega_K(R_*)} \right) \right]^2, \quad (1.22)$$

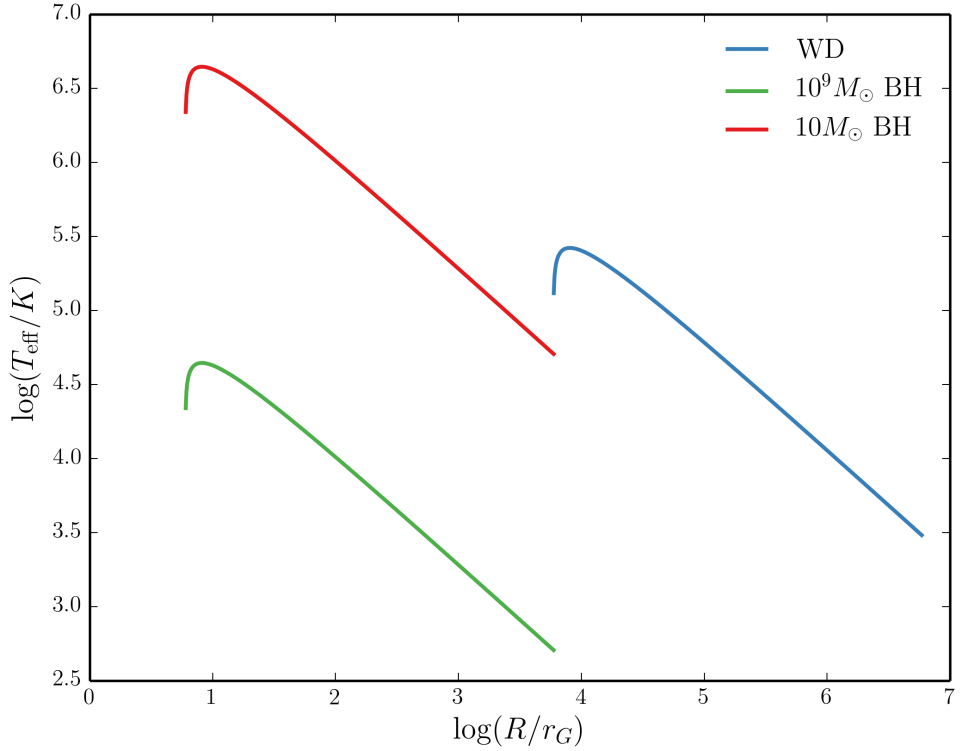


FIGURE 1.1: The temperature profile of an accretion disc for three different classes of compact object.

where $\Omega_K(R_*)$ is the Keplerian angular velocity at R_* , assuming the thickness, b , of the BL is small. When $\Omega_K(R_*) \gg \Omega_*$, this reduces to $L_{BL} = 1/2 L_{\text{acc}} = L_{\text{disc}}$. Any remaining energy is imparted to the WD as rotational energy.

In cataclysmic variables, BLs can be approximated with blackbodies and their temperatures estimated indirectly via the [Zanstra \(1929\)](#) method (e.g. [Hoare & Drew 1991, 1993](#)). However, they likely exhibit a variety of atomic features ([Suleimanov et al. 2014](#)). Extreme-UV (EUV) datasets have confirmed the existence of boundary layer emission in non-magnetic CVs ([Mauche 1996](#)), although these observations are limited in number.

Clearly, in BH systems a boundary layer cannot exist in the same way, due to the lack of a physical surface. Instead, the energy must either go into growing the BH, contributing to its angular momentum or being channeled into a jet or other radiative source (see section 1.5.2). The question of what happens at the inner disc edge is complicated further by the fact that the disc cannot extend to the event horizon of the BH. Instead, there is an ‘innermost stable circular orbit’ (ISCO) beyond which the accreting matter will simply fall into the BH along nearly radial paths. The radius of this orbit, R_{ISCO} ,

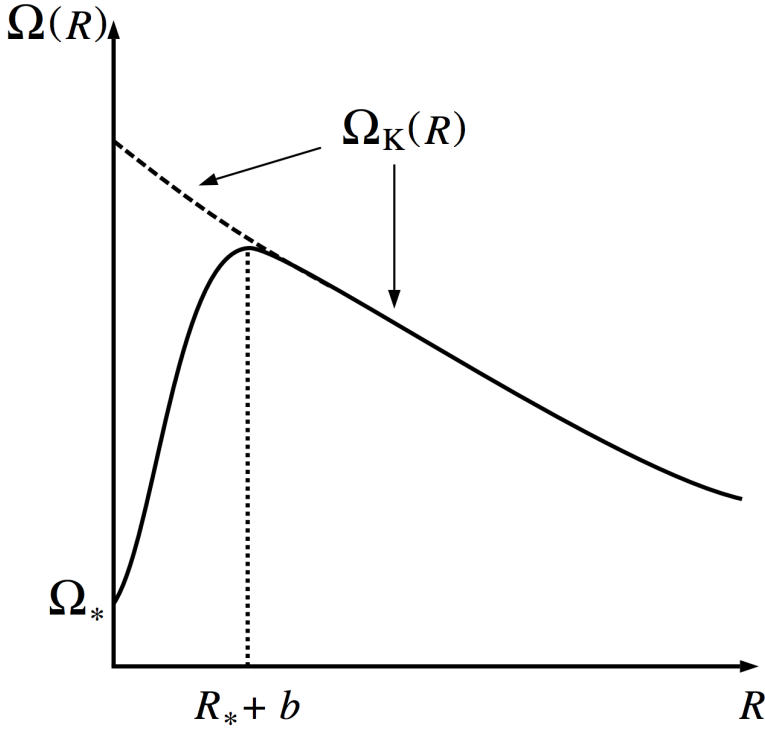


FIGURE 1.2: Credit: Frank et al. 2002. Angular velocity as a function of radius in an accretion disc around a rotating compact object with angular velocity Ω_* . Ω_K is the Keplerian angular velocity. This graph also helps explain why there is a turnover in the temperature-radius relation, as $D(R)$ is proportional to the square of the *derivative* of this quantity. The boundary condition responsible for this turnover is briefly discussed in the text.

and the horizon radius, R_H , is shown for different values of the BH spin parameter, a_* , in Fig. 1.3, showing how matter can orbit closer to a prograde spinning BH. In estimating the luminosity of a Keplerian disc around a BH, we should really set $R_* = R_{\text{ISCO}}$ when calculating the BH accretion efficiency, giving the interesting result that rapidly spinning (Kerr) BHs are more radiatively efficient than Schwarzschild BHs. A proper relativistic calculation of the binding energy at the ISCO gives accretion efficiencies of $\eta_{\text{ISCO}} \approx 0.06$ $\eta_{\text{ISCO}} \approx 0.4$ for Schwarzschild and Kerr BHs, respectively (e.g. Thorne 1974). The lack of an inner surface in the BH case also poses a problem to the SS73 model, as it assumed that the viscous torques go to zero at the inner boundary of the disc. This boundary condition may not be appropriate for BHs as it fails to properly describe the physics at the ISCO (e.g. Abramowicz & Fragile 2013). As a result, the turnover in the temperature profile caused by this boundary condition may not be present for BH discs.

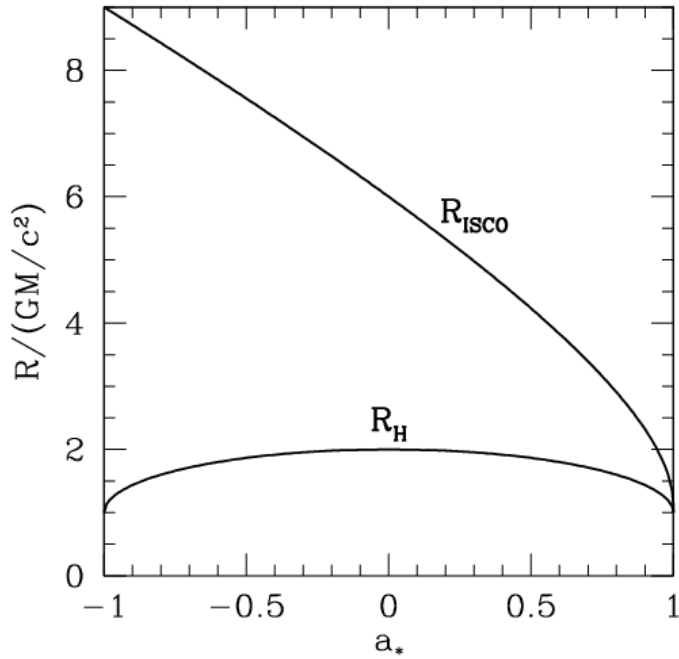


FIGURE 1.3: Credit: Narayan 2014. The radius of the ISCO, R_{ISCO} , and the horizon, R_H , is as a function of the BH spin parameter, a_* . $a_* = 0$ corresponds to a Schwarzschild BH, and $a_* = 1$ and $a_* = -1$ to prograde and retrograde Kerr BHs, respectively. Note that this figure ignores the counteracting torque of photons swallowed by the BH, which actually limits a_* to a value of around 0.998 (Thorne 1974).

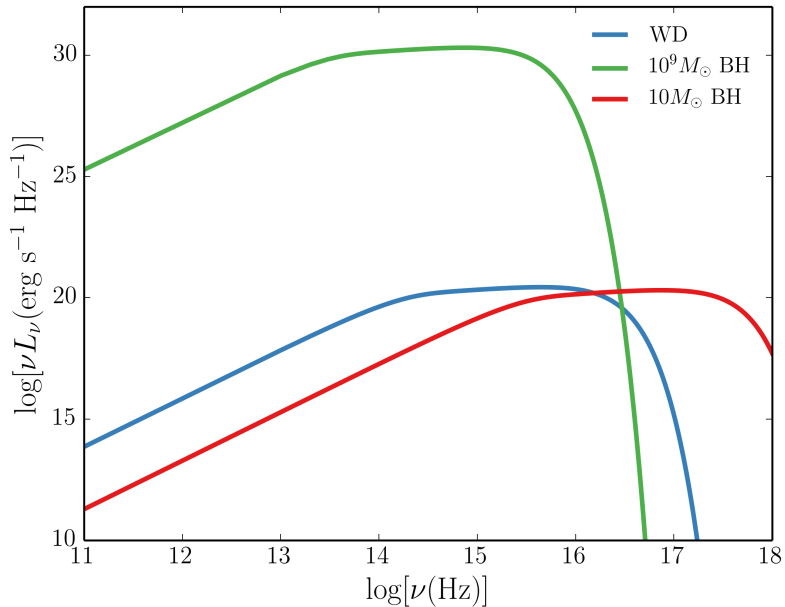


FIGURE 1.4: Accretion disc SEDs for three different compact objects, corresponding roughly to a quasar, an XRB and a CV. The SEDs are computed via an area-weighted sum of blackbodies with effective temperatures governed by equation 1.19, and the $\nu^{1/3}$ shape in the middle of the spectra can be seen.

1.1.4 The Emergent Spectrum

It is important to recognise that the steady-state disc treatment *does not specify the exact shape of the disc SED*. What it does do is say where energy is originally released. The simplest assumption is that each annulus emits as a blackbody with temperature $T_{\text{eff}}(R)$, i.e. that the specific intensity through the emitting surface follows Planck's law:

$$B_\nu(T) = \frac{2h\nu^3}{c^2} \frac{1}{\exp(h\nu/kT) - 1}. \quad (1.23)$$

Under this assumption, it is possible to show that at intermediate frequencies, where $kT(R_{\text{max}}) \ll h\nu \ll kT_*$, the spectrum appears as a ‘stretched blackbody’, with monochromatic flux, F_ν , of the form

$$F_\nu \propto \nu^{1/3}. \quad (1.24)$$

Fig. 1.4 shows the blackbody SEDs expected for the same objects as in Fig. 1.1, in which the $\nu^{1/3}$ portion can be clearly seen. A stellar atmosphere model with frequency-dependent opacity creates a somewhat different (and more realistic) spectrum. Fig. 1.5 shows a comparison between a disc spectrum computed with stellar atmosphere models and standard multi-temperature blackbody disc, showing how the two treatments can have a significantly different spectral shape when one includes frequency-dependent opacities in the atmosphere. It is of course possible that *neither* a blackbody treatment or the current stellar atmosphere models produce accurate disc spectra. I shall therefore devote a little time to discussing the observational appearance of accretion discs and reviewing the different classes of accreting objects.

1.2 Accreting Compact Binaries

Accreting compact binaries form many different classes, but all are characterised by matter streaming from a donor onto a compact object. When the compact object is more massive than the donor, it is designated as the ‘primary’, and its companion as the ‘secondary’. In high-mass X-ray binaries (HMXBs), the opposite is formally true. There are only two ways by which matter can transfer from the secondary to the compact object. One is by Roche lobe-overflow (RLOF), where the donor star expands to fill its Roche lobe, a critical surface of equipotential around the star (see section 1.2.1). The alternative is that the donor may expel material in an outflow, some of which can be

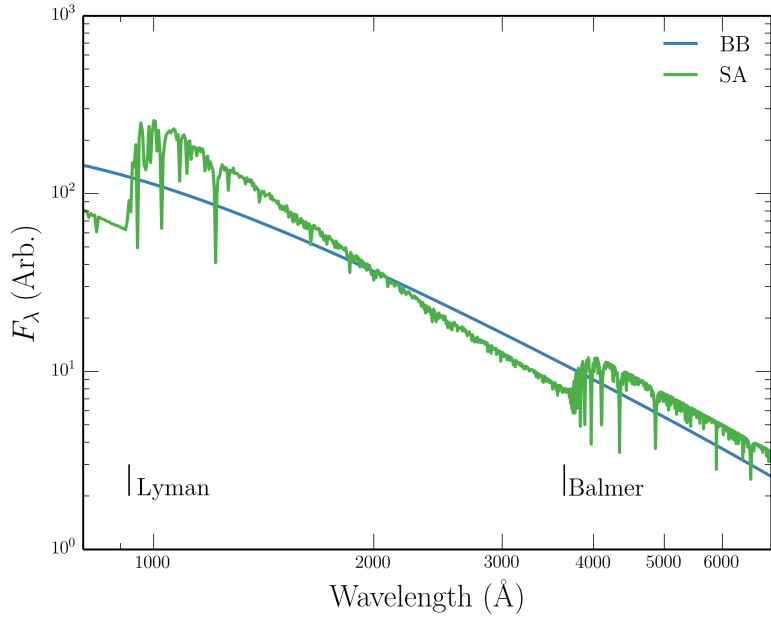


FIGURE 1.5: A comparison between a disc spectrum computed with stellar atmosphere models and standard multi-temperature blackbody disc. The major photoabsorption edges are marked. Flux is reprocessed into different wavelengths by bound-free opacities, and line blanketing also has a big effect on the spectrum. The Hydrogen and Helium lines also experience a degree of pressure broadening.

captured by the compact object. Although accretion from a wind or circumstellar disc is common in HMXBs (Bartlett 2013), here I will focus on RLOF as it is more common in the systems that possess high-state accretion discs and associated outflows. Two examples of these are shown in Fig. 1.6

1.2.1 Roche Lobe-Overflow

Let us consider a binary system containing two point sources with masses M_1 and M_2 at positions \vec{r}_1 and \vec{r}_2 . The Roche potential, Φ_R , in this system is then

$$\Phi_R = -\frac{GM_1}{|\vec{r} - \vec{r}_1|} - \frac{GM_2}{|\vec{r} - \vec{r}_2|} - 1/2(\vec{\omega} \times \vec{r})^2, \quad (1.25)$$

where $\vec{\omega}$ is the angular velocity of the binary and is a vector normal to the orbital plane. This potential is plotted in Fig. 1.7 for a mass ratio, $q_M = M_2/M_1 = 0.25$.

In the context of semi-detached binary systems, the most important equipotential is the dumbbell-shaped region enclosing both masses. Each of these enclosed regions is known as the ‘Roche lobe’ of the object. A good approximation for the size of the Roche lobe

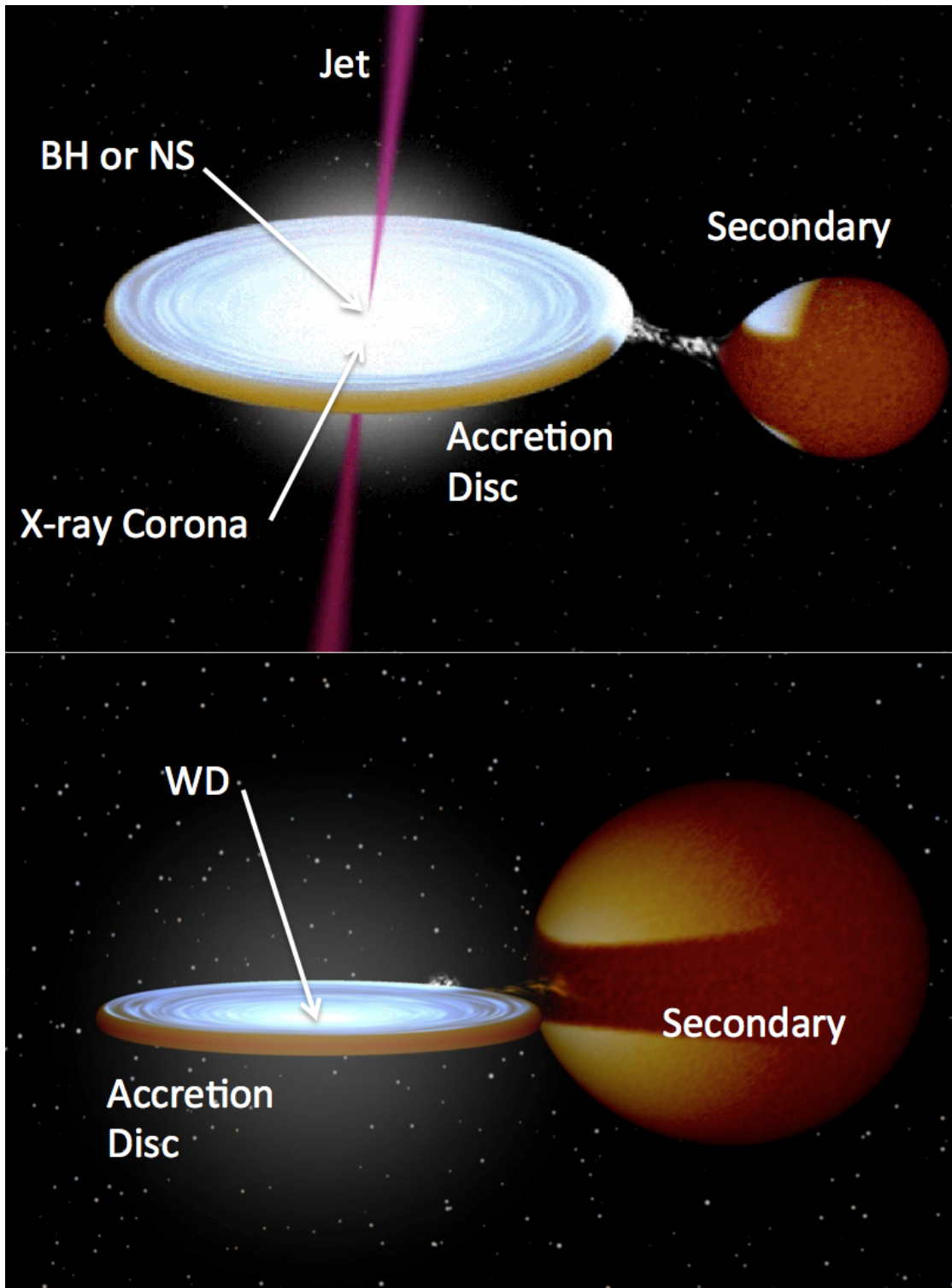


FIGURE 1.6: Credit: Rob Hynes. Artist's impression of a low-mass X-ray binary (top) and cataclysmic variable (bottom). The key components are marked, and the clear similarity in overall structure is apparent.

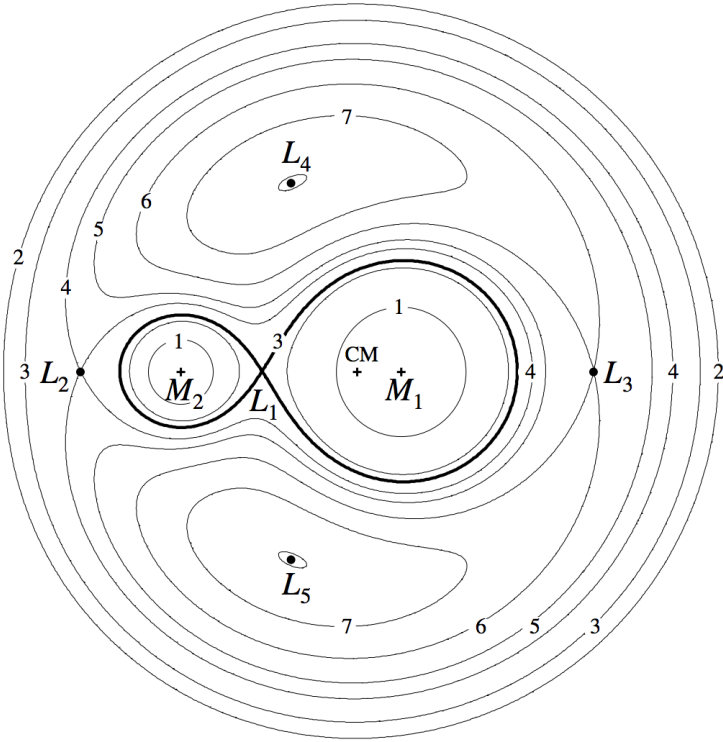


FIGURE 1.7: Credit: Frank et al. 2002. The Roche potential in a binary system for $q_M = M_2/M_1 = 0.25$. The Lagrangian points are marked, as are the locations of the individual and system centres of mass.

takes the form ([Eggleton 1983](#))

$$\frac{R_2}{a} = \frac{0.49 q_M^{2/3}}{0.6 q_M^{2/3} + \ln(1 + q_M^{1/3})}. \quad (1.26)$$

Here, R_2 is the radius of a sphere with the same volume as the Roche lobe for the secondary star, which we can see depends only on q_M and the orbital separation, a . If this secondary expands enough to fill its Roche lobe, then matter will fall onto the other object through the L_1 Lagrangian point. This process is known as Roche lobe overflow (RLOF) and is vitally important in astrophysics. Any accretion from RLOF will alter the mass ratio of the binary system and thus affects the evolution of binary systems. This is reflected in the orbital period distribution of binaries (e.g. [Knigge et al. 2011](#)) and also affects the delay time distribution of Type Ia Supernovae, for which CVs are one of the progenitor candidates (e.g. [Wang & Han 2012](#)). It is also worth noting that the existence of gravitational waves has been required in models to explain the orbital period evolution of CVs since the 1960s ([Kraft et al. 1962](#)).

1.2.2 Cataclysmic Variables

Cataclysmic variables (CVs) are systems in which a WD accretes matter from a donor star via Roche-lobe overflow (see the ‘CV bible’, [Warner 2003](#)). CVs are not always dominated by their accretion luminosity; for example, novae undergo dramatic eruptions caused by thermonuclear runaway, and the so-called ‘supersoft sources’ show evidence of nuclear burning on the WD surface. Accretion-dominated CVs – the focus here – can be classified according to the magnetic field strength of their WD primary (B_{WD}) and their photometric activity. Magnetic systems are classified as either ‘Polars’ ($B_{WD} \gtrsim 10^7$ G) or ‘Intermediate Polars’ (IPs; $10^6 \lesssim B_{WD} \gtrsim 10^7$ G); in these systems the accretion flow inside the some critical radius (related to the Alfvén radius) is dominated by the WDs magnetic field. In polars, this radius is large enough, due to the strong magnetic field, that no disc forms at all ([Liebert & Stockman 1985](#)). In IPs the accretion disc is truncated at the magnetospheric boundary, and accretion ‘curtains’ channel the material onto the WD (e.g. [Patterson 1994](#); [Evans et al. 2004](#)). When $B_{WD} \lesssim 10^6$ G the accretion disc can extend all the way down to the WD boundary, and the CV is classified as non-magnetic. Here, I consider only non-magnetic CVs, which come in two flavours: dwarf novae and nova-like variables.

1.2.2.1 Dwarf Novae and the Disc-instability Model

Dwarf novae (DNe) are CVs that are characterised by repeated cycles of quiescence – where the system is in a faint, low flux state – followed by a dramatic bright outburst. One of the most famous DNe is SS Cyg, whose light curve is shown in Fig. 1.8. The repeated outbursts can be clearly seen, and SS Cyg itself has been undergoing this behaviour over the full century for which it has been observed. A spectrum over the course of a typical outburst is shown in Fig. 1.9 and is characterised by the appearance of a blue, optically thick accretion disc continuum – note the similarity to the stellar atmosphere disc spectrum computed in section 1.1.2.1 and to the intermediate inclination nova-like variables discussed in the next section.

The leading scenario for explaining DN outbursts, and in fact also the outbursts in low mass X-ray binaries or ‘soft X-ray transients’, is the disc-instability model (DIM; [Osaki 1974](#); [Hōshi 1979](#); [Meyer & Meyer-Hofmeister 1981](#); [Lasota 2001](#)). In this model, the disc is in a cool, low viscosity state in quiescence, and H is mostly neutral. The constant mass

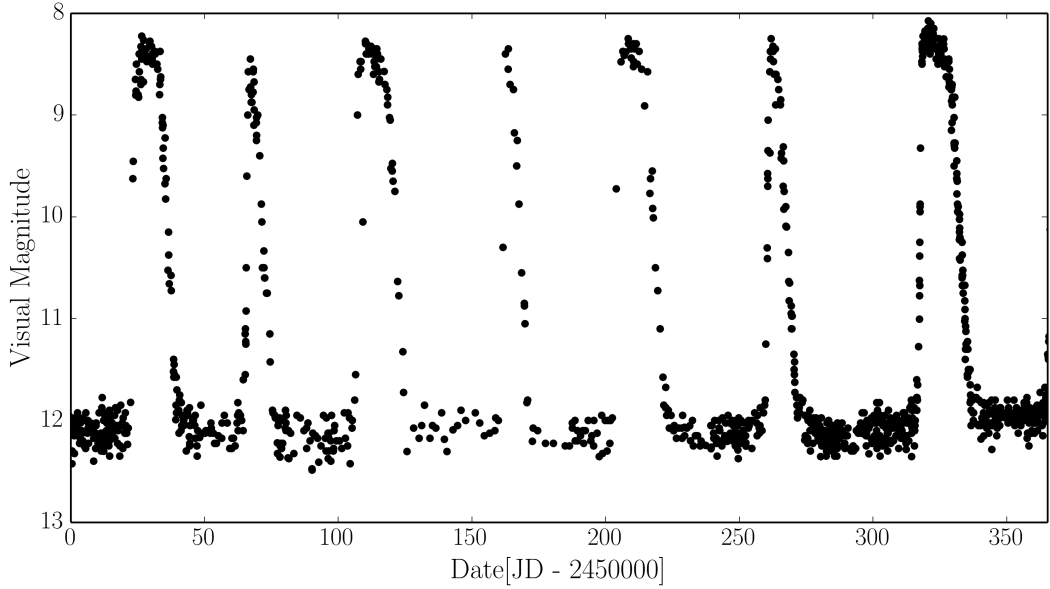


FIGURE 1.8: *Data: AAVSO.* A year in the life of SS Cyg, showing the characteristic repeated outbursts and periods of quiescence typical of a DN. SS Cyg has been undergoing this activity since it was first observed in 1896.

supply from the donor causes a gradual build up of mass in the disc. Eventually, the disc hits a critical temperature, around 7000 K, and H becomes ionized. This causes an increase in viscosity and temporarily allows a higher accretion rate through the disc. In this state, the disc becomes geometrically thin and optically thick. It can now undergo efficient radiative cooling, meaning that a significant increase in brightness is observed. This state is relatively short-lived, as the accretion rate through the disc will be lower than the supply rate from the donor star, so eventually the disc will drop below the critical temperature and back onto the cool, low viscosity branch.

1.2.2.2 Nova-like Variables

Nova-like variables (NLs) are similar to DNe, except that the disc is always in a relatively high-accretion-rate state ($\dot{M} \sim 10^{-8} M_{\odot} \text{ yr}^{-1}$). NLs are therefore one of the best ‘laboratories’ for testing the steady-state accretion disc theory described in section 1.1.2.1. In the optical, NLs generally exhibit a series of H and He emission lines superposed on a blue continuum. In many cases, and particularly in the SW Sex subclass of NLs (Honeycutt et al. 1986; Dhillon & Rutten 1995), these lines are single-peaked. This is contrary to theoretical expectations for lines formed in accretion discs, which are predicted to be double-peaked (Smak 1981; Horne & Marsh 1986). *Low-state* CVs (dwarf novae in quiescence) do, in fact, exhibit such double-peaked lines (Marsh & Horne 1990).

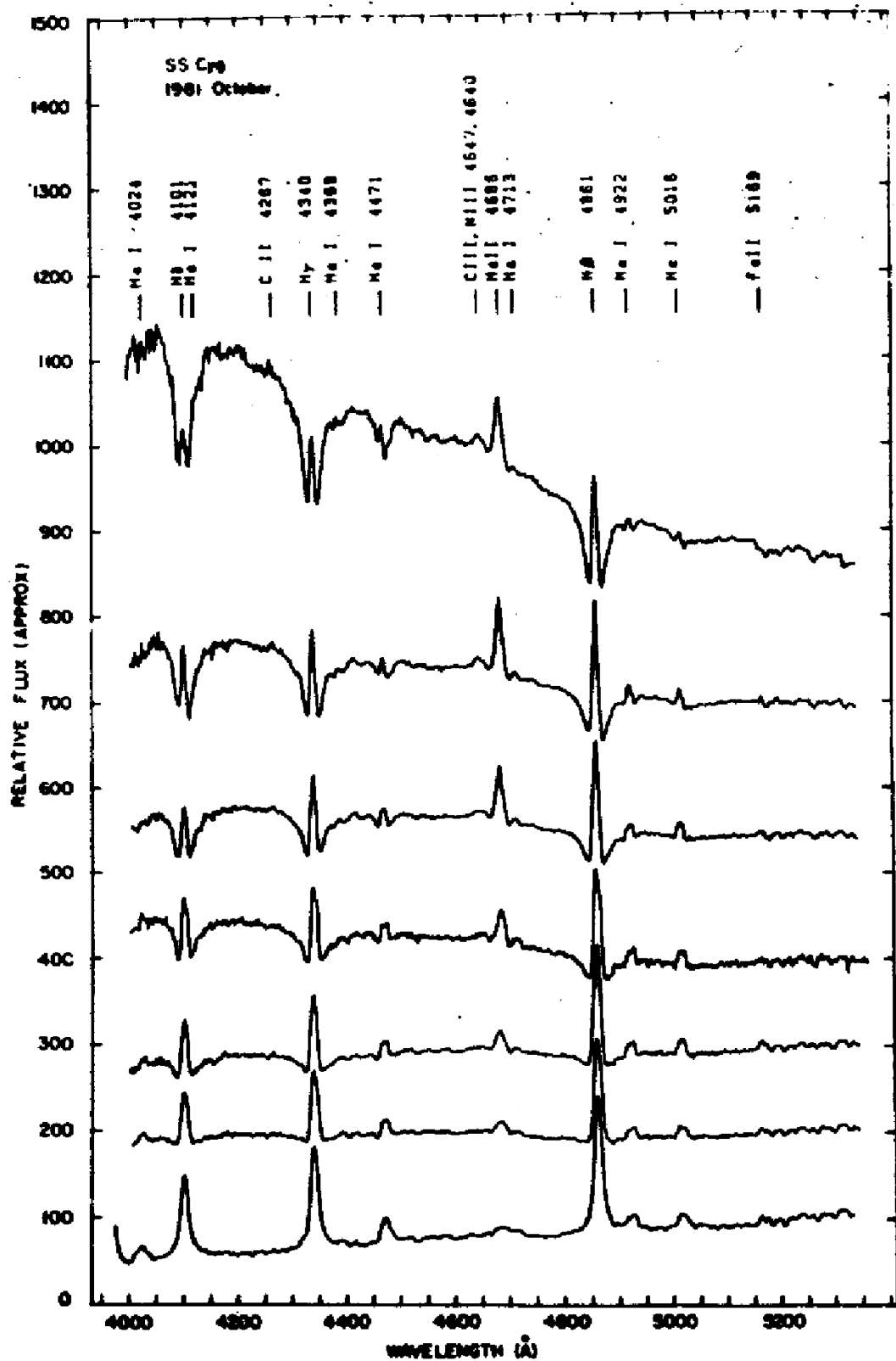


FIGURE 1.9: Credit: Hessman et al. 1984 / Dhillon et al. 1996. Spectra of SS Cyg during an outburst cycle, showing the evolution from minimum to maximum light. The rise is characterised by the appearance of an optically thick accretion disc spectrum. The flux scale is approximate.

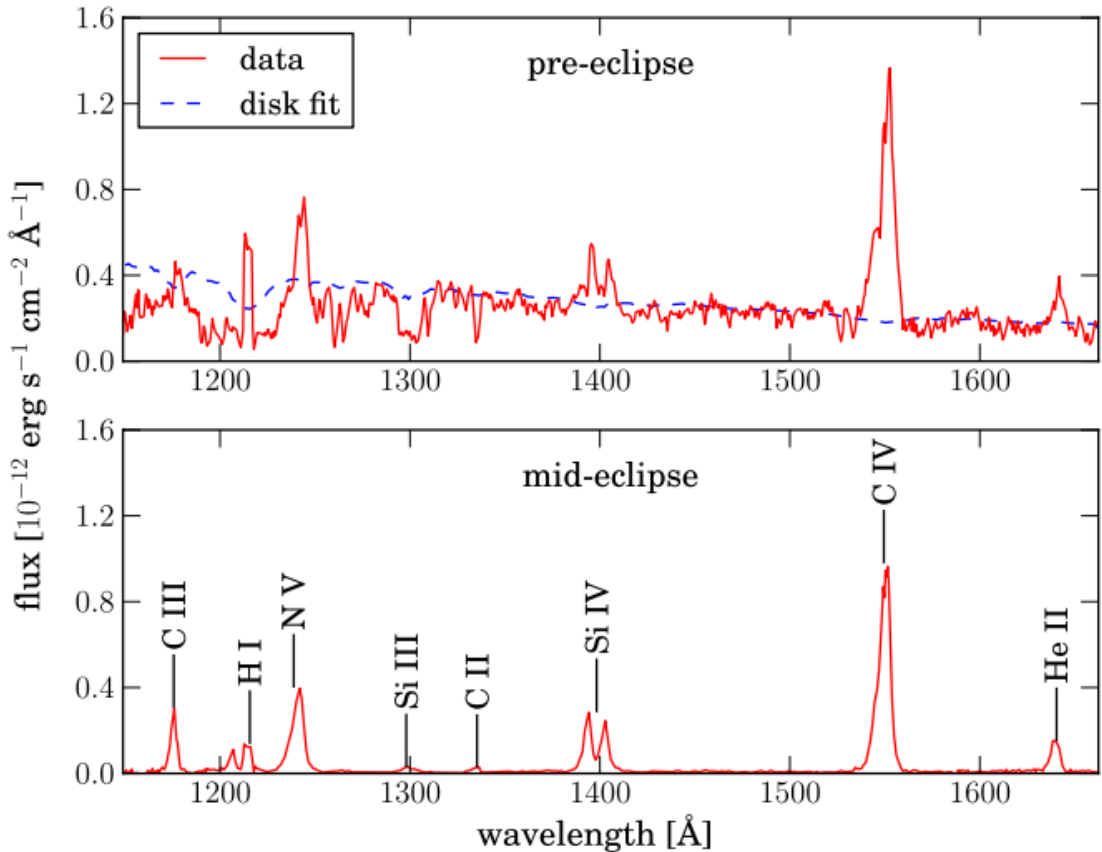


FIGURE 1.10: Credit: Noebauer et al. 2010. UV spectrum of RW Tri in and out of eclipse, showing strong lines in C IV 1550 Å and Ly α , among others.

The UV spectra of NLs also show strong emission lines (see Fig. 1.10), and at low to intermediate inclinations dramatic blue-shifted absorption lines can be seen in some objects (see section 2.1.1). The emission line equivalent widths in both the optical and the UV show clear trends with inclination (Hessman et al. 1984; Echevarria 1988; Noebauer et al. 2010). This can be seen clearly in Fig. 1.11 and is connected to the correlation between line strength and absolute magnitude found by Patterson (1984); that is, the decrease in equivalent width at low inclination is caused by an *increase* in continuum flux, rather than a decrease in line flux. This is discussed further in chapters 4 and 6, but also has relevance to AGN and quasar unification schemes mentioned later in this introduction. The optical and UV spectra of NL CVs are discussed further in the context of winds in chapter 2.

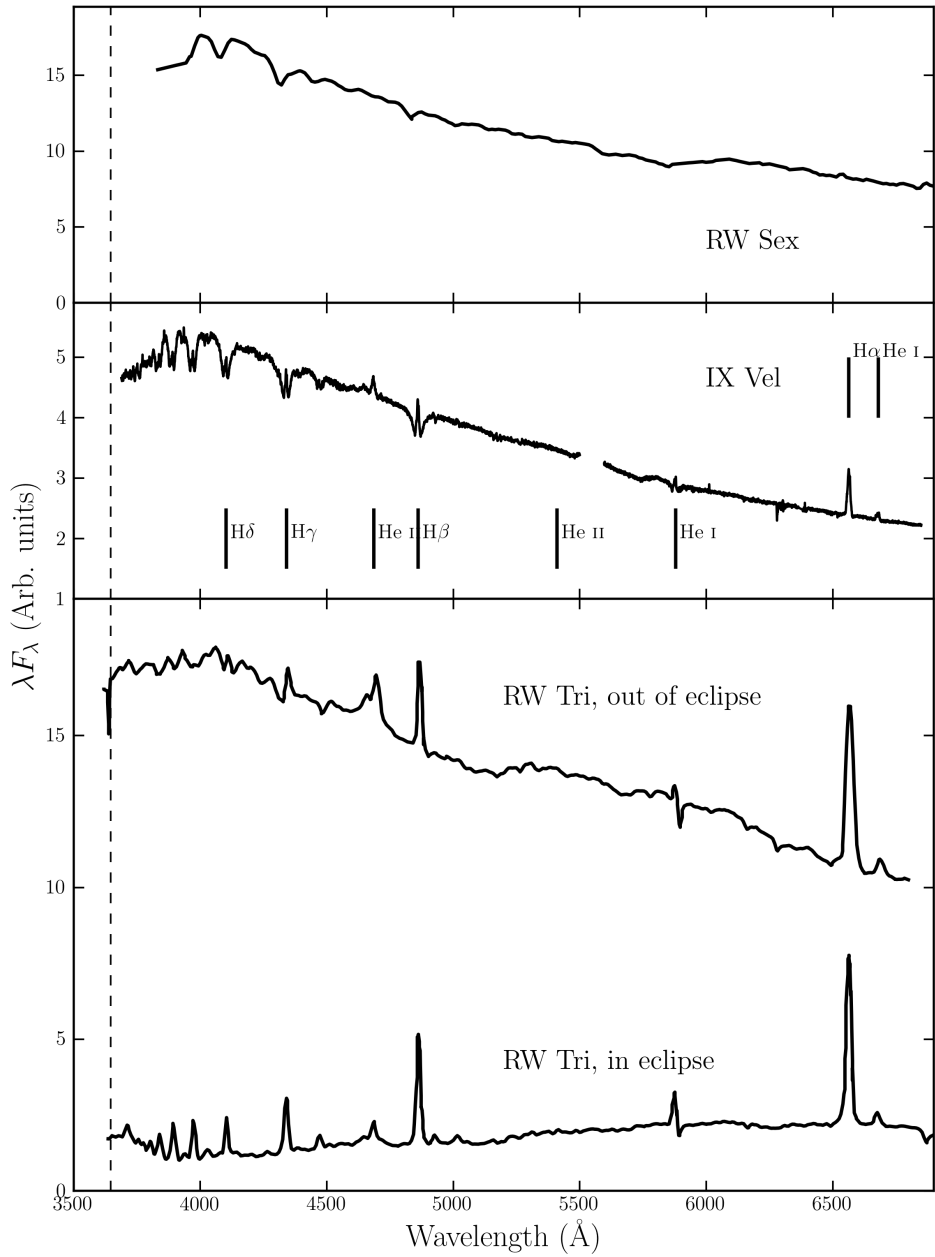


FIGURE 1.11: Optical spectra of three nova-like variables: RW Sex (top; Beuermann et al. 1992), IX Vel (top middle; A. F. Pala & B. T. Gaensicke, private communication) and RW Tri in and out of eclipse (bottom two panels; Groot et al. 2004). The data for RW Sex and RW Tri were digitized from the respective publications, and the IX Vel spectrum was obtained using the XSHOOTER spectrograph on the Very Large Telescope on 2014 October 10. These systems have approximate inclinations of 30°, 60° and 80° respectively. The trend of increasing Balmer line emission with inclination can be seen. In RW Tri strong single-peaked emission in the Balmer lines is seen even in eclipse, indicating that the lines may be formed in a spatially extensive disc wind, and there is even a suggestion of a (potentially wind-formed) recombination continuum in the eclipsed spectrum. I have attempted to show each spectrum over a similar dynamic range.

1.2.3 Low Mass X-ray Binaries

Although I do not study low-mass X-ray binaries (LMXBs) directly in this thesis, it is instructive to briefly discuss their observational appearance, as it is relevant to the connections between accretion and outflows. LMXBs are similar to CVs in structure (see Fig. 1.6), but the compact object is either a neutron star (NS) or a black hole (BH). The accretion disc emits in the soft X-ray regime, and an additional hard X-ray power law is also seen in the spectrum. This hard component is normally attributed to Compton up-scattering of seed disc photons by some kind of ‘corona’ of hot electrons close to the BH (e.g. [White et al. 1988](#); [Mitsuda et al. 1989](#); [Uttley et al. 2014](#)). The discovery that XRBs and CVs follow similar tracks on a hardness-intensity diagram (HID; [Körding et al. 2008](#)) is particularly interesting, especially since [Ponti et al. \(2012\)](#) showed that broad Fe absorption lines are only seen in the soft-state high-inclination systems (see section 2.1.2). This implies that equatorial outflows may be intrinsic to the accretion process. Although the outflow driving mechanism is probably different to CVs (e.g. [Díaz Trigo & Boirin 2015](#)), the general structure of LMXBs – that of a disc around a compact object with an associated outflow – is strikingly similar to models for CVs and quasars.

1.3 Quasars and Active Galactic Nuclei

Spectra of AGN have now been studied for over 100 years, and we have known that they exhibit strong, broad emission lines since the first spectrum was taken by [Fath \(1909\)](#). However, it wasn’t until the work of [Seyfert \(1943\)](#) that the systematic classification of AGN really began, leading to the phrase ‘Seyfert galaxy’. This label was applied to galaxies possessing a bright nucleus, spectroscopically characterised by a blue continuum and a series of strong emission lines. The first real physical insight into the extraordinary nature of AGN was provided by [Woltjer \(1959\)](#), who noted that (i) the nuclei must have sizes < 100 pc, based on the fact that they were unresolved, and (ii) the mass of the nucleus must be very high, based on virial estimates. While both of these observations were based on simple arguments, the fact that these ultra-luminous celestial objects are both *compact* and *supermassive* is perhaps the defining insight into the nature of AGN.

Although the study of AGN was established in the optical waveband, radio astronomy also significantly furthered our understanding of AGN in the mid-20th century. A number of surveys, such as the Cambridge ([Edge et al. 1959](#)), Parkes ([Ekers 1969](#)) and

Ohio ([Ehman et al. 1970](#)) surveys discovered a great many bright radio point sources distributed isotropically across the sky. These sources eventually became known as ‘quasi-stellar radio sources’, or *quasars*, and were soon found to be coincident with bright optical sources or ‘quasi-stellar objects’ (QSOs) at high redshifts ([Schmidt 1963, 1965a,b](#)). Nowadays, the term quasar normally has very little to do with radio emission and is often used interchangeably with QSO. Indeed, throughout this thesis I shall use the term quasar simply to mean a bright, massive AGN; with a sufficiently high luminosity to dominate the emission from its host galaxy.

One of the main classification schemes for AGN is a spectroscopic one, based on whether an object possesses broad emission lines in its spectrum, such as C IV, H β and Ly α , in addition to the narrow lines that are always present. If these broad lines are seen, then the AGN is classed as type 1; if not, it is classed as type 2 ([Fig. 1.12](#)). These designations were originally applied to Seyfert galaxies ([Seyfert 1943](#)), but can also be used to classify the more luminous quasar class, despite the apparent difficulty in finding the expected number of type 2 quasars ([Zakamska et al. 2003](#)). This classification scheme is complicated somewhat by the existence of two unusual types of AGN: narrow line Seyfert 1s (NLSIs), which may be explained by super-Eddington accretion ([Done & Jin 2015](#)) or perhaps simply an orientation effect ([Baldi et al. 2016](#)), and so-called ‘true type 2’ AGN, in which the broad line region is absent ([Tran 2001; Shi et al. 2010](#)) rather than obscured (see next section). Despite this muddying of the waters, what was originally a clear dichotomy in spectral type provided a profound motivation for attempting to *unify* AGN via geometric arguments.

1.3.1 AGN Unification and the Dusty Torus

Although Seyfert had identified type 1 and 2 AGN, a physical explanation for this dichotomy was not forthcoming until a study by [Antonucci & Miller \(1985, AM85\)](#). They showed unambiguously that the nearby Seyfert 2 NGC 1068 is simply an obscured type 1 AGN, by finding that broad emission lines appeared in the spectrum of *polarised* flux. This provided the basis for the first successful attempt to unify AGN behaviour, as it elegantly explained the apparent disconnect between the two types of AGN as simply a viewing angle effect: in type 1s, an observer can look directly into the broad line region (BLR) near the nucleus, but, in type 2s, this region is hidden from view. Narrow lines are seen in both types as they are formed in the narrow-line region (NLR), which is on

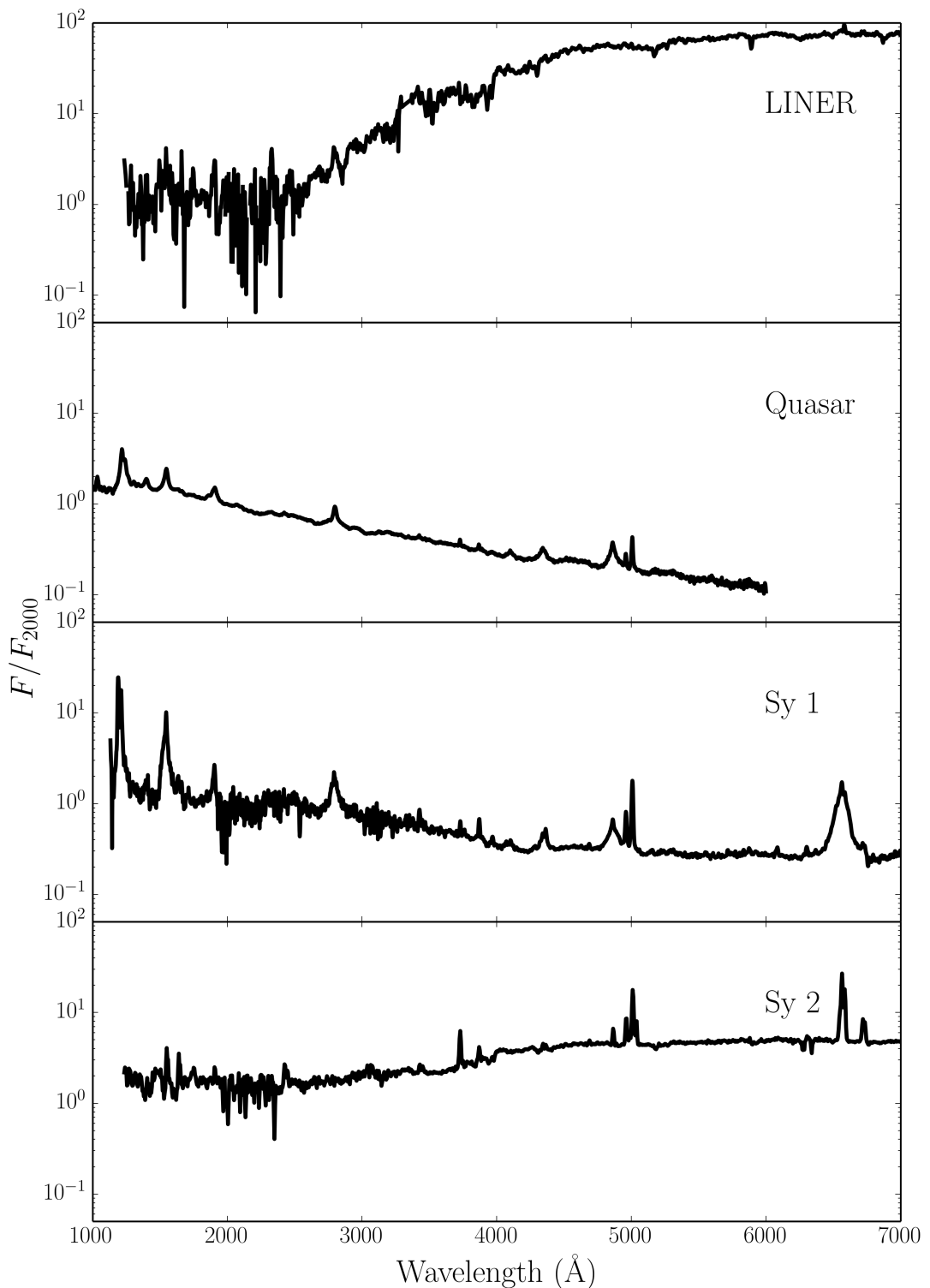


FIGURE 1.12: Template spectra, from the AGN atlas, for four common types of AGN.
Obtained from http://www.stsci.edu/hst/observatory/crds/cdbs_agn.html.

a significantly larger scale and is thus always visible. The obscuring structure became known as the ‘torus’ (Krolik & Begelman 1986), due to its proposed geometry, and it was soon realised that this structure may be made of dust, in which case it could also be responsible for the infra-red (IR) bump in AGN spectra (Neugebauer et al. 1979).

Urry & Padovani (1995, UP95) went further than the original unification model proposed by AM85, as they also tried to account for the dichotomy in AGN radio properties (radio-loud/radio-quiet). The picture they proposed is shown in Fig. 1.13. This model attempts to explain all types of AGN solely in terms of viewing angle and presence, or absence, of a radio jet. Models such as this also describe the series of ‘bumps’ observed in AGN – the portions of the spectrum that dominate the luminosity, shown in Fig. 1.14. In most models, the ‘Big Blue Bump (BBB)’ is ascribed to thermal emission from an accretion disc, and the ‘Small Blue Bump’ to optically thin Balmer continuum and Fe II emission from the BLR. The latter can just be seen between $\sim 2000 \text{ \AA}$ and $\sim 4000 \text{ \AA}$ in the Seyfert 1 and quasar templates in Fig. 1.12. Our understanding of the BBB is still unsatisfactory (see section 1.4).

Since the seminal works by AM85 and UP95, the picture has become somewhat more complicated. Variable X-ray absorption has been detected in so-called ‘changing look’ AGN (Matt et al. 2003; Puccetti et al. 2007), including even NGC 1068 itself (Marinucci et al. 2016). Changes in type have also been seen in the optical lines; the broad H β component in some AGN can dramatically disappear or reappear (e.g. Tohline & Osterbrock 1976; Cohen et al. 1986; Denney et al. 2014). The explanation for this could be variable absorption (Elitzur 2012) or a change in the accretion state of the disc. In the latter case, it has even been suggested that a disc wind could be directly responsible for this switch (Elitzur et al. 2014). Furthermore, dusty *polar* outflows have been found to be important IR emitters (Hönig et al. 2013), implying that, even when it comes to dust, the torus is not the whole picture. Despite these complications, the AGN torus unification picture still explains a lot of AGN phenomenology and represents a useful framework that can be tested with observations.

1.3.2 X-ray Properties of AGN

Approximately 10% of the bolometric luminosity of AGN comes out in the X-ray band, between ≈ 0.1 and ≈ 100 keV. Thus, AGN dominate the cosmic X-ray background

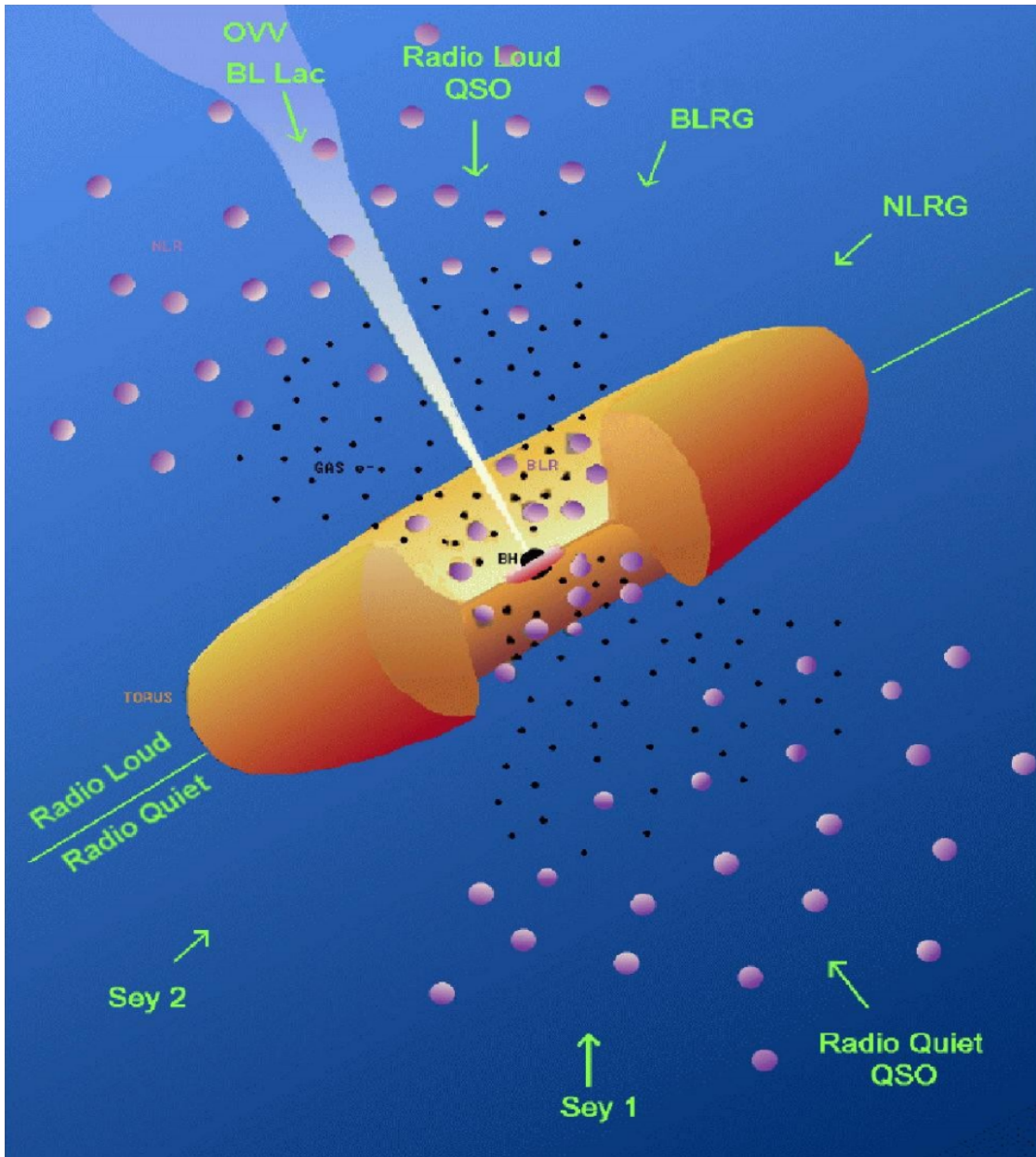


FIGURE 1.13: A unified scheme for AGN. The broad line region is compact and can thus be obscured from view by a dusty torus, whereas the larger narrow line region is always visible. The radio-loud/radio-quiet dichotomy is explained by the presence or absence of a radio jet.

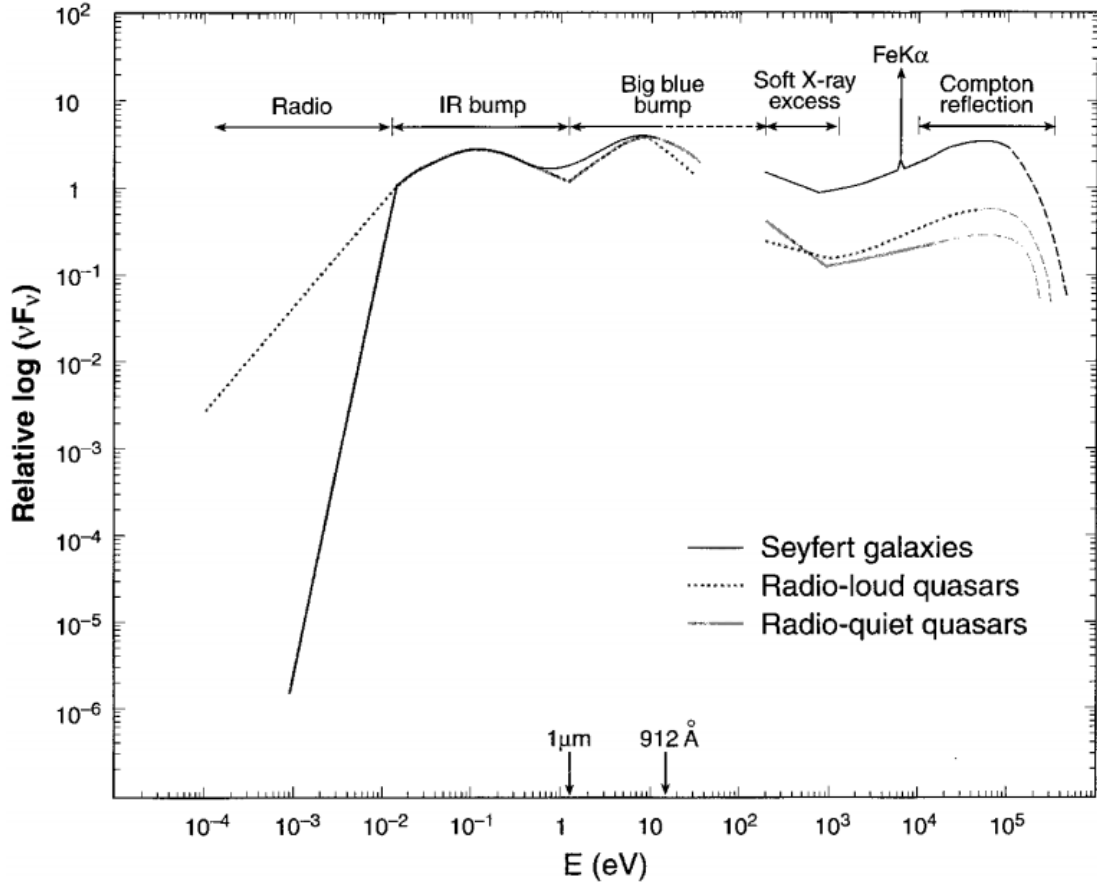


FIGURE 1.14: Credit: Koratkar & Blaes 1999 Approximate average broadband SEDs for a few types of AGN. The series of characteristic bumps can be clearly seen. The Soft-X-ray excess is also visible (see section 1.3.2.1).

(Madau et al. 1994). The hard X-ray emission typically follows a power law shape with spectral index -0.9 (e.g. Koratkar & Blaes 1999), widely considered, as in LMXBs, to come from a hot ‘corona’ of electrons close to the BH that upscatters disc seed photons (e.g. Haardt & Maraschi 1991). The compactness of this X-ray corona has been confirmed by microlensing (Chartas et al. 2009; Dai et al. 2010) and variability studies (Green et al. 1993; Crenshaw et al. 1996; Risaliti et al. 2007; Emmanoulopoulos et al. 2014). Indeed, X-rays in AGN can be highly variable, both in terms of their intrinsic X-ray emission, but also due to changes in the absorption characteristics (Risaliti et al. 2002; Miller et al. 2008; Connolly et al. 2014). I discuss X-ray absorption in more detail in chapter 2, particularly with respect to disc winds.

The hard X-ray spectra of AGN also tend to exhibit a number of reflection features. Typically, these consist of a strong Fe K α emission line and a ‘Compton hump’ at high energies. The latter is produced by Compton down-scattering of high energy photons (Pounds et al. 1989; Nandra & Pounds 1994). It is still unclear exactly where these

features originate, but a common interpretation is that they are caused by reflection off the inner parts of the accretion disc (Fabian et al. 1995; Iwasawa et al. 1996a; Reynolds 1999). If this is the case, and the broadening of the iron line is relativistic, this would allow for measurements of the BH spin (Laor 1991; Iwasawa et al. 1996b; Dabrowski et al. 1997). This hypothesis is somewhat controversial, as many of the relativistic features supposedly imprinted by BH spin can also be explained by Comptonisation or absorption (e.g. Misra & Kembhavi 1998; Miller & Turner 2013). In addition, an outflow can naturally produce the characteristic broad red Fe K α wing (Sim et al. 2010a).

In Compton-thick AGN, the intrinsic continuum is heavily absorbed by columns of $N_H \gtrsim 10^{24} \text{ cm}^{-2}$ – this absorption is normally attributed to the dusty torus, but disc winds could also contribute. Compton-thick AGN are required in large numbers in order to explain the cosmic X-ray background (Setti & Woltjer 1989). In these sources, reflection features can actually dominate the X-ray spectrum (Alexander et al. 2011; Gandhi et al. 2013), but the Fe line is formed from low ionization stages of Fe on $\sim 0.1 \text{ pc}$ scales (Gandhi et al. 2015).

1.3.2.1 The Soft X-ray Excess

If one interpolates between the $\nu^{1/3}$ law from the BBB in the UV, and the power law in the hard X-rays, a curious excess of flux is often found in type 1 AGN (see Fig. 1.14, and Koratkar & Blaes 1999). This is known as the soft X-ray excess (SXES), which is too hot to be explained by thermal disc emission, as a thin disc around an AGN should never approach the temperatures required. Many models have been proposed to explain this excess, including relativistically smeared photoabsorption (Gierliński & Done 2004, 2006), relativistically smeared line and free-free emission (Ross & Fabian 2005; Crummy et al. 2006) and a variety of cool Comptonised component geometries, such as an inner accretion flow (Magdziarz et al. 1998; Done et al. 2012) or a geometrically thin layer on top of the disc (Janiuk et al. 2001). While the SXES poses a challenge to the simplest pictures of AGN, it may also solve some of the outstanding puzzles, since some of the geometries proposed may help to explain the accretion disc size problem discussed in section 1.4 (Gardner & Done 2016).

1.3.3 The Broad Line Region: Connection to Winds and Unification

In the UP95 unification model, the broad emission lines come from a series of virialised clouds close to the disc plane. As noted by [Murray et al. \(1995\)](#), hereafter MCGV95), there are a number of problems with the BLR ‘cloud’ model, perhaps most notably that there is no obvious physical origin for such virialised clouds. Testing alternative models for the BLR is therefore important. Indeed, MCGV95 proposed a disc wind model in order to explain both BALs and BELs in quasars. A disc wind model was also discussed by [Elvis \(2000\)](#), who proposed a structure for quasars that attempted to explain much of the behaviour of luminous AGN merely as a function of viewing angle. It is worth noting that there is observational support for the unification paradigm; for example, it has been suggested that orientation is a key driver of the so-called ‘Eigenvector 1’ relationship in quasars ([Boroson & Green 1992](#); [Sulentic et al. 2000](#); [Marziani et al. 2001](#); [Shen & Ho 2014](#)). Disc wind unification models are discussed further in section 2. The philosophy of these models is that, before invoking additional degrees of freedom in a model, we should first test if known quasar phenomenology (disc winds) can explain other aspects of their observational appearance. I have illustrated this general principle with the ‘Occam’s quasar’ cartoon shown in Fig. 1.15. This is the picture that I will quantitatively test in the latter, quasar-focused sections of this thesis. The same general principle can also be applied to cataclysmic variables and other accreting objects.

1.4 The Current Understanding of the Disc Continuum

The SS73 model is still the most common way to fit accretion disc spectra and infer information about the underlying physics. However, a number of issues have been raised concerning the thin-disc model and its applicability to accreting systems.

1.4.1 The Spectral Shape of CV Discs

Attempts to fit the observed SEDs of high-state CVs with simple disc models have met with mixed success. In particular, the SEDs predicted by most stellar/disc atmosphere models are too blue in the UV ([Wade 1988](#); [Long et al. 1991, 1994](#); [Knigge et al. 1998a](#)) and exhibit stronger-than-observed Balmer jumps in absorption ([Wade 1984](#); [Haug 1987](#); [La Dous 1989a](#); [Knigge et al. 1998a](#)). One possible explanation for these problems is

OCCAM'S QUASAR: THE PRINCIPLE THAT IN EXPLAINING A QUASAR NO MORE ASSUMPTIONS SHOULD BE MADE THAN ARE NECESSARY.

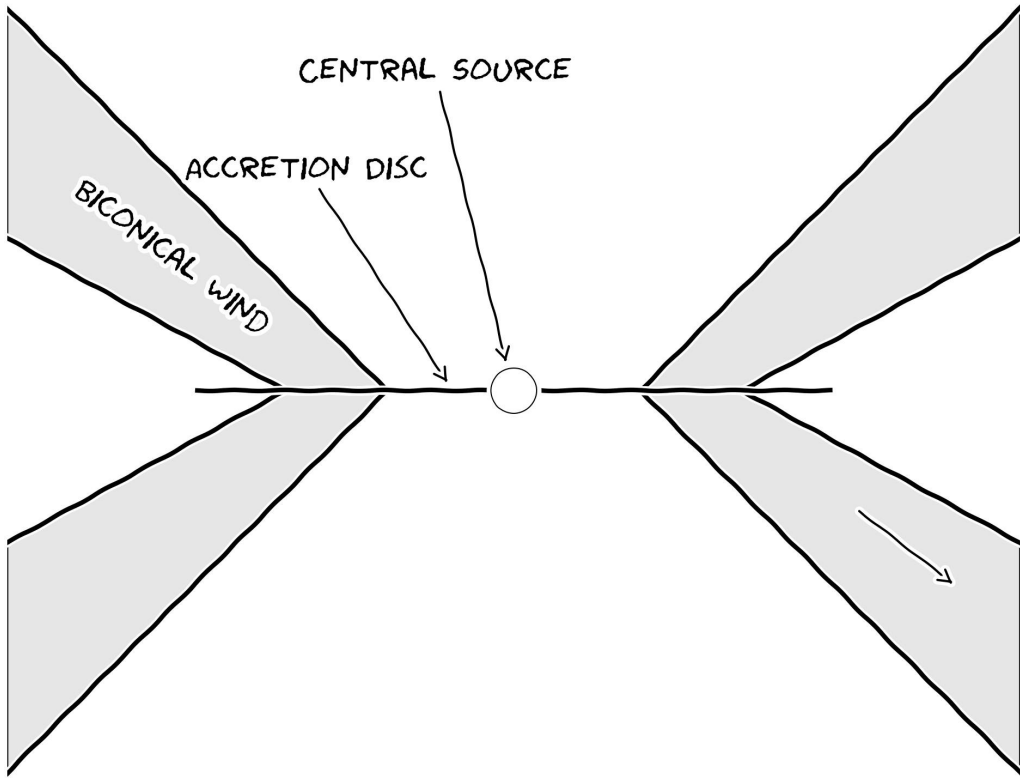


FIGURE 1.15: Occam's quasar. How far can this general picture take us when trying to explain the behaviour of quasars and other accreting compact objects?

that these models fail to capture all of the relevant physics. Indeed, it has been argued that a self-consistent treatment can produce better agreement with observational data (e.g. [Shaviv & Wehrse 1991](#), but see also [Idan et al. 2010](#)). However, an alternative explanation, suggested by [Knigge et al. \(1998b\)](#) and [Hassall \(1985\)](#), is that recombination continuum emission from the base of the disc wind might fill in the disc's Balmer absorption edge and flatten the UV spectrum.

Alternatively, it may just be that CV disks are never really in a steady state, and so we should only expect the $R^{-3/4}$ temperature profile to hold in a limited portion of the disc. From eclipse mapping, it has been shown that the inferred accretion rate increases with radius in NLs ([Rutten et al. 1992](#); [Horne 1993](#)). These results suggest that a non-radiative form of energy loss is present in the inner regions of the disc, of which potential forms may be advection or mass loss. This is yet another piece of evidence that the understanding of accretion and outflow are intertwined, although hopefully not

inextricably.

1.4.2 The Big Blue Bump in AGN

Does the SS73 model apply well to AGN spectra? There are contrasting views on the matter. On the one hand, [Antonucci \(2013\)](#) claims that “most of the AGN community is mesmerized by unphysical models that have no predictive power”. Yet a recent spectral fitting study by [Capellupo et al. \(2015\)](#) concludes that “altogether, these results indicate that thin accretion discs are indeed the main power houses of AGN”. So, what are the main problems when confronting thin disc models with observation?

1.4.2.1 The Accretion Disc Size Problem

One of the most interesting results of recent years relating to AGN and accretion discs is the discovery that the continuum emission region size appears to be a factor ~ 3 larger than predicted by standard thin disc theory. This result has been found independently in both microlensing ([Morgan et al. 2010; Dai et al. 2010](#)) and reverberation ([Edelson et al. 2015](#)) studies, and poses a challenge to the current best-fit model for the big blue bump in AGN. One proposed solution is that the discs in AGN are inhomogeneous, consisting of individual clumps with independently varying temperatures ([Dexter & Agol 2011](#)), but this is very much still an active area of research. It is worth noting that the impact of winds on these results has not yet been properly quantified, something our team is currently trying to address ([Mangham et al. 2016](#)).

1.4.2.2 Fitting AGN Spectra and the 1000 Å Break

AGN spectra do not, in general, exhibit the canonical $\nu^{1/3}$ slope (e.g. [Koratkar & Blaes 1999; Davis et al. 2007; Shankar et al. 2016](#)) or colour-mass scalings ([Bonning et al. 2007](#)) expected from theoretical predictions. Furthermore, there is a characteristic break in AGN spectra at around 1000 Å ([Lusso et al. 2015](#)), which does not scale with BH mass or luminosity, as one might expect for a break associated with an accretion disc. There is also no evidence in AGN of the expected polarisation signatures from an optically thick disc atmosphere ([Stockman et al. 1979; Antonucci 1988; Antonucci et al. 1996](#)).

Despite these problems, recent work suggests that the thin disc model still has some potential. Capellupo et al. (2015) were able to fit a number of AGN spectra in the UV and optical with thin disc models, although successful fits were only found once they included effects such as Comptonisation and mass loss, as well as correcting for extinction. BH spin also had a reasonable effect on the spectral fits, although it is somewhat difficult to constrain from spectral fitting alone. The 1000 Å break has also been explained with mass-losing discs (Laor & Davis 2014), and Lusso et al. (2015) suggested that incorrect IGM corrections may be exacerbating the effect. So, while many problems exist, it may not be time to abandon the good ship “Shakura-Sunyaev” just yet.

1.5 The Universality of Accretion

Accretion appears to be an important physical processes across ~ 10 orders of magnitude in mass. But is this process the same on all scales? Does any behaviour manifest in all accreting systems?

1.5.1 The RMS-flux relation

Broad-band variability is common in all types of accretion disc. It has been known for some time that there exists a linear relationship between the flux and absolute root-mean-square (rms) amplitude of this variability. This was discovered first in XRBs and AGN (Uttley & McHardy 2001; Uttley et al. 2005; Heil et al. 2012), but it has been shown more recently that the relationship extends to CVs and even YSOs (Scaringi et al. 2012, 2015). The relationship is also not limited to just one type of CV but is present in both NLs and DNe (Van de Sande et al. 2015).

One model that can successfully reproduce this behaviour is the so-called ‘fluctuating accretion disc’ model (Lyubarskii 1997; Kotov et al. 2001; Arévalo & Uttley 2006; Hogg & Reynolds 2015). More generally, additive processes cannot reproduce this behaviour, and a multiplicative mechanism is required (Uttley et al. 2005). Regardless of the mechanism, the rms-flux relation is one of the most clear-cut examples of a universal accretion phenomenon. It tells us that at least some of the behaviour in CV discs is

also present in AGN and XRBs, strengthening the argument that CVs can be used as ‘accretion laboratories’.

1.5.2 Accretion states and disc-jet coupling

Variable and transient sources are common in astrophysics, particularly when the sources are accreting. It turns out that when one plots the colour and luminosity evolution over the course of an outburst cycle it follows very similar tracks in both CVs and XRBs (see Fig. 1.16, Körding et al. 2008). This colour-luminosity behaviour traces the accretion state of the system. The detection of radio jets is intrinsically linked to this accretion state (disc-jet coupling), as jets only appear in the ‘hard’ accretion state, to the right of the so-called ‘jet line’ (Fender 2001; Fender et al. 2004). Körding et al. (2008) showed that this behaviour also occurs in CVs, as radio emission in the DN SS Cyg is detected in the same region of colour-luminosity space. In addition, there is a well-known correlation between radio and X-ray luminosities in low-hard states (Gallo et al. 2003).

Clear connections between disc state and radio loudness have also been found in AGN. Perhaps the most obvious piece of evidence that disc-jet coupling is scale invariant is the so-called ‘fundamental plane of BH activity’ (Merloni et al. 2003), which extends from LMXBs right up to quasars. AGN have been shown to occupy similar regions of colour-luminosity space to the LMXBs (Körding et al. 2006), and simulations involving scaled-up LMXB discs have been successful in reproducing AGN accretion states (Sobolewska et al. 2011). Correlations in X-ray photon index are present in AGN and LMXBs; ‘softer when brighter’ behaviour is found at relatively high Eddington ratios (McHardy et al. 1999; Gu & Cao 2009), while ‘harder when brighter’ is observed in low states (Gu & Cao 2009; Emmanoulopoulos et al. 2012; Connolly et al. 2016).

Despite this apparently universal behaviour, the jet production mechanism in BHs is not well known. Theoretical work suggests that radio jets should be correlated with BH spin (Penrose & Floyd 1971; Blandford & Znajek 1977), but whether such a correlation exists in LMXBs is controversial (Fender et al. 2010; Narayan & McClintock 2012). This has significant implications for AGN; if powerful radio jets are associated exclusively with rotating BHs then the number of radio-loud AGN would imply a large fraction of them must be rapidly spinning, with high radiative efficiencies. Further evidence that radio jets are not simply produced by RIAFs onto spinning BHs is found when one considers

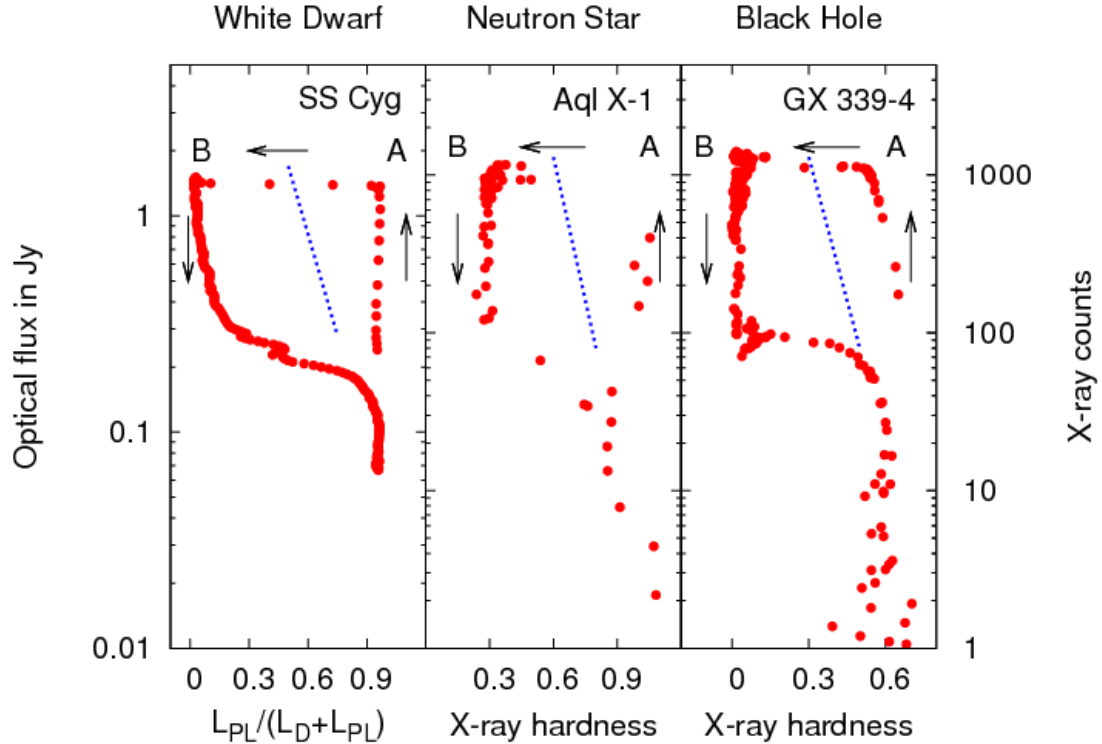


FIGURE 1.16: Credit: Kording et al. 2008. Hardness-intensity diagrams for three types of accreting compact objects: the dwarf nova SS Cyg (left), in addition to neutron star (middle) and black hole (right) LMXBs. The dotted line shows the ‘jet line’ in LMXBs and the arrows show the expected temporal evolution of the system. For SS Cyg the x -axis shows the fraction of the hard X-ray power law component in the system compared to the luminosity of the combined luminosity of disc and power law. This quantity is analogous to the X-ray hardness in LMXBs.

that NLs show evidence of synchrotron radio emission ([Coppejans et al. 2015](#)). This important result suggests that our understanding of jets is incomplete, and that the links between accretion state and jet production are fundamental, but unsolved. Disc winds may complicate, or simplify, matters, depending on one’s outlook (see chapter 2).

1.5.3 A Global Picture

Clearly, accretion physics is relevant to a plethora of astrophysical phenomena, and at least some of the physics of accretion is applicable to *all* classes of accreting object. It would also appear that the outflowing material observed in accreting systems has a profound effect on the accretion process itself, and possibly significantly affects the observational appearance of disc-accreting systems (c.f. Elvis’ unification model). Hence, in the next chapter, I will review the evidence for winds and discuss some of the relevant background theory.

Chapter 2

Accretion Disc Winds

“A view of space, with an elephant
obstructing it”

Mike Vennart, Silent/Transparent

2.1 Observational Evidence

Observational evidence for mass-loaded outflows or winds is widespread across the entire astrophysical mass range and most of the electromagnetic spectrum. Before exploring this evidence, it is pertinent to briefly discuss the ‘smoking gun’ used to unambiguously detect winds – the presence of blue-shifted BALs or ‘P-Cygni’ profiles in an object’s spectrum.

Fig. 2.1 shows how a spherical outflow presenting significant line opacity will cause these characteristic profile shapes to form, as scattering out of the line of sight causes a dip in the blue wing of the line, while scattering into the line of sight from other portions of the outflow causes an increase in flux in the red wing of the line. The situation is much more complex in most astrophysical situations; for example, the geometry is rarely spherically symmetric, and the line is rarely a pure scattering case. Indeed, the potential for complicated radiative transfer effects and the variety in line formation mechanisms (e.g. recombination, collisional excitation) is one of the reasons why 3D Monte Carlo radiative transfer simulations are necessary to effectively model disc winds (see chapter 3).

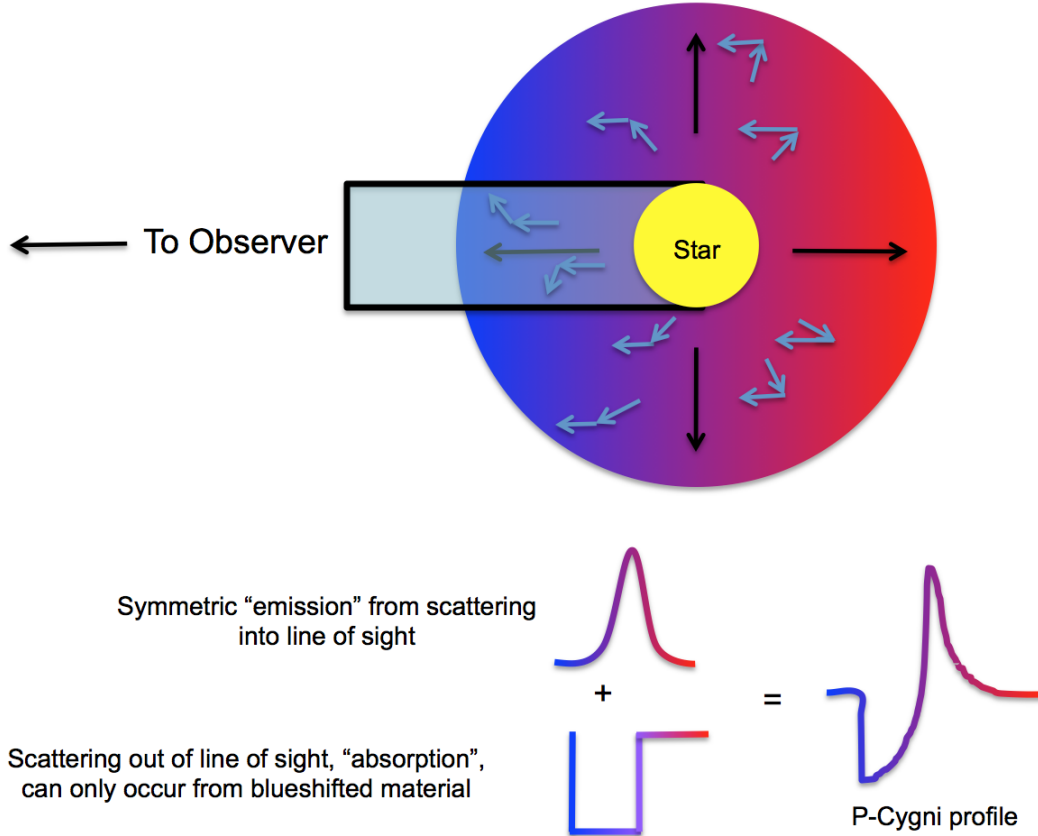


FIGURE 2.1: Diagram showing how an expanding envelope or wind presenting significant line opacity around a continuum source leads to the formation of P-Cygni profiles. The black arrows denote the outflow direction and the blue arrows typical scattering interactions.

2.1.1 Cataclysmic Variables

It has been known for a long time that winds emanating from accretion discs are important in shaping the ultraviolet (UV) spectra of high-state CVs (Heap et al. 1978; Greenstein & Oke 1982). The most spectacular evidence for such outflows are the P-Cygni-like profiles seen in UV resonance lines such as C IV 1550 Å (e.g. Cordova & Mason 1982, see Fig. 2.2). Considerable effort has been spent over the years on understanding and modelling these UV features (e.g. Drew & Verbunt 1985; Mauche & Raymond 1987; Shlosman & Vitello 1993; Knigge et al. 1995; Knigge & Drew 1997; Knigge et al. 1997; Long & Knigge 2002; Noebauer et al. 2010; Puebla et al. 2011). The basic picture emerging from these efforts is of a slowly accelerating, moderately collimated bipolar outflow that carries away $\simeq 1\% - 10\%$ of the accreting material. State-of-the-art simulations of line formation in this type of disc wind can produce UV line profiles that are remarkably similar to observations, as shown in Fig. 2.3.

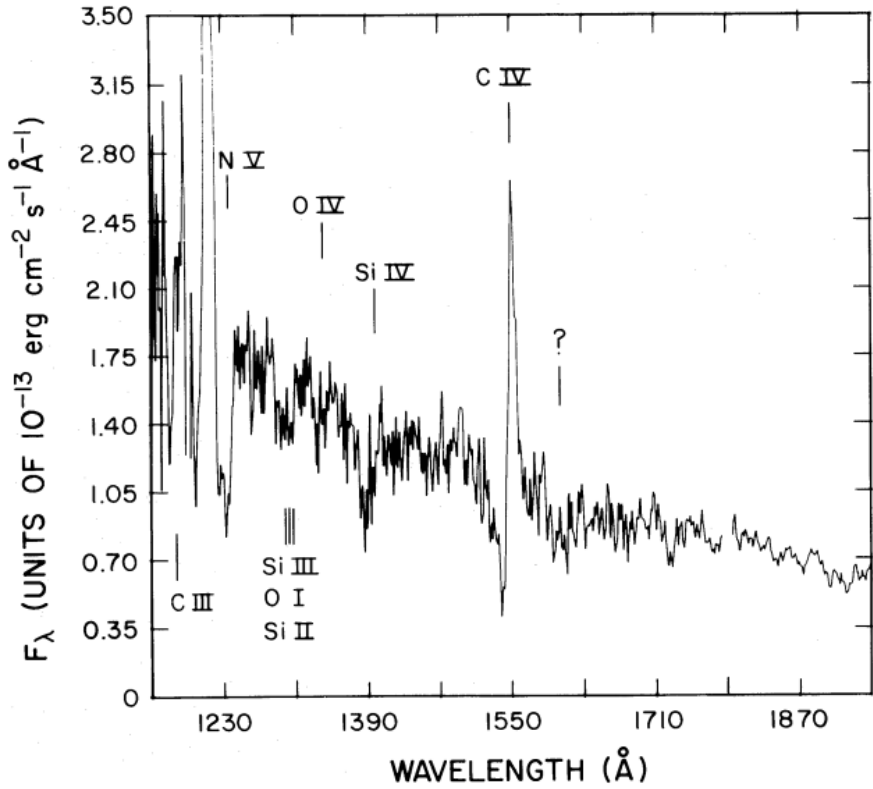


FIGURE 2.2: Credit: Cordova & Mason 1982. UV spectrum of the DN TW Vir during outburst. The P-Cygni profiles can be seen clearly, demonstrating that a strong, fast outflow is present in the system.

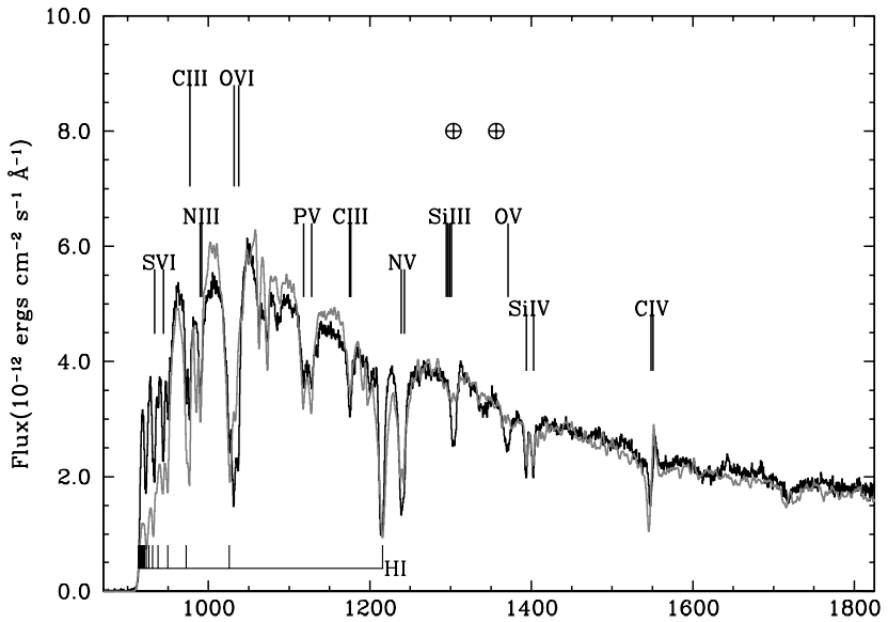


FIGURE 2.3: Credit: Long & Knigge 2002. UV spectrum of Z Cam (black), compared to a synthetic spectrum from MCRT simulations (grey).

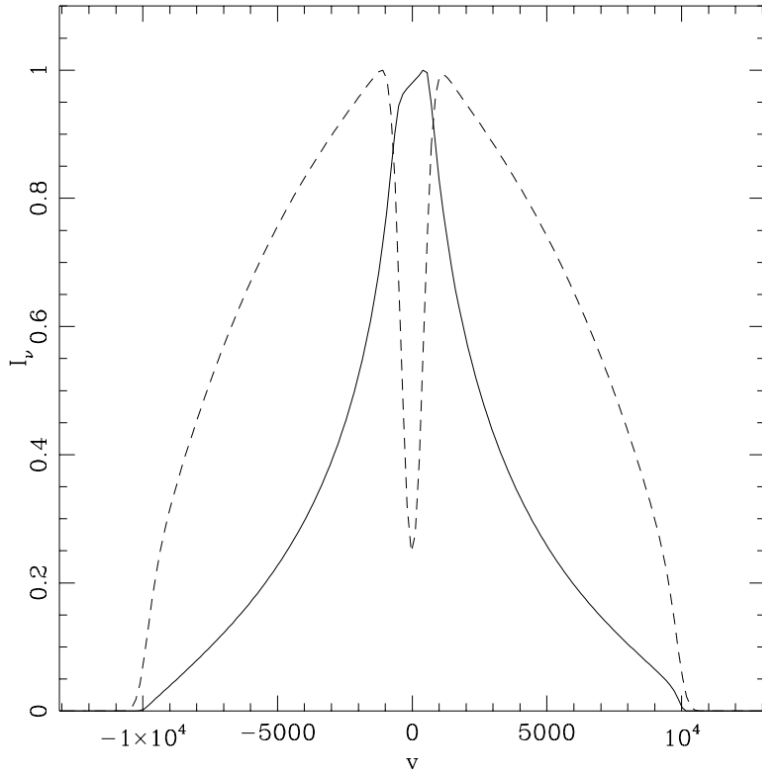


FIGURE 2.4: Credit: Murray & Chiang (1997). A comparison between a line profile, normalised to have peak intensity of 1, produced from a Keplerian disk (solid line) and the same model with an additional disc wind (dashed line). The radial velocity component of the disc wind modifies the escape probabilities across the disc, causing a single-peaked line to form.

Much less is known about the effect of these outflows on the optical spectra of high-state CVs. Direct evidence of wind-formed lines comes from isolated observations of P-Cygni-like line profiles in H α and He I 5876 Å, (Patterson et al. 1996; Ringwald & Naylor 1998; Kafka & Honeycutt 2004). However, the effect of a wind on the *emission* lines in the optical spectrum is unclear. Murray & Chiang (1996, 1997) have shown that the presence of disc winds may offer a natural explanation for the single-peaked optical emission lines in high-state CVs, since they can strongly affect the radiative transfer of line photons (Fig. 2.4; also see Flohic et al. 2012). Stronger support for a significant wind contribution to the optical emission lines comes from observations of eclipsing systems. There, the single-peaked lines are often only weakly eclipsed, and a significant fraction of the line flux remains visible even near mid-eclipse (e.g. Baptista et al. 2000; Groot et al. 2004). This points to line formation in a spatially extended region, such as a disc wind. It is also possible that a wind may affect the continuum emission of CVs, as described in section 1.4. The effect of an accretion disc wind on the optical line and continuum emission of CVs is addressed directly in chapter 4.

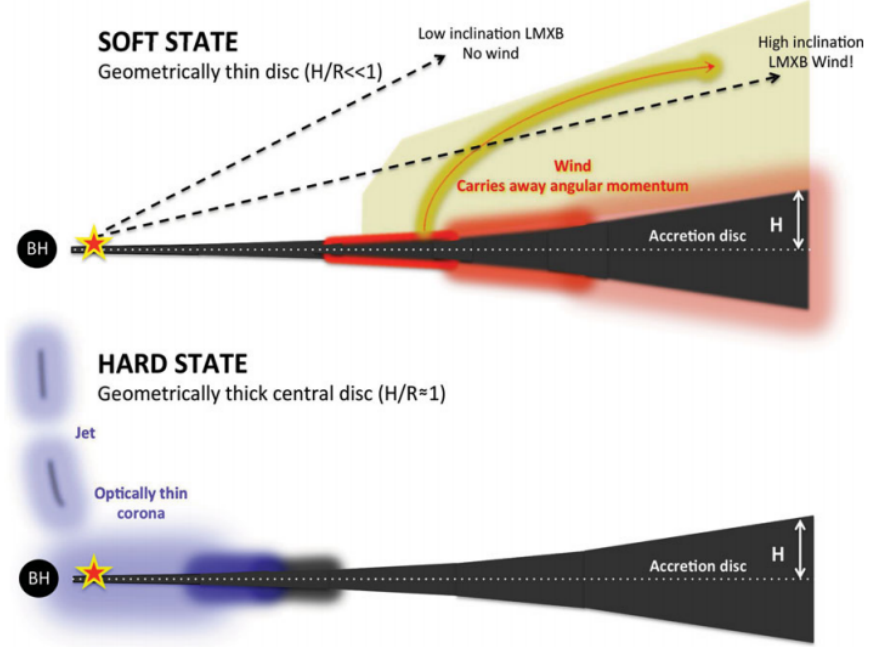


FIGURE 2.5: Credit: Ponti et al. 2012. A cartoon illustrating the expected geometry of the disc and outflows in LMXBs in the soft and hard states.

2.1.2 X-ray Binaries

As in CVs, evidence for fast outflows in LMXBs is not constrained to a single waveband. UV absorption in outflows was detected when Ioannou et al. (2003) observed C IV 1550 Å P-Cygni profiles with blueshifts of $\sim 1500 \text{ km s}^{-1}$ in the LMXB X2127+119. A series of studies also found X-ray absorption features in similar objects (Ueda et al. 1998; Kotani et al. 2000; Parmar et al. 2002). These absorption features appeared to be preferentially detected in ‘dipping’ LMXBs. Dips in X-ray flux are thought to occur in systems with inclinations $\gtrsim 70^\circ$ (van der Hooft et al. 1998; Tanaka et al. 2003; Church et al. 2005), and possible explanations involve disc precession (Barnard et al. 2006; Shaw et al. 2013), failed state transitions (Soleri et al. 2013; Shaw et al. 2016) or low ionization material partially covering the X-ray source (Tanaka et al. 2003). Ponti et al. (2012) confirmed that broad absorption in highly ionized Fe lines occurred only in the dipping LMXBs in their sample, and proposed an equatorial outflow geometry based on this association (see Fig. 2.5). The same study also demonstrated that the winds only appeared in the soft, disc dominated accretion state, on the opposite side of the HID to the region where jets are common (Fig. 2.6). This exciting result illustrates how important winds are to our understanding of accretion and requires that we expand the discussion of accretion states from ‘disc-jet’ coupling to also include winds.

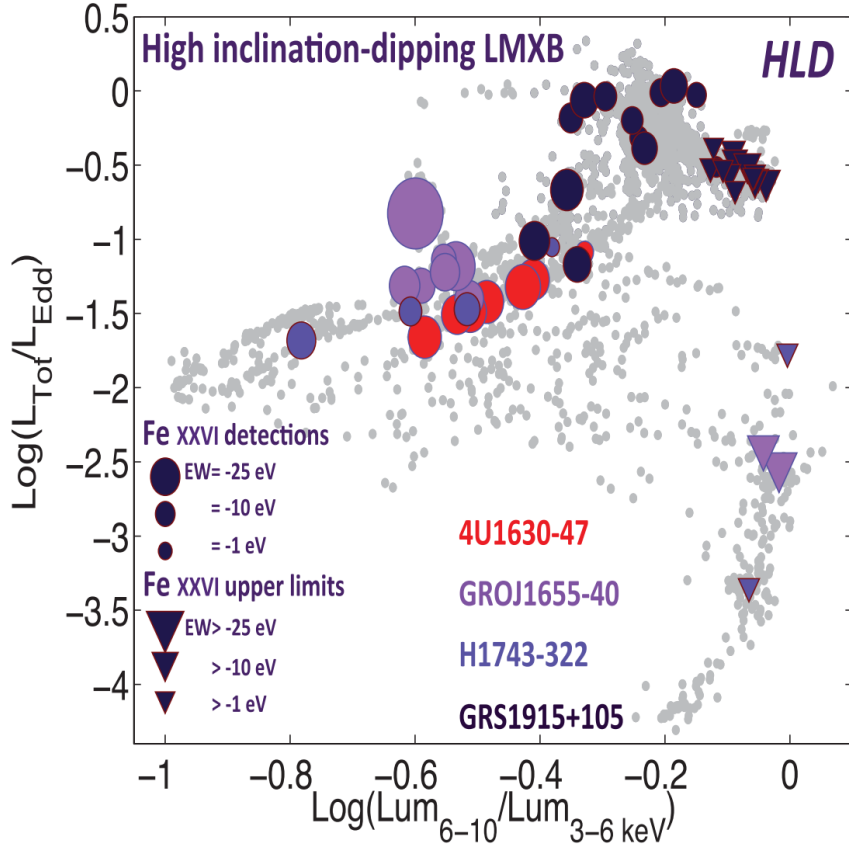


FIGURE 2.6: Credit: Ponti et al. 2012. Hardness-luminosity diagram for four dipping LMXBs, demonstrating that winds appear only in the soft state. The points are colour-coded by system, and are shown against the background grey points of all LMXBs studied by Ponti et al. (2012). None of the low inclination sources in their sample show Fe XXVI absorption detections.

2.1.3 AGN and Quasars

2.1.3.1 Broad Absorption Line Quasars

Perhaps the clearest evidence of outflows in AGN is provided by the blueshifted ($\sim 0.1 c$) ultraviolet BALs seen in approximately 20% of quasars (Weymann et al. 1991; Knigge et al. 2008; Dai et al. 2008; Allen et al. 2011). High-ionization BAL quasars (HiBALs) only show broad, blue-shifted absorption in species such as C IV, Si IV, N V and O VI, the most prominent BAL profile often being associated with the C IV 1550 Å line. In addition to the more common HiBALs, approximately 10% of BALQSOs also show absorption in lower ionization species such as Mg II and Al III (LoBALs; Voit et al. 1993; Gibson et al. 2009); an even smaller subset also show absorption in Fe II and III (FeLoBALs; Becker et al. 2000; Hall et al. 2002). Some example spectra of BAL quasars

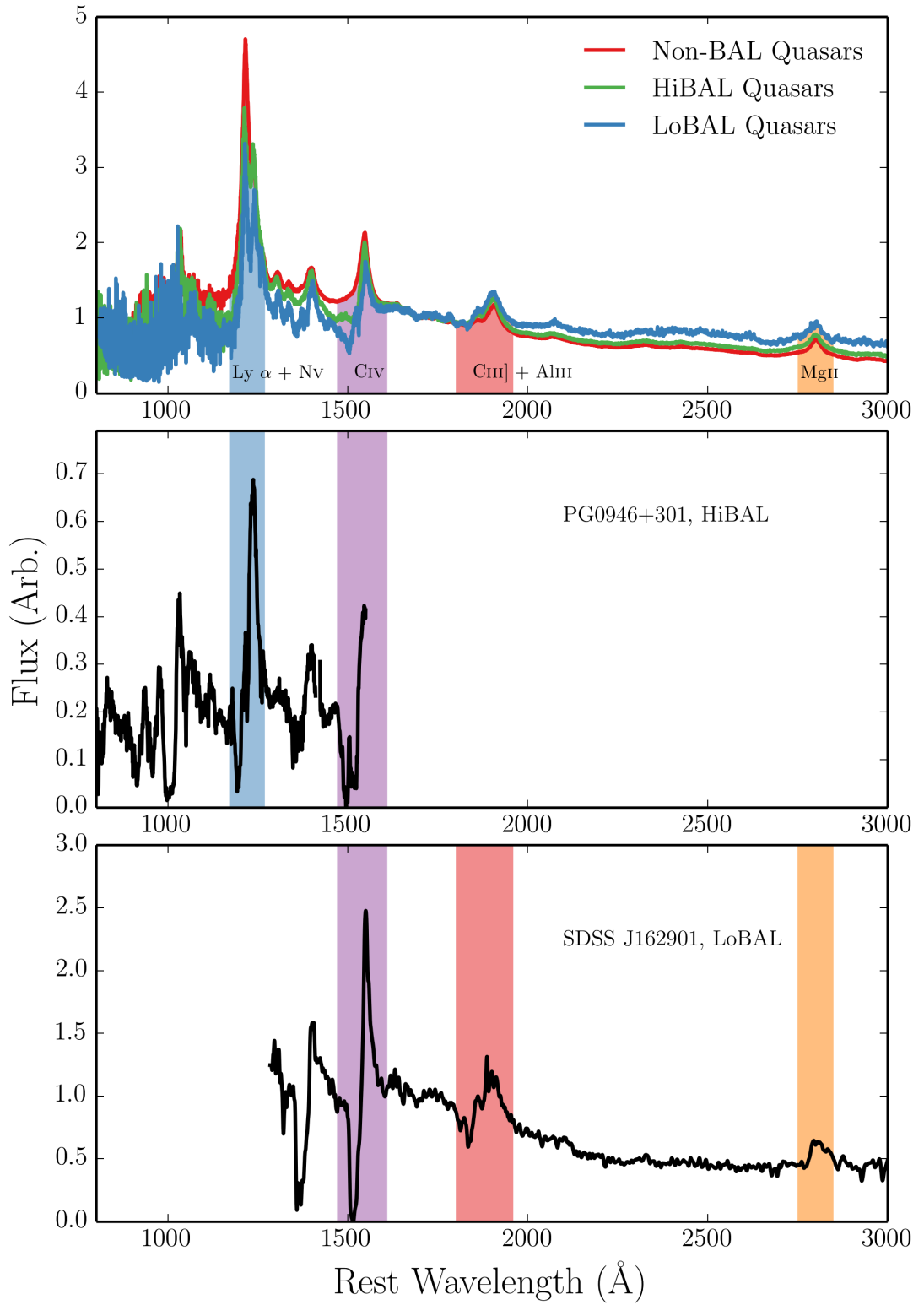


FIGURE 2.7: Top Panel: A comparison between the SDSS non-BAL, HiBAL and LoBAL composite spectra as presented in [Reichard et al. \(2003\)](#). Bottom Two Panels: Two individual examples of a HiBAL and LoBAL quasar spectrum, respectively. In all panels some of the more prominent lines are labeled and shaded, and the object name is given in the bottom two plots.

from the HST and SDSS archives are shown in Fig. 2.7, with important spectral lines marked.

The simplest explanation for the incidence of BAL quasars (BALQSOs) is in terms of an accretion disc wind viewed from different angles. This principle of geometric unification is very similar to the idea behind the UP95 and AM95 models discussed in Chapter 1. According to this paradigm, a biconical wind rises from the accretion disc so that the BALQSO fraction is associated with the covering factor of the outflow. This fraction has been estimated by various authors using different selection criteria, with values ranging between 10% and 40% depending on the treatment of selection effects and the classification scheme used (Weymann et al. 1991; Trump et al. 2006; Knigge et al. 2008; Dai et al. 2008; Allen et al. 2011)

BAL quasars can also be interpreted in an *evolutionary* context, in which quasars spend a certain proportion of their life in the ‘BAL phase’. Models generally put this phase near the start of the quasar lifetime (Hazard et al. 1984; Surdej & Hutsemekers 1987; Boroson & Meyers 1992; Zubovas & King 2013), after a dust-enshrouded phase, but before the main quasar period. It is perhaps more likely that *both* evolutionary and geometric effects are at work (Borguet & Hutsemékers 2010; Dai et al. 2012). One of the main problems with testing these two paradigms is that many of the properties of BAL quasars fit naturally into either picture, and so disentangling their true nature is challenging. The latter chapters of this thesis attempt to address this issue by testing the geometric unification model and seeing how close this simple picture can get to explaining the BAL phenomenon.

The BAL fraction, f_{BAL} , is a very useful number and must be at least related to the covering factor of the outflow. However, selection effects associated with the reduction in flux by the BALs themselves (Knigge et al. 2008) and enhanced reddening/extinction in BALQSOs (Reichard et al. 2003; Allen et al. 2011) could lead to significant underestimates of f_{BAL} . The angular dependence of the continuum causes further problems, as objects viewed from higher inclinations could be severely under-represented in a flux-limited sample (Goodrich 1997; Krolik & Voit 1998). Unfortunately, accurately correcting for these effects is difficult. The degree of collimation of the BAL wind is also not well known. Polarisation studies suggest that the wind is roughly equatorial (Goodrich & Miller 1995; Cohen et al. 1995), as also found from hydrodynamical and radiative transfer simulations (Proga et al. 2000; Proga & Kallman 2004; Higginbottom

et al. 2013; Borguet & Hutsemékers 2010). However, there is also evidence for polar BAL outflows in radio-loud (RL) sources (Zhou et al. 2006; Ghosh & Punsly 2007). In addition to these uncertainties, the physical scale of the BAL phenomenon is also disputed and may vary from object to object. A common assumption is that the BAL region is roughly co-spatial with the BLR, which is reasonable considering the similar velocity widths and ionization states in BELs and BALs. In this case, the radius of the absorbing material can be estimated as $\sim 100 r_G - 1000 r_G$ from reverberation mapping and microlensing (e.g., for BLRs in BALQSOs, Sluse et al. 2015; O'Dowd et al. 2015). However, distances of ~ 0.1 pc ($\sim 10^4 r_G$) have been estimated in at least some objects from photonization modelling, conducted using densities calculated from absorption line doublets (Borguet et al. 2013; Chamberlain et al. 2015).

BAL quasars display a wide variety of different trough shapes. The line profiles themselves often show complex structure (Foltz et al. 1987; Ganguly et al. 2006; Simon & Hamann 2010) and can be time variable (Hall et al. 2011; Capellupo et al. 2011, 2012, 2014; Filiz Ak et al. 2012). Furthermore, a subset of quasars show BAL-like absorption troughs with much smaller velocity widths. Depending on their width, these are known as narrow absorption lines (NALs) or ‘mini-BALs’ (Misawa et al. 2007, 2008; Nestor et al. 2008). While some of this behaviour can be explained once again as a viewing angle effect (e.g. Ganguly et al. 2001), the BAL profile variety and variability implies that BALQSOs are far from a homogenous population, and perhaps suggests the existence of dense substructures (clumps) in their flows. Such clumpiness has been invoked in several disc wind unification models for AGN and quasars (see section 2.3)

The X-ray properties of BAL quasars are particularly important due to the strong ionizing potential of the X-ray radiation. Observationally, BALQSOs are X-ray weak when compared to non-BAL quasars (Gibson et al. 2009). This X-ray weakness is often attributed to the presence of absorbing material with column densities of $N_H \sim 10^{22-24}$ cm $^{-2}$ along the line of sight (Gallagher et al. 1999, 2002; Green et al. 2001; Grupe et al. 2003a; Stalin et al. 2011), although there is also evidence that BALQSOs are *intrinsically* X-ray weak (Sabra & Hamann 2001; Clavel et al. 2006; Morabito et al. 2013). The X-ray properties of BAL quasars are fundamentally coupled to the properties of the wind – the X-ray absorption may, in fact, be caused by the outflow, which in turn has its ionization state determined by the X-ray radiation. Furthermore, the true X-ray luminosities cannot be reliably inferred until the inclinations of BALQSOs are

constrained, as gravitational lensing can significantly alter the emergent angular distribution of X-ray emission even for an intrinsically isotropic source (Chen et al. 2013a,b).

Although the observed X-ray emission in BALQSOs is weaker than in otherwise similar quasars, it still still possesses strong ionizing power. This leads to what has become known as the ‘over-ionization problem’ in BALQSOs: how is the moderate ionization state of the BAL gas maintained in the presence of ionizing X-rays? A number of potential solutions have been proposed, which can be broadly separated into ‘shielding’ models (Murray et al. 1995; Proga & Kallman 2004) and ‘clumpy’ models (de Kool & Begelman 1995; Hamann et al. 2013). Some of these models are discussed further in section 2.3 and chapter 5.

2.1.3.2 Warm Absorbers

Warm absorbers (WAs) are regions of photoionized plasma responsible for some of the characteristic absorption features seen in the soft X-ray spectra of AGN (Reynolds & Fabian 1995). In particular, they produce photoelectric continuum absorption (e.g. Halpern 1984; Cappi et al. 1996; Kriss et al. 1996) and a series of narrow absorption lines in H-like and He-like ions of C, N, O, Si, Ne, and Fe (Kaastra et al. 2000). A wind origin is a common hypothesis for WAs (e.g. Krolik & Kriss 2001). Clear evidence for this comes from the measured blueshifts of the lines, typically on the order of a few 100 km s^{-1} (e.g. Kaastra et al. 2000). X-ray absorption and WAs are often variable (Fabian et al. 1994; Otani et al. 1996), which may be interpreted in terms of the changing kinematics of an accretion disc wind (Connolly et al. 2014). There is also evidence of contemporary and associated UV and X-ray absorption in NGC 5548 (Kaastra et al. 2014) and in mini-BALs (Giustini et al. 2011), and, as mentioned above, BALQSOs often show strong X-ray absorption. A number of other AGN also show simultaneous absorption in their X-ray and UV spectra (e.g. Crenshaw et al. 2003; Crenshaw & Kraemer 2012), although can often arise from absorbers that are not directly associated. Overall, there is evidence that the same outflow may produce observational signatures across a large range of ionization states and line energies.

Some WAs can be modelled well with single absorbers (Kaastra et al. 2000), but most require multiple absorption components with different ionization states (e.g. Kriss et al. 1996; Orr et al. 1997; Krolik & Kriss 2001; Connolly et al. 2014). One common way to

parameterise the ionization state of a plasma is via an ionization parameter proportional to the ionizing luminosity, given by (e.g. [Reynolds & Fabian 1995](#))

$$\xi = \frac{L_H}{n_H R^2}, \quad (2.1)$$

where L_H is the luminosity above 13.6 eV, and n_H is the number density of H atoms. If the absorber is stratified and the SED subject to absorption, self-consistent ionization and radiative transfer models should really be used to model the spectrum (see e.g. chapter 3). This is because optically thin ionization parameter estimates will not properly capture the ionization physics due to the variation of the SED shape within the medium. The overall body of observations points towards an outflow with a stratified ionization structure ranging from $\log(\xi/\text{erg s}^{-1} \text{ cm}) \sim 0 - 2$ and densities on the order of 10^7 cm^{-3} , located at around $\sim 10^{16} \text{ cm}$. These physical conditions or scales are not well constrained, and the connection to other outflows, such as the ultra-fast outflows introduced in the next section, is unknown. Timing observations may help to shed light on the properties of the mysterious, but ubiquitous, AGN WAs ([Silva et al. 2015](#)).

2.1.3.3 Ultra-fast Outflows

In addition to acting as WAs, winds can also imprint clear absorption features in highly ionized Fe K α lines in AGN such as PDS 456 ([Reeves et al. 2003](#); [Gofford et al. 2014](#); [Matzeu et al. 2016](#)), MCG-5-23-16 ([Braito et al. 2007](#)) and PG 1211+143 ([Pounds & Reeves 2009](#); [Fukumura et al. 2015](#)). These outflow signatures are fairly common in Seyfert galaxies ([Tombesi et al. 2010](#); [Gofford et al. 2013](#)). One example of such a feature is shown in Fig. 2.8, along with a simple spherical outflow model fit ([Nardini et al. 2015](#)). The high velocities ($\sim 0.1c$) inferred from the line blueshifts have lead to these winds becoming known as ultra-fast outflows, or UFOs.

UFOs are characterised by ionization parameters in the range $\log(\xi/\text{erg s}^{-1} \text{ cm}) \sim 3 - 4$ and column densities $N_H > 10^{22} \text{ cm}^{-2}$. Their high mass-loss rates and large energy budgets mean that they are natural candidates for AGN feedback (see section 2.5). Measurements of their kinetic luminosities suggest that UFOs have sufficient energy to affect their host galaxy ([Gofford et al. 2015](#)). In fact, a large-scale molecular outflow has recently been detected in one UFO host, possibly driven by the UFO itself ([Tombesi et al. 2015](#)). As with WAs, many of the models used to constrain physical parameters

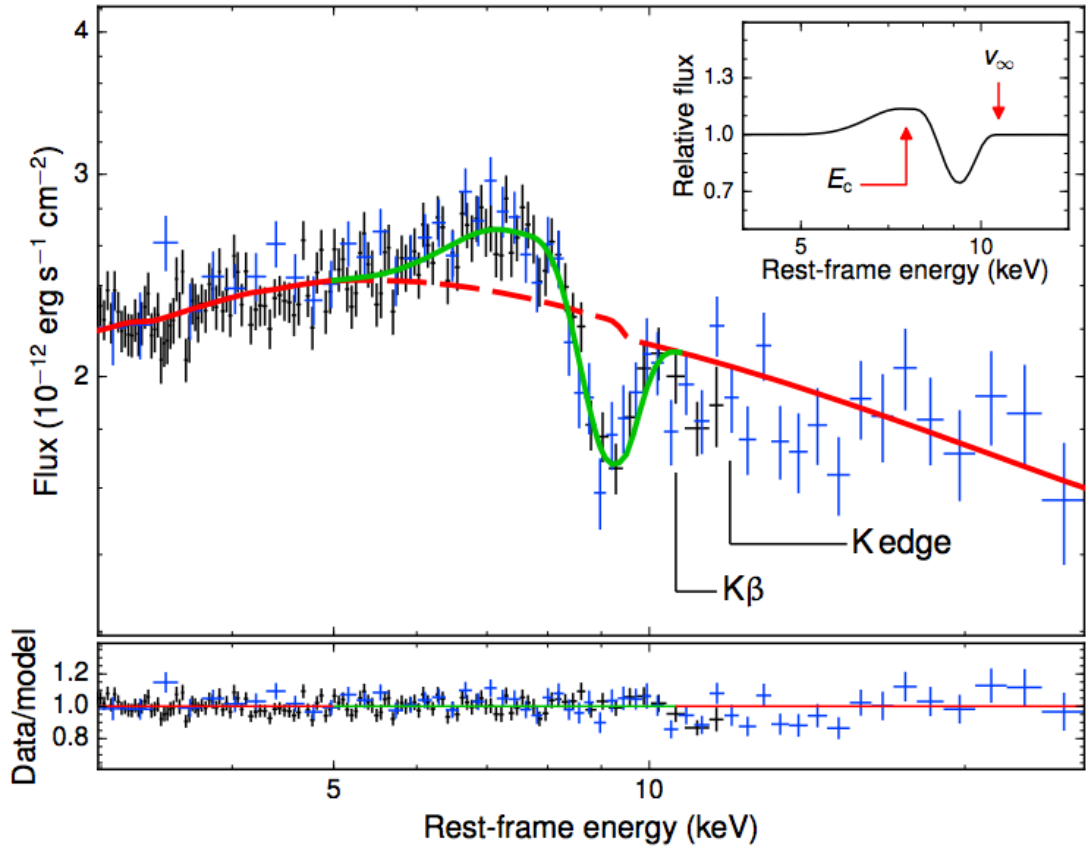


FIGURE 2.8: Credit: Nardini et al. 2015. X-ray spectrum of PDS 456 fitted with a P-Cygni profile from a spherical outflow model. *XMM-Newton* data is shown in black with two combined *NuStar* observations in blue.

are simplistic, and assume single ionization parameters, large covering factors and thin expanding shells of outflow. Under the assumption of a thin expanding shell, the mass-loss rate can be estimated using (e.g. Borguet et al. 2012)

$$\dot{M}_W \sim \Omega \mu N_H m_p v_{\text{out}} R_{\text{out}}, \quad (2.2)$$

where Ω is the solid angle covered by the outflow, N_H is the column density, m_p is the proton mass, μ is the mean molecular weight, v_{out} is the outflow velocity and R_{out} is the radius of the shell, often approximated as the launch radius of the outflow. In reality, the absorber is probably much more complex, and full RT and photoionization simulations are required to accurately model the expected spectrum. In a series of papers, Sim et al. (2008, 2010b,b) carried out such calculations and found that reasonable verisimilitude with Fe line profiles could be achieved. However, as with many models of AGN, a holistic, broad wavelength range fit is still required.

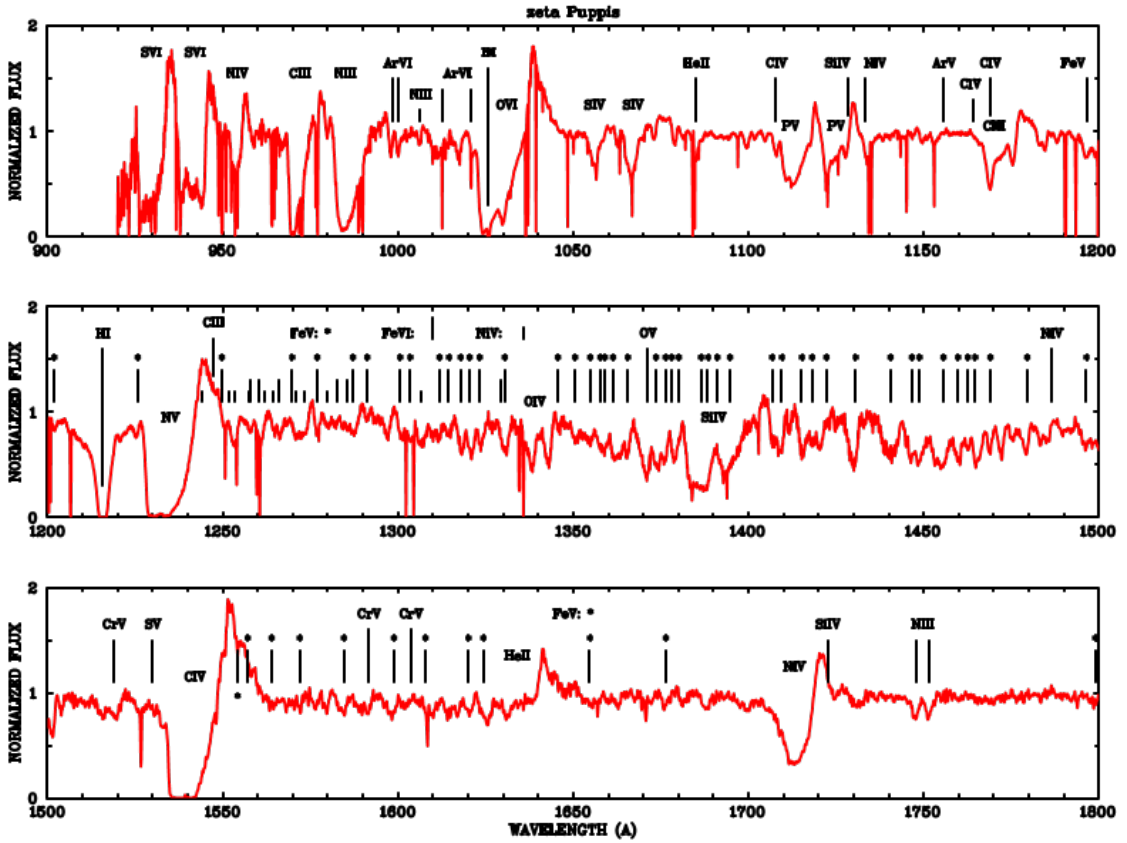


FIGURE 2.9: Credit: Pauldrach et al. 1994. UV spectrum of one of the brightest massive O stars, the O4 supergiant ζ Puppis. The spectrum is merged from Copernicus and IUE UV observations, and the prominent lines are marked.

2.1.4 Stellar Winds

Although stellar winds are clearly not accretion disc winds, they provide a useful, and better understood, testing ground for much of the physics of radiatively-driven outflows. Wolf-Rayet (WR) stars and O-stars possess strong outflows with mass-loss rates of up to $10^{-5} M_{\odot} \text{ yr}^{-1}$, thought to be driven by radiation pressure mediated by spectral lines (see section 2.2.3). Over the typical lifetime of a massive star ($\sim 10^6$ yr), this can have a significant impact on the overall stellar mass, causing losses of around $10 M_{\odot}$ of material.

As with the systems described previously, the P-Cygni profiles seen in hot, massive stars provide the key evidence for the presence of a strong wind (see Fig. 2.9). Mass-loaded winds are also thought to be responsible for the emission lines seen in hot star spectra (e.g. Pauldrach et al. 1994). Indeed, emission line diagnostics have been particularly important in determining the mass-loss rates of stellar winds and have also been used to demonstrate that line-driven stellar winds are clumpy.

2.1.4.1 Clumping in Stellar Winds

Evidence for clumping in hot star winds comes from a range of sources. Perhaps the most conclusive is from electron scattering wings in emission lines: homogenous models overestimate the strength of these wings, whereas clumpy models produce good agreement with data (Hillier 1984, 1991; Hamann et al. 1992, 1994; Schmutz 1997). Further evidence for clumping comes from line variability (Prinja & Smith 1992) and polarisation (Brown et al. 1995). Clumping is theoretically expected in line-driven winds (see section 2.2.3 and the review by Owocki 2014) and is directly dealt with in this thesis. In chapter 5, I describe the treatment of clumping I have implemented in our radiative transfer code, before presenting results from a clumpy AGN wind model.

2.1.5 Outflow Physics

The spectra in figures 2.2, 2.7 and 2.9 show striking similarities – characteristic broad, P-Cygni-like absorption features in UV resonance lines extending to high blueward velocities – despite vast differences in mass and scale. Furthermore, some of the phenomena observed in e.g. stellar winds may naturally solve some of the unanswered questions in other systems. For example, clumping may prevent over-ionization in AGN outflows. It would seem that at least some of the physics of outflows, like accretion physics, is universal, and that lessons learned from smaller-scale systems may be scaleable to AGN and quasars. In order to understand if the similarity extends beyond a cosmetic one, I will discuss some of the underlying physical mechanisms that may be responsible for accelerating these outflows.

2.2 Driving Mechanisms

Let us consider a parcel of ideal gas. By imposing nothing more than conservation of mass, energy and momentum on that parcel, and using Maxwell's equations, we can write down three equations of magnetohydrodynamics (MHD):

$$\frac{D\rho}{Dt} + \rho \nabla \cdot \vec{v} = 0, \quad (2.3)$$

$$\rho \frac{Dv}{Dt} = -\nabla P + \frac{1}{4\pi}(\nabla \times \vec{B}) \times \vec{B} + \rho \vec{g}_{rad} + \rho \vec{g}, \quad (2.4)$$

$$\rho \frac{D}{Dt} \left(\frac{u}{\rho} \right) = P(\nabla \cdot \vec{v}) + \rho \mathcal{L}. \quad (2.5)$$

Here, D denotes a derivative within the comoving frame of the gas parcel, \vec{v} is the velocity, ρ is the gas density, \vec{B} is the local magnetic field, \vec{g}_{rad} is the radiation force per unit mass, \mathcal{L} is the cooling rate of the gas, u is the energy density and \vec{g} denotes the gravitational acceleration vector.

Equation 2.3 is the *continuity equation* and describes conservation of mass. Equation 2.4 is the *equation of motion* and describes conservation of momentum. Equation 2.5 is the *equation of energy conservation*. Equation 2.4 can be used to neatly demonstrate how an outflow can be driven. I have deliberately written equation 2.4 so that all the force terms lie on the RHS. For an outflow to be driven from an accreting object, one of the terms on the RHS must dominate over gravity, $\rho \vec{g}$. These terms thus signify three potential driving mechanisms.

- Magnetic / Lorentz Forces, $\frac{1}{4\pi}(\nabla \times \vec{B}) \times \vec{B}$.
- Radiative Forces, $\rho \vec{g}_{rad}$.
- Thermal Pressure, $-\nabla P$.

We can now examine under what physical conditions (and in which corresponding astrophysical objects) we might expect these forces to overcome gravity and cause a parcel of mass to escape to infinity. In other words: *what might drive a wind?*

2.2.1 Thermal Winds

In a disc in hydrostatic equilibrium (HSE), thermal pressure balances gravity in the vertical direction. The equation of motion in this z direction can then be written as

$$\rho \frac{Dv_z}{Dt} = -\frac{\partial P}{\partial z} + \rho g_z = 0. \quad (2.6)$$

Clearly, if the thermal pressure is significantly increased, this equilibrium condition no longer holds. This can occur in accretion discs at temperatures in excess of $\sim 10^7$ K – where other forces are negligible compared to thermal pressure – and where the escape velocities are relatively low (i.e. far out in the disc). Due to the temperature and gravity scalings, this means that XRBs are natural candidates for showing evidence of thermally driven winds. The outer disc can be heated to the Compton temperature by the central X-ray source, potentially driving relatively high mass-loss rate outflows (Begelman et al. 1983; Woods et al. 1996). This driving mechanism has been proposed as a natural explanation for the ever-present equatorial outflows in soft state XRBs (Ponti et al. 2012). However, they are much less likely candidates in CVs and AGN, because there the escape velocity tends to greatly exceed the thermal velocity.

2.2.2 Radiatively Driven Winds

Under spherical symmetry and for opacities dominated by electron scattering, one simply obtains the Eddington limit discussed in section 1.1.1 when $\rho\vec{g}_{rad} = \rho\vec{g}$. Hence, sources must be fairly close to the Eddington luminosity in order to drive an outflow purely from radiation pressure on electrons. There are a number of accreting systems that may drive super-Eddington (or close to Eddington) outflows, such as AGN with UFOs (e.g. Reeves et al. 2002; Pounds et al. 2016), NLSIs (Done & Jin 2015) and ultra-luminous X-ray sources (ULXs; Walton et al. 2013). However, high-state CVs are significantly below the Eddington limit (Warner 2003), and at least some BALQSOs have low Eddington fractions ($\sim 25\%$ have $L/L_{\text{Edd}} < 0.1$; Grupe & Nousek 2015). These systems may nevertheless be capable of radiatively driving strong outflows due to the influence of line opacity.

2.2.3 Line-driven Winds

Under the right ionization conditions, radiation pressure mediated by spectral lines can be a significant acceleration term in a partially ionized plasma (Castor et al. 1975, hereafter CAK). The most common way to parameterise the cumulative effect of lines on the radiation force is via the *CAK force multiplier*, $\mathcal{M}(t)$, which modifies the equation

for the acceleration due to radiation pressure on electrons to give (Castor 1974, CAK)

$$\vec{g}_{rad} = \frac{\sigma_T F}{\mu c m_p} \mathcal{M}(t), \quad (2.7)$$

where F is the flux, and μ is the mean atomic weight. $\mathcal{M}(t)$ can be approximated by (Abbott 1982)

$$\mathcal{M}(t) = t^{-\alpha} \left(\frac{n_e}{10^{11} \text{ cm}^{-3}} \right)^\delta, \quad (2.8)$$

where t is the dimensionless optical depth, given by

$$t = \frac{\sigma_T \rho v_{th}}{m_p |d(v_i)/ds|}. \quad (2.9)$$

Here, k , α and δ are parameters with best-fit values of 0.28, 0.56 and 0.90, respectively, in O-star winds (Abbott 1982), and v_i is the component of the velocity field in the direction being considered. This is normally a line between the source of radiation and any given location in the wind. It is possible to show (CAK, Owocki et al. 1988) that the maximum force multiplier, $\mathcal{M}_{\max}(t)$, is around 2000–4000. This is already an interesting result, as it tells us that line-driven outflows can be accelerated when accretion rates / luminosities are much lower than the Eddington limit. Indeed, using equation 2.7 we can see that a radiatively driven wind can be accelerated when $L > L_{\text{Edd}}/M(t)$, where $M(t)$ will depend in detail on the spectral lines in question and their relative ionization and excitation fractions. Line-driven winds are present in O-stars and Wolf-Rayet stars, and the theory produces good matches with observations (e.g. Friend & Abbott 1986; Pauldrach et al. 1986, 1994; Hamann et al. 2008). It is also a strong candidate for driving the winds seen in high-state CVs when the accretion disc is UV bright (Pereyra et al. 1997; Proga et al. 1998; Proga 2005, see also section 2.3.4).

Line driving may be a promising mechanism to explain BAL outflows as well, since the strong UV resonance lines seen in absorption in O stars are also present in BALQSOs. The presence of ‘line-locked’ features (Bowler et al. 2014) and the ‘ghost of Ly α ’ (Arav et al. 1995; Arav 1996; North et al. 2006) in the spectra of some BALQSOs also suggests that line-driving is at least contributing to the acceleration of the wind (but see also Cottis et al. 2010). However, the presence of an X-ray source complicates matters. I have already briefly touched on the ‘over-ionization’ problem in AGN outflows, but it now has another consequence. Not only will strong X-rays prevent the right features forming in the spectrum, but, if the outflow is line-driven, they may prevent the wind existing in

the first place. Despite these problems, some hydrodynamic simulations of line-driven AGN winds have been successful in producing high mass-loss rates (see section 2.3.4).

Line-driving is subject to a strong instability known as the line deshadowing instability (LDI; Lucy & Solomon 1970; MacGregor et al. 1979; Owocki & Rybicki 1984, 1985). The basic idea is that any velocity perturbation in a line-driven flow can cause a ‘deshadowing’ effect, as the fluid element will now be in resonance with a region of the spectrum that is less absorbed. Thus, an increase in the line force will occur in proportion with this velocity perturbation, and the instability can grow. Time-dependent numerical modelling of the LDI has shown that it can produce a clumpy flow (Owocki et al. 1988; Feldmeier 1995; Šurlan et al. 2012; Owocki 2014) that may explain the observational characteristics of clumping in stellar winds (see section 2.1.4.1). The LDI is also of interest in CV and AGN winds, as it may affect the ionization state of the flow and possibly the inferred mass-loss rates.

2.2.4 Magnetic Winds

There is still great uncertainty over the magnetic fields in accretion discs and the physics of these magnetic processes. However, the MRI is one of the leading candidates for explaining angular momentum transport in accretion discs, implying that magnetic processes are important in their dynamics. Thus, in many senses, magnetic driving is an attractive wind driving mechanism. There are two main ways in which magnetic forces can drive an accretion disc wind, which are best explained by writing down an alternative form for the Lorentz force,

$$\vec{F}_m = \frac{1}{4\pi}(\nabla \cdot \vec{B})\vec{B} - \nabla \frac{B^2}{8\pi}, \quad (2.10)$$

where $B = |\vec{B}|$. The first term can be thought of as a magnetic *tension* associated with the field lines and the second as an isotropic magnetic *pressure*.

Historically, the most popular magnetic wind model has been the ‘bead on a wire’ mechanism proposed by Blandford & Payne (1982) and Pelletier & Pudritz (1992). In these models, the poloidal magnetic field is dominant and is anchored in the accretion disc. A wind can then be driven by magnetic tension, as the first term in the above equation operates on fluid elements (‘beads’) on the surface of the accretion disc. This can accelerate a wind when the poloidal component of the field makes an angle of $> 30^\circ$

with the normal to the disc surface. These models are known as magnetocentrifugal winds, as it is the interaction between centrifugal forces and a strong, large-scale, ordered magnetic field threading the disc that drives the wind. Magnetocentrifugal wind models have been proposed for both AGN and YSOs (Pelletier & Pudritz 1992; Konigl & Kartje 1994; Kudoh & Shibata 1997), and numerical simulations have demonstrated that this mechanism can produce jets and outflows (Romanova et al. 1997; Ouyed & Pudritz 1997; Ustyugova et al. 1999).

In an alternative MHD model the isotropic magnetic pressure is responsible for driving the outflow (Proga 2003). In this case the toroidal component dominates over the poloidal component and drives a slow, dense outflow which behaves more like a thermally-driven wind (i.e. it conserves specific angular momentum rather than angular velocity).

2.3 Accretion Disc Wind Models

A number of different wind models have appeared in the literature over the years, each attempting to explain the different observational characteristics of quasars and CVs with a mixture of conceptual frameworks and underlying physics. In AGN and quasars, the authors behind the models attempt to explain the origins of BELs and BALs, although some extend their remit into the infra-red, radio and X-ray regimes. In CVs, the picture is slightly more straightforward, as the geometry of the outflow is better constrained (see section 2.1.1). Below, I will briefly discuss a few examples that have gained traction over the years, particularly those describing quasars and unification, before outlining the kinematic prescription I have used in the modelling that forms part of this thesis. This prescription has been successfully applied to both CVs and AGN.

2.3.1 MCGV95: A Line-driven Wind Model for AGN

MCGV95 proposed a model in which a smooth wind rises from an accretion disc with a launch radius of around 10^{16} cm. The wind is equatorial, with an opening angle of 5° , and is accelerated by line forces up to a terminal velocity of $0.1c$. A sketch of the geometry is shown in Fig. 2.10. One of the key features of the model is the presence of

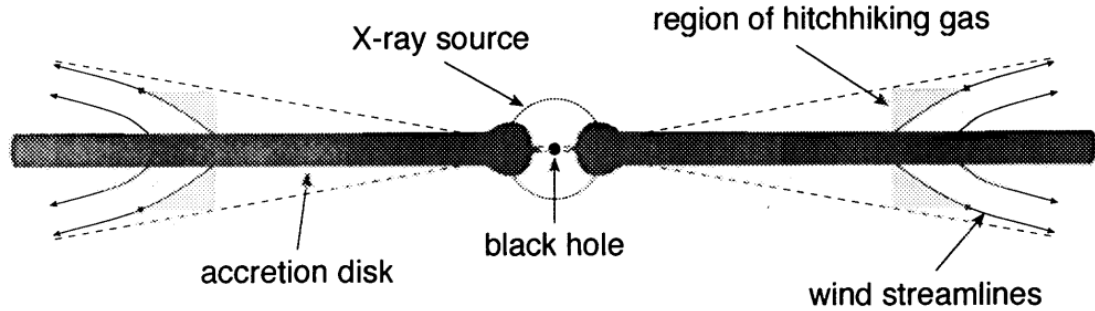


FIGURE 2.10: Credit: Murray et al. 1995. Cartoon showing the geometry of the MCGV95 model.

a ‘shield’ of hitchhiking gas, which protects the outflow from X-ray over-ionization and allows radiation pressure on UV resonance lines to efficiently accelerate the flow.

MCGV95 found that BAL profiles were seen for an observer looking into the wind cone, and significant collisionally excited line *emission* emerged at low inclinations. This line emission came from a relatively small BLR ($r_{BLR} \sim 10^{16}$ cm) at the base of the wind, where densities were high ($n_e \approx 10^{10}$ cm $^{-3}$). The MCGV95 model was one of the first successful disc-wind unification models. It is especially impressive as it includes photoionization calculations and quantitative estimates of the resultant line EWs. However, the effects of multiple scattering and complex radiative transfer effects could not be included in the calculations (see chapter 5).

2.3.2 De Kool & Begelman: A Radiatively Driven, Magnetically Confined Wind

It is, of course, possible that radiation and magnetic fields are both important in determining the outflow characteristics. In the [de Kool & Begelman \(1995\)](#) model, radiation pressure drives an outflow from an accretion disc and also compresses the magnetic field lines that are dragged along with the flow. This causes the magnetic field strength in certain regions to be comparable to the gas pressure, meaning that clouds can be magnetically confined in the flow. A diagram is shown in Fig. 2.11. The authors find that such a model would naturally emerge at a fairly equatorial angle with a covering factor of around 10%, and that lower ionization material would be intercepted when the system was viewed from higher inclinations, potentially explaining some of the properties of LoBALQSOs.

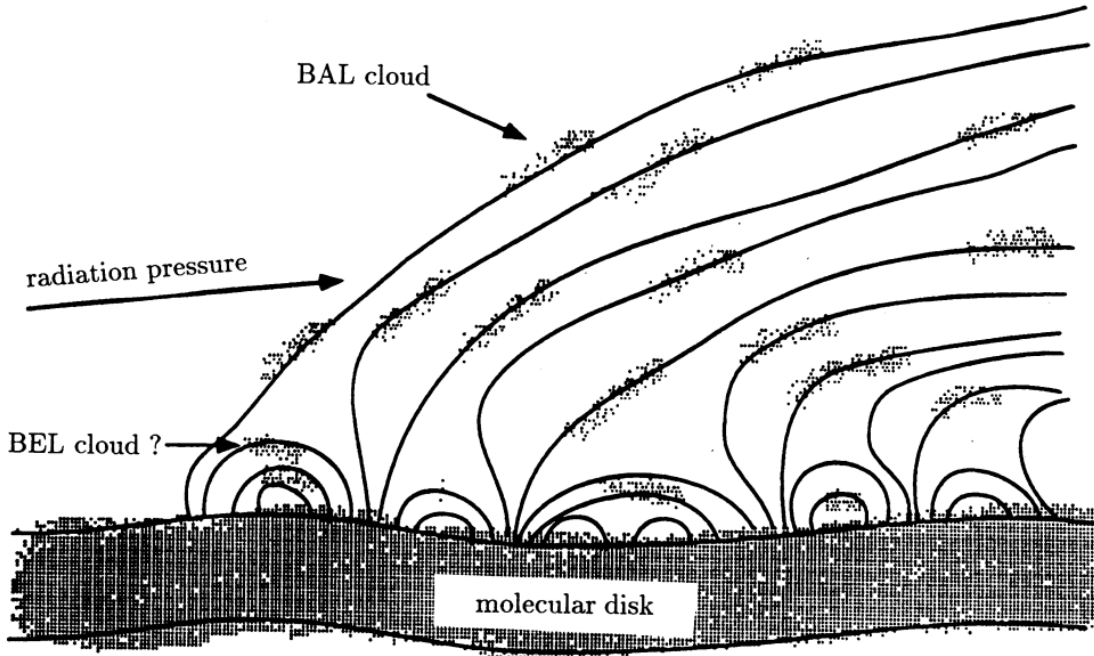


FIGURE 2.11: Credit: De Kool & Begelman 1995. A cartoon showing the components in the De Kool & Begelman model.

2.3.3 Elvis 2000: A Structure for Quasars

[Elvis \(2000\)](#) expanded on the work of MCGV95 by proposing a simple disc wind model, empirically designed to explain as much of quasar phenomenology as possible within one unifying framework. The geometry of Elvis' is shown in Fig. 2.12. As in the two previous models, observers looking into the wind cone will see a BALQSO, whereas observers looking down onto the wind will see a type 1 quasar. Initially, the wind rises vertically, so that observers looking underneath the flow will see NALs, due to the small range of velocities intercepted by their line of sight.

The flow conserves angular momentum, such that the initial Keplerian velocities determine the BEL widths, before accelerating to BAL-like velocities of $\sim 0.1c$. The wind is assumed to be two-phase, with BEL and BAL clouds embedded in a warm, highly ionized medium (WHIM). This WHIM is responsible for WA-like absorption and the X-ray scattering phenomena seen in AGN. It is also responsible for confining the BAL and BEL clouds, allowing high densities and cooler temperatures to exist within the flow. The ionization structure for the wind is stratified, such that the material further out along the disc plane is somewhat shielded from the inner disc and X-rays. This allows the lower ionization BEL profiles to form in the right locations, and also means that LoBAL profiles would be seen at a subset of inclinations.

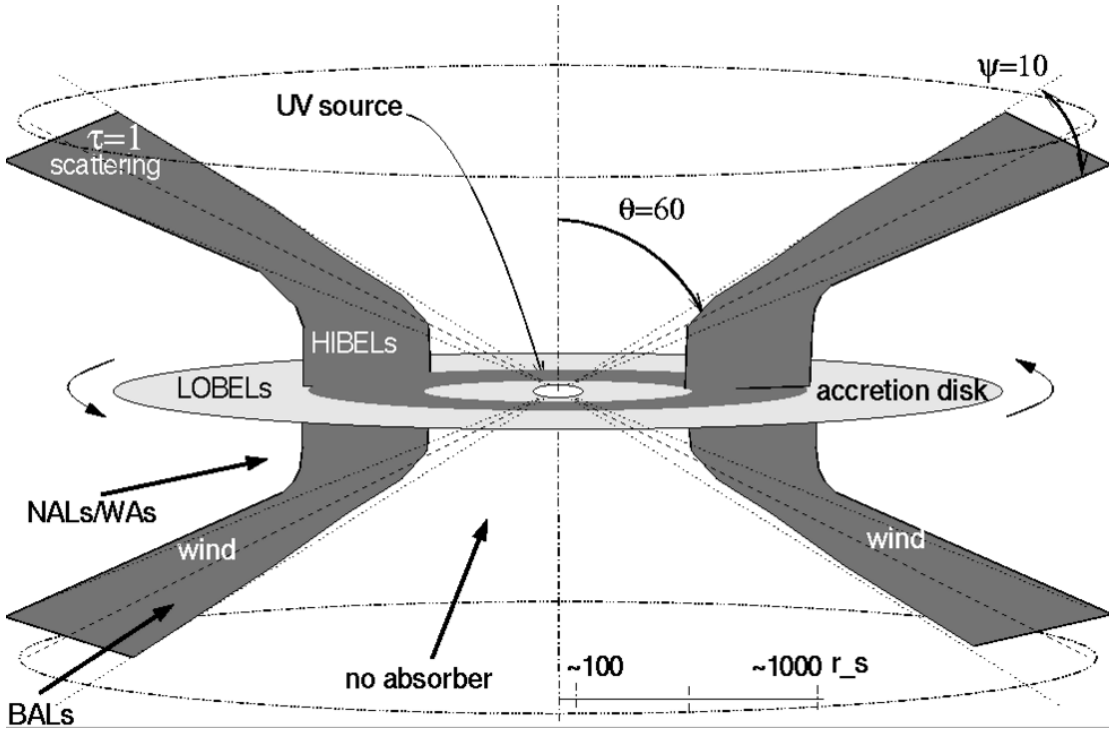


FIGURE 2.12: Credit: Martin Elvis. A schematic showing the main features of the Elvis model. A biconical wind rises from an accretion disc, and the observed spectrum is determined purely by the viewing angle of the observer.

2.3.4 Proga et al.: Line-driven Hydrodynamic Models for AGN and CVs

Around the turn of the century, Daniel Proga and collaborators published a series of important papers in which they conducted hydrodynamic simulations of line-driven disc winds in AGN and CVs. In the first of these, the problem considered was that of disc winds in CVs (Proga et al. 1998). In their model, the disc was assumed to radiate according to the α -disc model, and the central WD was also included as a radiating source. They found that when the disc has $L/L_{\text{Edd}} \gtrsim 1/\mathcal{M}_{\max}(t) \approx 0.001$, then strong, line-driven outflows are driven from a few WD radii with bending angles of $\sim 45^\circ$. This result agreed qualitatively with outflows in CVs, and later efforts to compute synthetic line profiles produced promising results (Proga et al. 2002a). This was the first successful demonstration of line driving in a full hydrodynamic simulation.

The same principle was then applied to the problem of AGN outflows, with the additional complication of an ionizing X-ray source now included (Proga et al. 2000; Proga & Kallman 2004, hereafter PK04). A snapshot from the PK04 model is shown in Fig. 2.13. An inner ‘failed’ wind forms in this simulation, which initially rises up from the disc

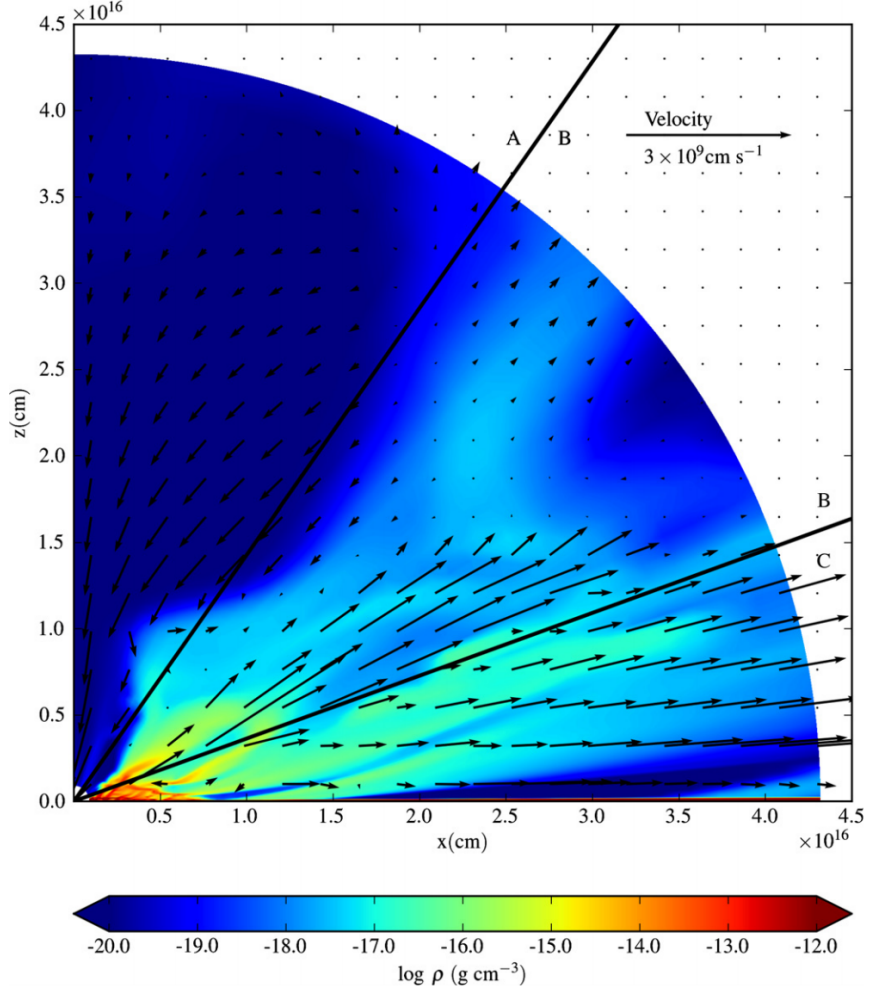


FIGURE 2.13: Credit: Higginbottom et al. 2014.. A snapshot of the PK04 model. Colours shows the density and arrows show the velocity of the flow. The radial lines separate three areas described by H14.

before being over-ionized by the central X-rays. Crucially, this acts as a shield, similarly to the hitchhiking gas proposed by MCGV95, and allows a line-driven wind to be accelerated further out in the disc. This outflow can be seen clearly in Fig. 2.13.

One of the interesting results of these simulations is that they tended to produce somewhat unsteady, clumpy flows. In the CV case, this was caused by the interaction between the line force and gravity, as both force terms vary differently with height. In the AGN case, it was instead due to the critical importance of the ionization state on the line force. Parcels of gas can only be accelerated if they have the ‘right’ ionization state, and this depends critically on both their density and the radiation field they see. This causes a coupling between the dynamics of the flow and the path of ionizing radiation. The radiation field also helps determine the geometry of the outflow, as increasing the strength of the radiation interior to the launch radius tends to flatten out the wind and

lead to more equatorial outflows ([Proga 2005](#)). This is particularly important when considering quasar unification, as it means the viewing angles of BALQSOs can provide information about where the wind is launched.

It is worth noting that the smaller scale LDI could not be included in this model, partly for computational reasons and partly because of the approximations used to treat the radiation field. Treating the radiation transport is also important for other reasons. [Higginbottom et al. \(2014\)](#), hereafter H14 showed that, in this particular geometry, multiple scattering actually makes shielding ineffective, and radiation will simply find its way around the failed wind to over-ionize the flow beyond (see also [Sim et al. 2010b](#)). Ideally, full radiative transfer and hydrodynamical simulations would be used to estimate the viability of line-driven winds. Our team is currently working on this problem (see H14 for the first step); however, much can also be learned from simpler, kinematic prescriptions for outflows, which can already be modelled with full treatments of radiative transfer and ionization.

2.4 A Kinematic Prescription for a Biconical Wind

[Shlosman & Vitello \(1993\)](#), hereafter SV93 expanded on the work of the stellar wind community (e.g. [Abbott & Lucy 1985](#)) in proposing a kinematic model for an accretion disc wind. Unlike hydrodynamical models, this model has no real predictive power in terms of velocities and mass-loss rates. Instead, one sets these quantities in advance and examines the resultant properties of the flow and the emergent spectra. The SV93 prescription is the most common way of describing the outflow in the radiative transfer code PYTHON (see chapter 3) and has been used to simulate spectra for CVs ([Long & Knigge 2002](#); [Matthews et al. 2015](#), chapter 4), AM CVn systems ([Kusterer et al. 2014](#)) and AGN/quasars ([Higginbottom et al. 2013](#); [Matthews et al. 2016](#); [Yong et al. 2016](#), chapter 5). An alternative description was developed by [Knigge et al. \(1995\)](#) and has been used in similar applications ([Long & Knigge 2002](#); [Sim et al. 2008, 2010a](#)), as well as for young-stellar objects (YSOs; [Sim et al. 2005](#)). Kinematic prescriptions have thus been a useful tool in allowing quantitative tests of conceptual models, specifically for assessing their ability to reproduce the observed spectra of a variety of astrophysical systems.

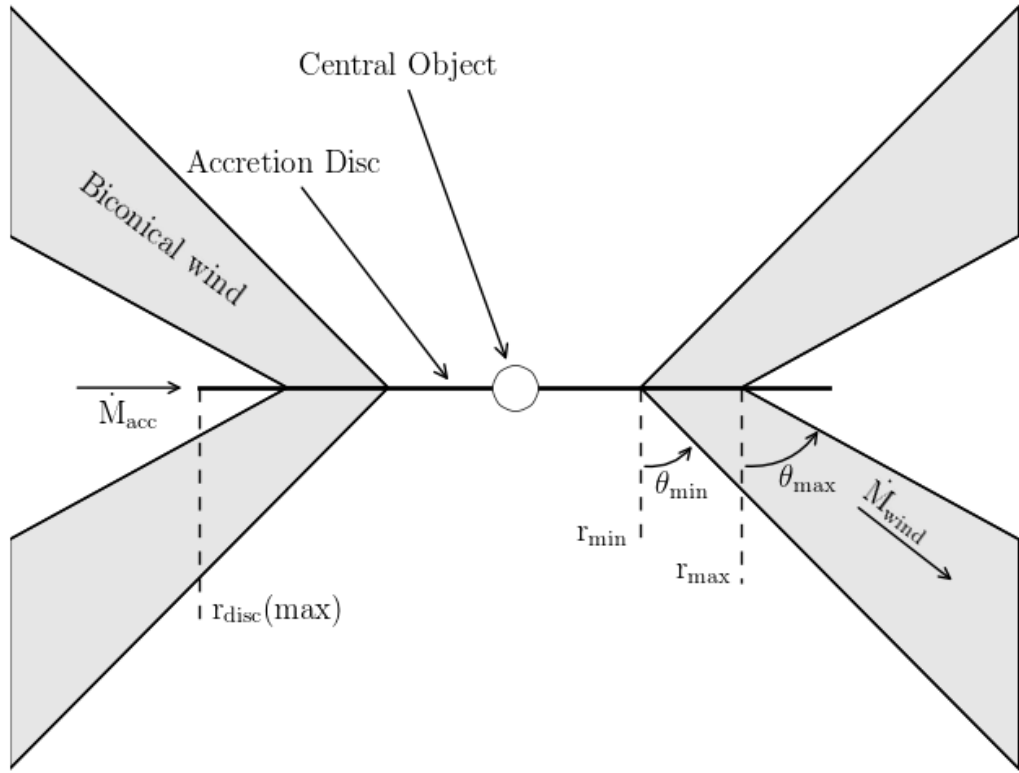


FIGURE 2.14: A schematic showing the geometry and kinematics of the SV93 model.

In the SV93 parametrization, a smooth, biconical disc wind emanates from the accretion disc between r_{\min} and r_{\max} . A schematic is shown in Fig. 2.14. The covering fraction of the outflow is also controlled by the inner and outer opening angles of the wind, θ_{\min} and θ_{\max} , and the launch angle of the other streamlines is given by

$$\theta(r_0) = \theta_{\min} + (\theta_{\max} - \theta_{\min}) \left(\frac{r_0 - r_{\min}}{r_{\max} - r_{\min}} \right)^{\gamma}, \quad (2.11)$$

where r_0 is the launch radius of the streamline.

The poloidal (non-rotational) velocity field of the wind, v_l , is given by

$$v_l = v_0 + [v_{\infty}(r_0) - v_0] \frac{(l/R_v)^{\alpha}}{(l/R_v)^{\alpha} + 1}, \quad (2.12)$$

where l is the poloidal distance along a particular wind streamline. The terminal velocity along a streamline, v_{∞} , is set to a fixed multiple of v_{esc} , the escape velocity at the launch point. The terminal velocity will therefore be higher for streamlines closer to the inner disc edge. The launch velocity from the disc surface, v_0 , is assumed to be constant (set to 6 km s^{-1}). Once the wind is launched, it accelerates, reaching half

of its terminal velocity at $l = R_v$. The velocity law exponent, α , controls how quickly the wind accelerates. Larger values of α cause the main region of acceleration to occur close to R_v , whereas smaller values correspond to fast acceleration close to the disc (see Fig. 2.15). The rotational velocity, v_ϕ , is Keplerian at the base of the streamline, and the wind conserves specific angular momentum, such that

$$v_\phi r = v_k r_0, \quad (2.13)$$

where $v_k = (GM_{WD}/r_0)^{1/2}$. The mass-loss rate per unit surface area, \dot{m}' , can be controlled by a free parameter, λ_m , such that

$$\dot{m}' \propto \dot{M}_W r_0^{\lambda_m} \cos[\theta(r_0)], \quad (2.14)$$

where \dot{M}_W is the total mass loss rate in the wind. This equation is normalised so that when integrated over both sides of the disc the correct \dot{M}_W emerges. I have adopted $\lambda = 0$ throughout this thesis, which corresponds to uniform mass loss across the disc. This could have an effect on the level of shielding present in the flow, and the location of the emission line regions, but should not affect the qualitative conclusions; this is briefly discussed in section 5.4.1. The density at a given point can then be calculated by imposing mass conservation and using the velocity law. At the base of the wind, the density is given by

$$\rho(r_0) = \frac{\dot{m}'(r_0)}{v_z(r_0)}. \quad (2.15)$$

At a coordinate (r, z) in the wind, the density is then

$$\rho(r, z) = \frac{r_0}{r} \frac{dr_0}{dr} \frac{\dot{m}'(r_0)}{v_z(r, z)}, \quad (2.16)$$

where the corresponding r_0 is found by considering the streamline that passes through (r, z) . These equations govern the kinematics and densities in the wind in the SV93 prescription, which is used extensively throughout this thesis.

2.5 The big picture: AGN Feedback

The event horizon of a $10^9 M_\odot$ BH is approximately 10^{15} cm, a billionth of the radius of a typical galactic bulge. This is roughly the ratio in size between a small coin and

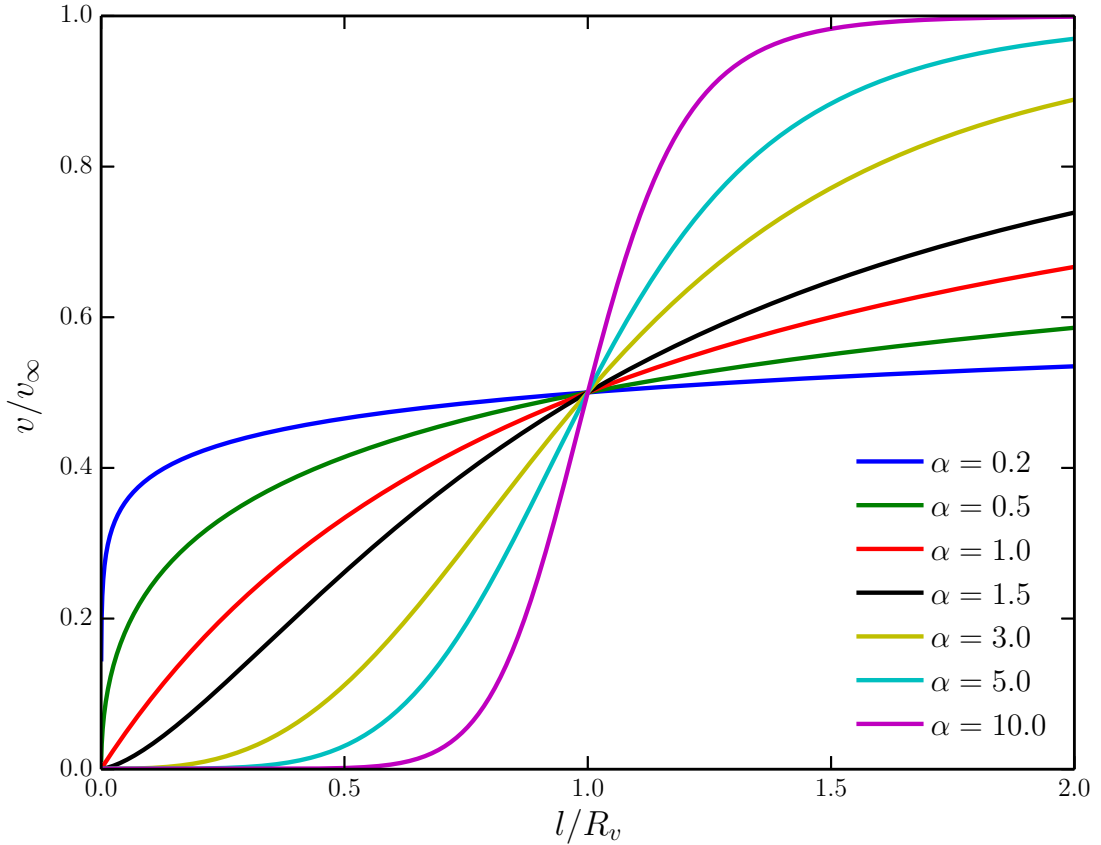


FIGURE 2.15: The SV93 velocity law for various values of the acceleration exponent, α .

the Earth. Even the sphere of gravitational influence of the BH is roughly 1000 times smaller than the size of the galactic bulge. Despite this vast difference in scale, there is strong evidence that the physics on the scale of the gravitational radius of the BH affects the evolution and dynamics of its host galaxy. This becomes less surprising when considering the *energetics* of accretion. The binding energy of a galactic bulge, with mass M_{bulge} and velocity dispersion σ_* , is

$$E_{\text{bulge}} \approx M_{\text{bulge}} \sigma_*^2, \quad (2.17)$$

while the energy released in growing a black hole to a mass M'_{BH} is (equation 1.3, assuming $\eta = 0.1$)

$$E_{BH} \approx 0.1 M'_{BH} c^2. \quad (2.18)$$

By combining these two equations, and substituting in typical numbers ($\sigma_* = 0.001c$, $M'_{BH}/M_{\text{bulge}} = 10^{-3}$), we can show that

$$\frac{E_{BH}}{E_{\text{bulge}}} \approx 10^{-4} \left(\frac{c}{\sigma_*} \right)^2 \sim 10. \quad (2.19)$$

In other words, the energy released when growing a BH can significantly exceed the binding energy of the galactic bulge. This energetic argument is, of course, not sufficient to claim that the accreting BH must affect its host. For example, if the radiated energy never experienced an optical depth of ~ 1 , it could not couple to the galactic bulge. However, we have already seen that many outflows in AGN possess kinetic luminosities that are significant compared to the bolometric luminosity. Thus, outflows (and jets) may provide a mechanism by which the vast accretion energies can be transferred to the BH environment.

2.5.1 Observational evidence for feedback

Perhaps the most famous pieces of evidence for some kind of long-distance relationship between a central BH and its host galaxy are the $M_{BH} - \sigma_*$ (Ferrarese & Merritt 2000; Gebhardt et al. 2000; Gultekin et al. 2009) and $M_{BH} - M_{\text{bulge}}$ (Magorrian et al. 1998; Häring & Rix 2004; McConnell & Ma 2013) correlations, shown in Fig. 2.16 and Fig. 2.17, respectively. By themselves, these correlations would not necessarily imply that the AGN is having an impact on its environment. Indeed, there are many different theoretical models for the origin of these relations (e.g. Somerville et al. 2001; Adams et al. 2001; Burkert & Silk 2001; King 2003; Croton et al. 2006; Kormendy & Ho 2013). However, there are many other clues that outflows and jets from AGN can affect the host galaxy evolution and morphology.

The galaxy luminosity function describes the number of galaxies as a function of luminosity and is generally modelled with the Schechter (1976) function. Theories of galaxy evolution tend to overpredict the number of galaxies at the high luminosity end, which can be avoided by invoking quenching of star formation by the central AGN (e.g. Read & Trentham 2005; Bongiorno et al. 2016). Galaxies also show bimodality in their colour distributions (Strateva et al. 2001; Bell et al. 2003; Baldry et al. 2004), with a clear separation between a blue, star-forming main sequence, and a red sequence with lower specific star formation rate (sSFR). Furthermore, these two sequences tend to lie in the

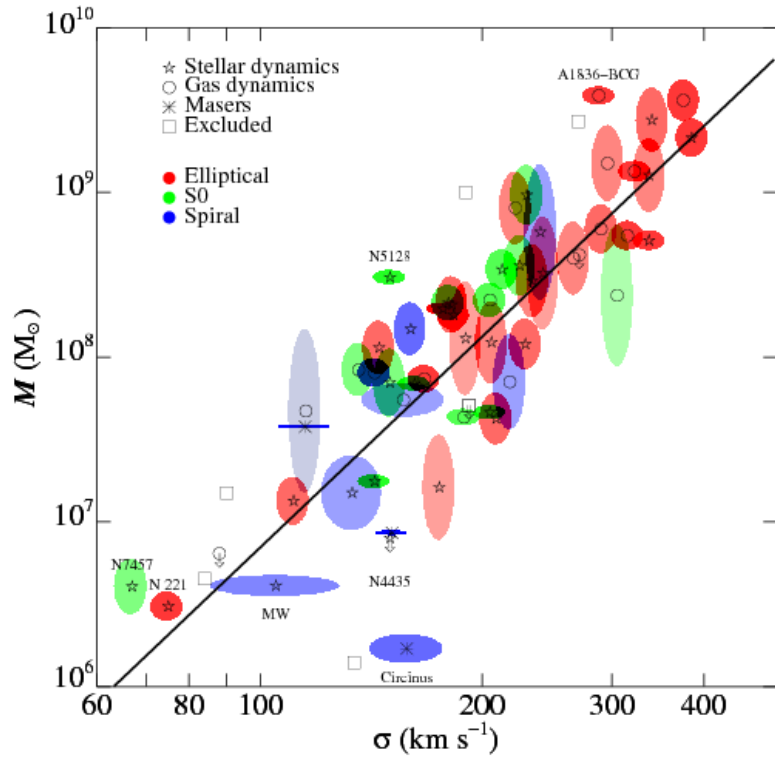


FIGURE 2.16: Credit: Gultekin et al. 2009. The $M_{BH} - \sigma_*$ correlation.

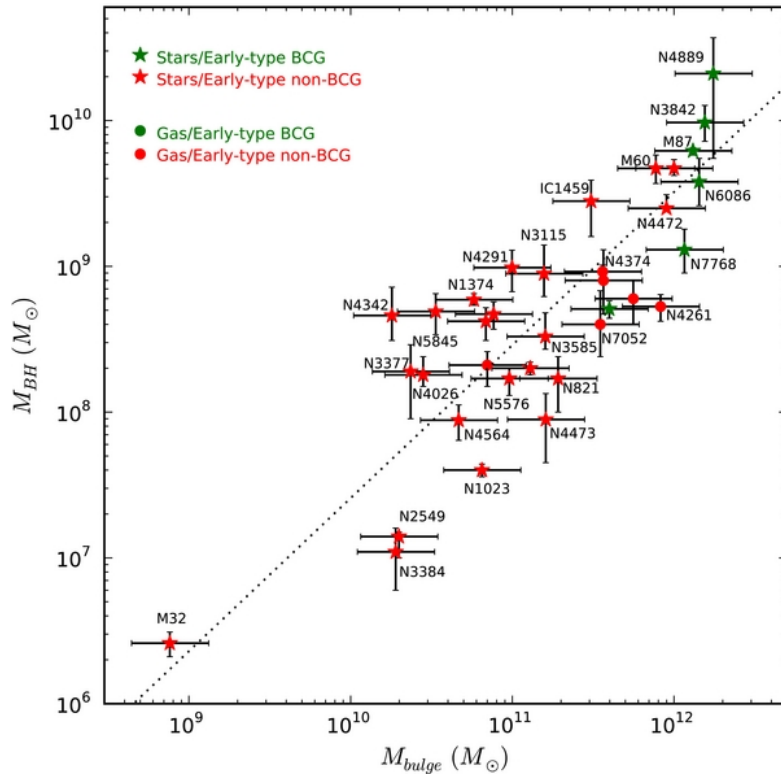


FIGURE 2.17: Credit: McConnell & Ma 2013. The $M_{BH} - M_{bulge}$ correlation.

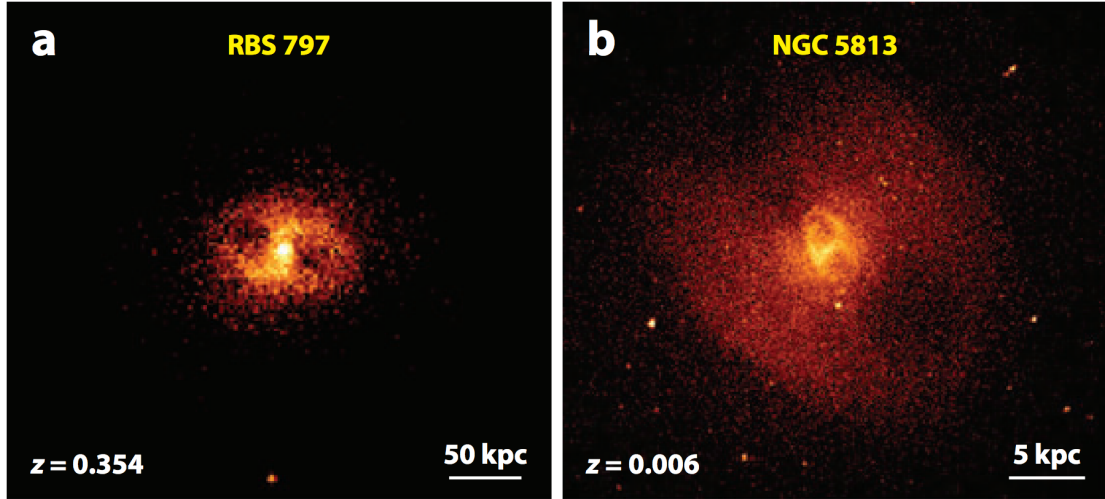


FIGURE 2.18: *Figure adapted from Fabian 2012.* Chandra X-ray images showing two examples of X-ray cavities, illustrating how a radio jet from an AGN can have a dramatic impact on its environment. a) The RBS 797 Cluster (Cavagnolo et al. 2011). b) elliptical galaxy NGC 5813 (Randall et al. 2011).

same regions of colour space as the host galaxies of high and low Eddington fraction AGN, respectively, implying that the AGN may be directly responsible for quenching star formation and moving a galaxy onto the ‘red and dead’ branch. This has been demonstrated in several numerical simulations (e.g. Springel et al. 2005; Croton et al. 2006).

There is also evidence that AGN are energetically significant on scales larger than the galactic bulge. X-ray observations of cool core clusters and elliptical galaxies can show dramatic X-ray cavities or bubbles up to 50 kpc across, with a radio-loud AGN at the centre (Randall et al. 2011; Cavagnolo et al. 2011; Fabian 2012, Fig. 2.18). This shows how radio jets can significantly impact the surrounding gas, a flavour of feedback known as ‘radio’ or ‘kinetic’ mode. These cavities also provide an estimate of the kinetic power of a radio jet, as the volume of the bubble and surrounding gas pressure gives a rough estimate of the PV work done by the jet. This can be divided by an age estimate for the cavity, giving powers of up to 10^{46} erg s $^{-1}$, which are weakly correlated with the radio luminosity of the source and can be large even for modest radio power (Bîrzan et al. 2008).

However, jets are not the only way for AGN to interact with their environment. I have already briefly discussed in section 2.1.3.3 how fast AGN winds can drive larger-scale molecular outflows. This can be seen spectacularly in the FeLoBALQSO Mrk231, where integrated field spectroscopy shows kiloparsec-scale neutral gas outflows (see Fig. 2.19;

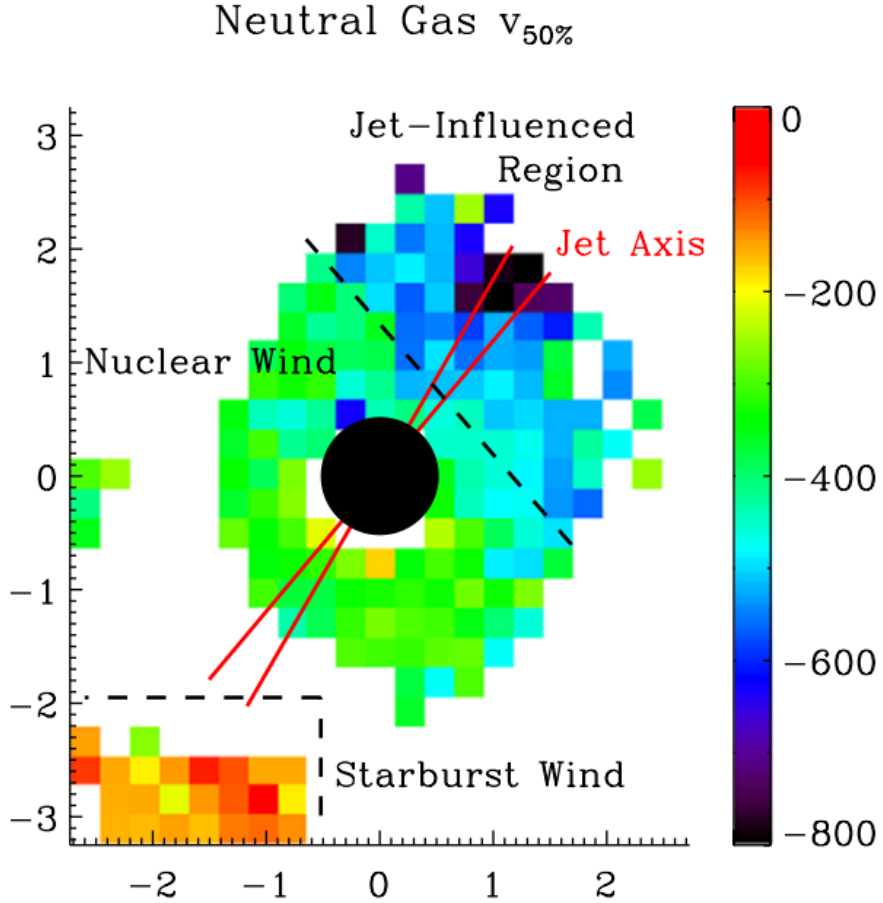


FIGURE 2.19: Credit: Rupke & Veilleux 2011. Results of Gaussian line profile fitting to integral field spectroscopy of Mrk 231. The quantity shown, $v_{50\%}$, corresponds to the centre of the fitted Gaussian profile and indicates that high outflow velocities are present in the neutral gas.

Rupke & Veilleux 2011). Furthermore, King (2003) expanded on the ideas of Silk & Rees (1998) and considered a super-Eddington, momentum-driven outflow expanding into the surrounding gas. This model naturally reproduces the observed slope of the $M_{BH} - \sigma_*$ relation. This line of argument was used to suggest that super-Eddington accretion must be common near the end of a quasar cycle, although it is worth noting that line-driving, or non-radiative driving, means that super-Eddington accretion rates are not necessarily required to drive such an outflow. Intriguingly, it follows that understanding outflow physics has implications for understanding the accretion history of BHs.

2.5.2 Alternative Explanations

It cannot yet be proven that AGN are the drivers of the observed galaxy colour evolution, high-end luminosity function discrepancy or BH-bulge correlations. In particular, it is also possible that mergers are responsible for these phenomena. For example, major

galaxy mergers may explain the ‘red and dead’ branch of the galaxy colour bimodality (e.g. Somerville et al. 2001; Baldry et al. 2004). However, AGN winds and jets are clearly energetically significant with respect to their host galaxies, so estimating their kinetic powers accurately is important in discriminating between in-situ and ex-situ scenarios.

Having established the astrophysical importance of outflows, I will now move on to discussing how we might go about accurately modelling the ionization states of accretion disc winds and their emergent spectra.

Chapter 3

Monte Carlo Radiative Transfer and Ionization

“I’m splashing greys where once was
glowing white”

Mike Vennart, Silent/Transparent

In the previous chapters I have given an introduction to the field and some relevant background relating to accretion discs and their associated outflows. Now it proves useful to discuss the specific *methods* I will use in order to answer some of the questions raised so far. In particular, I will discuss radiative transfer and photoionization techniques.

Notation: This section contains a lot of algebraic quantities and sums over ions, levels, and so on. Throughout, I use N to denote fractional populations of ions and n to denote fractional populations of levels. The primed quantities ℓ' and u' follow the convention of Lucy (2002) in that they denote sums over all lower/upper levels. The symbol \mathcal{R} denotes a total rate (radiative + collisional), and the symbol C is a collisional rate, whereas \mathcal{C} is a cooling rate. Starred quantities are evaluated at the stated temperature but in local thermodynamic equilibrium, following Mihalas (1978). An S superscript denotes that the estimator pertains to simple-atoms.

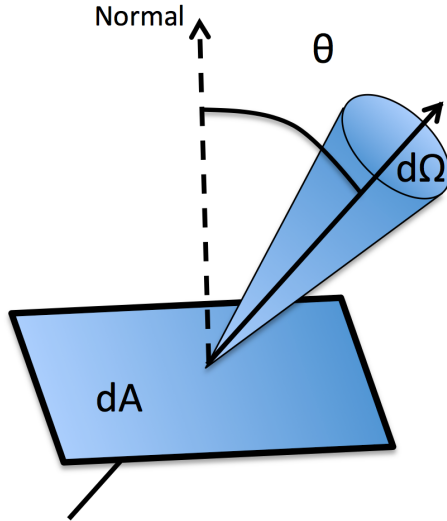


FIGURE 3.1: A schematic showing a ray obliquely incident on a surface of area dA . The labeled quantities are used in the definition of specific intensity.

3.1 Fundamentals of Radiative Transfer

Let us consider a ray passing through a reference surface dA and making an angle θ with the normal to this surface. The energy flow can then be related to the *specific intensity*, I_ν , by

$$I_\nu = \frac{dE}{d\Omega dt dA d\nu}, \quad (3.1)$$

which has units of $\text{erg s}^{-1} \text{Hz}^{-1} \text{sr}^{-1} \text{cm}^{-2}$. The specific intensity is the most fundamental quantity of radiative transfer as it describes everything about the radiation field: its time, angular, spatial and frequency dependence. By successively multiplying by $\cos \theta$ and integrating over solid angle we can obtain the first and second ‘moments’ of the radiation field. These are the flux, F_ν and momentum flux, p_ν , respectively, given by

$$F_\nu = \int I_\nu \cos \theta d\Omega, \quad (3.2)$$

$$p_\nu = \frac{1}{c} \int I_\nu \cos^2 \theta d\Omega. \quad (3.3)$$

The *mean intensity*, J_ν , is

$$J_\nu = \frac{1}{4\pi} \int I_\nu d\Omega. \quad (3.4)$$

The mean intensity is particularly useful when one wants to ignore the solid angle dependence of the radiation, for example when considering the impact of an ionizing radiation field.

The equation describing the specific intensity change along a path element ds is the radiative transfer equation,

$$\frac{dI_\nu}{ds} = -\kappa_\nu I_\nu + j_\nu, \quad (3.5)$$

where κ_ν and j_ν are the absorption and emission coefficients, respectively. If we define the optical depth, $d\tau_\nu = \kappa_\nu ds$, this can be recast as

$$\frac{dI_\nu}{d\tau_\nu} = -I_\nu + S_\nu, \quad (3.6)$$

where $S_\nu = j_\nu / \kappa_\nu$ is the source function. This equation can be solved to give the *formal solution to the radiative transfer equation*,

$$I_\nu = I_{\nu,0} e^{-\tau_\nu} + \int_0^{\tau_\nu} S_\nu(\tau'_\nu) e^{\tau'_\nu - \tau_\nu} d\tau'_\nu. \quad (3.7)$$

A useful limit is when the source function is constant in the absorbing medium, in which case the integral can be easily evaluated to give

$$I_\nu = I_{\nu,0} e^{-\tau_\nu} + S_\nu(1 - e^{-\tau_\nu}). \quad (3.8)$$

3.1.1 Spectral Line Formation

From the above equations, it is trivial to show how emission and absorption lines form when the source function is approximately constant. Say we have a plasma illuminated by a blackbody of temperature T_0 , such that $I_{\nu,0} = B_\nu(T_0)$. The plasma layer then has a different temperature, T , such that $S_\nu = B_\nu(T)$ in that medium. By inspecting equation 3.8 we can see that if we are optically thick within the line, but optically thin in the continuum, then inside the line the source term is dominant and outside the line the first $I_{\nu,0} e^{-\tau_\nu}$ term dominates. Therefore, if $T > T_0$ we will see an emission line, and if $T < T_0$ we will see an absorption line.

3.1.2 Local Thermodynamic Equilibrium

An important physical limit is that of local thermodynamic equilibrium (LTE). This is a first-order way to describe the physical conditions of a plasma and assumes that all the properties of the plasma, such as the level populations and source function, are the same as those in thermodynamic equilibrium for local values of temperature and density.

For this to be the case, the principle of *detailed balance* must also apply, in which every process by which electrons transition between states must be exactly balanced by its inverse process. In LTE, the electron temperature, T_e , is equal to the temperature of the radiation field, T_R , and the source function is given by a blackbody, i.e. $S_\nu = B_\nu(T_R)$. Three microscopic requirements of LTE also follow ([Mihalas 1978](#)):

- a) The velocities of the electrons and ions in the plasma obey Maxwellian distributions, such that

$$f(v) = 4\pi \left(\frac{m_e}{2\pi k T_e} \right)^{3/2} v^2 \exp\left(-\frac{m_e v^2}{2k T_e}\right), \quad (3.9)$$

where m_e is the mass of an electron.

- b) The ionization state of the plasma is governed by the *Saha equation*, which states that two adjacent ions have relative populations given by

$$\frac{N_{i+1} n_e}{N_i} = \frac{2g_{i+1}}{g_i} \left(\frac{2\pi m_e k T_e}{h^2} \right)^{3/2} \exp(-h\nu_0/kT), \quad (3.10)$$

where g_i is the multiplicity of ion i and ν_0 is the threshold frequency.

- c) The excitation state of the plasma is governed by *Boltzmann statistics*. A level j then has a population relative to ground governed by

$$\frac{n_j}{n_1} = \frac{g_j}{g_1} \exp(-E_j/k T_e), \quad (3.11)$$

where E_j is the energy difference between the two levels and g_j is the statistical weight of level j .

Although these three assumptions are sometimes valid, in many astrophysical situations there can be large departures from LTE. A good example of these departures is when the SED is not a blackbody and is affected by absorption – as is the case in AGN and other accreting systems. The Maxwellian assumption is probably the most reliable, but even this may break down when high-energy photons create suprathermal electron distributions ([Humphrey & Binette 2014](#)).

3.1.2.1 Dilute Approximation

A first step away from LTE is to introduce the dilute approximation. In this case, we relax the assumption that $T_R = T_e$ and assume that the mean intensity is given by a

dilute blackbody, i.e.

$$J_\nu = WB_\nu(T_R), \quad (3.12)$$

where W is the dilution factor. The ionization state can then be approximated with a modified Saha equation (Abbott & Lucy 1985; Mazzali & Lucy 1993),

$$\frac{N_{i+1}n_e}{N_i} = W[\xi + W(1 - \xi)] \left(\frac{T_e}{T_R}\right)^{1/2} \left(\frac{N_{i+1}n_e}{N_i}\right)_{T_R}^*, \quad (3.13)$$

where ξ is the fraction of recombinations that go directly to the ground state. The excitation state can also be approximated (fairly poorly) with a dilute Boltzmann equation (Abbott & Lucy 1985; Lucy 1999b)

$$\frac{n_j}{n_1} = W \frac{g_j}{g_1} \exp(-E_j/kT_R). \quad (3.14)$$

3.1.3 The Two Level Atom

The two level atom formalism is well described by Mihalas (1978). Let us consider an atomic model consisting of two levels that are linked by radiative and collisional transitions. Whilst this model is clearly a simplification, it nonetheless allows for a first step into non-LTE line transfer and proves useful for modelling the resonance lines briefly touched on in chapter 2.

To construct our simple model a few assumptions are necessary. The first is the assumption of *statistical equilibrium*. This is the principle that the total rate into a given atomic level/state is equal to the total rate out of said state. This is clearly true whenever the timescale to establish this equilibrium is shorter than the timescale on which the ambient conditions change. The second is the assumption of *complete redistribution (CRD)*, which states that the emission and absorption line profiles are identical for a given transition. These assumptions allow us to formulate rate equations and derive the Einstein relations.

3.1.3.1 Einstein coefficients

Within a two level atom, the statistical equilibrium rate equation between two levels can be written as

$$B_{lu}\bar{J}_{ul}n_l = B_{ul}\bar{J}_{ul}n_u + A_{ul}n_u, \quad (3.15)$$

where B_{lu} , B_{ul} and A_{ul} are the *Einstein coefficients* for absorption, stimulated emission and spontaneous emission, respectively. The ‘mean intensity in the line’, \bar{J}_{ul} , is given by

$$\bar{J}_{ul} = \int \phi(\nu) J_\nu d\nu, \quad (3.16)$$

where $\phi(\nu)$ is the line profile. We can then rearrange equation 3.15 in terms of the mean intensity, giving

$$\bar{J}_{ul} = \frac{A_{ul}/B_{ul}}{(n_l/n_u)(B_{lu}/B_{ul}) - 1}. \quad (3.17)$$

In LTE, $\bar{J}_{ul} = B_\nu(T)$ and the level populations obey Boltzmann statistics, so equations 1.23, 3.11 and 3.17 can be combined to give

$$\frac{2h\nu_{ul}^3}{c^2} \frac{1}{\exp(h\nu_{ul}/kT) - 1} = \frac{A_{ul}/B_{ul}}{(g_l/g_u)(B_{lu}/B_{ul}) \exp(h\nu_{ul}/kT) - 1}. \quad (3.18)$$

This must be true at all values of T , so we can simply equate coefficients to show that

$$\frac{A_{ul}}{B_{ul}} = 2h\nu_{ul}^3/c^2, \quad (3.19)$$

$$\frac{B_{lu}}{B_{ul}} = g_u/g_l. \quad (3.20)$$

These two equations are known as the *Einstein relations* and have no dependence on temperature. They are therefore relations between purely atomic properties.

3.1.4 The Sobolev Approximation

The Sobolev approximation (SA) is a useful limit for treating line transfer in fast-moving flows. Originally the theory was mostly applied to stellar winds, although since then a wide variety of astrophysical objects have been modelled using Sobolev treatments, such as accreting systems (this work) and supernovae. The underlying theory of Sobolev optical depths and the associated escape probability formalism was originally developed by Sobolev (1957, 1960), but has since been expanded on by multiple authors (e.g. Rybicki 1970; Rybicki & Hummer 1978; Hubeny 2001).

The Sobolev limit applies when the local bulk velocity gradients in a flow dominate other any thermal broadening. In the presence of these steep velocity gradients, one can assume that the interaction of a photon of a given frequency with a particular bound-bound transition takes place over a small resonant zone, known as a ‘Sobolev surface’.

The length of this zone is roughly

$$l_s \approx \frac{v_{th}}{dv/ds}, \quad (3.21)$$

where v_{th} is the mean thermal speed of the particles in the flow, and dv_s/ds is the velocity gradient along the direction of the ray. The Sobolev length is thus always defined both as a function of the position in the flow and the direction of the ray in question. It is important that the physical conditions of the plasma do not change on this scale. If this is the case, then we can assume that all line interactions for a given frequency will occur at a single ‘resonant’ point. The location at which a given photon will interact with a line of frequency ν_{ul} is then given, in velocity space, by

$$v_s = c \left(1 - \frac{\nu_{ul}}{\nu}\right), \quad (3.22)$$

where the scalar velocity here is $v_s = \vec{v} \cdot \vec{n}_s$, where \vec{v} is the velocity vector of the flow and \vec{n}_s is the unit vector describing the photon direction. The Sobolev optical depth is then

$$\tau_S = \frac{\pi q_e^2}{m_e c} \left(n_l - n_u \frac{g_l}{g_u}\right) \frac{f_{lu} \lambda_{lu}}{|dv/ds|}, \quad (3.23)$$

where q_e is the electron charge, f_{lu} is the oscillator strength of the transition, and λ_{lu} is the line wavelength. We can see that the physical quantities determining the line opacity are therefore the level populations in the plasma, the velocity gradient and the atomic physics associated with the bound-bound transition. An obvious consequence of the line opacities in a resonant zone is that many line interactions may occur if the line is optically thick. The more line interactions that occur, the higher the chance that an electron will collisionally de-excite, and the photon will be absorbed. It thus becomes useful to introduce the angle-averaged Sobolev escape probability, given by

$$\beta_{ul} = \int \frac{1 - \exp(\tau_S)}{\tau_S} d\Omega, \quad (3.24)$$

which can be approximated by taking an appropriate average, $\langle \tau_S \rangle$, of the Sobolev optical depth, giving

$$\beta_{ul} = \frac{1 - \exp(-\langle \tau_S \rangle)}{\langle \tau_S \rangle}. \quad (3.25)$$

3.1.4.1 Two-level Atom with Escape Probabilities

Let us now write down the rate equation linking our two-level atom,

$$B_{lu}\bar{J}_{ul}n_l + C_{lu}n_l = B_{ul}\bar{J}_{ul}n_u + \beta_{ul}A_{ul}n_u + C_{ul}n_u, \quad (3.26)$$

where I have introduced the collisional rates C_{ul} and C_{lu} , and included the effect of line trapping via the angle-averaged Sobolev escape probability. We now seek to find a relation between the source function in the line and the intensity that will simplify the coupled problem of radiative transfer and statistical equilibrium. When we consider a two-level atom this can be written as ([Mihalas 1978](#))

$$S_{ul} = (1 - q)\bar{J}_{ul} + qB(\nu_{ul}), \quad (3.27)$$

where $B(\nu_{ul})$ is the Planck function at line centre and q is the ‘absorption fraction’. This form can be obtained by splitting equation 3.5 into scattering and absorption components and then substituting in approximate forms for the opacities and emissivities. If we now consider that the emissivity in the line is simply given by $n_u A_{ul} h \nu_{ul} / 4\pi$, it is possible to show that the absorption fraction is given by

$$q = \frac{C_{ul}(1 - e^{-h\nu/kT_e})}{\beta_{ul}A_{ul} + C_{ul}(1 - e^{-h\nu/kT_e})}. \quad (3.28)$$

This quantity is approximately equal to the probability that an excited bound electron will collisionally de-excite and is used in the formulation of two-level atom estimators in section [3.4.2](#).

3.1.5 Monte Carlo Approaches

Simple radiative transfer problems can be solved analytically, but with more complicated geometries it is necessary to use numerical techniques, such as Monte Carlo radiative transfer (MCRT). MC techniques are easily implemented with modern computing approaches and are intuitively parallelisable problems. I will now describe one specific MCRT code, which has been used for the majority of the work in this thesis.

3.2 PYTHON: A Monte Carlo Ionization and Radiative Transfer Code

PYTHON¹ is a Monte Carlo ionization and radiative transfer code. The general philosophy of the code is to be able to produce synthetic spectra for astrophysical objects with outflows in 2.5D, using a self-consistent ionization treatment. The code is written in C, and has been in development since the mid-1990s. Throughout this time it has been used with application to CVs (Long & Knigge 2002, hereafter LK02), YSOs (Sim et al. 2005, hereafter SDL05), supernovae (Kerzendorf & Sim 2014) and AGN/quasars (Higginbottom et al. 2013, 2014, hereafter H13 and H14). It is also capable of producing spectra for stellar winds and conducting simple photoionization balance calculations for comparison with codes such as CLOUDY. Some more detail on code testing and development can be found in sections 3.8 and 3.9, respectively. Although PYTHON is well-described in the publications referenced above, it is central to this thesis, and I will thus provide substantial detail on its operation.

3.2.1 Basics

PYTHON operates in three distinct stages, shown in figure 3.2. First, the user specifies the photon sources, geometry and kinematics of the system, normally with a similar parameterisation to the SV93 model described in section 2.4. The code can operate with a number of different coordinate systems (e.g. spherical polar, cylindrical), but in this work I use only cylindrical coordinates. In this case, the outflow is discretised into a $n_x \times n_z$ logarithmic grid with user-specified dimensions. The co-ordinates, (x_i, z_i) , of the corner of the i th cell are then given by

$$x_i = L_x 10^{(i-1)\frac{\log(R_{\max}/L_x)}{n_x}}, \quad (3.29)$$

$$z_i = L_z 10^{(i-1)\frac{\log(R_{\max}/L_z)}{n_z}}, \quad (3.30)$$

where L_x and L_z are appropriately chosen (but hardwired) scale lengths, and R_{\max} is the extent of the simulation domain. From these co-ordinates the poloidal distance can be calculated and the velocity set according to equation 2.12. The density is then calculated from equation 2.16. An initial temperature, T_{init} is set by the user. The

¹Named c. 1995, predating the inexorable rise of a certain widely used programming language.

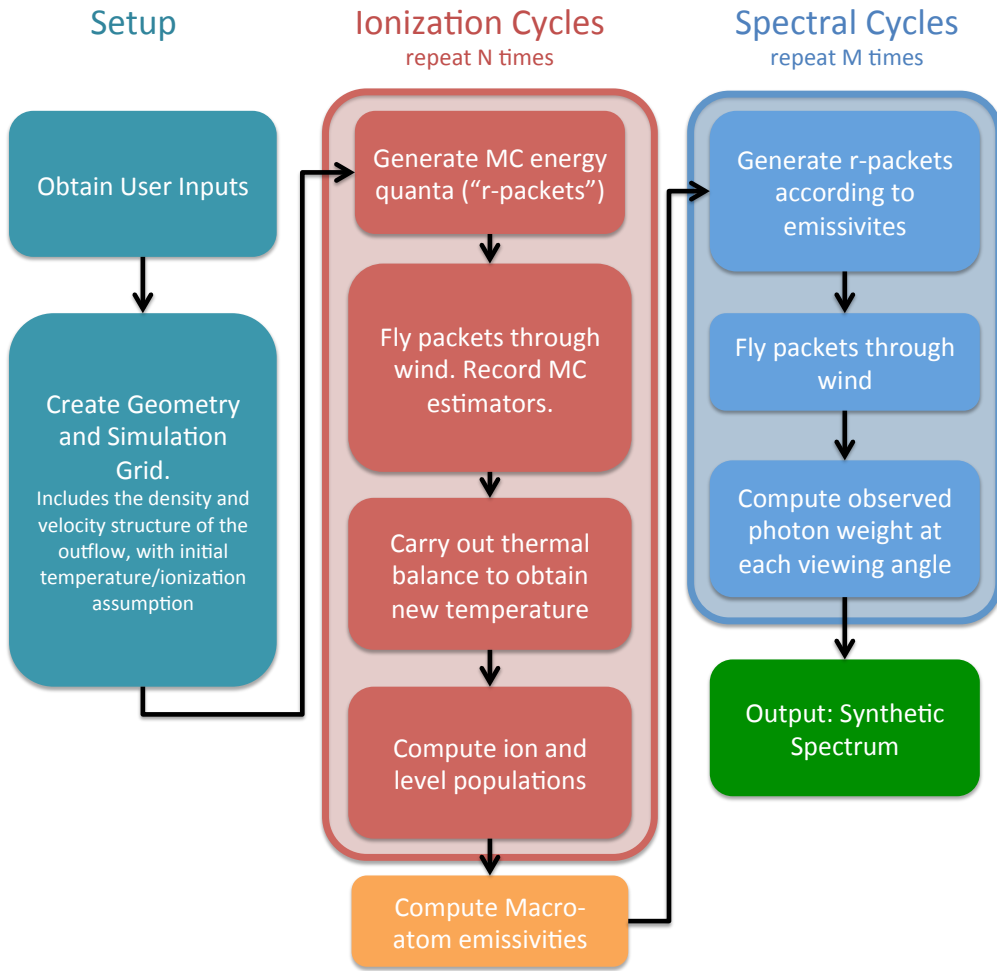


FIGURE 3.2: A flowchart showing the basic operation of PYTHON.

ionization fractions throughout the wind are then initiated to Saha (LTE) abundances at T_{init} , and the level populations are initially set according to the Boltzmann formula.

Once the basic setup process has been carried out, the ionization state, level populations and temperature structure are calculated. This is done via an iterative process, by transporting several populations of MC energy quanta ('photons' or 'r-packets') through the outflow. This process is repeated until the code converges. In each of these iterations ('ionization cycles'), the code records estimators that characterize the radiation field in each grid cell. At the end of each ionization cycle, a new electron temperature is calculated that more closely balances heating and cooling in the plasma. The radiative estimators and updated electron temperature are then used to revise the ionization state of the wind, and a new ionization cycle is started. The process is repeated until heating and cooling are balanced throughout the wind (see sections 3.5 and 3.5.1).

This converged model provides the basis for the second set of iterations ('spectral cycles'; section 3.6), in which the code computes the synthetic spectrum based on the MC estimators recorded during the ionization cycles. The emergent spectrum over the desired spectral range is synthesized by tracking populations of energy packets through the wind and recording the escaping energy packets for a number of user-specified viewing angles. In the ensuing sections, I will describe each of the above steps in more detail, particularly with regards to the macro-atom mode of operation (section 3.3).

3.2.2 Radiation Packets

Every energy packet in the simulation starts out as a radiation packet generated from one of N_S photon sources. To ensure that the frequency distribution of photons is adequately sampled in important frequency regimes, *stratified sampling* is used. A specified fraction, f_i , of photons must emerge each band i , whose frequency boundaries can be adapted for the astrophysical situation considered. The weight, w_i , of the radiation packets in a given energy band with boundaries ν_i and ν_{i+1} is then given by

$$w_i = \frac{\sum_j^{N_S} \int_{\nu_i}^{\nu_{i+1}} L_{\nu,j} d\nu}{f_i N_p}, \quad (3.31)$$

where N_p is the total number of photons desired, and $L_{\nu,j}$ is the monochromatic luminosity of photon source j . The frequency of photons is calculated by constructing a cumulative distribution function (CDF), $f_{C,i}(\nu)$, from the spectral energy distribution in each band i :

$$f_{C,i}(\nu) = \frac{\int_{\nu_i}^{\nu} L_{\nu} d\nu}{\int_{\nu_i}^{\nu_{i+1}} L_{\nu} d\nu}. \quad (3.32)$$

A photon frequency can then be generated by cycling through the bands. In each band, a random number is chosen between 0 and 1, and the frequency is then selected by interpolating on the sampled CDF. This process is repeated until each band has the specified number of photons, with the packet weights adjusted accordingly.

PYTHON can operate in two modes concerning the approach to energy packets. In the original mode described by LK02, continuum processes attenuate the weight of the radiation packets. This attenuation is accounted for by including the wind as an additional photon source. In the second mode, energy packets are indivisible and strict radiative equilibrium is enforced. From here on I will only be discussing this indivisible

packet scheme, as it is required in order to be able to use macro-atoms to accurately treat recombination in H and He.

3.2.3 Radiative Transfer Procedure

As a photon travels through a plasma, it has a finite probability of interacting with free or bound electrons and undergoing a scattering or absorption event. In order to deal with this in a Monte Carlo sense, a random optical depth is generated before an r -packet is moved,

$$\tau_R = -\ln(1 - \mathcal{Z}), \quad (3.33)$$

where \mathcal{Z} is a random number between 0 and 1. The r -packet is then gradually transported through a given cell. As it moves, the optical depth, τ' , it experiences is incremented continuously, representing continuum processes. When the r -packet comes into resonance with a line, according to equation 3.22, the Sobolev optical depth is calculated from equation 3.23 and added to τ' . This process is illustrated in Fig. 3.3 and continues until $\tau' \geq \tau_R$ or the r -packet leaves the cell. If the photon leaves the cell, the values of τ_R and τ' are preserved, and the process continues using the conditions in the new cell. If $\tau' \geq \tau_R$, then an interaction with the plasma has occurred, and the process governing this interaction must be identified. This is done by randomly picking an interaction process in proportion with their contributions to τ' . If the process is an electron scatter then a new, isotropic direction is generated for the r -packet. Otherwise, the packet must interact with either the thermal pool or the excitation energy of the plasma.

3.2.3.1 Continuum Opacities

In order to calculate τ' in the above approach, we need to know the opacities that will contribute to it. An opacity at a given frequency, $\kappa(\nu)$, is related to an optical depth, $\tau(\nu)$, by

$$\tau(\nu) = \kappa(\nu) \Delta s, \quad (3.34)$$

where Δs is the distance moved by the photon. The bound-free opacity is calculated from a sum over photoionization cross-sections (bfjumps), such that

$$\kappa_{bf} = \sum_{j\kappa}^{\text{bfjumps}} \sigma_{j\kappa}(\nu) n_j. \quad (3.35)$$

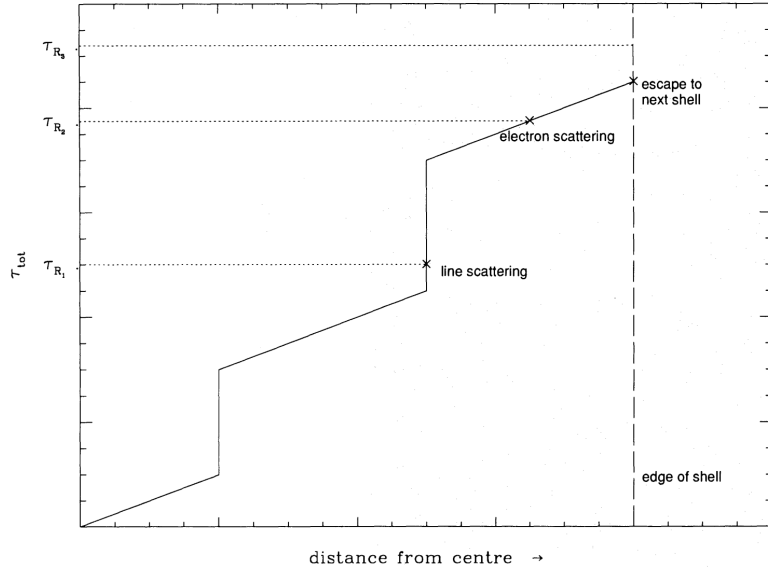


FIGURE 3.3: Credit: Mazzali & Lucy 1993. The process of choosing a scattering location in a cell.

The free-free emission coefficient for an individual ion i of charge Z_i is (Gayet 1970)

$$j_{ff,i}(\nu) = \bar{g}_{ff} \frac{8Z_i^2 q_e^6}{3m_e^2 c^3} \left(\frac{2\pi m_e}{3kT_e} \right)^{1/2} N_i n_e \exp(-h\nu/kT_e), \quad (3.36)$$

where \bar{g}_{ff} is the mean free-free Gaunt factor and formally depends on both frequency and temperature. The free-free opacity is calculated from Kirchhoff's law,

$$\kappa_{ff,i}(\nu) = \frac{j_{ff,i}(\nu)}{B_\nu(T_e)}. \quad (3.37)$$

These opacities are all used in the heating and cooling estimators introduced in section 3.3.3. For radiative transfer purposes, electron scattering is treated in the Thomson limit

$$\kappa_{es} = \sigma_T n_e. \quad (3.38)$$

However, for heating and cooling balance the electron scattering opacity is treated in the Compton limit, in order to estimate the Compton heating and cooling effect on the plasma. The Compton opacity is given by

$$\kappa_C = \sigma_{KN}(\nu) n_e, \quad (3.39)$$

where $\sigma_{KN}(\nu)$ is the cross-section computed from the Klein-Nishina formula (Klein & Nishina 1929) and, unlike σ_T , is frequency dependent.

3.2.3.2 Doppler Shifts

When calculating opacities, the photon frequency must be shifted from the rest frame of the photon into the rest frame of the plasma. This shift depends on the before and after directions of the photon. Let us denote these two directions with unit vectors \vec{n}_i and \vec{n}_f , respectively, and consider a situation when a photon scatters off an electron in a region of the wind moving at velocity \vec{v} . The final frequency of the photon with initial frequency ν_i is then

$$\nu_f = \nu_i \frac{1 - (\vec{v} \cdot \vec{n}_i)/c}{1 - (\vec{v} \cdot \vec{n}_f)/c}. \quad (3.40)$$

In the case of a resonance scatter with line transition $u \rightarrow j$, the new frequency is

$$\nu_f = \frac{\nu_{uj}}{1 - (\vec{v} \cdot \vec{n}_f)/c}. \quad (3.41)$$

When we consider that the resonant point is chosen according to equation 3.22, and that $v = \vec{v} \cdot \vec{n}_f$ in this case, it is clear that the above two equations are equivalent.

3.2.3.3 Choosing Packet Directions

The last variable, in addition to w_i and ν , needed to define a radiation packet is the direction of travel. In the case of isotropic emission, the direction of a photon packet is chosen so that the probability of emission in each bin of solid angle is the same. It follows that

$$p(\Omega) d\Omega \propto \cos \theta \sin \theta d\theta d\phi, \quad (3.42)$$

where the angles are in polar coordinates and relative to the local outward normal. For a spherical emitting source, such as a star, one must first generate a location on the star's surface and then calculate the photon direction relative to the normal at the point. For emission from optically thick surfaces the above equation can be modified to include linear limb darkening, $\eta(\theta)$:

$$p(\theta, \phi) d\theta d\phi = \eta(\theta) \cos \theta \sin \theta d\theta d\phi. \quad (3.43)$$

The Eddington approximation is usually adopted in the code, so that $\eta(\theta)$ is given by

$$\eta(\theta) = a(1 - \frac{3}{2} \cos \theta). \quad (3.44)$$

The constant a is normalised such that the total probability sums to 1. Whenever a radiation packet undergoes an electron scatter, the new direction is chosen to be isotropic. However, when the photon is a line photon, the new direction is chosen according to a line trapping model, which samples a probability distribution according to the Sobolev escape probability in different directions.

3.3 Macro-atoms

The macro-atom scheme was created by Leon Lucy and is outlined in his 2002/03 papers. It was implemented in PYTHON by Stuart Sim, initially for the study of recombination lines in YSOs (SDL05).

Lucy (2002, 2003, hereafter L02, L03) has shown that it is possible to calculate the emissivity of a gas in statistical equilibrium without approximation for problems with large departures from LTE. His ‘macro-atom’ scheme allows for all possible transition paths from a given level, dispensing with the two-level approximation, and provides a full non-LTE solution for the level populations based on Monte Carlo estimators. The macro-atom technique has already been used to model Wolf-Rayet star winds (Sim 2004), AGN disc winds (Sim et al. 2008; Tatum et al. 2012), supernovae (Kromer & Sim 2009; Kerzendorf & Sim 2014) and YSOs (SDL05). A full description of the approach can be found in L02 and L03.

Understanding macro-atoms requires something of a philosophical shift. Normally MCRT is described in the most intuitive way- that is, we imagine real photons striking atoms and either scattering or imparting energy to a bound electron. With Lucy’s scheme we instead reimagine the MC quanta as packets of quantised energy flow, so that the scheme becomes a purely *statistical* one. The amount of time a given energy quantum spends in a specific atomic level or thermal pool is then somewhat analogous to the absolute energy contained therein.

Following L02, let us consider an atomic species interacting with a radiation field. If the quantity ϵ_j represents the ionization plus excitation energy of a level j then the rates at which the level absorbs and emits radiant energy are given by

$$\dot{A}_j^R = R_{\ell' j} \epsilon_{j \ell'} \quad \text{and} \quad \dot{E}_j^R = R_{j \ell'} \epsilon_{j \ell'} , \quad (3.45)$$

where $\epsilon_{j\ell'} = \epsilon_j - \epsilon_{\ell'}$. Here, I have adopted Lucy's convention, in which the subscript ℓ' denotes a summation over all lower states ($\ell < j$), and u' a summation over all upper states ($u > j$). Similarly, the rates corresponding to *kinetic* (collisional) energy transport can then be written as

$$\dot{A}_j^C = C_{\ell'j}\epsilon_{j\ell'} \quad \text{and} \quad \dot{E}_j^C = C_{j\ell'}\epsilon_{j\ell'} , \quad (3.46)$$

Let us define \mathcal{R} as a total rate, such that $\mathcal{R}_{\ell'j} = R_{\ell'j} + C_{\ell'j}$. If we now impose statistical equilibrium

$$(\mathcal{R}_{\ell'j} - \mathcal{R}_{j\ell'}) + (\mathcal{R}_{u'j} - \mathcal{R}_{ju'}) = 0 , \quad (3.47)$$

we obtain

$$\begin{aligned} & \dot{E}_j^R + \dot{E}_j^C + \mathcal{R}_{ju'}\epsilon_j + \mathcal{R}_{j\ell'}\epsilon_{\ell'} \\ &= \dot{A}_j^R + \dot{A}_j^C + \mathcal{R}_{u'j}\epsilon_j + \mathcal{R}_{\ell'j}\epsilon_{\ell'} . \end{aligned} \quad (3.48)$$

This equation is the starting point for the macro-atom scheme. It shows that, when assuming radiative equilibrium, the energy flows through a system depend only on the transition probabilities and atomic physics associated with the levels the energy flow interacts with. By quantising this energy flow into radiant (r -) and kinetic (k -) packets, we can simulate the energy transport through a plasma discretised into volume elements (“macro-atoms”), whose associated transition probabilities govern the interaction of radiant and kinetic energy with the ionization and excitation energy associated with the ions of the plasma.

Although equation 3.48 assumes strict radiative equilibrium, it is trivial to adjust it to include non-radiative source and sink terms. For example, in an expanding parcel of plasma, adiabatic cooling may be included with a simple modification to the RHS of equation 3.48.

3.3.1 Transition Probabilities

Having interpreted equation 3.48 in a *stochastic* way, we can now construct our Monte Carlo scheme, following L02. A macro-atom in state j always has a finite probability of

'deactivating' radiatively or collisionally:

$$p_j^R = \dot{E}_j^R / D_j \quad \text{and} \quad p_j^C = \dot{E}_j^C / D_j, \quad (3.49)$$

where I have defined

$$D_j = \dot{E}_j^R + \dot{E}_j^C + \mathcal{R}_{ju'}\epsilon_j + \mathcal{R}_{j\ell'}\epsilon_{\ell'} = (\mathcal{R}_{j\ell'} + \mathcal{R}_{ju'})\epsilon_j. \quad (3.50)$$

The corresponding jumping probabilities, which describe the probability that the macro-atom transitions to a different state while remaining active, are given by

$$p_{ju} = \mathcal{R}_{ju}\epsilon_j / D_j \quad \text{and} \quad p_{jl} = \mathcal{R}_{jl}\epsilon_l / D_j. \quad (3.51)$$

Note that the jumping probability is always proportional to the energy of the lower level, whereas the emission probability is proportional to the energy *difference* between the levels, as $\dot{E}_j^R = R_{j\ell'}(\epsilon_j - \epsilon_{\ell'})$. We can also trivially show that the probabilities are correctly normalised, as

$$\begin{aligned} p_j^R + p_j^C + p_{jl} + p_{ju} &= (1/D_j)(\mathcal{R}_{ju}\epsilon_j + \mathcal{R}_{j\ell'}\epsilon_{\ell'} + \dot{E}_j^R + \dot{E}_j^C) \\ &= 1. \end{aligned} \quad (3.52)$$

With these transition probabilities identified, a Monte Carlo calculation can proceed by formulating the normal statistical equilibrium rate equations that will depend on the ambient conditions of the plasma. The effect of these ambient conditions is expressed through the use of Monte Carlo estimators.

3.3.2 Rate equations

The macroscopic transition probabilities above depend on the traditional rate equations formulated according to statistical equilibrium. In the framework of the Sobolev escape probability formalism (see section 3.1.4), the bound-bound excitation rate, \mathcal{R}_{ju} , in an ion is given by

$$\mathcal{R}_{ju} = B_{ju}n_j J_{\text{est}} \left(1 - \frac{n_j g_u}{n_u g_j} \right) + q_{ju}n_j n_e, \quad (3.53)$$

where u is now a specific upper level, and q_{ju} is the collisional rate coefficient (see section 3.3.2.1). The $(1 - n_j g_u / n_u g_j)$ term is the correction for stimulated emission from

equation 3.20, and requires that there are no population inversions (see section 3.3.7). The quantity J_{est} is the Monte Carlo estimator for the mean intensity impinging on the Sobolev region, weighted by an angle-dependent escape probability, given by (Sim 2004)

$$J_{\text{est}} = \frac{c}{4\pi\nu_{uj}V} \sum_i^{\text{photons}} w_i \frac{1 - e^{-\tau_{s,i}}}{\tau_{s,i}} \frac{1}{(dv/ds)_i}. \quad (3.54)$$

Here w_i is the photon weight (in luminosity units), ν_{uj} is the line frequency, dv/ds is the velocity gradient and τ_s is the Sobolev optical depth. The sum is over all photons that come into resonance with the line, and thus represents an integral over solid angle. This is essentially the MC estimator form of $\beta_{uj}\bar{J}_{uj}$, and reduces to the estimator in equation 20 of L02 in the limit of homologous flow or symmetric escape probabilities. The corresponding de-excitation rate is then

$$\mathcal{R}_{uj} = \beta_{ju}A_{uj}n_u + B_{uj}n_uJ_{\text{est}} + q_{uj}n_u n_e. \quad (3.55)$$

The photoionization and collisional ionization rates between a lower level, l , and the continuum level κ (or, in the case of ions with more than one bound electron, the ground state of the upper ion), κ , are

$$\mathcal{R}_{j\kappa} = \gamma_{j\kappa}n_j - \alpha_{\kappa j}^{st}n_\kappa n_e + q_{j\kappa}n_j n_e. \quad (3.56)$$

Here, $q_{j\kappa}$ is the collisional ionization rate coefficient, $\gamma_{j\kappa}$ is the photoionization rate from $j \rightarrow \kappa$, and $\alpha_{\kappa j}^{st}$ is the stimulated recombination coefficient. This is included as a negative photoionization term rather than a positive recombination term as in L03, which requires that there are no population inversions (see section 3.3.7). The corresponding recombination rate is given by

$$\mathcal{R}_{\kappa j} = \alpha_{\kappa j}n_\kappa n_e + q_{\kappa j}n_\kappa n_e, \quad (3.57)$$

where $\alpha_{\kappa l}$ is the radiative recombination coefficient to level l , and is given by

$$\alpha_{\kappa j} = 4\pi \left(\frac{n_j}{n_e n_\kappa} \right)_{T_e}^* \int_{\nu_0}^{\infty} \frac{\sigma_{j\kappa}(\nu)}{h\nu} \frac{2h\nu^3}{c^2} \exp\left(\frac{-h\nu}{kT_e}\right) d\nu. \quad (3.58)$$

This treatment means that radiative and collisional rates to and from all levels can be considered when calculating the ionization state, level populations and transition probabilities, although ionization directly to excited levels of the upper ion is neglected.

3.3.2.1 Collision Strengths

The bound-bound collisional de-excitation rate coefficient, q_{uj} , is calculated from the van Regemorter (1962) approximation, given by

$$q_{uj} = \bar{g} f_{ju} \frac{8.629 \times 10^{-6}}{g_u T_e^{1/2}} \frac{8\pi}{\sqrt{3}} \frac{g_j}{g_u} \frac{\nu_{\text{Ryd}}}{\nu_{uj}} \quad (3.59)$$

where λ_{uj} is the wavelength of the transition, ν_{Ryd} is the frequency at 13.6 eV and \bar{g} is an effective gaunt factor of order unity. The inverse rate is calculated by considering detailed balance, such that

$$q_{ju} = q_{uj} \frac{g_u}{g_j} \exp\left(\frac{-h\nu_{uj}}{kT_e}\right). \quad (3.60)$$

Using equation 3.59 means that collisions between radiatively forbidden transitions are not taken into account when one splits levels into l - and s -subshells, as well as principal quantum number, n (as done with He I; for the CV models in chapter 4). Although this approximation is, in general, a poor one, the effect is second order in the physical regime where recombination lines are formed in the models presented here (see section 4.3.6).

The bound-free collision strengths are calculated using equation 5.79 of Mihalas (1978). The collisional ionization rate coefficient is

$$q_{j\kappa} = 1.55 \times 10^{-13} n_e \bar{g}_i \sigma_{j\kappa}(\nu_{kj}) \frac{h\nu_{kj}}{kT_e^{3/2}} \exp\left(\frac{-h\nu_{kj}}{kT_e}\right), \quad (3.61)$$

where $\sigma_{j\kappa}(\nu_{kj})$ is the photoionization cross-section at the threshold energy. The effective gaunt factor for ion i , \bar{g}_i , is approximately equal to 0.1, 0.2, 0.3 for $Z = 1, 2$ and > 2 , respectively, where Z is the atomic number. Note that the use of this estimator implies a ν^{-3} shape to the photoionization cross-section, which is only strictly true for hydrogenic ions. The collisional (three-body) recombination rate is found using the Saha equation and given by

$$q_{kj} = q_{j\kappa} \left(\frac{n_j}{n_e n_\kappa} \right)_{T_e}^*. \quad (3.62)$$

For numerical reasons, the above two expressions are combined in PYTHON where possible, in order to avoid multiplying two exponentials.

3.3.3 Macro-atom estimators

In order to solve the above rate equations and compute the transition probabilities, it is necessary to construct estimators for the various properties of the radiation field that appear in the macro-atom rate equations. This is done by converting integrals over the radiation field into summations over r -packets passing through a cell. This represents the stochastic nature of a MC simulation and is by no means unique to the macro-atom formalism. The first step is to apply the energy-density argument of Lucy (1999a), which gives, for a time-independent code

$$J_\nu \, d\nu = \frac{1}{4\pi} \frac{1}{V} \sum_{d\nu} w_i \Delta s, \quad (3.63)$$

where the summation is over all photons between $(\nu, \nu + d\nu)$. This allows the formulation of estimators in a MC sense, rather than in integral form.

3.3.3.1 Bound-free estimators

The estimator for the photoionization rate is

$$\gamma_{j\kappa} = \frac{1}{V} \sum_i^{\text{photons}} \frac{w_i \sigma_{j\kappa}(\nu)}{h\nu} \Delta s \quad (3.64)$$

and that for the stimulated recombination rate is

$$\alpha_{\kappa j}^{st} = \left(\frac{n_j}{n_e n_\kappa} \right)_{T_e}^* \frac{1}{V} \sum_i^{\text{photons}} \frac{w_i \sigma_{j\kappa}(\nu)}{h\nu} \exp(-h\nu/kT_e) \Delta s, \quad (3.65)$$

where $\sigma_{j\kappa}(\nu)$ is the photoionization cross-section for this transition. We also need to define modified rate coefficients to represent the rates at which bound-free transitions add energy to, and remove energy from, the radiation field. These are required for photoionization, spontaneous recombination and stimulated recombination and are given by

$$\gamma_{j\kappa}^E = \frac{1}{V} \sum_i^{\text{photons}} \frac{w_i \sigma_{j\kappa}}{h\nu_{\kappa j}} \Delta s, \quad (3.66)$$

$$\alpha_{\kappa j}^E = 4\pi \left(\frac{n_j}{n_e n_\kappa} \right)_{T_e}^* \int_{\nu_{\kappa j}}^\infty \frac{\sigma_{j\kappa}(\nu)}{h\nu_{\kappa j}} \frac{2h\nu^3}{c^2} \exp\left(\frac{-h\nu}{kT_e}\right) d\nu, \quad (3.67)$$

$$\alpha_{\kappa j}^{st,E} = \left(\frac{n_j}{n_e n_\kappa} \right)_{T_e}^* \frac{1}{V} \sum_i^{\text{photons}} \frac{w_i \sigma_{j\kappa}(\nu)}{h\nu_{\kappa j}} \exp(-h\nu/kT_e) \Delta s. \quad (3.68)$$

The rate at which recombinations convert thermal *and* ionization energy into radiant energy is then $\alpha^E h\nu_{\kappa j} n_\kappa n_e$, where $h\nu_{\kappa j}$ the energy difference between the continuum state κ and the level j the electron is recombining into. The amount of this energy which is removed from the thermal pool therefore given by the estimator

$$\mathcal{C}_{bf} = \sum_{j\kappa}^{\text{bfjumps}} \left[(\alpha_{\kappa j}^E + \alpha_{\kappa j}^{st,E} - \alpha_{\kappa j} - \alpha_{\kappa j}^{st}) n_\kappa + q_{j\kappa} n_j \right] n_e h\nu_{\kappa j} V, \quad (3.69)$$

where the sum is over all the macro-atom bound-free transitions ($j \rightarrow \kappa$) in the simulation, set by the number of photoionization cross-sections. For bound-free heating, a similar expression can be derived. The rate at which a level j absorbs energy by bound-free transitions is given by $\gamma_{j\kappa}^E h\nu_{\kappa j} n_\kappa n_e$, of which $\gamma_{j\kappa} h\nu_{\kappa j} n_l$ goes into ionization energy, leaving

$$\mathcal{H}_{bf} = \sum_{j\kappa}^{\text{bfjumps}} \left[(\gamma_{j\kappa}^E - \gamma_{j\kappa}) n_j + n_\kappa n_e^2 q_{\kappa j} \right] h\nu_{\kappa j} V \quad (3.70)$$

as the rate at which radiant energy heats the plasma via bound-free transitions.

3.3.3.2 Bound-bound estimators

The heating and cooling rates for macro-atom bound-bound transitions are the rates of collisional excitations and de-excitations - i.e. the rate at which thermal energy is converted into bound-bound excitation energy and vice versa. These heating and cooling rate estimators are:

$$\mathcal{H}_{bb} = \sum_{ju}^{\text{lines}} q_{uj} n_u n_e h\nu_{uj} V, \quad (3.71)$$

$$\mathcal{C}_{bb} = \sum_{ju}^{\text{lines}} q_{ju} n_j n_e h\nu_{uj} V. \quad (3.72)$$

3.3.3.3 Other heating and cooling estimators

Although I have now defined the estimators required to calculate the transition probabilities, level populations, heating rates and cooling rates in macro-atoms, there are still a number of heating and cooling mechanisms that do not involve macro-atoms.

The free-free cooling estimator is calculated from the emission coefficient in equation 3.36,

$$\mathcal{C}_{ff} = V \sum_i^{\text{ions}} \int \frac{j_{ff,i}(\nu)}{4\pi} d\nu, \quad (3.73)$$

where the integral is over all frequencies included in the simulation, and the sum is also over all ions included in the simulation. The corresponding heating rate is then

$$\mathcal{H}_{ff} = \sum_i^{\text{photons}} w_i \kappa_{ff} \Delta s. \quad (3.74)$$

Compton heating and cooling is included in the thermal balance and as ($r \rightarrow k$) and ($k \rightarrow r$) transitions:

$$\mathcal{C}_{\text{comp}} = 16\pi\sigma_T V J \frac{kT_e}{m_e c^2}, \quad (3.75)$$

$$\mathcal{H}_{\text{comp}} = n_e \sum_i^{\text{photons}} \frac{h\nu}{m_e c^2} w_i \kappa_C \Delta s, \quad (3.76)$$

where the estimator for the frequency-integrated mean intensity is

$$J = \frac{1}{4\pi V} \sum_i^{\text{photons}} w_i \Delta s. \quad (3.77)$$

Induced Compton heating is then given by (Ferland et al. 2013)

$$\mathcal{H}_{\text{ind comp}} = n_e \sum_i^{\text{photons}} \frac{J_\nu c^2}{h\nu^3} \frac{h\nu}{m_e c^2} w_i \kappa_C \Delta s, \quad (3.78)$$

where $J_\nu c^2/h\nu^3$ represents the photon occupation number, and J_ν is either calculated from the spectral model described in section 3.4.2.1 or from a dilute blackbody. The adiabatic cooling rate is derived by considering the PdV work done by the flow and is given by

$$\mathcal{C}_a = kT_e V (\nabla \cdot v) \left(n_e + \sum_{i=1}^{\text{ions}} N_i \right), \quad (3.79)$$

where $\nabla \cdot v$ is the divergence of the velocity field at the centre of the cell. The sum is over all ions included in the simulation.

3.3.4 k -packets

k -packets represent quantised kinetic or thermal energy, and any interaction chain involving a k -packet thus represents interaction with the thermal pool of ions and electrons. k -packets can be produced either directly via a continuum heating process ($r \rightarrow k$), or by the collisional de-activation of a macro-atom ($r \rightarrow \dots \rightarrow A^* \rightarrow k$) in accordance with equation 3.49.

Once they are produced, k -packets never move, as they represent the quantised thermal energy flow in a finite volume element. Hence, when they are produced, their destruction path is decided according to the different cooling mechanisms in the plasma. A k -packet then has a probability of being destroyed by process i that is given by

$$p_{i,\text{destruct}} = \mathcal{C}_i / (\mathcal{C}_{bf} + \mathcal{C}_{ff} + \mathcal{C}_{bb} + \mathcal{C}_{\text{comp}} + \mathcal{C}_a). \quad (3.80)$$

Note that only adiabatic cooling leads to an actual destruction of the energy packet, as a departure from radiative equilibrium. All other processes will lead to the creation of an active macro-atom or an r -packet.

3.3.5 Putting it All Together

I have now defined all quantities needed to write down the transition probabilities in a macro-atom simulation. Fig. 3.4 shows the decision tree traversed by an energy packet in the simulation, showing the complicated set of interactions it can undergo each time it scatters.

3.3.6 Ionization Fractions and Level Populations

In section 3.1.2 I described how it is possible to calculate the ionization and excitation of a plasma under LTE or dilute approximations. Macro-atoms are not approximated – their level and ion populations are calculated by solving the rate equations formulated in section 3.3.2. This is done via matrix inversion. For an element with n ions and

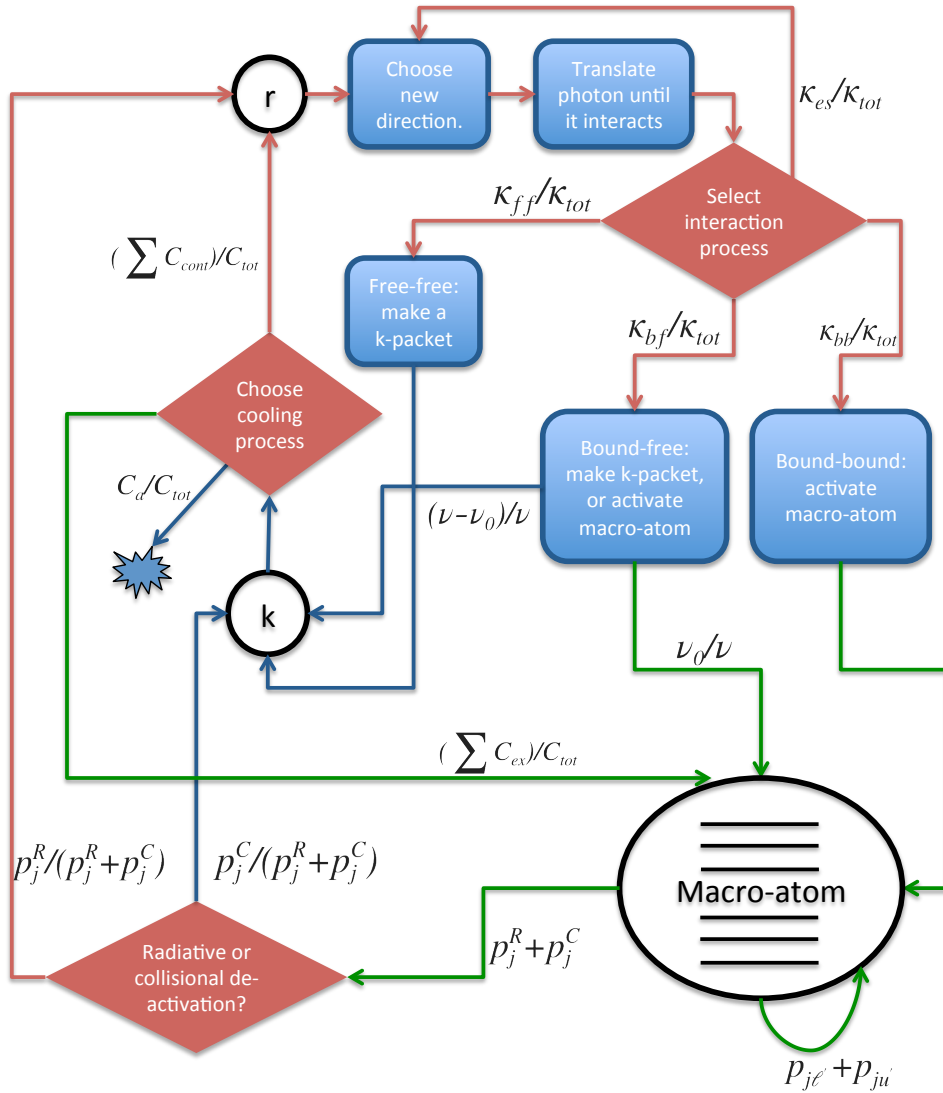


FIGURE 3.4: The decision tree traversed by an energy packet in macro-atom mode, depicting the interaction between radiation (r -packets), the thermal pool (k -packets), and ionization and ionization/excitation energy (macro-atoms). The probabilities at each decision point are marked, and are defined in the text. The red, blue and green coloured arrows represent radiant, kinetic and ionization/excitation energy respectively. The symbols are defined in the text, except C_{cont} and C_{ex} which refer to cooling contributions to radiative and excitation energy respectively.

m_i levels in each ion, we construct a square matrix with dimensions $m = \sum_i^n m_i$. This element then has a total number density of $N_{elem} = \sum_i^n N_i$. In order to turn the system of rate equations for this element into matrix form, we populate the j th diagonal of the matrix with the negative of the rate out of level j , $-(\mathcal{R}_{j\ell'} + \mathcal{R}_{ju'})$, and populate the off-diagonals (j, k) with the positive rate \mathcal{R}_{jk} . These are then multiplied by a vector containing the fractional level populations and must equal a vector of zeros, due to statistical equilibrium. Our matrix equation is then

$$\begin{bmatrix} -\mathcal{R}_{1u'} & \mathcal{R}_{21} & \mathcal{R}_{31} & \dots & \mathcal{R}_{m1} \\ \mathcal{R}_{12} & -(\mathcal{R}_{2\ell'} + \mathcal{R}_{2u'}) & \mathcal{R}_{32} & \dots & \mathcal{R}_{m2} \\ \mathcal{R}_{13} & \mathcal{R}_{23} & -(\mathcal{R}_{3\ell'} + \mathcal{R}_{3u'}) & \dots & \mathcal{R}_{m3} \\ \vdots & \vdots & \vdots & \ddots & \vdots \\ \mathcal{R}_{1m} & \mathcal{R}_{2m} & \mathcal{R}_{3m} & \dots & -\mathcal{R}_{m\ell'} \end{bmatrix} \begin{bmatrix} n_1/N_{elem} \\ n_2/N_{elem} \\ n_3/N_{elem} \\ \vdots \\ n_m/N_{elem} \end{bmatrix} = \begin{bmatrix} 0 \\ 0 \\ 0 \\ \vdots \\ 0 \end{bmatrix}. \quad (3.81)$$

This problem is not yet soluble, as a valid solution is that all levels could simply have occupation numbers of 0. In order to close the problem, we must impose the boundary condition that the sum of the fractional populations is 1, i.e.

$$\sum_i \frac{N_i}{N_{elem}} = 1. \quad (3.82)$$

In matrix form, this is equivalent to replacing the entire first row of the rate matrix with 1, and the first entry of the RHS vector with a 1, so that we have

$$\begin{bmatrix} 1 & 1 & 1 & \dots & 1 \\ \mathcal{R}_{12} & -(\mathcal{R}_{2\ell'} + \mathcal{R}_{2u'}) & \mathcal{R}_{32} & \dots & \mathcal{R}_{m2} \\ \mathcal{R}_{13} & \mathcal{R}_{23} & -(\mathcal{R}_{3\ell'} + \mathcal{R}_{3u'}) & \dots & \mathcal{R}_{m3} \\ \vdots & \vdots & \vdots & \ddots & \vdots \\ \mathcal{R}_{1m} & \mathcal{R}_{2m} & \mathcal{R}_{3m} & \dots & -\mathcal{R}_{m\ell'} \end{bmatrix} \begin{bmatrix} n_1/N_{elem} \\ n_2/N_{elem} \\ n_3/N_{elem} \\ \vdots \\ n_m/N_{elem} \end{bmatrix} = \begin{bmatrix} 1 \\ 0 \\ 0 \\ \vdots \\ 0 \end{bmatrix}. \quad (3.83)$$

This matrix equation can now be solved. The actual matrix manipulation in the code is handled by the GNU scientific libraries (GSL; [Gough 2009](#)) implementation of LU decomposition ([Turing 1948](#)). This is a fast and reliable way of inverting large matrices that includes error handling and enables checking of, for example, singular rate matrices.

3.3.7 Numerical Issues and Population Inversions

An inherent problem in MC simulations is noise, particularly when the MC estimators involved rely on specific frequencies of photons in order to be incremented. One of the side effects of this is that population inversions can occur. A population inversion is present when

$$n_u > n_l \frac{g_u}{g_l}. \quad (3.84)$$

This can cause problems, for example, with the inclusion of stimulated recombination rates as negative photoionization terms. Inspection of equations 3.53 and 3.56 reveals that a negative excitation rate would be obtained in this situation.

In order to prevent this problem, the level populations are ‘cleaned’ after each matrix calculation, as suggested by L03. This is done by cycling through the levels after the calculation has been carried out and checking if condition 3.84 is ever satisfied. If it is, then the upper population is simply set to a value just below this limit. This is only necessary when there is a permitted dipole transition between the two levels being compared.

In addition to the population inversion problem, it is also possible to produce singular rate matrixes when photon statistics are poor, particularly in heavily absorbed portions of the wind. In order to deal with this issue, I have written a routine in PYTHON that checks if the rate matrix is singular and if any anomalous (negative or non-finite) populations exist in the solution found. If either of these conditions are met, the calculation is redone using dilute estimators. This procedure is also carried out for the simple-atom ionization calculation when the rate matrix approach is in use (see section 3.4.2.1).

3.4 A hybrid line transfer scheme: including simple-atoms

I have now described in detail how the macro-atom approach is implemented in PYTHON. A pure macro-atom approach can be easily used for some situations – for example, in the YSO application described by SDL05, which uses a H-only model. However, in accretion disc winds, the densities can be very high, and higher Z elements must be included. Including all these elements as macro-atoms is not currently computationally feasible in PYTHON for anything but the simplest models. I will thus now describe a

'hybrid scheme', which treats H and He with the macro-atom approach, but models all other atoms as 'simple-atoms'.

3.4.1 Line Transfer

Simple-atoms still interact with r - and k -packets, but do not possess internal transition probabilities. As a result, they are analogous to the two-level atom treatment, as any excitation is immediately followed by a deactivation into an r - or k -packet. The choice of radiative or kinetic deactivation is made according to the relative rates in the two-level atom formalism. For a bound-bound transition $u \rightarrow j$, these two probabilities are then

$$p_{uj}^{S,R} = \frac{A_{uj}\beta_{uj}}{A_{uj}\beta_{uj} + C_{uj} \exp(-h\nu_{uj}/kT_e)} = 1 - q \quad (3.85)$$

and

$$p_{uj}^{S,C} = \frac{C_{uj} \exp(-h\nu_{uj}/kT_e)}{A_{uj}\beta_{uj} + C_{uj} \exp(-h\nu_{uj}/kT_e)} = q. \quad (3.86)$$

For a bound-free transition, the code assumes radiative recombination, and thus any bound-free simple-atom activation is immediately followed by the creation of an r -packet. This approximates the bound-free continuum, even when compared to other two-level atom radiative transfer schemes. This is discussed further and tested in section 3.8.3.

This hybrid approach preserves the fast treatment of, for example, UV resonance lines, while accurately modelling the recombination cascades that populate the levels responsible for, e.g., H and He line emission. As a result of this hybrid scheme, a separate set of estimators must be recorded for simple-atoms, and the ionization and excitation of these elements is calculated with a different, approximate approach. In order to include simple-atoms, we must add in a few extra pathways to Fig. 3.4, so that energy packets can also activate simple-atoms, through either bound-free or bound-bound processes. The relative probabilities of these channels are set in proportion with the simple-atom opacities.

3.4.2 Heating and Cooling Estimators

The bound-bound heating rate is computed during the photon propagation and is a sum over photons which come into resonance with each line, given by

$$\mathcal{H}_{bb}^S = \sum_i^{\text{photons}} \sum_{ju}^{\text{lines}} (1-q)(1-e^{-\tau_{S,ju}})w_i. \quad (3.87)$$

Similarly, the bound-bound cooling rate is given by

$$\mathcal{C}_{bb}^S = \sum_{ju}^{\text{lines}} q \left(n_j \frac{g_u}{g_j} - n_u \right) q_{uj} n_e \frac{(1-e^{-h\nu_{ju}/kT_e})}{(e^{h\nu_{ju}/kT_e} - 1)} h\nu_{ju}. \quad (3.88)$$

These estimators are fundamentally different quantities from the corresponding macro-atom estimators and are not used to calculate k-packet probabilities. Instead, they represent the amount of energy transferred to and from the plasma by the radiation field, whereas in the macro-atom case they represent the rate of collisional excitations and de-excitations. The bound-free heating rate is given by

$$\mathcal{H}_{bf}^S = \sum_i^{\text{photons}} \sum_{j\kappa}^{\text{bfjumps}} w_i e^{-\tau} \frac{\nu - \nu_{j\kappa}}{\nu} \quad (3.89)$$

where ν is the frequency of the photon in question, and $\nu_{j\kappa}$ is the ionization threshold. The bound-free cooling rate is then

$$\mathcal{C}_{bf}^S = \sum_{j\kappa}^{\text{bfjumps}} \int_{\nu_{j\kappa}}^{\infty} h\nu \left(\frac{2\pi m_e k T_e}{h^2} \right)^{-3/2} \frac{2h\nu^3}{c^2} \frac{g_j}{g_\kappa g_e} T_e^{-3/2} \sigma_{j\kappa}(\nu) \exp(-h(\nu - \nu_{j\kappa})/kT_e). \quad (3.90)$$

3.4.2.1 Radiation Field Estimators, Ionization and Excitation

For simple-atoms we do not record radiation field estimators for discrete transitions, as we do for macro-atoms. Instead, we record estimators to give us a model of the radiation field. The estimators needed depend on the ionization mode employed. The radiation temperature, T_R , is estimated by first recording the mean frequency, $\bar{\nu}$, of the photons passing through a cell

$$\bar{\nu} = \frac{\sum_{\text{photons}} w_i \nu_i \Delta s}{\sum_{\text{photons}} w_i \Delta s}. \quad (3.91)$$

This is then used to estimate a radiation temperature by considering the value expected from a blackbody (Mazzali & Lucy 1993):

$$T_r = \frac{h\bar{\nu}}{3.832 k} \quad (3.92)$$

The dilution factor can be calculated by comparing the estimator for the mean intensity (equation 3.77) to the Stefan-Boltzmann law:

$$W = \frac{\pi J}{\sigma T_r^4}. \quad (3.93)$$

This set of estimators is sufficient to describe the radiation field if the dilute approximation is adopted (section 3.1.2.1).

H13 improved on the dilute blackbody approximation by modelling the SED in the cell using a series of band-limited radiation field estimators. In this scheme, a series of bands is defined in which to record these estimators. These bands are different to those discussed in section 3.2.2, as those instead govern photon generation. In H13, the band-limited estimators were used to construct a correction factor that could be used in a modified Saha equation (similar in form to equation 3.13). However, the code has now been improved further, so that the ion populations are computed by solving the rate equations. Thus we now simply need to calculate photoionization rate estimators for simple ions, which rely on being able to integrate a modelled form of the mean intensity.

The mean intensity is modelled in each band i using either a power law or exponential with respective forms of

$$J_{\nu,i} = K_{PL} \nu^{\alpha_{PL}} \text{ and} \quad (3.94)$$

$$J_{\nu,i} = K_{exp} \exp(-h\nu/kT_{exp}), \quad (3.95)$$

where T_{exp} and α_{PL} are fit parameters, and K_{PL} and K_{exp} are normalisation constants, which are obtained by ensuring that the model reproduces the band limited mean intensity from equation 3.77. An example of a modeled spectrum compared to the recorded MC spectrum from the summed photons is shown in figure 3.5, showing how this scheme faithfully reproduces the SED in situations where there are large departures from a blackbody.

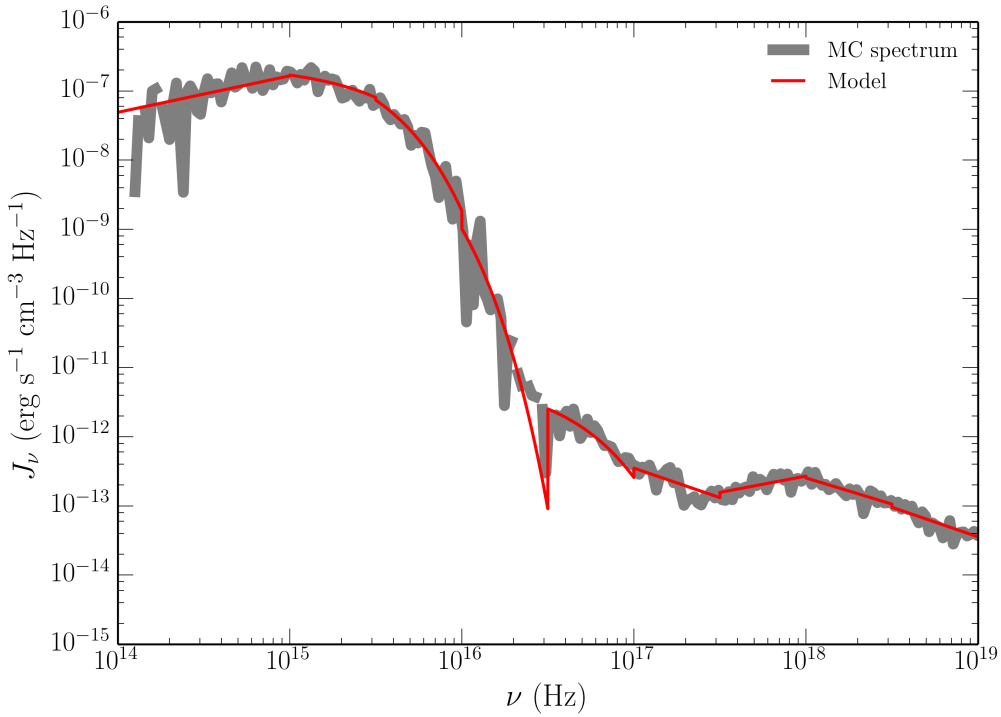


FIGURE 3.5: An example of a modeled spectrum in PYTHON compared to the recorded MC spectrum, from an individual cell in an AGN model.

Once the model for the mean intensity has been calculated, it is possible to formulate a photoionization rate estimator from ion i to $i + 1$ for simple-atoms,

$$\gamma_{i,i+1}^S = \sum_i^{\text{bands}} \int_{\nu_i}^{\nu_{i+1}} \sum_j^{\text{levels}} \frac{J_{\nu,i} \sigma_{jk}(\nu)}{h\nu} d\nu. \quad (3.96)$$

Recombination rate coefficients are then obtained from either tabulated data (see section 3.7) or, failing that, the Milne relation (equation 3.58).

The rate matrix used to calculate the ionization state of simple-atoms can now be populated. An example rate matrix for H and He would be

$$\begin{bmatrix} 1 & 1 & 0 & 0 & 0 \\ \gamma_{H\text{I},H\text{II}}^S & -n_e \alpha_{H\text{II},H\text{I}} & 0 & 0 & 0 \\ 0 & 0 & 1 & 1 & 1 \\ 0 & 0 & \gamma_{He\text{I},He\text{II}}^S & -n_e \alpha_{He\text{II},He\text{I}} - \gamma_{He\text{II},He\text{III}}^S & 0 \\ 0 & 0 & 0 & \gamma_{He\text{II},He\text{III}}^S & -n_e \alpha_{He\text{III},He\text{II}} \end{bmatrix} \begin{bmatrix} N_{H\text{I}} \\ N_{H\text{II}} \\ N_{He\text{I}} \\ N_{He\text{II}} \\ N_{He\text{III}} \end{bmatrix} = \begin{bmatrix} n_H \\ 0 \\ n_{He} \\ 0 \\ 0 \end{bmatrix}. \quad (3.97)$$

Thus the problem is very similar to solving for level populations in macro-atoms, except that it is bounded differently.

The rate matrix method with a banded spectral model for the mean intensity is used in chapter 5 of this thesis, whereas for chapter 4 the dilute approximation is adopted and ion fractions are obtained from a modified Saha equation (equation 3.13). Regardless of the ionization mode used, the relative excitation fractions of simple-atoms within each ionization stage of a given species are estimated via a modified (dilute) Boltzmann equation (equation 3.14). This equation is approximate, and, in general, this approximation is not good. We therefore endeavour to treat any species in which the excitation state of the ions is thought to be important in determining either the ionizing radiation field, or emergent spectrum, as macro-atoms.

3.5 Heating And Cooling Balance

I have already given the estimators used to calculate heating and cooling rates in the plasma. These are not only used in the creation and elimination of k -packets, but also in the heating and cooling balance carried out in PYTHON to achieve a self-consistent temperature structure in the wind.

At the end of each ionization cycle, the code has stored a new set of MC estimators for radiative heating of the plasma. We then assume that each cell is in thermal equilibrium, so that the appropriate electron temperature is simply the value of T_e that is a solution to the equation

$$\mathcal{H}_{\text{tot}} - \mathcal{C}_{\text{tot}}(T_e) = 0, \quad (3.98)$$

where \mathcal{H}_{tot} and \mathcal{C}_{tot} are the total heating and cooling rates in the plasma. A number of checks are in place to ensure numerical stability, namely a maximum temperature and a maximum change in temperature from cycle to cycle. This is especially important in cases where the initial guess at the wind temperature is far from the true value.

3.5.1 Convergence

PYTHON always runs a fixed number of ionization cycles, rather than terminating when a convergence criterion is reached. As a result, it is up to the user to check that the simulation is converged. An individual cell is considered converged when a) the temperature

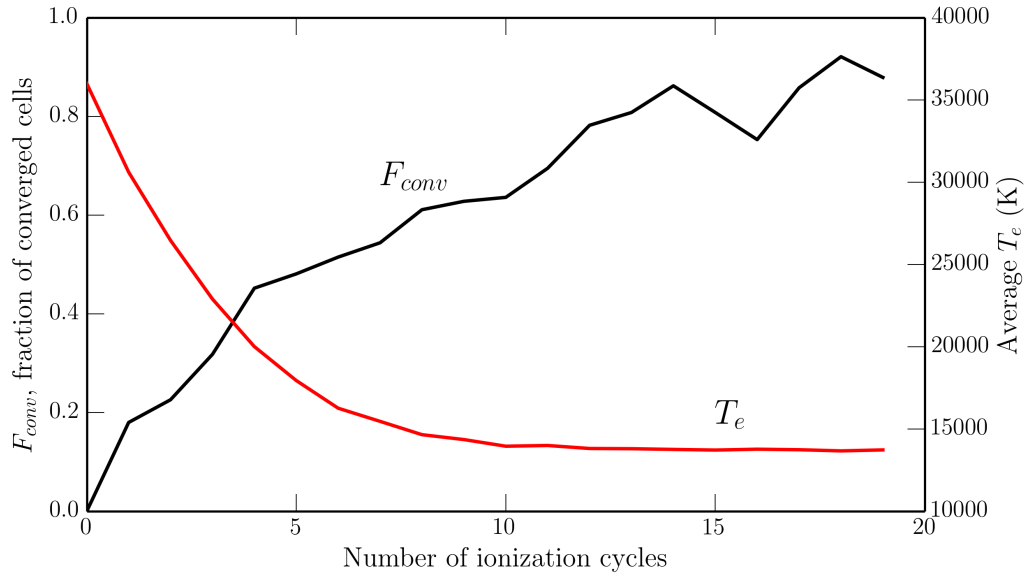


FIGURE 3.6: The average temperature and fraction of converged cells in a typical CV model, shown as a function of the number of ionization cycles completed.

stops changing significantly, i.e. both T_R and T_e satisfy

$$\frac{|T_{\text{new}} - T_{\text{old}}|}{T_{\text{new}} + T_{\text{old}}} < 0.05, \quad (3.99)$$

and b) the heating and cooling rates are well balanced, such that

$$\frac{|\mathcal{H}_{\text{tot}} - \mathcal{C}_{\text{tot}}|}{\mathcal{H}_{\text{tot}} + \mathcal{C}_{\text{tot}}} < 0.05. \quad (3.100)$$

These criteria could doubtless be improved, but they are nonetheless a good way of ensuring that thermal and radiative equilibrium holds in the plasma. An example of how the average temperature and fraction of converged cells changes over the course of the ionization cycles in a typical CV model is shown in Fig. 3.6.

3.6 Spectral Cycles

The primary output from PYTHON is a synthetic spectrum over a specific wavelength range produced at user-specified viewing angles. This spectrum is produced in a separate cycle from the calculation of the ionization state, as we are then concerned with producing detailed, high-resolution spectra in a specific wavelength regime that can then be compared to observations.

The code utilises a variance reduction technique in order to minimise the amount of time spent in this portion of the code. This technique is based on a similar method implemented by Woods (1991) and is known in the code as the ‘extract’ method. This method works by tracking photon packets until they scatter or interact with the plasma, according to the procedure described in section 3.2.3. At the scattering location, the optical depth the photon would experience were it to escape to infinity along each requested viewing angle, $\tau_{\text{extract}}(\theta_i)$, is calculated. The spectrum at each viewing angle θ_i is then incremented by an amount

$$\Delta L = w f(\theta_i) \exp(-\tau_{\text{extract}}(\theta_i)), \quad (3.101)$$

where w is the weight of the photon, and $f(\theta_i)$ is a weighting proportional to the probability that the photon would have scattered in direction θ_i . Once this value has been added to the corresponding wavelength bin, the photon proceeds as normal in its new random direction.

In the alternative ‘live or die’ method this extraction procedure is not carried out, and a user simply has to run a sufficient number of photons to ensure that enough will happen to fall into the finite solid angle bins requested. This is significantly less efficient. A comparison between the two methods is shown in figure 3.7 for a standard CV model, showing that the spectrum produced is identical in shape, but with significantly higher signal-to-noise (for fixed number of cycles) in the ‘extract’ case.

3.6.1 Macro-atom Emissivity Calculation

In order to preserve the philosophy that a detailed spectrum is calculated in a limited wavelength regime, PYTHON carries out a macro-atom emissivity calculation before the spectral cycles. The aim of this step is to calculate the luminosity contributed by macro-atoms – equivalent to the total amount of reprocessed emission – in the wavelength range being considered.

This process can be very computationally intensive, especially if the wavelength regime being simulated has very little emission from bound-free and line processes in the wind, but the overall broad-band emissivity is high. During the ionization cycles, the amount of energy absorbed into k -packets and every macro-atom level is recorded using MC estimators. Once the ionization cycles are finished, and the model has converged, these

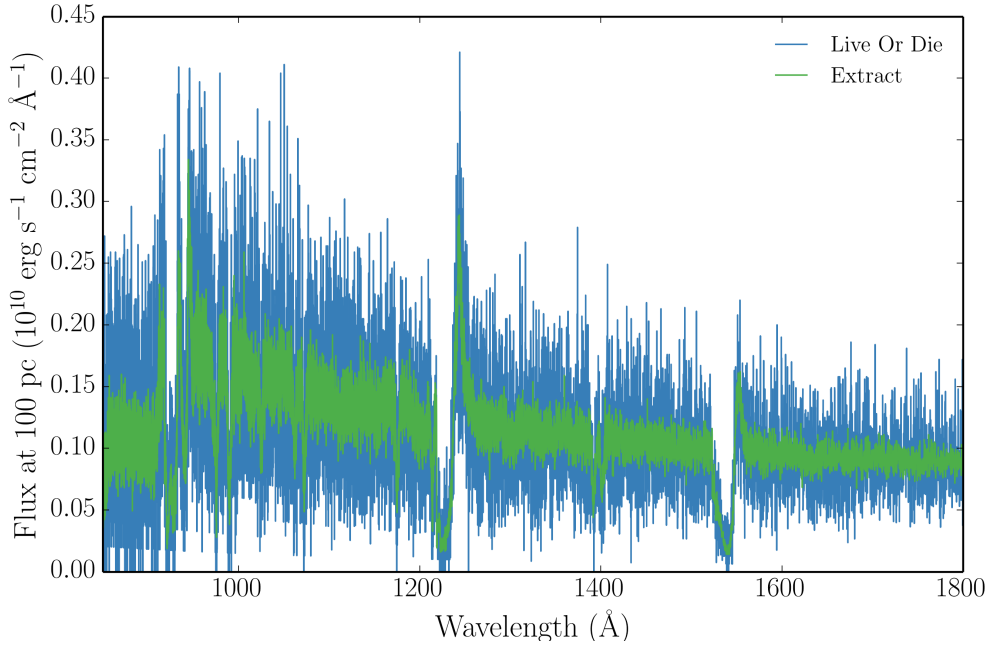


FIGURE 3.7: A synthetic spectrum after 30 spectral cycles with 100,000 photons from simple CV wind model at a 60° viewing angle. Spectra produced with both the extract and live or die modes are shown. The effectiveness of the extract variance reduction technique can be clearly seen, and we can see that the spectral shape is unaltered.

absorption energies are split into a certain number of packets and tracked through the macro-atom machinery until a deactivation occurs. When this happens, the emissivity of the level the macro-atom de-activated from is incremented if the packet lies in the requested wavelength range. If it does not, then the packet is thrown away. It is easy to see how what is essentially a MC rejection method can be an inefficient way of sampling this parameter space. Fortunately, this problem is parallelisable (see section 3.9.1).

Once the emissivities have been calculated, the spectral synthesis can proceed. This is done in a different way to the ionization cycles. Photons are generated from the specified photon sources over the required wavelength range, but are now also generated according to the calculated macro-atom and k -packet emissivities in each cell. These photons are ‘extracted’ according to the procedure outlined above. In order to ensure that radiative equilibrium still holds, any photon that interacts with a macro-atom or k -packet is immediately destroyed. The photons are tracked and extracted as normal until they escape the simulation; resonant scatters are dealt with by a combination of macro-atom photon production and destruction.

3.7 Atomic Data

One of the big challenges in building reliable photoionization and radiative transfer codes lies in the acquisition of accurate and complete atomic datasets. All of the rates described so far contain a term, such as the oscillator strength or dimensionless collision strength, that is dependent purely on the atomic physics associated with the transition. These quantities can be measured in laboratory experiments, or predicted from atomic structure codes that derive the atomic physics from quantum theory.

Throughout this work, I have used very similar atomic data to that described by LK02 and H13. Elements included are H, He, C, N, O, Ne, Na, Mg, Al, Si, S, Ar, Ca and Fe, although this can be easily be adapted. Solar abundances from [Verner et al. \(1994\)](#) are adopted, and ionization potentials and ion multiplicities are from [Verner et al. \(1996b\)](#). Line information for simple-atoms is obtained from [Verner et al. \(1996b, ~ 5,000 lines\)](#) and [Kurucz & Bell \(1995, ~ 55,000 lines\)](#). The level information for simple-atoms is constructed from the line lists using the technique described by [Lucy \(1999b\)](#).

Radiative recombination rate coefficients are taken from the CHIANTI database version 7.0 ([Dere et al. 1997](#); [Landi et al. 2012](#)). Ground state recombination rates from [Badnell \(2006\)](#) are adopted where available, otherwise the code defaults to calculating recombination rates from the Milne relation. Free-free Gaunt factors are from [Sutherland \(1998\)](#).

3.7.1 Macro-atom Level and Line Data

A 20-level model H atom was incorporated into PYTHON by SDL05, and includes line oscillator strengths from [Menzel & Pekeris \(1935\)](#). This model atom is only split according to principle quantum number n , and it is thus assumed that collisions in the plasma will cause the l -subshells to be populated according to statistical weights. This is known as *l-mixing* and is a good approximation for hydrogen in dense astrophysical plasmas due to the near degeneracy of the subshell energy levels.

In order to correctly model He recombination lines in CVs and AGN, such as the prominent He II 1640 Å line, I have expanded the atomic data set, so that PYTHON now contains all the atomic data needed for a He macro-atom. This data was obtained from TOPBASE, except for some inaccurate line wavelengths that were set to the experimental

values from the National Institute of Standards and Technology (NIST²). He I is split into l and s subshells so as to correctly model the singlet and triplet lines observed in many optical spectra. He II is assumed to be l -mixed, as it is hydrogenic.

For CV modelling (chapter 4), I used the full 20-level hydrogen atom, with 53 levels of He I up to principle quantum number 10, and 10 levels of He II. Modelling levels close to the continuum energy can provide a performance hit in macro-atom mode, but is necessary when modelling recombination lines from excited upper levels. In quasar models (chapter 5) this is not as important, and the plasma is generally more ionized. There, a 10-level hydrogen atom was used and He I was treated with only the ground state – this simplification had no effect on the temperature structure of the wind or emergent spectrum.

3.7.2 Photoionization Cross-sections

Photoionization cross-sections are from TOPBASE (Cunto et al. 1993) and from Verner et al. (1996a). Where possible, I use TOPBASE photoionization cross-sections. This is because these cross-sections are partial and represent the cross-section for a photoionization from a given *level*, and so can be used to specify macro-atom bound-free rates to and from all configurations of the lower ion. I neglect photoionizations to excited configurations of the upper ion. For simple-atoms, these cross-sections are included in the ionization calculation, by summing over levels, but are not used for a full level populations solution. The TOPBASE cross-sections have two major drawbacks in that they do not extend to particularly high energies and do not always contain accurate threshold energies.

In order to improve the TOPBASE cross-sections, I extrapolated them to larger energies. This was done by finding the slope, in log-log space, of the cross-section at the maximum energy, and extrapolating to 100 keV. In some cases, the slope near the maximum energy was anomalous due to resonances or similar structure in the cross-section, or possibly simply due to unknown problems in the TOPBASE calculations. These cases were identified by eye and a ν^{-3} extrapolation was then applied instead. The results of this extrapolation on the soft X-rays in an AGN model are shown in figure 3.8. Where previously there was a sharp, unphysical edge due to the lack of high energy

²<http://www.nist.gov/>

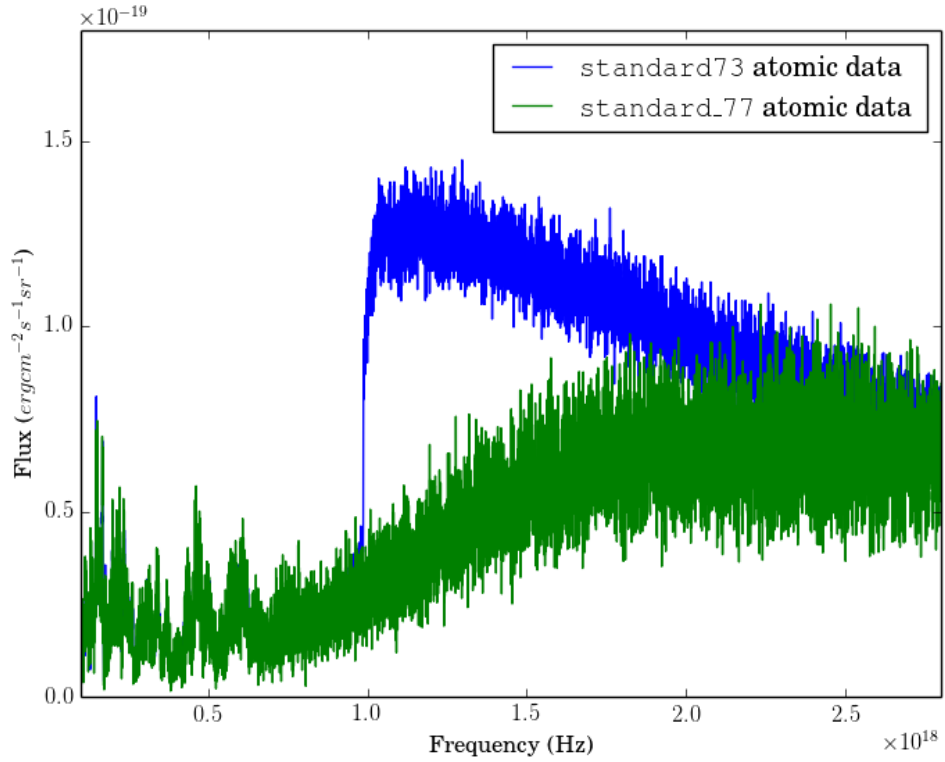


FIGURE 3.8: A comparison of the soft X-ray regime of the H13 model, with two different datasets. standard73 is the dataset with old, unextrapolated cross-sections and standard77 instead includes extrapolated cross-sections as described in the text.

($\nu \gtrsim 10^{18}$ Hz) data, there is now a smooth recovery to an X-ray power law we expect. I also manually adjusted the threshold energies in some cases to match the more accurate values from Verner et al. (1996a).

3.8 Code Validation

The main challenge for high performance scientific computing can be elegantly summarised by the Ferland (2002) epitaph, ‘Reliability in the face of complexity’. I have already delved into some of the complexity in this case, so it is important to establish whether the code is also reliable before I present results.

3.8.1 Testing Against Cloudy

CLOUDY is a spectral synthesis and photoionization code used to simulate the emergent spectrum and ionization conditions in nebulae and other plasma environments. As a

result, it uses many of the same techniques as PYTHON in order to compute ionization states, level populations and heating and cooling rates. It thus represents an excellent benchmarking tool. PYTHON has been tested extensively against CLOUDY in the past; some of these successful tests can be found in H13 and LK02.

Figs. 3.9 to 3.14 show a series of ionization plots with relative ion fractions plotted as a function of ionization parameter, U . The ionization parameter is a useful way to parameterise the ionization state of a plasma, and is given by

$$U = \frac{4\pi}{n_H c} \int_{13.6\text{eV}/h}^{\infty} \frac{J_{\nu} d\nu}{h\nu}. \quad (3.102)$$

Note the difference in form to equation 2.1, as U is proportional to the *number* of ionizing photons rather than the ionizing luminosity. In PYTHON, the ionization parameter in a cell is calculated via a MC estimator, such that

$$U_{\text{PYTHON}} = \frac{1}{c V n_H} \sum_i^{\text{photons}} \frac{w_i \Delta s}{h\nu}. \quad (3.103)$$

This test is designed to check that PYTHON still agrees well with CLOUDY when we turn on the full macro-atom machinery. The calculations are conducted using the same incident SEDs, densities and abundances, and PYTHON is operated in 1D, thin shell mode to simulate an optically thin plasma and facilitate comparison with CLOUDY. I have shown two separate ionization modes from PYTHON: (i) standard mode, in which nothing is treated as a macro-atom, and the spectral model ionization scheme of H13 is used to calculate ion fractions; (ii) hybrid mode, in which H and He are treated as macro-atoms, and their level populations and ion fractions are solved using MC estimators according to the routine described in section 3.3.6. In both cases the simple-atoms have their populations calculated using the H13 scheme.

In general, the calculated fractions are in excellent agreement, with a few exceptions. The first problem is with He at low ionization parameters (see Fig. 3.10), where there is a discrepancy between the macro-atom solution and the standard mode solution (the latter agrees well with CLOUDY). This is due to differences in the calculated recombination rate. In macro-atom mode, this is done using the Milne relation for all the bound-free jumps that have been identified, which currently includes all transitions from the lower ion but ignores transitions to excited states of the upper ion. By contrast, in standard mode, PYTHON uses the recombination rates from Chianti, which represent a weighted

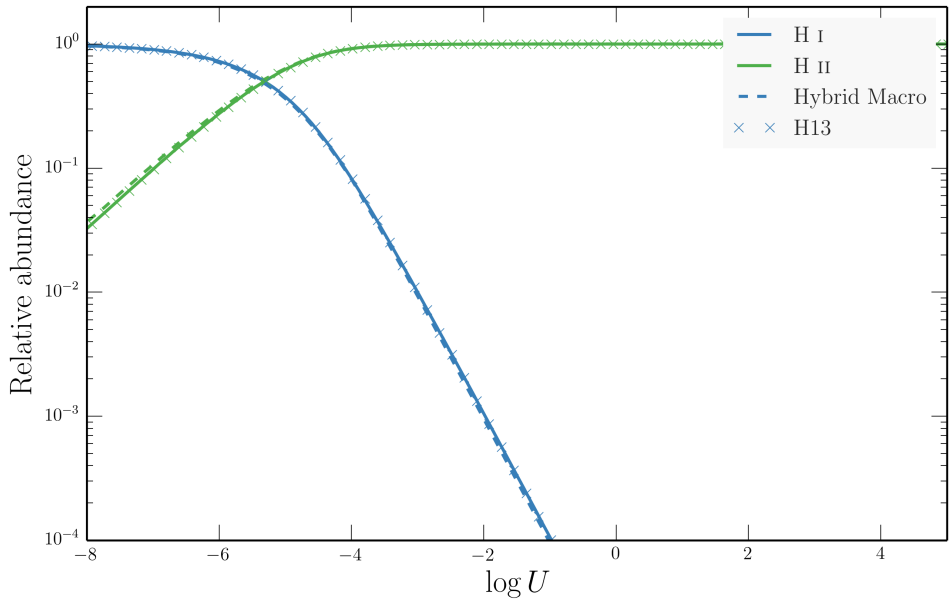


FIGURE 3.9: Relative ion fractions as a function of ionization parameter from the hybrid macro-atom scheme, with Hydrogen and Helium treated as a full macro-atom (dotted lines), compared to both CLOUDY (solid lines) and PYTHON in simple-atom only mode (H13, crosses). The colours correspond to the different ionic stages and are labeled for the CLOUDY case.

sum over all the possible bound-free transitions, and are thus in some ways more complete. Nevertheless, the macro-atom scheme is self-consistent, in that all photoionization pathways have a matching recombination pathway, and the level populations are calculated much more accurately. Furthermore, the models presented later generally have $\log U \gtrsim -2$, where the calculation agrees well with CLOUDY and standard mode. The second problem lies in Fe, where there can be quite large differences between PYTHON and CLOUDY. This is mainly due to Auger ionization and charge exchange and is currently been improved in PYTHON, but is not included here.

3.8.2 Macro-atom Testing Against Tardis and Theory

TARDIS is a 1D photoionization and radiative transfer code designed to model supernovae in a quick and easy python package; it is described in detail by [Kerzendorf & Sim \(2014\)](#). Although TARDIS is simpler in terms of geometry, it has many of the same capabilities of PYTHON and thus makes for an excellent comparison.

Fig. 3.15 shows the results of two code tests. In the top panel, I show a comparison of the Balmer series emissivities as predicted by PYTHON in the l-mixed Case B limit

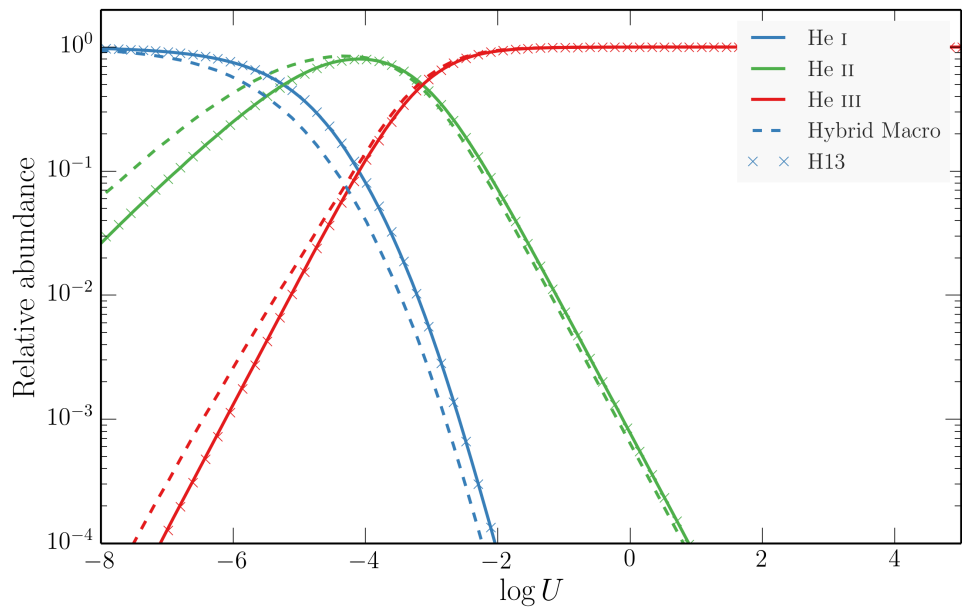


FIGURE 3.10: As figure 3.9, but for Helium.

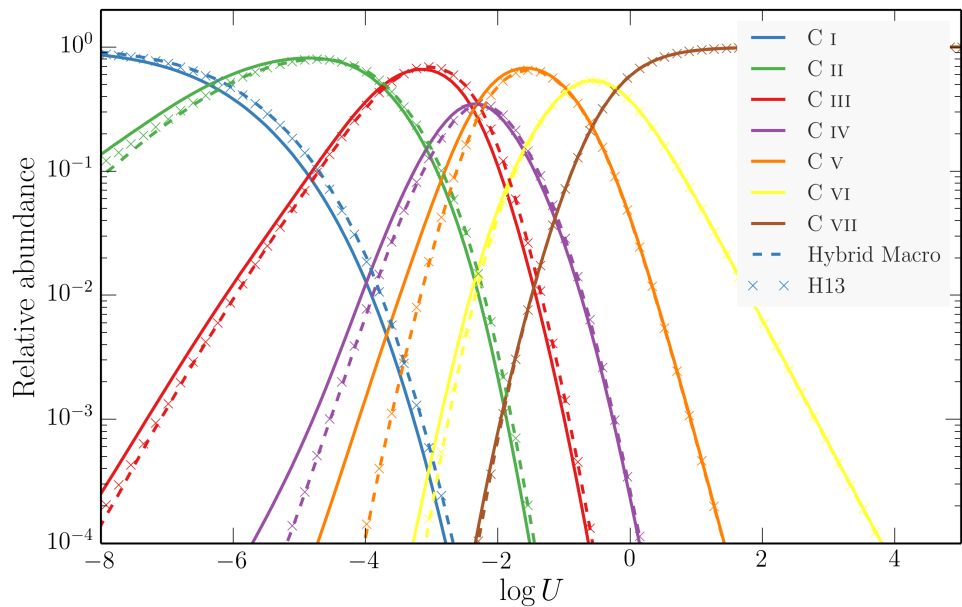


FIGURE 3.11: As figure 3.9, but for Carbon.

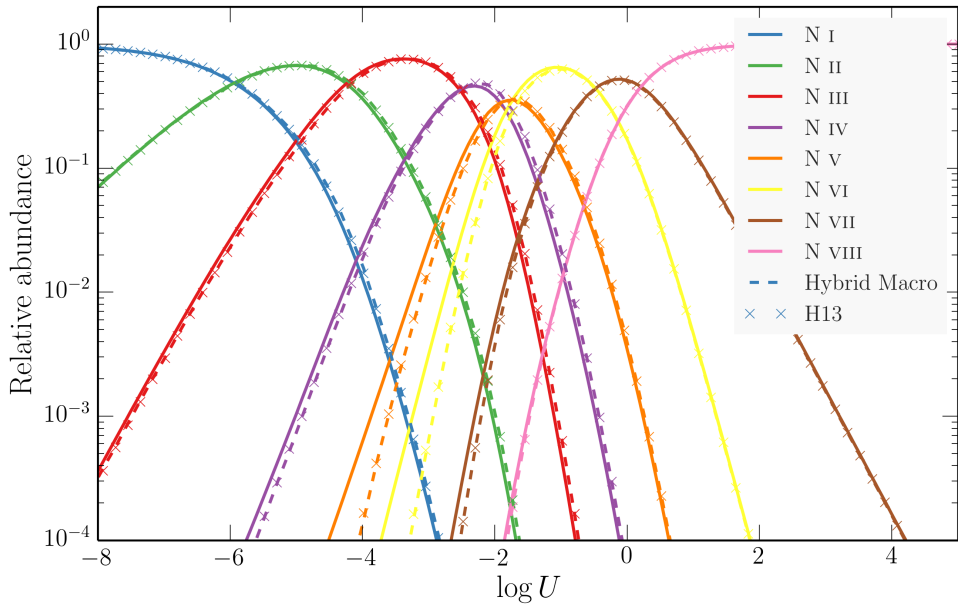


FIGURE 3.12: As figure 3.9, but for Nitrogen.

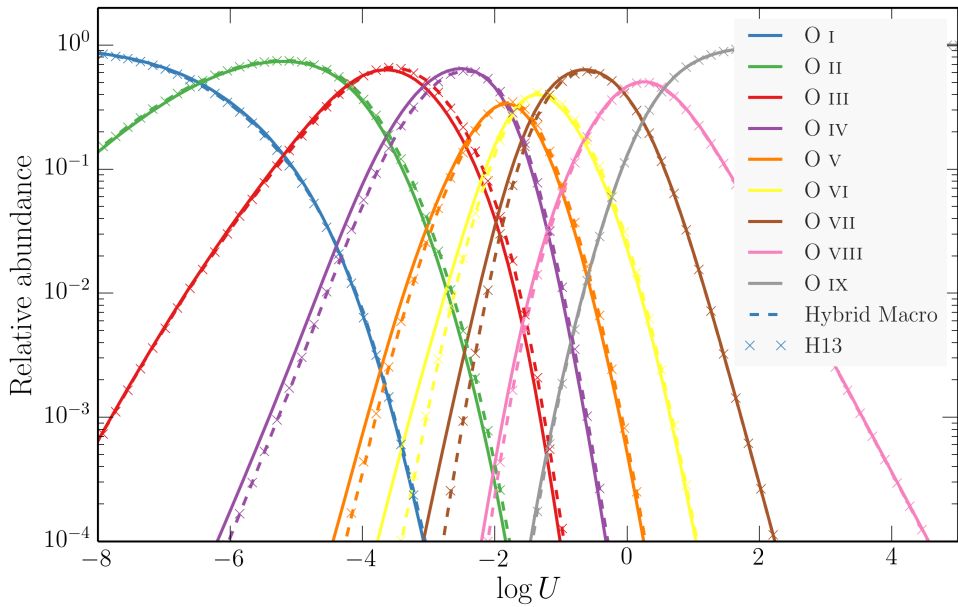


FIGURE 3.13: As figure 3.9, but for Oxygen.

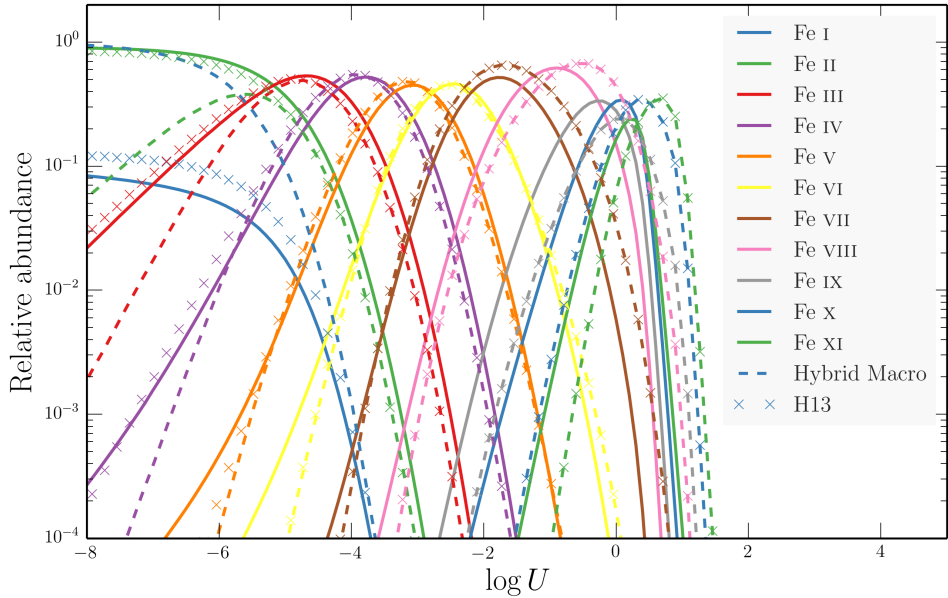


FIGURE 3.14: As figure 3.9, but for the first 11 ionization stages of Iron.

against the analytical calculations by [Seaton \(1959\)](#). Both calculations are calculated at $T_e = 10,000\text{K}$. Case B is an approximation commonly used in nebular astrophysics (see e.g. [Osterbrock 1989](#)) in which one assumes that all line transitions are optically thin, except for the Ly α transition, which is taken as optically thick. Thus, this test comparison is carried out using a thin shell of plasma in which the escape probabilities, β_{uj} are artificially set to 1 in all transitions except Ly α , which has its β_{uj} set to 0.

The bottom panel shows a comparison of He I level populations (the most complex ion currently treated as a macro-atom) between PYTHON and TARDIS models. The calculation is conducted with physical parameters of $n_e = 5.96 \times 10^4 \text{ cm}^{-3}$, $T_e = 30,600\text{K}$, $T_R = 43,482\text{K}$ and $W = 9.65 \times 10^{-5}$. Considering that the two codes use different atomic data, and that TARDIS, unlike PYTHON, includes a complete treatment of collisions between radiatively forbidden transitions, the factor of < 2 agreement is encouraging.

[Fig. 3.16](#) shows a comparison between TARDIS and PYTHON synthetic spectra from a simple 1D supernova model. This comparison was originally presented by [Kerzendorf & Sim \(2014\)](#), but I have since then discovered a bug in the Doppler shifting routine in PYTHON, introduced around PYTHON 76, which was present in this test. Fixing this issue leads to slightly better agreement between the two codes. The model involves a full computation of the ionization state in the dilute blackbody mode, and, although run in 1D, it still tests most of the radiative transfer machinery of the code. The spectra

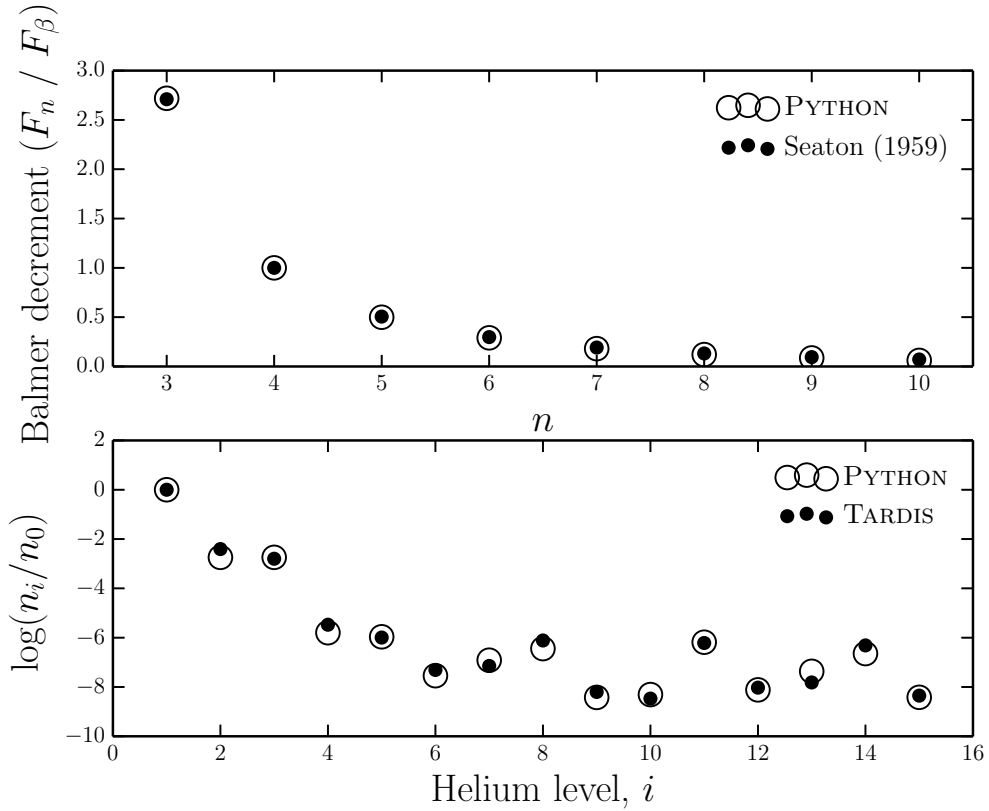


FIGURE 3.15: *Top Panel:* ‘Case B’ Balmer decrements computed with PYTHON compared to analytic calculations by Seaton (1959). Both calculations are calculated at $T_e = 10,000\text{K}$. *Bottom Panel:* a comparison of He I level populations (the most complex ion we currently treat as a macro-atom) between PYTHON and TARDIS models. The calculation is conducted in thin shell mode with physical parameters of $n_e = 5.96 \times 10^4 \text{ cm}^{-3}$, $T_e = 30,600\text{K}$, $T_R = 43,482\text{K}$ and $W = 9.65 \times 10^{-5}$.

are in good agreement, considering there are differences in their treatment of excitation and their atomic data. This comparison is particular encouraging when we consider that Kerzendorf & Sim (2014) also show comparisons with other supernova codes such as ARTIS (Kromer & Sim 2009), with similarly good agreement.

3.8.3 Testing Line Transfer Modes

The simple-atom approach has a few drawbacks. The first is that it cannot deal well with lines in which the lower level is an excited state, such as the Balmer lines. This means that it is important to treat recombination lines using the macro-atom approach. The second is that a bound-free continuum activation, in normal terms a photoionization, is followed by a radiative deactivation with the frequency chosen assuming a hydrogenic cross-section. This does not well represent reality, where recombining electrons tend to do so to a variety of levels, so there is a gradual redshifting of the radiation field.

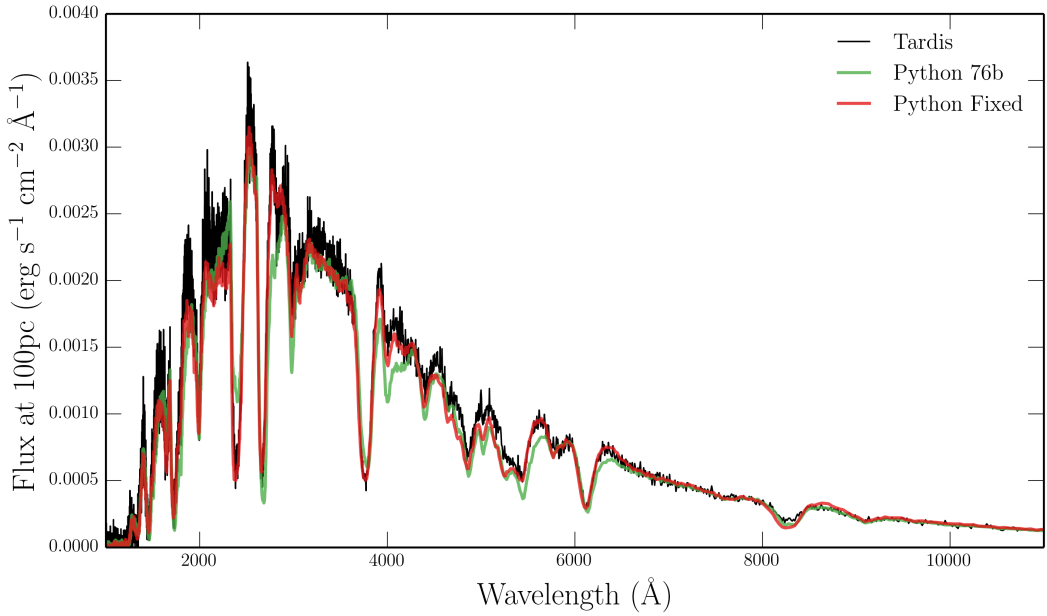


FIGURE 3.16: Comparison between TARDIS and PYTHON synthetic spectra from a simple 1D supernova model. A bug in Doppler shifting of photons was discovered around PYTHON 76, meaning that the code now gives even better agreement than presented in Kerzendorf & Sim 2014.

In addition, most ions are not hydrogenic. This problem has wider implications than the first, as it could mean that the global ionization and temperature structure of the wind was affected, if, for example, opacities due to elements such as C, N and O were important in determining the ionizing radiation field.

In order to verify that this is a second order effect, I show a test in Fig. 3.17 in which I compare the spectra calculated using the indivisible line transfer mode against spectra calculated using weight reduction mode (which does not make this approximation). The model shown is the fiducial BAL quasar model from H13, where modelling the absorption effect on the ionizing radiation field properly is important due to the stratified and self-shielding flow. As long as H and He are treated as macro-atoms, the agreement between the modes is good, and the ionization structure in the flow is very similar. Many of the differences in the ionization structure in the flow are actually caused by the improved treatment of the Balmer and Lyman continua.

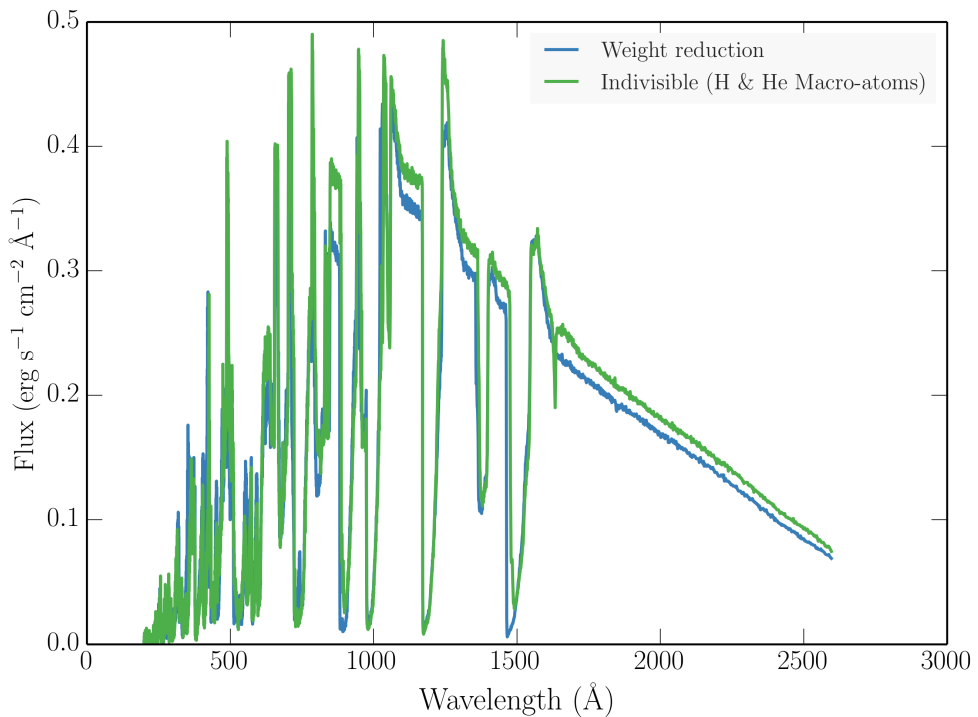


FIGURE 3.17: A comparison between weight reduction and line transfer mode. The model is the H13 fiducial BALQSO model – agreement is generally even better for CV models.

3.9 Code Maintenance and Version Control

In an effort to manage the expansion of the team working on PYTHON, I was responsible for bringing the code under the auspices of a robust version control system. Thanks to these efforts, the code is now hosted on GitHub at <https://github.com/agnwinds/python/>. Our team uses a Pull & Fork model for collaborative code development, in which major changes are made in a forked repository before the developer submits a ‘Pull request’ to the main repository. In order to test the code, we use a combination of Travis CI build tests – run for each commit to the upstream repository – and our own test suite, which is run every night on a multi-core server. I have written both of these test suites.

3.9.1 Parallelisation

Including macro-atoms in a simulation can have a significant impact on runtime, especially when simulating dense regions of plasma. By way of example, the CV model

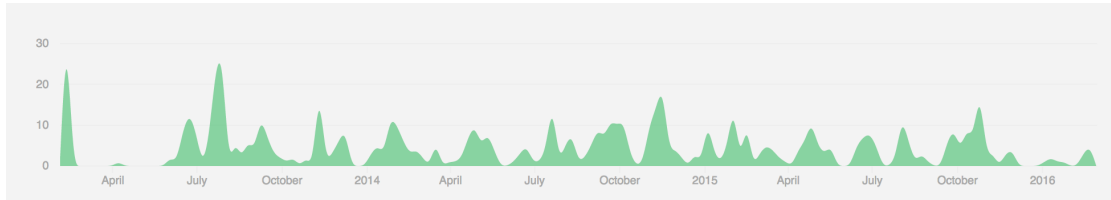


FIGURE 3.18: Commit history from Feb 3, 2013 to Feb 29, 2016, showing the regular code development that makes version control such a necessity to a collaborative code project. Produced using the Github API and plotting capability.

presented by LK02 takes approximately 118s to run one ionization cycle with 10^6 photons. One of the macro-atom models presented in chapter 4 takes 5651s to complete the same task.

Fortunately, MCRT codes are intuitively parallelisable, as is the macro-atom emissivity calculation described above, since operations on cells or photons can simply be divided up between processors. PYTHON is parallelised using an open source Message Passing Interface (MPI) implementation known as Open MPI ([Gabriel et al. 2004](#)). This library provides the core functions needed in order to share out computing tasks among a series of parallel processors with distributed memory. The parallelised elements of PYTHON include photon propagation, updating of wind ionization and temperature structure and the calculation of macro-atom emissivities. This involves a reasonable amount of book-keeping in that the radiation field estimators must be communicated between threads so as to correctly account for all the photons that have interacted with a given cell. I have been responsible for all of the parallelisation implemented that is specific to the macro-atom routines.

Fig. 3.19 shows the effect of parallelising a run. Due to the nature of MCRT, it is possible to achieve significant decrease in overall runtime. This improvement was crucial in order to be able to run the simulation grids used for chapters 4 and 5.

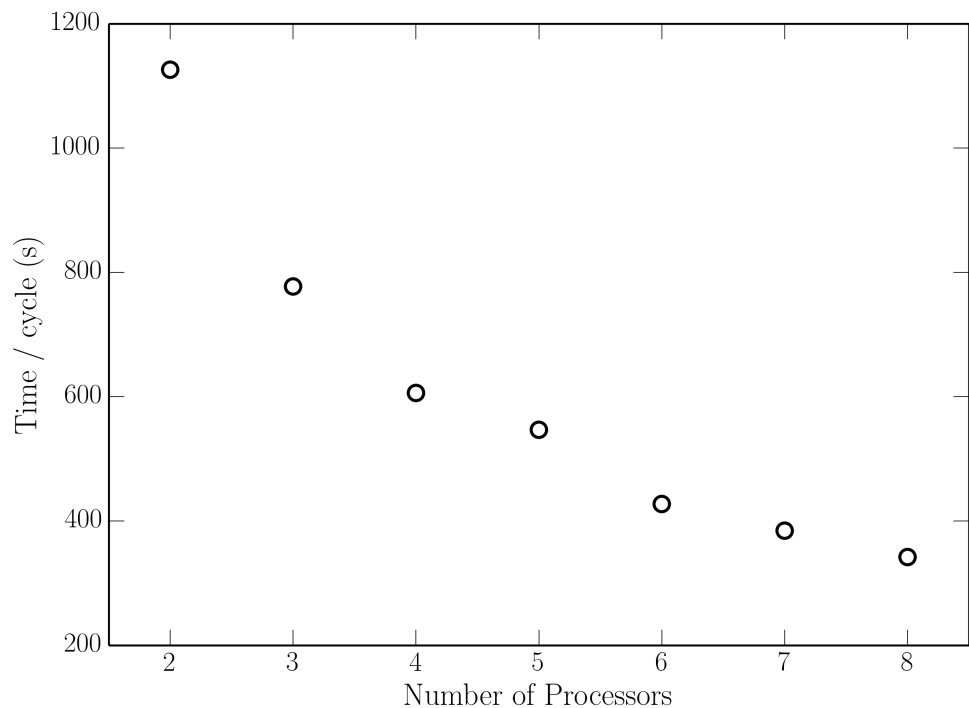


FIGURE 3.19: Total runtime per cycle for an AGN run as a function of the number of processors.

Chapter 4

The Impact of Accretion Disc Winds on the Optical Spectra of Cataclysmic Variables

This chapter is based on the publication:

Matthews J. H., Knigge C., Long K. S., Sim S. A., Higginbottom N., ‘The impact of accretion disc winds on the optical spectra of cataclysmic variables’, 2015, MNRAS, 450, 3331.

4.1 Introduction

Here, I present Monte Carlo radiative transfer simulations designed to assess the likely impact of accretion disc winds on the optical spectra of high-state CVs. The goal is to test whether the disc winds that produce the UV resonance absorption lines also naturally create significant amounts of optical emission. More specifically, I aim to investigate whether a disc wind model can reproduce the optical lines observed in CV spectra, such as H α , H β , He II 4686 Å and the He I lines, as well as the He II 1640 Å emission line. I also aim to explore whether the recombination continuum from the wind can successfully ‘fill-in’ the Balmer photoabsorption edge intrinsic to stellar or disc atmosphere spectra and to establish if a disc wind model can produce single-peaked

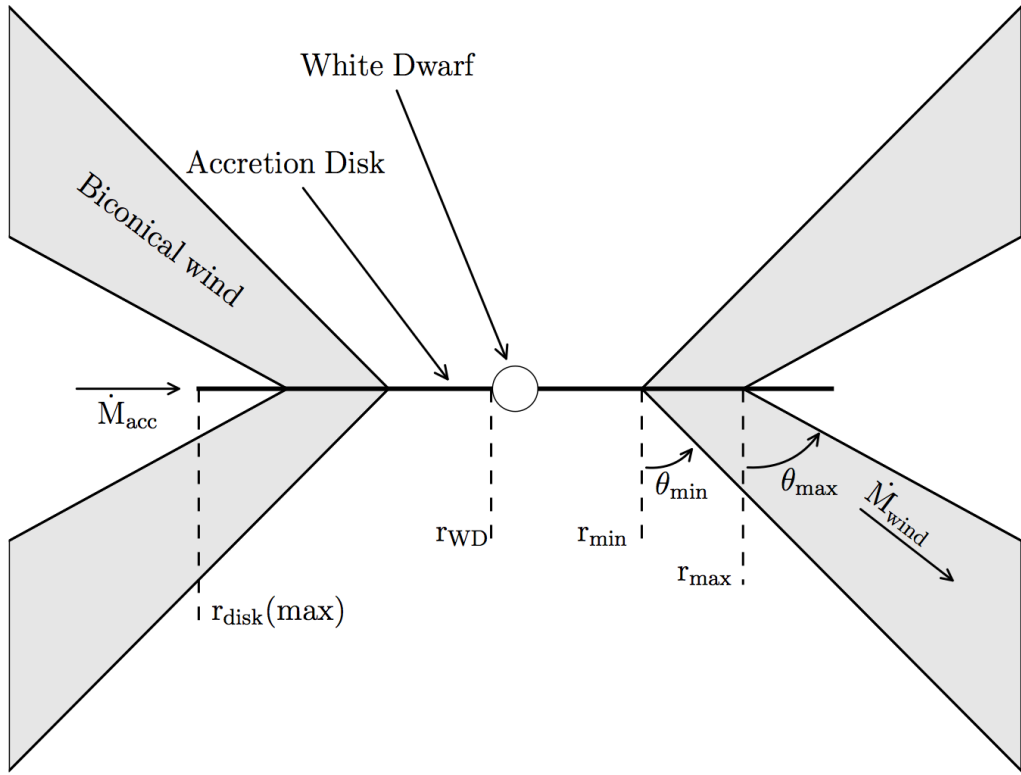


FIGURE 4.1: Cartoon illustrating the geometry and kinematics of the benchmark CV wind model.

lines as proposed by Murray & Chiang (1996, 1997, hereafter referred to collectively as MC96). The relevant background to this study is outlined in section 2.1.1.

In order to carry out these simulations and effectively model the optical spectra of CVs, I use the ‘macro-atom’ approach described in chapter 3. With this method, PYTHON is able to deal correctly with processes involving excited levels, such as the recombination emission observed in CV spectra. The prescription used to describe the wind is the biconical SV93 model described in section 2.4; a schematic for this specific application is shown in Fig. 4.1. The remainder of this chapter is organized as follows. I begin by describing the photon sources and input SED used in this modelling. In section 4.2, I present spectra simulated from the benchmark model employed by LK02. In section 4.3, I present a revised model optimized for the optical waveband, before summarising the findings in section 4.4.

4.1.1 Sources and Sinks of Radiation

The net photon sources in this CV model are the accretion disc, the WD and, in principle, a boundary layer with user-defined temperature and luminosity. All of these radiating bodies are taken to be optically thick, and photons striking them are assumed to be destroyed instantaneously. The secondary star is not included as a radiation source, but is included as an occulting body. This allows eclipses to be modelled. Finally, emission from the wind itself is also accounted for, but note that this assumes the outflow is in radiative equilibrium. Thus all of the heating of the wind, as well as its emission, is ultimately powered by the radiation field of the net photon sources in the simulation. In the following sections, I will describe the treatment of these system components in slightly more detail, which are also shown in Fig. 4.1.

4.1.1.1 Accretion disc

PYTHON has some flexibility when treating the accretion disc as a source of photons. The disc is broken down into annuli such that each annulus contributes an equal amount to the bolometric luminosity. The disc is geometrically thin, but optically thick, and I thus adopt the temperature profile of a standard [Shakura & Sunyaev \(1973\)](#) α -disc. An annulus can then be treated either as a blackbody with the corresponding effective temperature or as a stellar atmosphere model with the appropriate surface gravity and effective temperature. Here, blackbodies are used during the ionization cycles and to compute the Monte Carlo estimators. The input SED for the ionization cycles is shown in Fig. 4.2. However, during the spectral synthesis stage of the simulation stellar atmosphere models are used. This produces more realistic model spectra and allows a test of whether recombination emission from the wind base can fill in the Balmer jump, which is always in absorption in these models. The synthetic stellar atmosphere spectra are calculated with SYNSPEC¹ from either Kurucz ([Kurucz 1991](#)) atmospheres (for $T_{\text{eff}} \leq 50,000$ K) or from TLUSTY ([Hubeny & Lanz 1995](#)) models (for $T_{\text{eff}} > 50,000$ K).

¹<http://nova.astro.umd.edu/Synspec43/synspec.html>

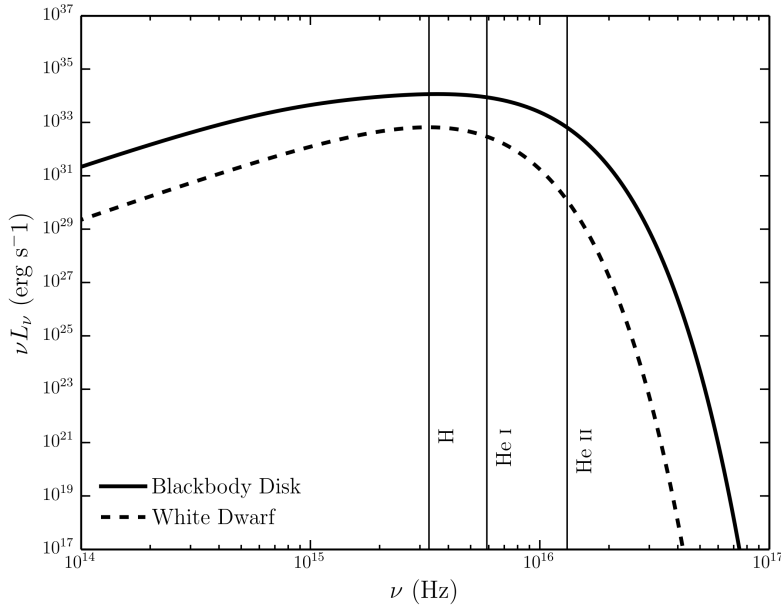


FIGURE 4.2: The spectral energy distribution of the accretion disc and white dwarf used in the ionization cycles for the CV modelling. The important ionization edges for hydrogen and helium are marked.

4.1.1.2 White Dwarf

The WD at the center of the disc is always present as a spherical occulting body with radius R_{WD} in PYTHON CV models, but it can also be included as a source of radiation. In the models presented here, the WD is treated as a blackbody radiator with temperature T_{WD} and luminosity $L_{WD} = 4\pi R_{WD}^2 \sigma T_{WD}^4$.

4.1.1.3 Boundary Layer

It is possible to include radiation from a boundary layer (BL) between the disc and the WD. In PYTHON, the BL is described as a blackbody with a user-specified effective temperature and luminosity. The models presented here initially follow LK02 in setting the BL luminosity to zero, partly as the temperature, luminosity, and even existence of a BL in CVs with strong winds is not certain (Hoare & Drew 1993). However, I have confirmed that the addition of an isotropic BL with $L_{BL} = 0.5L_{acc}$ and temperatures in the range $80 \text{ kK} \leq T_{BL} \leq 200 \text{ kK}$ would not change any of the main conclusions here. The influence of the BL on the heating and cooling balance in the wind, as well as the emergent spectrum, is briefly discussed in section 4.3.6.

Parameter	Model A	Model B
M_{WD}	$0.8 M_{\odot}$	
R_{WD}	7×10^8 cm	
T_{WD}	40,000 K	
M_2	-	$0.6 M_{\odot}$
q_M	-	0.75
P_{orb}	-	5.57 hr
a	-	$194.4 R_{WD}$
R_2	-	$69.0 R_{WD}$
\dot{M}_{acc}	$10^{-8} M_{\odot} \text{yr}^{-1}$	
\dot{M}_W	$10^{-9} M_{\odot} \text{yr}^{-1}$	
r_{\min}	$4 R_{WD}$	
r_{\max}	$12 R_{WD}$	
$r_{\text{disc}}(\text{max})$	$34.3 R_{WD}$	
θ_{\min}	20.0°	
θ_{\max}	65.0°	
γ	1	
v_{∞}	$3 v_{\text{esc}}$	
R_v	7×10^{10} cm	10^{11} cm
R_v/R_{WD}	100	142.9
α	1.5	4

TABLE 4.1: Parameters used for the geometry and kinematics of the benchmark CV model (model A), which is optimized for the UV band, and a model which is optimized for the optical band and described in section 4.3 (model B). For model B, only parameters which are altered are given - otherwise the model A parameter is used. P_{orb} is the orbital period (the value for RW Tri from Walker 1963 is adopted, see section 4.3.5) and R_2 is the radius of a sphere with the volume of the secondary's Roche lobe. Other quantities are defined in the text or Fig. 4.1. Secondary star parameters are only quoted for model B as I do not show eclipses with the benchmark model (see section 4.3.5).

4.1.1.4 Secondary Star

The donor star is included in the system as a pure radiation sink, i.e. it does not emit photons, but absorbs any photons that strike its surface. The secondary is assumed to be Roche-lobe filling, so its shape and relative size are defined by setting the mass ratio of the system, $q_M = M_2/M_{WD}$. The inclusion of the donor star as an occulting body allows eclipses of the disc and the wind to be modelled. For this purpose, I assume a circular orbit with a semi-major axis a and specify orbital phase such that $\Phi_{\text{orb}} = 0$ is the inferior conjunction of the secondary (i.e. mid-eclipse for $i \simeq 90^\circ$).

4.2 A Benchmark Disc Wind Model

The main goal is to test whether the type of disc wind model that has been successful in explaining the UV spectra of CVs could also have a significant impact on the optical

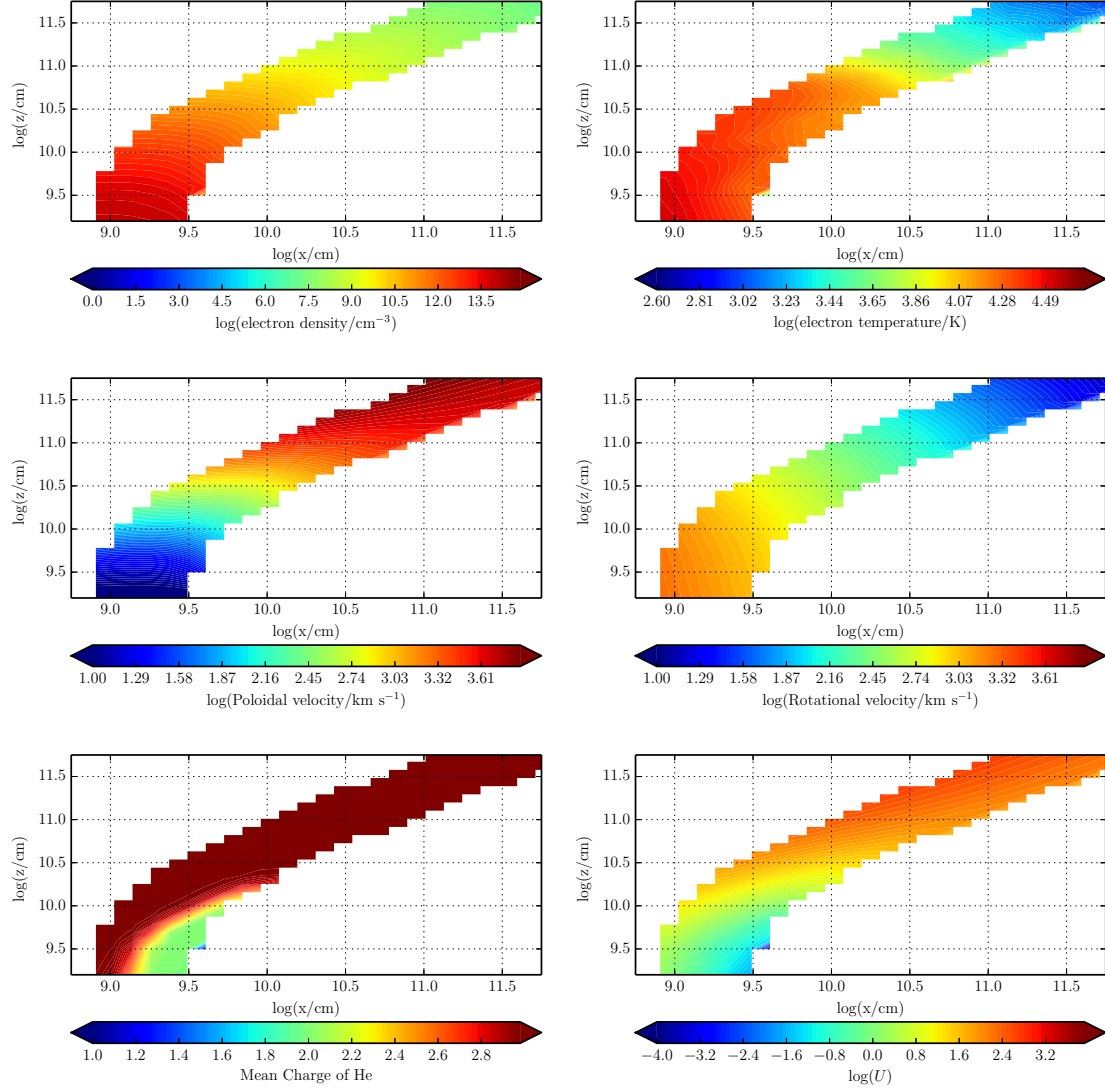


FIGURE 4.3: The physical properties of the wind – note the logarithmic scale. Near the disc plane the wind is dense, with low poloidal velocities. As the wind accelerates it becomes less dense and more highly ionized. The dominant He ion is almost always He III, apart from in a small portion of the wind at the base, which is partially shielded from the inner disc.

continuum and emission line spectra of these systems. In order to set a benchmark, I therefore begin by investigating one of the fiducial CV wind models that was used by SV93 and LK02 to simulate the UV spectrum of a typical high-state system. The specific parameters for this model (model A) are listed in table 4.1. A key point is that the wind mass-loss rate in this model is set to 10% of the accretion rate through the disc. I follow SV93 in setting the inner edge of the wind (r_{\min}) to $4 R_{WD}$. The sensitivity to some of these parameters is briefly discussed in section 4.3.4.

4.2.1 Physical Structure and Ionization State

Fig. 4.3 shows the physical and ionization structure of the benchmark disc wind model. The ionization parameter shown in the bottom right panel is given by equation 3.102. The ionization parameter is a useful measure of the ionization state of a plasma, as it evaluates the ratio of the number density of ionizing photons to the local H density.

There is an obvious drop-off in density and temperature with distance away from the disc, so any line formation process that scales as density squared – i.e. recombination and collisionally excited emission – should be expected to operate primarily in the dense base of the outflow. Moreover, a comparison of the rotational and poloidal velocity fields shows that rotation dominates in the near-disc regime, while outflow dominates further out in the wind.

The ionization equation used in the ‘simple atom’ approach used by LK02 (see section 3.4.2.1) should be a reasonable approximation to the photoionization equilibrium in the benchmark wind model. Even though the macro-atom treatment of H and He does affect the computation of the overall ionization equilibrium, the resulting ionization state of the wind should be similar to that found by LK02. The bottom panels in Fig. 4.3 confirm that this is the case. In particular, He is fully ionized throughout most of the outflow, except for a small region near the base of the wind, which is shielded from the photons produced by the hot inner disc. In line with the results of LK02, CIV is the dominant C ion throughout the wind, resulting in a substantial absorbing column across a large range of velocities. As we shall see, this produces the broad, deep and blue-shifted CIV 1550 Å absorption line that is usually the most prominent wind-formed feature in the UV spectra of low-inclination nova-like CVs.

4.2.2 Synthetic Spectra

I begin by verifying that the benchmark model still produces UV spectra that resemble those observed in CVs. This should be the case, since the ionization state of the wind has not changed significantly from that computed by LK02 (see section 4.2.1). The left column of panels in Fig. 4.4 shows that this expectation is met: all of the strong metal resonance lines – notably N V 1240 Å, Si IV 1400 Å and C IV 1550 Å – are present and exhibit clear P-Cygni profiles at intermediate inclinations. In addition, however, I now also find that the wind produces significant Ly α and He II 1640 Å emission lines.

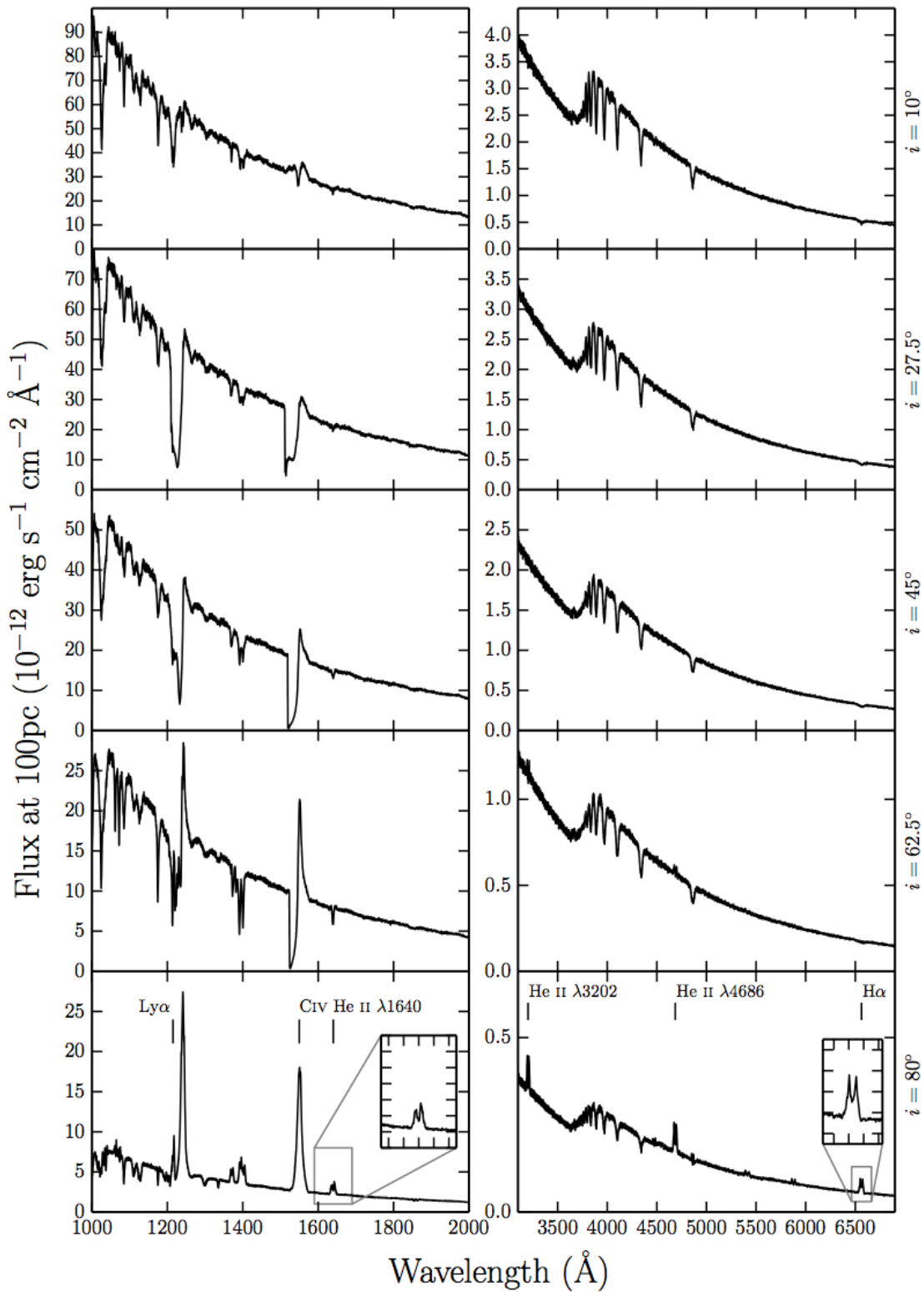


FIGURE 4.4: UV (left) and optical (right) synthetic spectra for model A, the benchmark model, computed at sightlines of 10, 27.5, 45, 62.5 and 80 degrees. The inset plots show zoomed-in line profiles for He II 1640 Å and H α . Double-peaked line emission can be seen in He II 1640 Å, He II 4686 Å, H α and some He I lines, but the line emission is not always sufficient to overcome the absorption cores from the stellar atmosphere models.

The model also produces a prominent He II 3202 Å line at high inclinations.

Fig. 4.4 (right-hand panel) and Fig. 4.5 show the corresponding optical spectra produced for the benchmark model, and these do exhibit some emission lines associated with H and He. There is a general trend from absorption lines to emission lines with increasing inclination, as we might expect from this wind geometry. This trend is consistent with observations, as discussed in section 1.2.2.2. However, it is clear that this particular model does not produce all of the lines seen in observations of high-state CVs. The higher-order Balmer series lines are too weak to overcome the intrinsic absorption from the disc atmosphere, and the wind fails to produce any observable emission at low and intermediate inclinations. This contrasts with the fact that emission lines are seen in the optical spectra of (for example) V3885 Sgr (Hartley et al. 2005) and IX Vel (Beuermann & Thomas 1990, see also Fig. 1.11).

The emissivity of these recombination features scales as density squared, meaning that they form almost entirely in the dense base of the wind, just above the accretion disc. Here, the velocity field of the wind is still dominated by rotation, rather than outflow, which accounts for the double-peaked shape of the lines. In principle, lines formed in this region can still be single peaked, since the existence of a poloidal velocity *gradient* changes the local escape probabilities (MC96). However, as discussed further in section 4.3.3, the radial velocity shear in the models is not high enough for this radiative transfer effect to dominate the line shapes.

The Balmer jump is in absorption at all inclinations for the benchmark model. This is due to the stellar atmospheres used to model the disc spectrum; it is not a result of photoabsorption in the wind. In fact, the wind spectrum exhibits the Balmer jump in *emission*, but this is not strong enough to overcome the intrinsic absorption edge in the disc spectrum. This is illustrated in Fig. 4.6, which shows the angle-integrated spectrum of the system, i.e. the spectrum formed by all escaping photons, separated into the disc and wind contributions. Even though the wind-formed Balmer recombination continuum does not completely fill in the Balmer absorption edge in this model, it does already contribute significantly to the total spectrum. This suggests that modest changes to the outflow kinematics might boost the wind continuum and produce emergent spectra with weak or absent Balmer absorption edges.

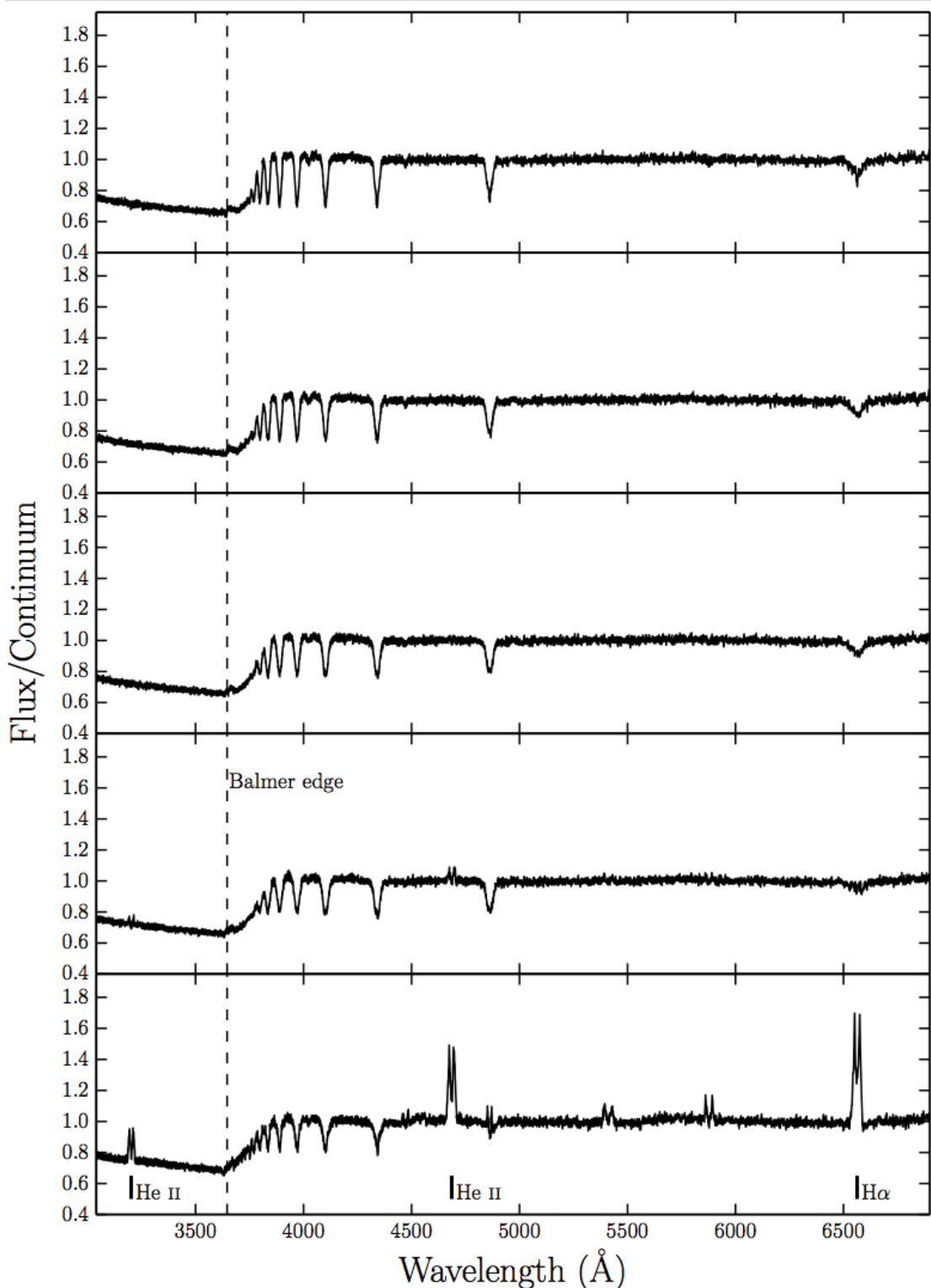


FIGURE 4.5: Synthetic optical spectra from model A computed for sightlines of 10, 27.5, 45, 62.5 and 80 degrees. In these plots the flux is divided by a polynomial fit to the underlying continuum redward of the Balmer edge, so that line-to-continuum ratios and the true depth of the Balmer jump can be shown.

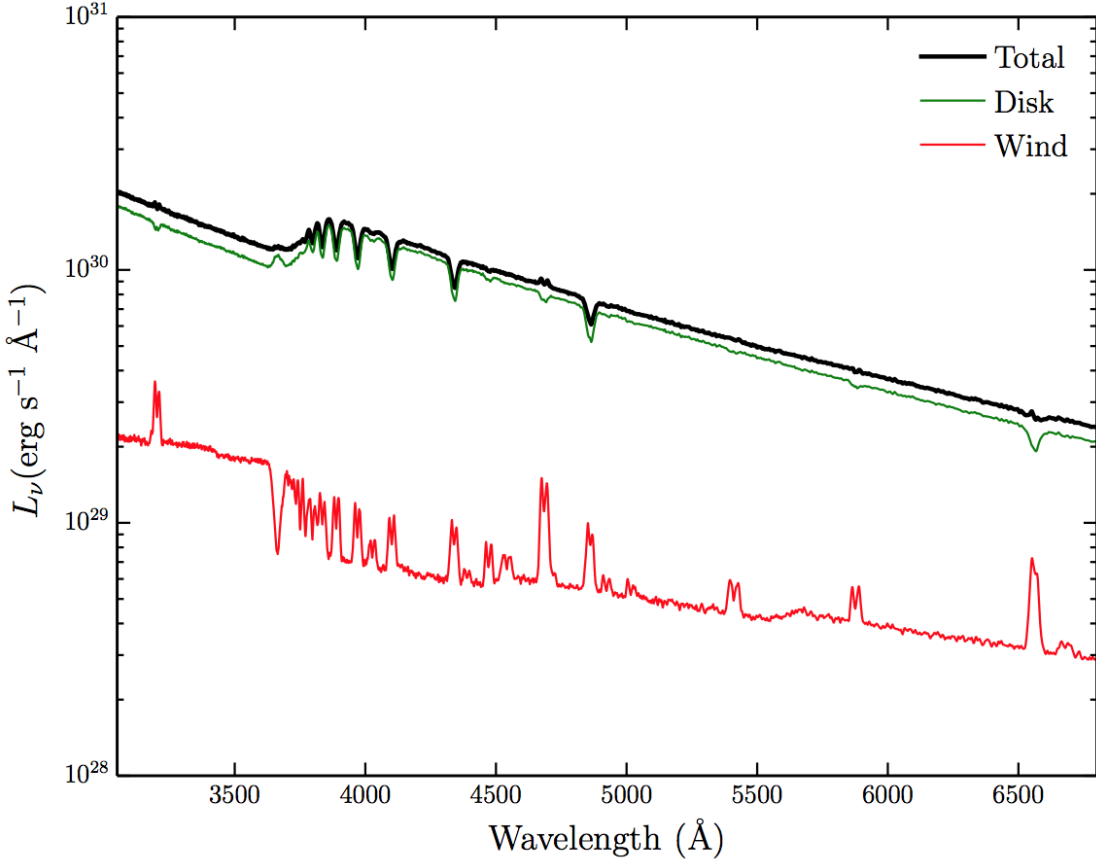


FIGURE 4.6: Total packet-binned spectra across all viewing angles, in units of monochromatic luminosity. The thick black line shows the total integrated escaping spectrum, while the green line shows disc photons which escape without being reprocessed by the wind. The red line show the contributions from reprocessed photons. Recombination continuum emission blueward of the Balmer edge is already prominent relative to other wind continuum processes, but is not sufficient to fill in the Balmer jump in this specific model.

4.3 A Revised Model Optimized for Optical Wavelengths

The benchmark model discussed in section 4.2 was originally designed to reproduce the wind-formed lines seen in the UV spectra of high-state CVs. This model does produce some observable optical emission, but I can now attempt to construct a model that more closely matches the observed optical spectra of CVs.

Specifically, I aim to assess whether a revised model can:

- account for all of the lines seen in optical spectra of CVs while preserving the UV behaviour;
- produce single-peaked Balmer emission lines;

- generate enough of a wind-formed recombination continuum to completely fill in the disc’s Balmer absorption edge for reasonable outflow parameters.

The emission measure of a plasma is directly proportional to its density. The simplest way to simultaneously affect the density in the wind (for fixed mass-loss rate), as well as the velocity gradients, is by modifying the poloidal velocity law. Therefore, I focus on just two kinematic variables:

- the acceleration length, R_v , which controls the distance over which the wind accelerates to $\frac{1}{2} v_\infty$;
- the acceleration exponent, α , which controls the rate at which the poloidal velocity changes near R_v .

The general behaviour we might expect is that outflows with denser regions near the wind base – i.e. winds with larger R_v and/or larger α – will produce stronger optical emission signatures. However, this behaviour may be moderated by the effect of the increasing optical depth through this region, which can also affect the line profile shapes. In addition, modifying R_v also increases the emission *volume*. Based on a preliminary exploration of models with different kinematics, I adopt the parameters listed in table 4.1 for this new, ‘optically optimized’ model (model B).

4.3.1 Synthetic Spectra

Fig. 4.7 shows the UV and optical spectra for the optically optimized model for the full range of inclinations. As expected, the trend from absorption to emission in the optical is again present, but in this revised model emission lines in the entire Balmer series are produced at high inclinations, as well as the observed lines in He II and He I. This can be seen more clearly in the continuum-normalized spectrum in Fig. 4.8.

Two other features are worth noting in the optical spectrum. First, the collisionally excited Ca II emission line at 3934 Å becomes quite prominent in the densest models. Second, the model predicts a detectable He II recombination line at 3202 Å. This is the He equivalent of Paschen β and should be expected in all systems that feature a strong He II 4686 Å line (the He equivalent of Paschen α). This line is somewhat unfamiliar

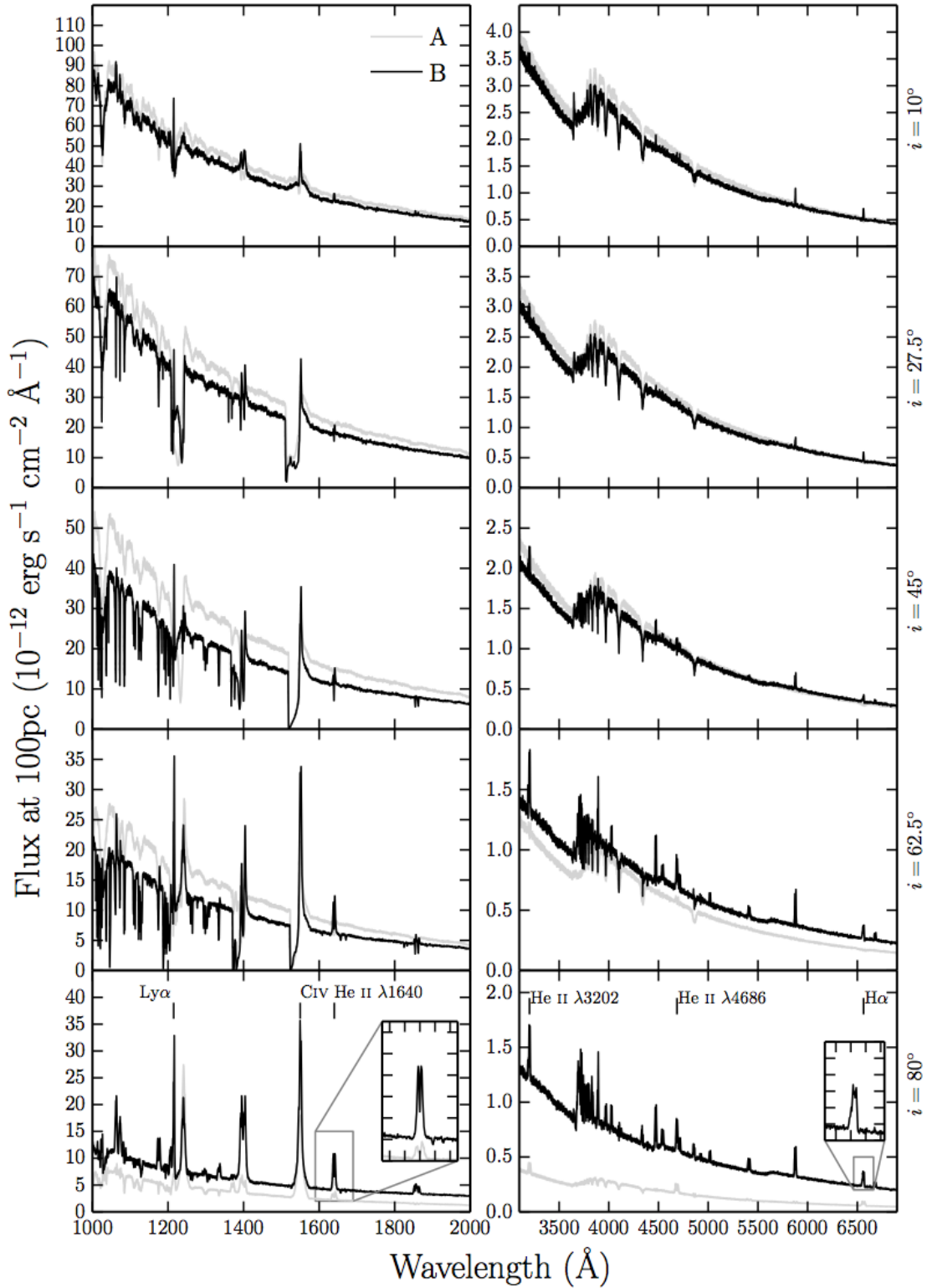


FIGURE 4.7: UV (left) and optical (right) synthetic spectra for model B computed at sightlines of 10, 27.5, 45, 62.5 and 80 degrees. Model A is shown in grey for comparison. The inset plots show zoomed-in line profiles for He II 1640 Å and H α . The Balmer and He are double-peaked, albeit with narrower profiles. Strong He II 4686 Å emission can be seen, as well as a trend of a deeper Balmer jump with decreasing inclination.

observationally, because it lies bluewards of the atmospheric cut-off, but also redwards of most ultraviolet spectra.

The synthetic spectra do not exhibit P-Cygni profiles in the optical lines. This is perhaps not surprising. LK02 and SV93 originally designed such models to reproduce the UV line profiles. Thus, most of the wind has an ionization parameter of $\log U \sim 2$ (see Fig. 4.3). This means H and He are mostly ionized throughout much of the wind and are successful in producing recombination features. However, the line opacity throughout the wind is too low to produce noticeable blue shifted absorption in these lines. It appears that the systems that exhibit such profiles must possess a higher degree of ionization stratification, although the lack of contemporary observations means it is not known for certain if the P-Cygni profiles in UV resonance lines and optical H and He lines exist simultaneously. Ionization stratification could be caused by a clumpy flow, in which the ionization state changes due to small scale density fluctuations, or a stratification in density and ionizing radiation field over larger scales. Invoking clumpiness in these outflows is not an unreasonable hypothesis. Theories of line-driven winds predict an unstable flow (MacGregor et al. 1979; Owocki & Rybicki 1984, 1985), and simulations of CV disc winds also produce density inhomogeneities (Proga et al. 1998, 2002b). Tentative evidence for clumping being directly related to P-Cygni optical lines comes from the fact that Prinja et al. (2000) found the dwarf nova BZ Cam’s outflow to be unsteady and highly mass-loaded in outburst, based on observations of the UV resonance lines. This system has also exhibited P-Cygni profiles in He I 5876 Å and H α when in a high-state (Patterson et al. 1996; Ringwald & Naylor 1998). The degree of ionization and density variation and subsequent line opacities may be affected by the model parameters and the specific parameterisation adopted.

In the UV, the model still produces all the observed lines, and deep P-Cygni profiles are produced in the normal resonance lines, as discussed in section 4.2.2. However, the UV spectra also display what is perhaps the biggest problem with this revised model, namely the strength of resonance line emission at low and intermediate inclinations. In order to generate strong optical wind signatures, I have adopted wind parameters that lead to very high densities at the base of the wind ($n_e \sim 10^{13} - 10^{14} \text{ cm}^{-3}$). This produces the desired optical recombination emission, but also increases the role of collisional excitation in the formation of the UV resonance lines. This explains the pronounced increase in the emission component of the CIV 1550 Å resonance line, for example, relative to what

was seen in the benchmark model (compare Figures 4.4 and 4.7). The strength of this component in the revised model is probably somewhat too high to be consistent with UV observations of high-state CVs (see e.g. Long et al. 1991, 1994; Noebauer et al. 2010).

4.3.2 Continuum Shape and the Balmer Jump

The wind now also has a clear effect on the continuum shape, as shown by Fig. 4.9. In fact, the majority of the escaping spectrum has been reprocessed in some way by the wind, either by electron scattering (the wind is now moderately Thomson-thick), or by bound-free processes. This is demonstrated by the flatter spectral shape and the slight He photoabsorption edge present in the optical spectrum (marked in Fig. 4.8). This reprocessing is also responsible for the change in continuum level between models A and B. In addition, Figures 4.7, 4.8 and 4.9 clearly demonstrate that the wind produces a recombination continuum sufficient to completely fill in the Balmer jump at high inclinations.² This might suggest that Balmer continuum emission from a wind can be important in shaping the Balmer jump region, as suggested by Knigge et al. (1998b) and Hassall (1985).

It should be acknowledged, however, that the Balmer jump in high-state CVs would naturally weaken at high inclinations due to limb darkening effects (La Dous 1989b,a). Although simple limb darkening law which affects the emergent flux at each inclination is included, it is not a *frequency dependent* opacity in the model. As a result, the efficiency of filling in the Balmer jump should really be judged at low and medium inclinations, where, although prominent, the recombination continuum does not overcome the disc atmosphere absorption. In addition, this effect could mean that any model which successfully fills in the jump at low inclinations could lead to a Balmer jump in emission at high inclinations. In any case, to properly understand this phenomenon, a fully self-consistent radiative transfer calculation of both the disc atmosphere and connected wind is required.

²Note that the apparent absorption feature just redward of the Balmer jump in these models is artificial. It is caused by residual line blanketing in the stellar atmospheres, which the models cannot fill in since they employ a 20-level H atom.

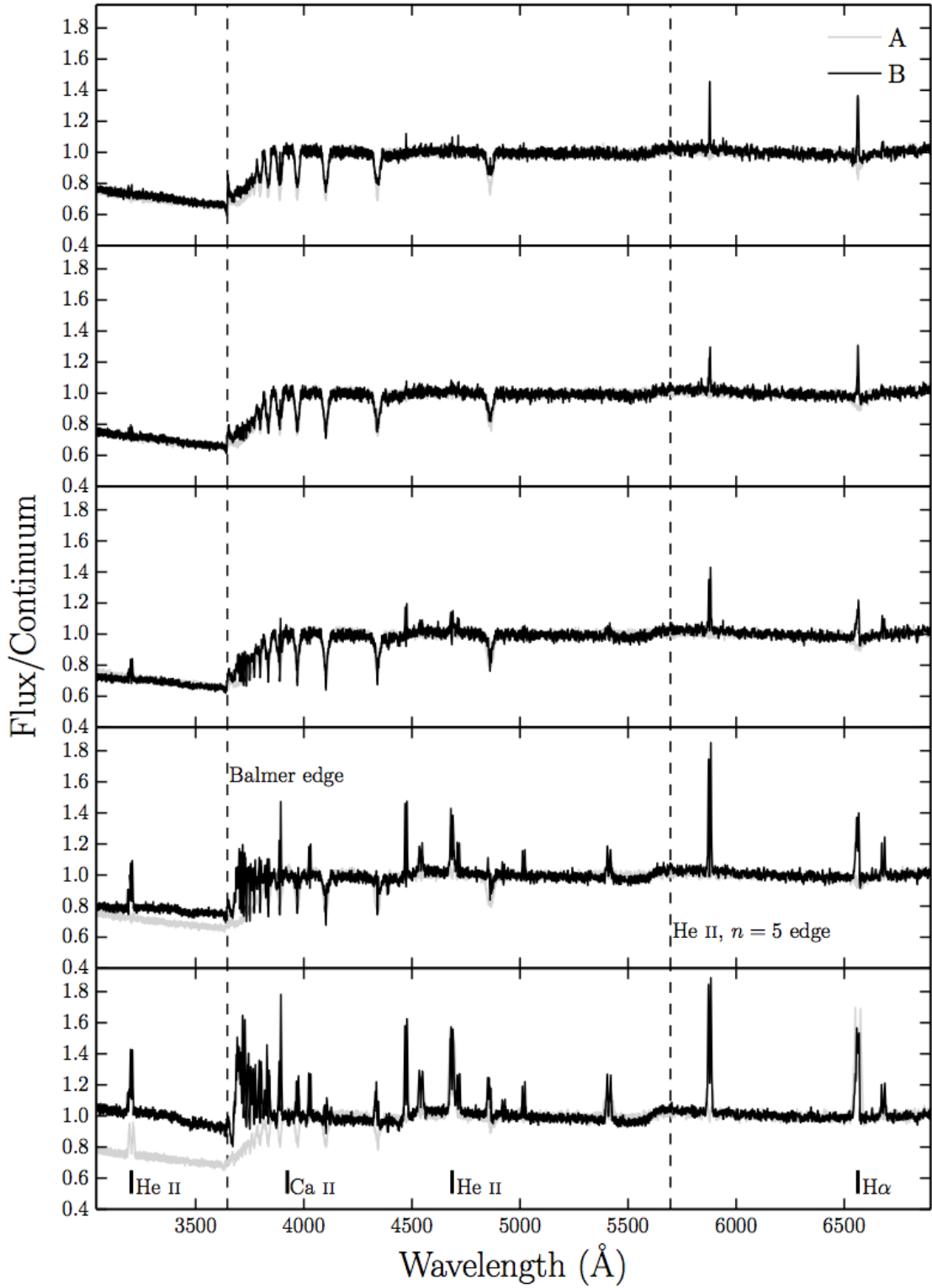


FIGURE 4.8: Synthetic optical spectra from model B computed for sightlines of 10, 27.5, 45, 62.5 and 80 degrees. Model A is shown in grey for comparison. In these plots the flux is divided by a polynomial fit to the underlying continuum redward of the Balmer edge, so that line-to-continuum ratios and the true depth of the Balmer jump can be shown.

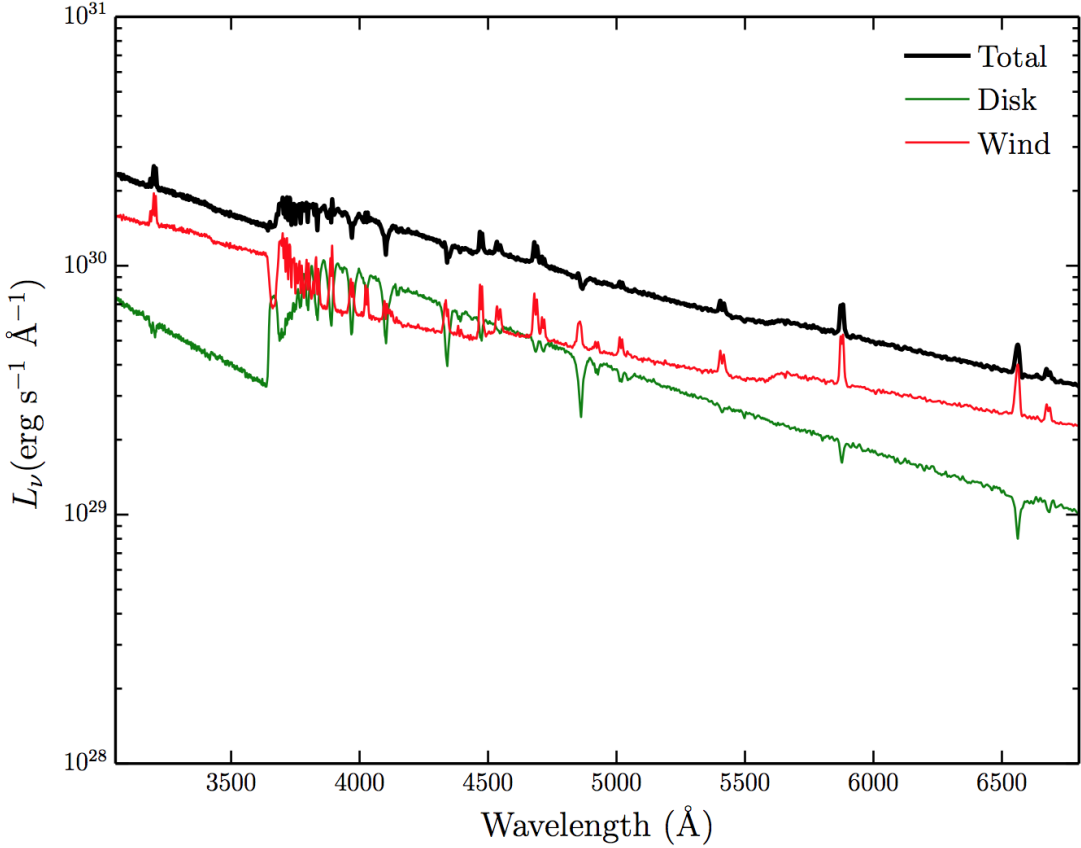


FIGURE 4.9: Total packet-binned spectra across all viewing angles, in units of monochromatic luminosity. The thick black line shows the total integrated escaping spectrum, while the green line shows disc photons which escape without being reprocessed by the wind. The red line show the contributions from reprocessed photons. In this denser model the reprocessed contribution is significant compared to the escaping disc spectrum. The Balmer continuum emission is prominent, and the wind has a clear effect on the overall spectral shape.

4.3.3 Line Profile Shapes: Producing Single-Peaked Emission

Fig. 4.10 shows how the H α profile changes with the kinematics of the wind for an inclination of 80°. The main prediction is that dense, slowly accelerating wind models produce narrower emission lines. This is *not* due to radial velocity shear. As stated by MC96, that mechanism can only work if poloidal and rotational velocity gradients satisfy $(dv_l/dr)/(dv_\phi/dr) \gtrsim 1$; in these models, this ratio is always $\lesssim 0.1$. Instead, the narrow lines predicted by the denser wind models can be traced to the base of the outflow becoming optically thick in the continuum, such that the line emission from the base of the wind cannot escape to the observer. In such models, the ‘line photosphere’ (the $\tau \simeq 1$ surface of the line-forming region) moves outwards, towards larger vertical and cylindrical distances. This reduces the predicted line widths, since the rotational velocities – which normally provide the main line broadening mechanism

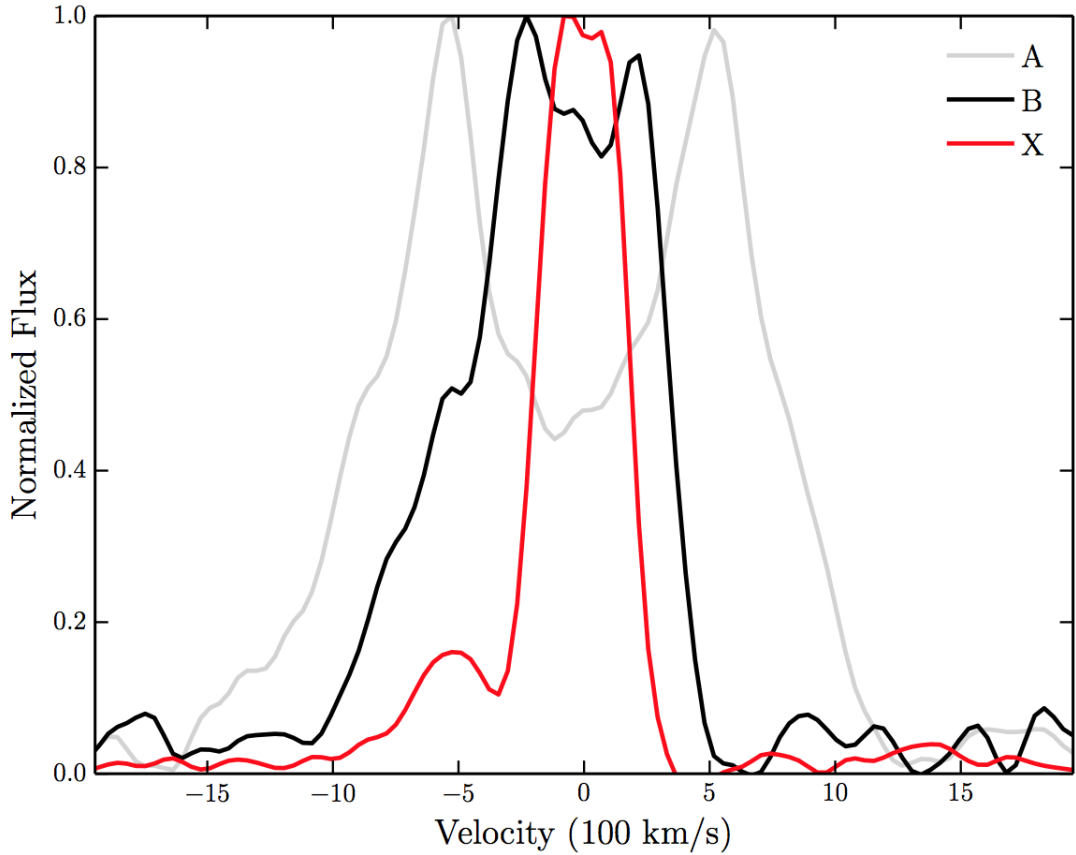


FIGURE 4.10: H α line profiles, normalized to 1, plotted in velocity space for three models with varying kinematic properties, computed at an inclination of 80°. The benchmark model and the improved optical model described in section 4.3 are labeled as A and B respectively, and a third model (X) which has an increased acceleration length of $R_v = 283.8 R_{WD}$, and $\alpha = 4$ is also shown. The x -axis limits correspond to the Keplerian velocity at $4 R_{WD}$, the inner edge of the wind. There is a narrowing of the lines, and a single-peaked line in model X. This is not due to radial velocity shear (see section 4.3.3).

at high inclination – drop off as $1/r$ in the outflow. This $1/r$ behaviour occurs due to the wind conserving specific angular momentum, and is initially in Keplerian rotation (see equation 2.13). The fact that the MC96 mechanism does not significantly affect the line profiles in this specific model does not mean that it could not be at work in CV winds. For example, it would be worth investigating alternative prescriptions for the wind velocity field, as well as the possibility that the outflows may be clumped. An inhomogeneous flow (which has been predicted in CVs; see section 4.3.1) might allow large radial velocity shears to exist while still maintaining the high densities needed to produce the required level of emission. However, such an investigation is beyond the scope of the present study.

In these models, single-peaked line profiles are produced once the line forming region has been pushed up to $\sim 10^{11}$ cm ($\sim 150 R_{WD}$) above the disc plane. This number may

seem unrealistically large, but the vertical extent of the emission region is actually not well constrained observationally. In fact, multiple observations of eclipsing NLs show that the H α line is only moderately eclipsed compared to the continuum (e.g. [Baptista et al. 2000](#); [Groot et al. 2004](#), see also section 4.3.5), implying a significant vertical extent for the line-forming region. This type of model should therefore not be ruled out *a priori*, but this specific model was not adopted as the optically optimized model due to its unrealistically high continuum level in eclipse.

4.3.4 Sensitivity to Model Parameters

This revised model demonstrates that one can achieve a more realistic optical spectrum by altering just two kinematic parameters. However, it may also be possible to achieve this by modifying other free parameters such as \dot{M}_W , the opening angles of the wind and the inner and outer launch radii. For example, increasing the mass-loss rate of the wind increases the amount of recombination emission (which scales with density squared), as well as lowering the ionization parameter and increasing the optical depth through the wind. Larger launching regions and covering factors tend to lead to a larger emitting volume, but this is moderated by a decrease in density for a fixed mass-loss rate. I also note that the inner radius of $4 R_{WD}$ adopted by SV93 affects the emergent UV spectrum seen at inclinations $< \theta_{\min}$ as the inner disc is uncovered. This causes less absorption in the UV resonance lines, but the effect on the optical spectrum is negligible. I have verified this general behaviour, but I suggest that future work should investigate the effect of these parameters in more detail, as well as incorporating a treatment of clumping. If a wind really does produce the line and continuum emission seen in optical spectra of high-state CVs, then understanding the true mass-loss rate and geometry of the outflow is clearly important.

4.3.5 Comparison to RW Tri

Fig. 4.11 shows a comparison of the predicted out-of-eclipse and mid-eclipse spectra against observations of the high-inclination nova-like RW Tri. The inclination of RW Tri is somewhat uncertain, with estimates including 70.5° ([Smak 1995](#)), 75° ([Groot et al. 2004](#)), 80° ([Longmore et al. 1981](#)) and 82° ([Frank & King 1981](#)). Here, we adopt $i = 80^\circ$, but the qualitative conclusions are not particularly sensitive to this choice. I follow

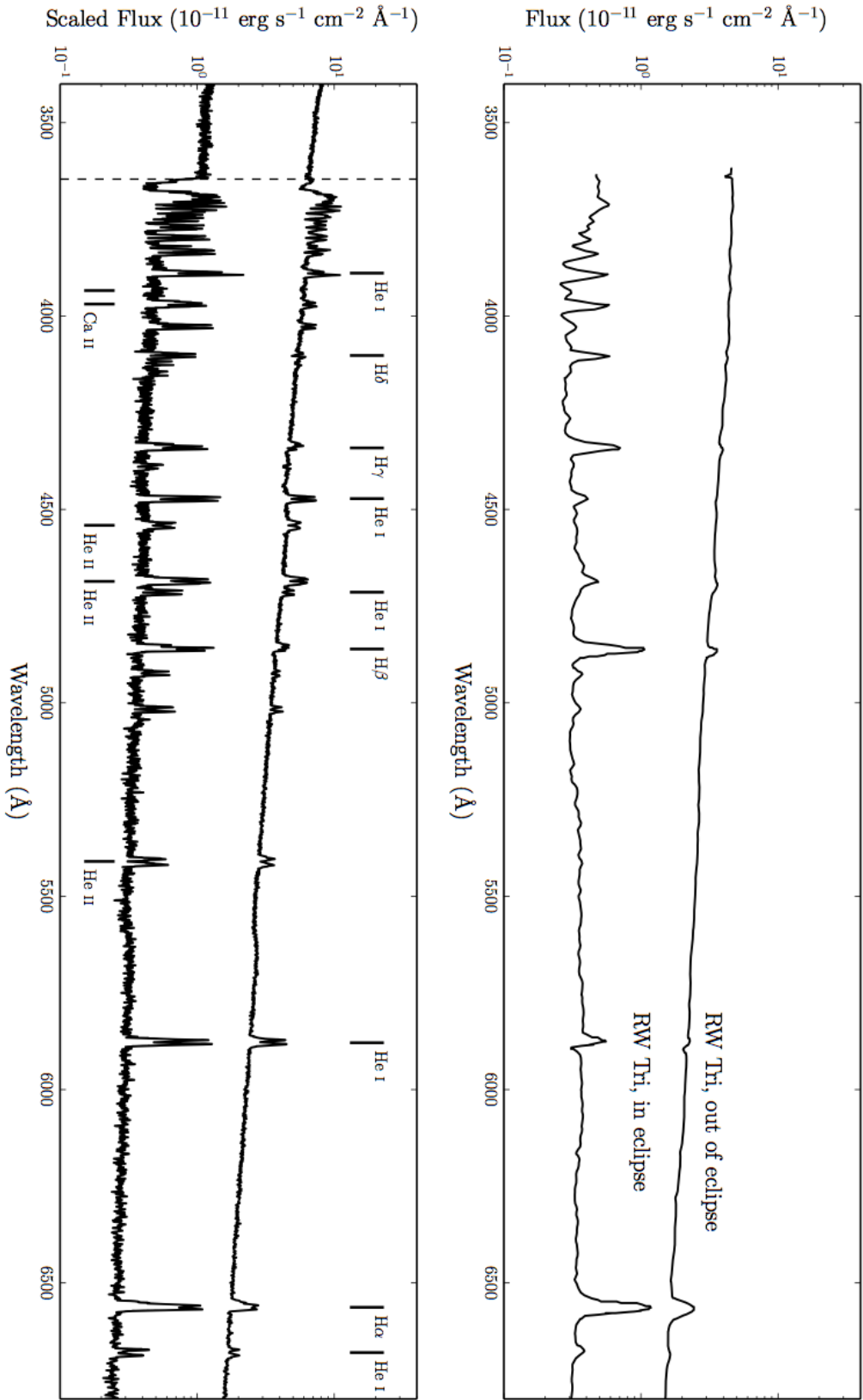


FIGURE 4.11: Top Panel: In and out of eclipse spectra of the high inclination NL RW Tri. Bottom Panel: In and out of eclipse synthetic spectra from model B. The artificial ‘absorption’ feature just redward of the Balmer jump is due to the reasons described in section 5.2.

LK02 is setting the value of $r_{\text{disc}}(\text{max})$ (the maximum radius of the accretion disc) to $34.3 R_{WD}$. When compared to the semi-major axis of RW Tri, this value is perhaps lower than one might typically expect for NLs (Harrop-Allin & Warner 1996). However, it is consistent with values inferred by Rutten et al. (1992). I emphasize that this model is in no sense a fit to this – or any other – data set.

The similarity between the synthetic and observed spectra is striking. In particular, the revised model produces strong emission in all the Balmer lines, with line-to-continuum ratios comparable to those seen in RW Tri. Moreover, the line-to-continuum contrast increases during eclipse, as expected for emission produced in a disc wind. This trend is in line with the observations of RW Tri, and it has also been seen in other NLs, including members of the SW Sex class (Neustroev et al. 2011). As noted in section 4.3.1, the majority of the escaping radiation has been reprocessed by the wind in some way (particularly the eclipsed light).

However, there are also interesting differences between the revised model and the RW Tri data set. For example, the synthetic spectra exhibit considerably stronger He II features than the observations, which suggests that the overall ionization state of the model is somewhat too high. As discussed in section 4.3.3, the optical lines are narrow, but double-peaked. This is in contrast to what is generally seen in observations of NLs, although the relatively low resolution of the RW Tri spectrum makes a specific comparison difficult. In order to demonstrate the double-peaked nature of the narrower lines, I do not smooth the synthesized data to the resolution of the RW Tri dataset. If the data was smoothed, the H α line would appear single-peaked.

4.3.6 A Note on Collision Strengths

PYTHON uses the van Regemorter (1962) approximation (see section 3.3.2.1) to calculate collision rates. This approach uses an effective gaunt factor, \bar{g} , of order unity. To conduct these specific simulations a value of $\bar{g} = 1$ was adopted. There are two main concerns when using this approach. The first is related to accuracy, as poorly estimating collision strengths could lead to incorrect heating and cooling balance in the flow, with knock-on effects on the emergent spectrum. This is of particular concern here as line heating is the dominant heating mechanism in the dense base of the wind. I have verified that the main conclusions of this study are fairly insensitive to the gaunt factor; for example, if

I adopt $\bar{g} = 0.2$ as suggested by, e.g., Ferland (2005) than the wind still produces a host of recombination lines. If improved collision strengths were to significantly reduce the wind temperature a boundary layer might actually be required to produce the higher ionization lines such as He II 4686 Å (see e.g. Hoare & Drew 1991), arguably making the model more realistic.

The second concern is that collisions between radiatively forbidden transitions are not taken into account when one splits levels into l - and s -subshells, as well as principal quantum number, n (as I have done with He I; see section 3.7). However, I have verified that in this case the plasma is dense enough, and ionized enough, that recombination dominates the level populations, at least in the regions responsible for the optical line emission. In other words, two levels that are linked only by a forbidden transition have their relative populations determined by their recombination rates from the upper ion. Nevertheless, for future efforts, it would be desirable to include collisional data for forbidden transitions, an effort that has now been started (see chapter 7).

4.4 Conclusions

I have investigated whether a disc wind model designed to reproduce the UV spectra of high-state CVs would also have a significant effect on the optical spectra of these systems. I find that this is indeed the case. In particular, the model wind produces H and He recombination lines, as well as a recombination continuum blueward of the Balmer edge. The spectra do not show P-Cygni profiles in the optical H and He lines, which are seen in a small fraction of CV optical spectra. Possible reasons for this are briefly discussed in section 4.3.1.

A revised benchmark model was also constructed to more closely match the optical spectra of high-state CVs. This optically optimized model produces all the prominent optical lines in and out of eclipse and achieves reasonable verisimilitude with the observed optical spectra of RW Tri. However, this model also has significant shortcomings. In particular, it predicts stronger-than-observed He II lines in the optical region and too much of a collisionally excited contribution to the UV resonance lines. Incorporating more accurate collisional data into PYTHON will help assess this discrepancy in more detail.

Based on these results, I argue that recombination emission from outflows with sufficiently high densities and/or optical depths might produce the optical lines observed in CVs. It may also fill in the Balmer absorption edge in the spectrum of the accretion disc, thus accounting for the absence of a strong edge in observed CV spectra. In section 4.3.3, I demonstrated that although the double peaked lines narrow and single-peaked emission can be formed in the densest models, this is not due to the radial velocity shear mechanism proposed by MC96. I suggest that ‘clumpy’ line-driven winds or a different wind parameterization may nevertheless allow this mechanism to work. I also note the possibility that, as seen in the densest models I have presented, the single-peaked lines are formed well above the disc, where rotational velocities are lower.

It is not yet clear whether a wind model such as this can explain all of the observed optical features of high-state CVs – further effort is required on both the observational and modelling fronts. However, this work demonstrates that disc winds may not just be responsible for creating the blue-shifted absorption and P-Cygni profiles seen in the UV resonance lines of high-state CVs, but can also have a strong effect on the optical appearance of these systems. In fact, most of the optical features characteristic of CVs are likely to be affected – and possibly even dominated – by their disc winds. Given that optical spectroscopy plays a central role in observational studies of CVs, it is critical to know where and how these spectra are actually formed. I believe it is high time for a renewed effort to understand the formation of spectra in accretion discs and associated outflows.

Chapter 5

Testing Quasar Unification: Radiative Transfer In Clumpy Winds

This chapter is based on the publication:

Matthews J. H., Knigge C., Long K. S., Sim S. A., Higginbottom N., Mangham S. W., ‘Testing quasar unification: radiative transfer in clumpy winds’, 2016, MNRAS, 458, 293.

5.1 Introduction

In chapters 1 and 2, I reviewed the observational evidence for accretion disc winds in quasars and luminous AGN, and showed how they may be responsible for more than just the broad absorption lines and P-Cygni profiles seen in quasar spectra. In particular, they offer a natural way to *unify* much of the complex phenomenology into one simple picture.

Here, I aim to test that picture using PYTHON, with the specific aim of determining whether it is possible to reproduce the key properties of AGN spectra, including those of BALQSOs, using simple kinematic prescriptions for biconical disc winds. Past results have been encouraging: H13 produced simulated spectra that resembled those of BALQSOs, as long as the luminosity of the X-ray source was relatively low, of order

10^{43} erg s $^{-1}$, and the mass-loss rate was relatively high, of order the mass accretion rate. However, at higher X-ray luminosities, the wind was so ionized that UV absorption lines were not produced. In addition, and in part due to limitations inherent in the radiative transfer methods, the model failed to produce spectra with strong emission lines at any inclination angle.

Here I attempt to address both of these issues, by allowing for clumping in the outflow and introducing a more complete treatment of H and He in the radiative transfer calculations. Thus, the simulations presented in this chapter treat H and He as full macro-atoms and metals as simple-atoms, as described extensively in chapter 3. In order to correctly model the ionizing spectrum for simple-atoms, I dispense with the dilute blackbody modified-Saha approach and fully solve the ionization balance using the spectral modelling approach described in section 3.4.2.1. Macro-atoms still have their ionization and excitation states calculated from MC estimators.

The kinematic model used once again follows the SV93 prescription, and is described, together with the clumping implementation, in section 5.2. Section 5.3 contains the results obtained from the clumped wind model, including comparisons to observational data, as well as some discussion. I discuss the results further, and examine their sensitivity to model parameters and viewing angle in section 5.4, which expands somewhat on the work presented in Matthews et al. (2016). Finally, I summarise my findings in section 5.5.

5.2 A Clumpy Biconical Disk Wind Model for Quasars

Here, I once again adopt the SV93 kinematic prescription for a biconical disc wind model described in section 2.4. A schematic is shown in Fig. 5.1, with key aspects marked. As previously mentioned, the purpose of this purely kinematic wind model is to provide a simple tool for exploring different outflow geometries. The conclusions are therefore not limited to – nor do they make specific predictions about – the potential wind-driving mechanisms discussed in chapter 2. The general biconical geometry is similar to that invoked by Murray et al. (1995) and Elvis (2000) to explain the phenomenology of quasars and BALQSOs.

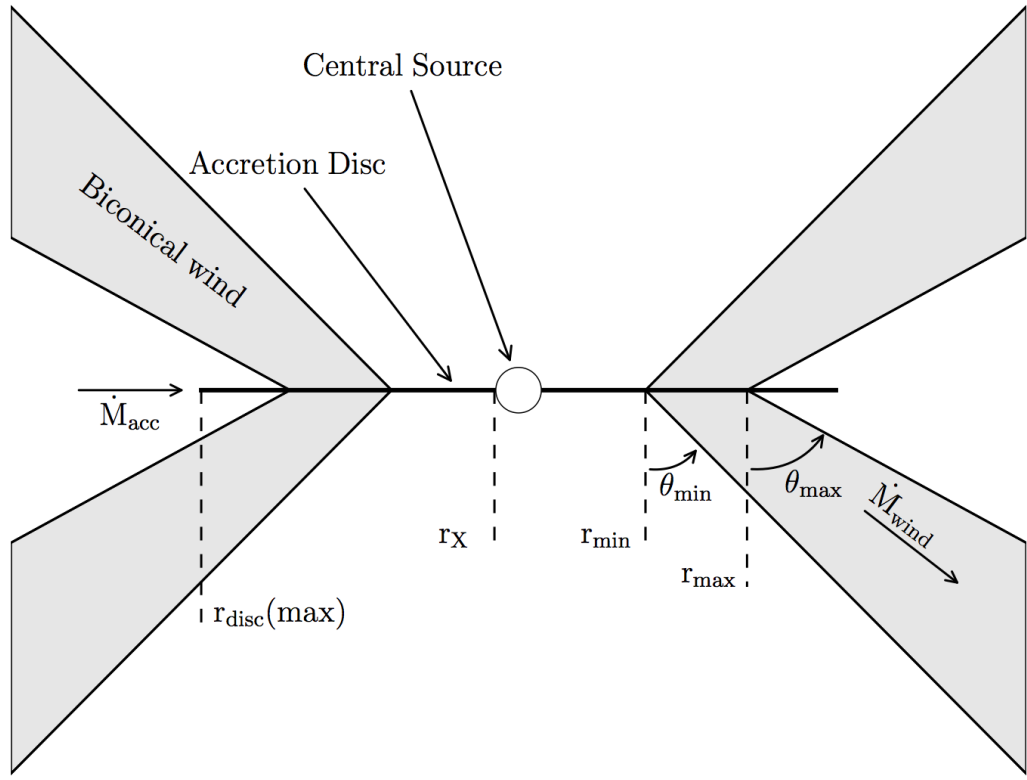


FIGURE 5.1: A cartoon showing the geometry and some key parameters of the biconical quasar wind model.

5.2.1 Photon Sources

Two sources of r -packets are included in the model: An accretion disc and a central X-ray source. The accretion disc is assumed to be geometrically thin, but optically thick. Accordingly, the disc is modelled as an ensemble of blackbodies with a [Shakura & Sunyaev \(1973\)](#) effective temperature profile. The emergent SED is then determined by the specified accretion rate (\dot{M}) and central BH mass (M_{BH}). All photon sources in the model are opaque, meaning that r -packets that strike them are destroyed. The inner radius of the disc extends to the innermost stable circular orbit (ISCO) of the BH. I assume a Schwarzschild BH with an ISCO at $6 r_G$, where $r_G = GM_{BH}/c^2$ is the gravitational radius. For a $10^9 M_\odot$ BH, this is equal to 8.85×10^{14} cm or $\sim 10^{-4}$ pc.

The X-ray source is treated as an isotropic sphere at the ISCO, which emits r -packets according to a power law in flux with index α_X , of the form

$$F_X(\nu) = K_X \nu^{\alpha_X}. \quad (5.1)$$

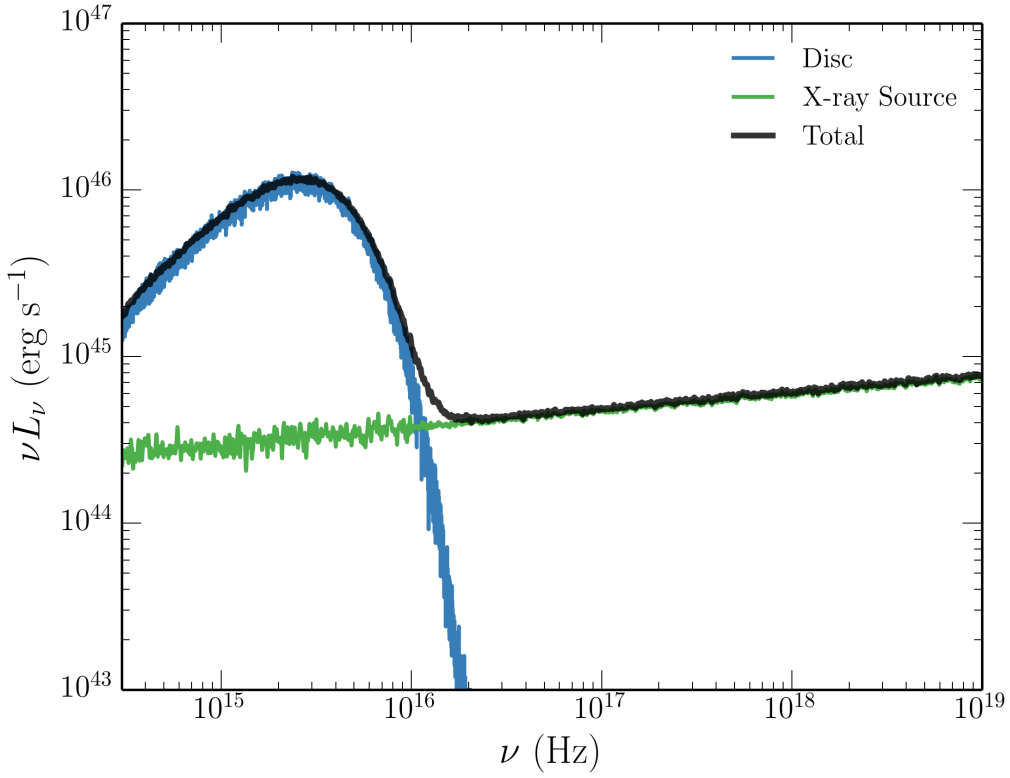


FIGURE 5.2: The input spectrum used for the quasar modelling. Note that although the X-ray power law is allowed to extend to very high frequencies, the radiation beyond $\sim 10^{-18}$ Hz is unimportant due to the rapid decline in the photoionization cross-sections at high energies. The results here are thus insensitive to the maximum frequency adopted for this power law component.

The normalisation, K_X of this power law is such that it produces the specified 2-10 keV luminosity, L_X . The input spectrum for the simulations is therefore a simple combination of a power law X-ray component and accretion disc spectrum; an example input spectrum is shown in Fig. 5.2. In actual fact, this spectrum will be angle dependent due to the geometry of the system and the angular emissivity profile of the accretion disc (see sections 5.3.3 and 5.4.2). Photons, or r -packets, produced by the accretion disc and central X-ray source are reprocessed by the wind. This reprocessing is dealt with by enforcing strict radiative equilibrium (*modulo* adiabatic cooling; see section 3.3.3) via the indivisible energy packet constraint.

5.2.2 A Simple Approximation for Clumping

In previous modelling efforts with PYTHON, a smooth outflow was assumed, such that the density at a given point was determined only by the kinematic parameters and mass loss rate. However, as already discussed, AGN winds exhibit significant substructure –

the outflow is expected to be *clumpy*, rather than smooth, and probably on a variety of scales. A clumpy outflow offers a possible solution to the so-called ‘over-ionization problem’ in quasar and AGN outflows (e.g. [Junkkarinen et al. 1983](#); [Weymann et al. 1985](#); [Hamann et al. 2013](#)). This is the main motivation for incorporating clumping into the model.

Deciding on how to implement clumping into the existing wind models was not straightforward. First, and most importantly, the physical scale lengths and density contrasts in AGN outflows are not well-constrained from observations or theory. As a result, while one could envision in principle, clouds with a variety of sizes and density contrasts varying perhaps as function of radius, there would have been very little guidance on how to set nominal values of the various parameters of such a model. Second, there are significant computational difficulties associated with adequately resolving and realistically modelling a series of small scale, high density regions with a MCRT – or for that matter, a hydrodynamical – code. Given the lack of knowledge about the actual type of clumping, I have implemented a simple approximation used successfully in stellar wind modelling, known as *microclumping* (e.g. [Hamann & Koesterke 1998](#); [Hillier & Miller 1999](#); [Hamann et al. 2008](#)).

The underlying assumption of microclumping is that clump sizes are much smaller than the typical photon mean free path, and thus the clumps are both geometrically and optically thin. This approach allows one to treat clumps only in terms of their volume filling factor, f_V , instead of having to specify separately their size and density distributions. In this model, f_V is independent of position. The inter-clump medium is modeled as a vacuum, although the outflow is still non-porous and axisymmetric. This approach therefore assumes that the inter-clump medium is unimportant in determining the output spectrum, which is expected to be true only when density constraints are large and the inter-clump medium is both very ionized and of low emissivity and opacity. The density of the clumps is multiplied by the “density enhancement” $D = 1/f_V$. Opacities, κ , and emissivities, j , can then be expressed as

$$\kappa = f_V \kappa_C(D); \quad j = f_V j_C(D). \quad (5.2)$$

Here the subscript C denotes that the quantity is calculated using the enhanced density in the clump. The resultant effect is that, *for fixed temperature*, processes that are linear in density, such as electron scattering, are unchanged, as f_V and D will cancel

out. However, any quantity that scales with the square of density, such as collisional excitation or recombination, will increase by a factor of D . In PYTHON, the temperature is not fixed, and is instead set by balancing heating and cooling in a given cell. In the presence of an X-ray source, this thermal balance is generally dominated by bound-free heating and line cooling. The main effect of including clumping in this modelling is that it moderates the ionization state due to the increased density. This allows an increase in the ionizing luminosity, amplifying the amount of bound-free heating and also increasing the competing line cooling term (thermal line emission).

The shortest length scale in a Sobolev MCRT treatment such as that used here is normally the Sobolev length, given by

$$l_S = \frac{v_{th}}{|dv/ds|} \quad (5.3)$$

This is typically $\sim 10^{13}$ cm near the disc plane, increasing outwards. The Sobolev length calculated from the mean velocity gradient in a cell is shown, together with the size of the cell and Thomson mean free path, in Fig. 5.3. The mean density is used to calculate the Sobolev optical depth, which assumes that l_S is greater than the typical clump size. Thus for the microclumping assumption to be formally correct, clumps should be no larger than $\sim 10^{12}$ cm. This size scale is not unreasonable for quasar outflows, as [de Kool & Begelman \(1995\)](#) suggest that BAL flows may have low filling factors with clump sizes of $\sim 10^{11}$ cm.

This clumping treatment is necessarily simple; it does not adequately represent the complex substructures and stratifications in ionization state expected in AGN outflows. Nevertheless, this parameterization allows simple estimates of the effect clumping has on the ionization state and emergent line emission.

5.2.3 The Simulation Grid

Using this prescription, I conducted a limited parameter search over a 5-dimensional parameter space involving the variables r_{\min} , θ_{\min} , f_V , α and R_v . The grid points are shown in table 5.1. The aim here was to first fix M_{BH} and \dot{M} to their H13 values, and increase L_X to 10^{45} erg s $^{-1}$ (a more realistic value for a quasar of $10^9 M_\odot$ and an Eddington fraction of 0.2; see section 5.3.3).

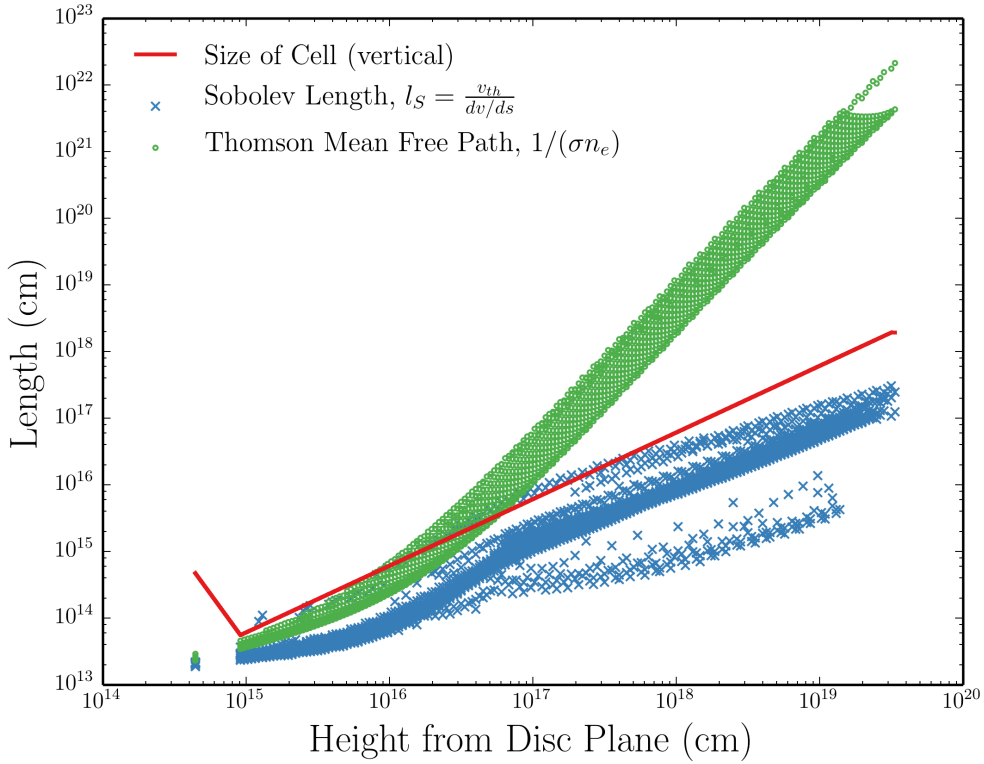


FIGURE 5.3: Some typical length scales for the fiducial model. This places a formal limit of $\sim 10^{12}$ cm on clump sizes in the microclumping framework, and confirms that the cells are sufficiently larger than the Sobolev length in almost all cases.

These models were then evaluated based on how closely their synthetic spectra reproduced the following properties of quasars and BALQSOs:

- UV absorption lines with $BI > 0$ at $\sim 20\%$ of viewing angles (e.g. Knigge et al. 2008);
- Line emission emerging at low inclinations, with $EW \sim 40$ Å in C iv 1550 Å (e.g. Shen et al. 2011);
- H recombination lines with $EW \sim 50$ Å in Ly α (e.g. Shen et al. 2011);
- Mg II and Al III (LoBAL) absorption features with $BI > 0$ at a subset of BAL viewing angles;
- X-ray luminosities consistent with those observed in BAL and non-BAL quasars.
- Verisimilitude with quasar composite spectra; specifically, synthetic spectra showing the expected line widths, continuum shape, and range of ionization states observed in quasars.

Parameter	Grid Point Values			
r_{\min}	$60r_g$	$180r_g$	$300r_g$	
θ_{\min}	55°	70°		
R_v	10^{18} cm	10^{19} cm		
α	0.5	0.6	0.75	1.5
f_V	0.01	0.1		

TABLE 5.1: The grid points used in the parameter search. The sensitivity to some of these parameters is discussed further in section 5.4.1

Here BI is the ‘Balmicity Index’ (Weymann et al. 1991), given by

$$BI = \int_{3000 \text{ km s}^{-1}}^{25000 \text{ km s}^{-1}} C \left(1 - \frac{f(v)}{0.9} \right) dv. \quad (5.4)$$

The constant $C = 0$ everywhere, unless the normalized flux has satisfied $f(v) < 0.9$ continuously for at least 2000 km s^1 , whereby C is set to 1.

In the next section, I present one of the most promising models, which I refer to as the fiducial model, and discuss the various successes and failures with respect to the above criteria. This allows insight into fundamental geometrical and physical constraints to be gained, and the potential for unification assessed. I then discuss the sensitivity to key parameters in section 5.4.1. The full grid, including output synthetic spectra and plots can be found at jhmatthews.github.io/quasar-wind-grid/.

5.3 Results and Analysis from a Fiducial Model

Here I describe the results from a fiducial model, and discuss these results in the context of the criteria presented in section 5.2.3. The parameters of this model are shown in table 5.2. Parameters differing from the benchmark model of H13 are highlighted with an asterisk. In this section, I examine the physical conditions of the flow, and present the synthetic spectra, before comparing the X-ray properties of this particular model to samples of quasars and luminous AGN.

5.3.1 Physical Conditions and Ionization State

Fig. 5.4 shows the physical properties of the wind. The wind rises slowly from the disc at first, with densities within clumps of $n_H \sim 10^{11} \text{ cm}^{-3}$ close to the disc plane, where n_H is the local number density of H. To illustrate the degree of scale and density ranges

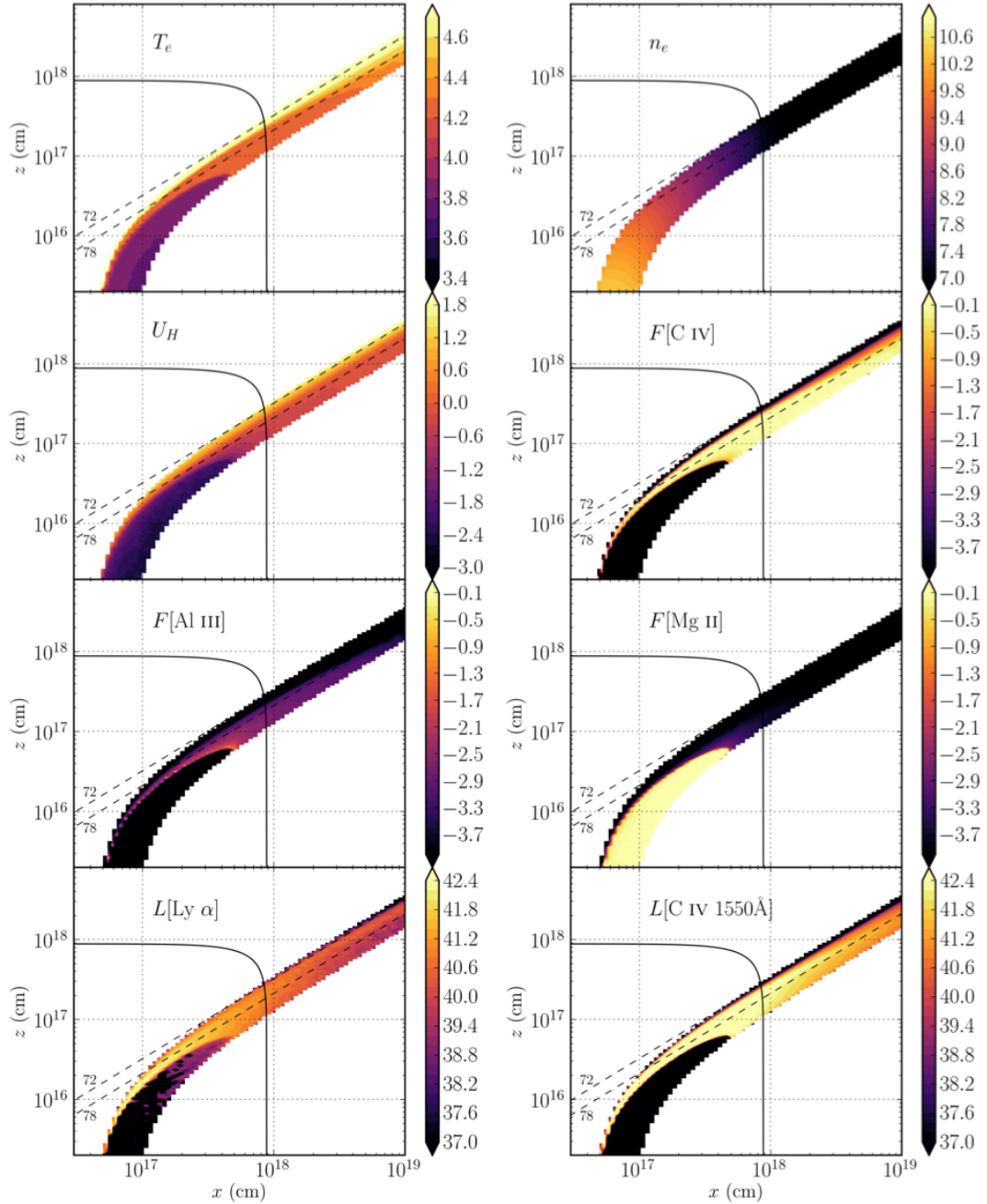


FIGURE 5.4: Contour plots showing the logarithm of some important physical properties of the outflow. The spatial scales are logarithmic and the x and z scales are not the same. The panels show the electron temperature, T_e , electron density, n_e , the ionization parameter, U_H , ion fractions, F , for three different ions and line luminosities, L , for two different lines. The line luminosities represent the luminosity of photons escaping the Sobolev region for each line. These photons do not necessarily escape to infinity. The solid black line marks a sphere at $1000 r_G$. The dotted lines show the 72° and 78° sightlines to the centre of the system, and illustrate that different sightlines intersect material of different ionization states.

Parameter	Value
M_{BH}	$1 \times 10^9 M_\odot$
\dot{M}_{acc}	$5 M_\odot \text{yr}^{-1} \simeq 0.2 \dot{M}_{\text{Edd}}$
α_X	-0.9
L_X	$10^{45} \text{ erg s}^{-1*}$
$r_{\text{disc}}(\text{min}) = r_X$	$6r_g = 8.8 \times 10^{14} \text{ cm}$
$r_{\text{disc}}(\text{max})$	$3400r_g = 5 \times 10^{17} \text{ cm}$
\dot{M}_W	$5 M_\odot \text{yr}^{-1}$
r_{min}	$300r_g = 4.4 \times 10^{16} \text{ cm}$
r_{max}	$600r_g = 8.8 \times 10^{16} \text{ cm}$
θ_{min}	70.0°
θ_{max}	82.0°
$v_\infty(r_0)$	$v_{\text{esc}}(r_0)$
R_v	10^{19} cm^*
α	0.5*
f_V	0.01*
n_x	100
n_z	200

TABLE 5.2: Wind geometry parameters used in the fiducial model, as defined in the text and Fig. 5.1. Parameters differing from the benchmark model of H13 are highlighted with an asterisk.

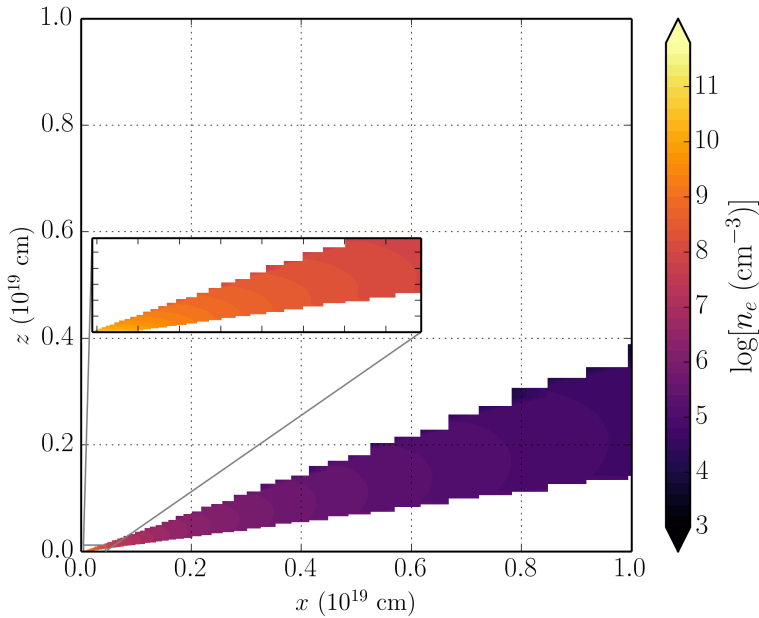


FIGURE 5.5: The electron density in the model, this time on linear axes in order to illustrate the density contrasts and scale of the system. The plot is on the scale of the acceleration length, whereas the inset is a box of $2700 \times 800r_G$, where the bottom left corner corresponds to the base of the innermost streamline.

in the model I also show n_e in the wind on a linear scale in Fig. 5.5. The flow then accelerates over a scale length of $R_V = 10^{19}$ cm up to a terminal velocity equal to the escape velocity at the streamline base ($\sim 10,000$ km s $^{-1}$). This gradual acceleration results in a wind that exhibits a stratified ionization structure, with low ionization material in the base of the wind giving way to highly ionized plasma further out. This is illustrated in Fig. 5.4 by the panels showing the ion fraction $F = n_j/n_{tot}$ of some important ions. The clumped wind produces the range of ionization states observed in quasars and BALQSOs, while adopting a realistic 2 – 10 keV X-ray luminosity of $L_X = 10^{45}$ erg s $^{-1}$. Without clumping, this wind would be over-ionized to the extent that opacities in e.g., C IV would be entirely negligible (see H13).

One common way to quantify the ionization state of a plasma is through the ionization parameter, U_H , given by equation 3.102. Shown in Fig. 5.4, the ionization parameter is a useful measure of the global ionization state, as it represents the ratio of the number density of H ionizing photons to the local H density. It is, however, a poor representation of the ionization state of species such as C IV as it encodes no information about the shape of the SED. In this case, the X-ray photons are dominant in the photoionization of the UV resonance line ions. This explains why a factor of 100 increase in X-ray luminosity requires a clumping factor of 0.01, even though the value of U_H decreases by only a factor of ~ 10 compared to H13.

The total line luminosity also increases dramatically compared to the unclumped model described by H13. This is because the denser outflow can absorb the increased X-ray luminosity without becoming over-ionized, leading to a hot plasma which produces strong collisionally excited line emission. This line emission typically emerges on the edge of the wind nearest the central source. The location of the line emitting regions is dependent on the ionization state, as well as the incident X-rays. The radii of these emitting regions is important, and can be compared to observations. The line luminosities, L , shown in the figure correspond to the luminosity in erg s $^{-1}$ of photons escaping the Sobolev region for each line. As shown in Fig. 5.4, the C IV 1550 Å line in the fiducial model is typically formed between 100 – 1000 r_G ($\sim 10^{17} – 10^{18}$ cm). This is in rough agreement with the reverberation mapping results of Kaspi et al. (2007) for the $2.6 \times 10^9 M_\odot$ quasar S5 0836+71, and also compares favourably with microlensing measurements of the size of the C IV 1550 Å emission line region in the BALQSO H1413+117 (O'Dowd et al. 2015).

5.3.2 Synthetic Spectra: Comparison to Observations

Fig. 5.6 shows the synthetic spectrum in the UV from the fiducial model. To assess the ability of the synthetic spectra to match real quasar spectra, I also show *Sloan Digital Sky Survey* (SDSS) quasar composites from [Reichard et al. \(2003\)](#), normalised to the flux at 2000 Å for low inclinations. Unfortunately, the wide variety of line profile shapes and internal trough structure in BALQSOs tends to ‘wash out’ BAL troughs in composite spectra to the extent that BALQSO composites do not resemble typical BALQSOs. Because of this, I instead compare to a *Hubble Space Telescope* STIS spectrum of the high BALnicity BALQSO PG0946+301 ([Arav et al. 2000](#)), and an SDSS spectrum of the LoBAL quasar SDSS J162901.63+453406.0, for the angles of 73° and 76°, respectively. A cartoon illustrating how geometric effects determine the output spectra is shown in Fig. 5.7.

5.3.2.1 Broad Absorption Lines (‘BALQSO-like’ angles)

The UV spectrum is characterised by strong BAL profiles at high inclinations ($> 70^\circ$). This highlights the first success of the model: clumping allows the correct ionization state to be maintained in the presence of strong X-rays, resulting in large resonance line opacities. At the highest inclinations, the cooler, low ionization material at the base of the wind starts to intersect the line of sight. This produces multiple absorption lines in species such as Mg II, Al III and Fe II. The potential links to LoBALQSOs and FeLoBALQSOs are discussed in section 5.3.4.

The high ionization BAL profiles are often saturated, and the location in velocity space of the strongest absorption in the profile varies with inclination. At the lowest inclination BAL sight lines, the strongest absorption occurs at the red edge, whereas at higher inclinations (and for the strongest BALs) the trough has a sharp edge at the terminal velocity. This offers one potential explanation for the wide range of BALQSO absorption line shapes (see e.g. [Trump et al. 2006](#); [Knigge et al. 2008](#); [Filiz Ak et al. 2014](#)).

The absorption profiles seen in BALQSOs are often non-black, but saturated, with flat bases to the absorption troughs ([Arav et al. 1999a,b](#)). This is usually explained either as partial covering of the continuum source or by scattered contributions to the BAL troughs, necessarily from an opacity source not co-spatial with the BAL forming region. The scattered light explanation is supported by spectropolarimetry results ([Lamy &](#)

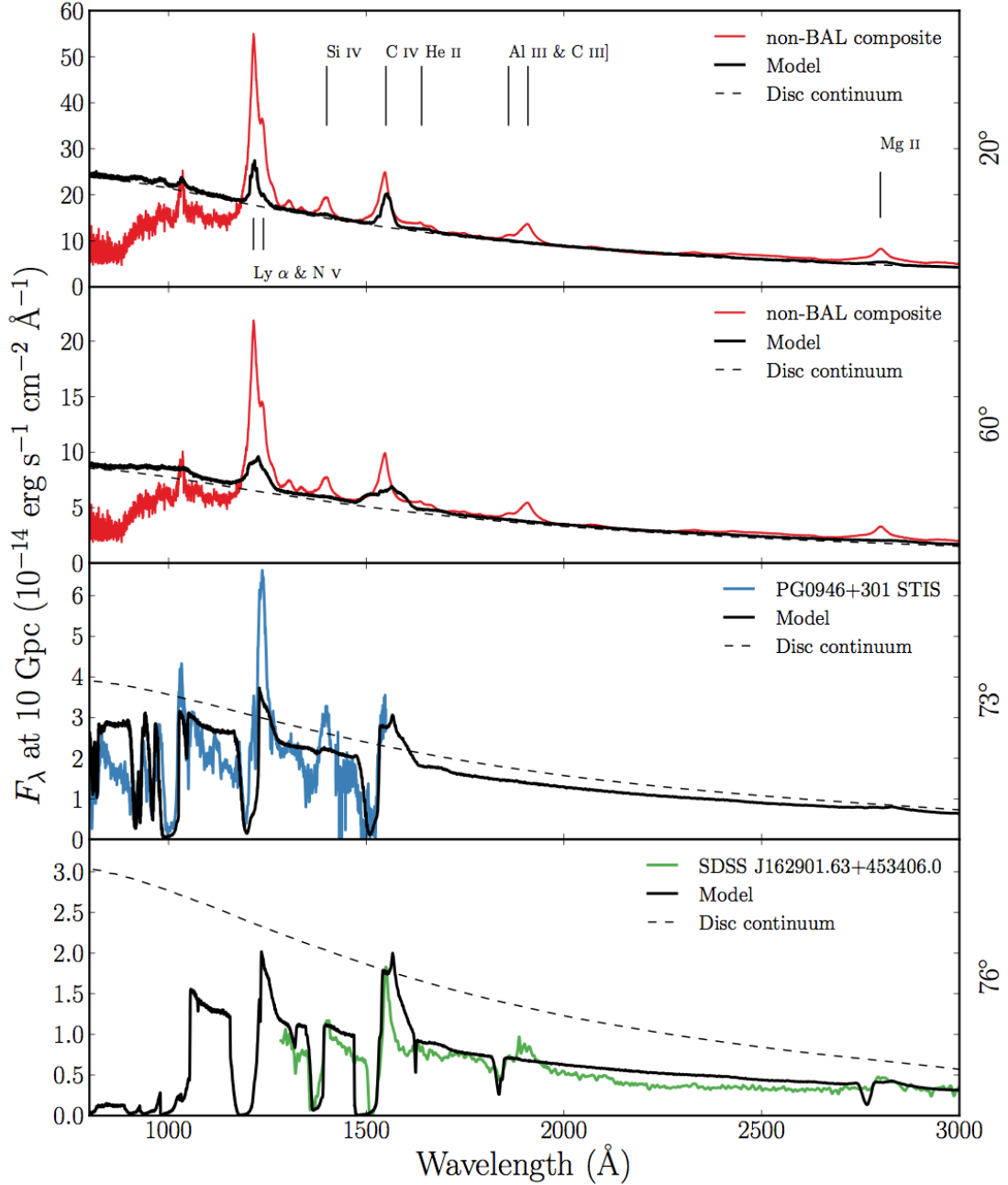


FIGURE 5.6: Synthetic spectra at four viewing angles for the fiducial model. At 20° and 60° I show a comparison to an SDSS quasar composite from Reichard et al. (2003). At 73° and 76° I show a comparison to an *HST* STIS spectrum of the high BALnicity BALQSO PG0946+301 (Arav et al. 2000), and an SDSS spectrum of the LoBAL quasar SDSS J162901.63+453406.0, respectively. The dotted line shows the effect of the outflow on the continuum level. All the spectra are scaled to the model flux at 2000 Å, except for the *HST* STIS spectrum of PG0946+301, which is scaled to 1350 Å due to the incomplete wavelength coverage.

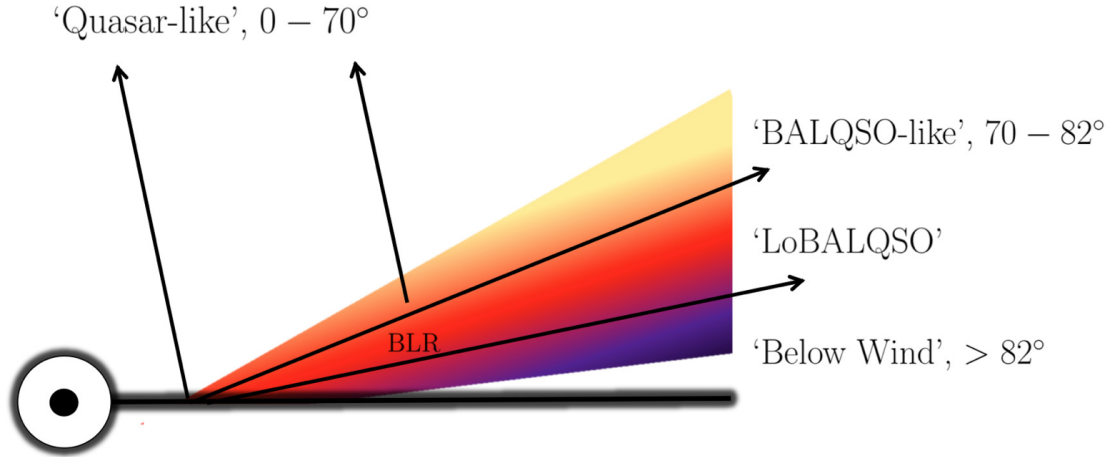


FIGURE 5.7: A cartoon describing the broad classes of sightline in the fiducial model, illustrating how geometric effects lead to the different emergent spectra. The colour gradient is approximate, but indicates the stratified ionization structure, from highly ionized (yellow) to low ionization (purple) material.

[Hutsemékers 2000](#)). The synthetic spectra do not show non-black, saturated profiles. Black, saturated troughs are seen at angles $i > 73^\circ$, and the BALs are non-saturated at lower inclinations. The reasons for this are inherent in the construction of the model. First, the microclumping assumption does not allow for porosity in the wind, meaning that it does not naturally produce a partial covering absorber. To allow this, an alternative approach such as *macroclumping* would be required (e.g. [Hamann et al. 2008](#); [Šurlan et al. 2012](#)). Second, the wind does not have a significant scattering contribution along sightlines which do not pass through the BAL region, meaning that any scattered component to the BAL troughs is absorbed by line opacity. This suggests that either the scattering cross-section of the wind must be increased (with higher mass loss rates or covering factors), or that an additional source of electron opacity is required, potentially in a polar direction above the disc. I note the scattering contribution from plasma in polar regions is significant in some ‘outflow-from-inflow’ simulations ([Kurosawa & Proga 2009](#); [Sim et al. 2012](#)).

5.3.2.2 Broad Emission Lines (‘quasar-like’ angles)

Unlike H13, significant collisionally excited line emission now emerges at low inclinations in the synthetic spectra, particular in the C IV and N V lines. Strong Ly α and weak

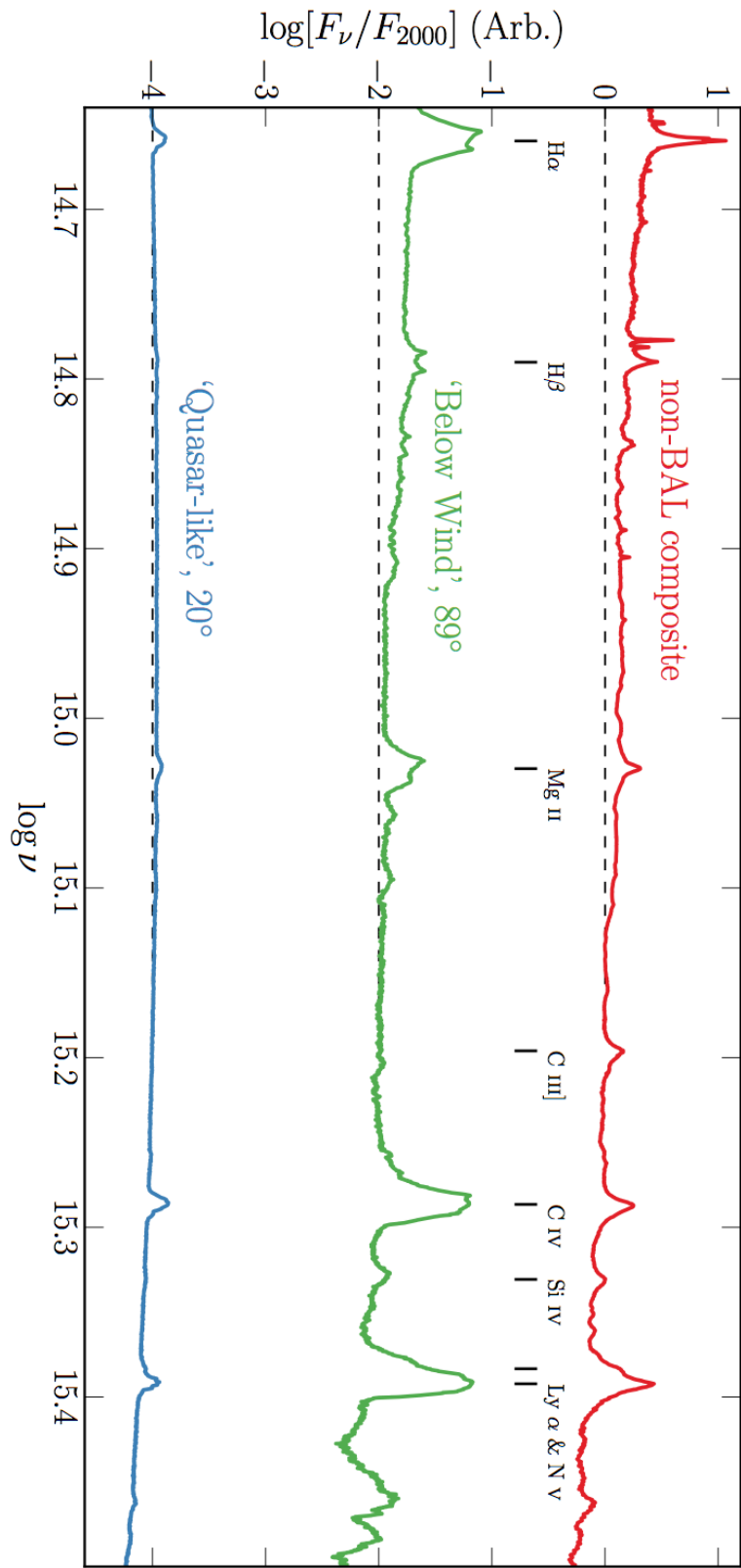


FIGURE 5.8: Synthetic spectra at two viewing angles, this time in frequency space and including the optical band, compared to the non-BAL SDSS quasar composite. The spectra are normalised to the flux at 2000 Å, then an offset of 2 is applied per spectrum for clarity – the dotted lines show the zero point of F_ν/F_{2000} in each case.

Property	Synthetic, 20°	Observed (S11)
$\log L[\text{C IV}]$	44.60	44.42 ± 0.32
$\log L[\text{Mg II}]$	43.92	43.54 ± 0.28
$\log(\nu L_\nu)_{1350}$	46.42	46.01 ± 0.30
$\log(\nu L_\nu)_{3000}$	46.18	45.79 ± 0.30

TABLE 5.3: Some derived spectral properties of the fiducial model, at 20°, compared to observations. The observed values are taken from the Shen et al. (2011) SDSS DR7 Quasar catalog, and correspond to mean values with standard deviations in log space from a subsample with $8.5 > \log(M_{BH}) < 9.5$ and $-1.5 < \log(L_{\text{bol}}/L_{\text{Edd}}) < 0$, where the BH mass is a C IV virial estimate. Units are logarithms of values in erg s⁻¹.

He II 1640 Å lines are also observed as a result of the improved treatment of recombination using macro-atoms. In the context of unification, this is a promising result, and shows that a biconical wind can produce significant emission at ‘quasar-like’ angles. To demonstrate this further, I show line luminosities and monochromatic continuum luminosities from the synthetic spectra in table 5.3. These are compared to mean values from a subsample of the SDSS DR7 quasar catalog (Shen et al. 2011) with BH mass and Eddington fraction estimates similar to the fiducial model values (see caption). The spectra do not contain the strong C III] 1909 Å line seen in the quasar composite spectra, but this is due to a limitation of the current treatment of C; semi-forbidden (intercombination) lines are not included in this modelling.

In Fig. 5.8, I show an F_ν spectrum with broader waveband coverage that includes the optical, showing that the synthetic spectra also exhibit H α and H β emission. In this panel, I include a low inclination and also a very high inclination spectrum, which looks underneath the wind cone. This model shows strong line emission with very similar widths and line ratios to the quasar composites, and the Balmer lines are double peaked, due to velocity projection effects. Such double-peaked lines are seen in so-called ‘disc emitter’ systems (e.g. Eracleous & Halpern 1994) but not the majority of AGN. The line equivalent widths (EWs) increase at high inclination due to a weakened continuum from wind attenuation, disc foreshortening and limb darkening. This effect also leads to a redder continuum slope, as seen in quasars, which is due to Balmer continuum and Balmer and Fe II line emission. This extreme 89° viewing angle cannot represent a typical quasar within a unified model, but does show that a model such as this can naturally reproduce quasar emission lines if the emissivity of the wind is increased *with respect to the disc continuum*. In addition, it neatly demonstrates how a stratified outflow can naturally reproduce the range of ionization states seen in quasars.

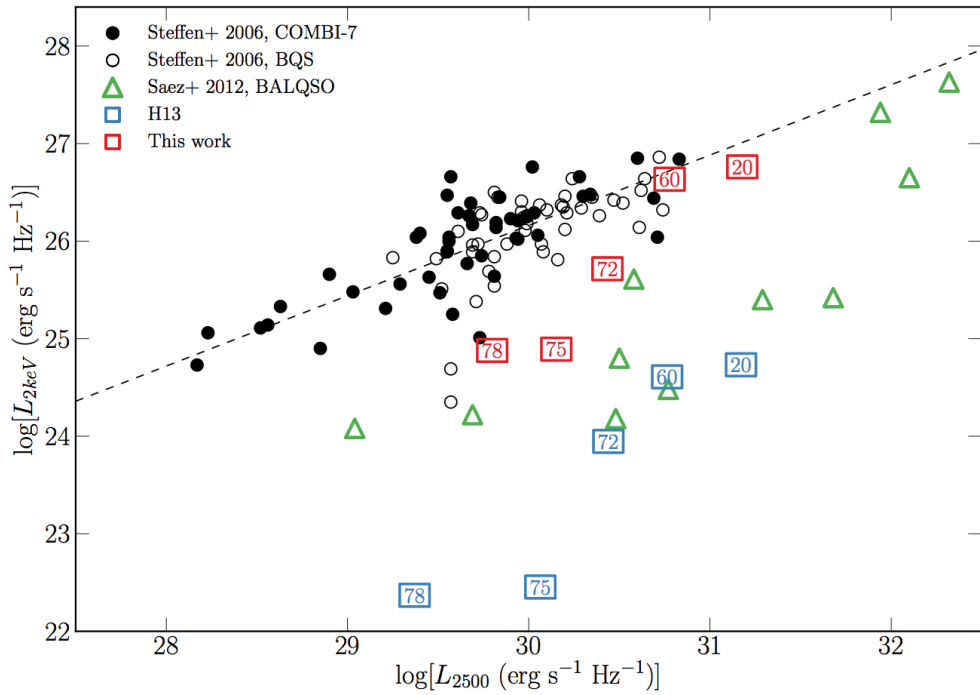


FIGURE 5.9: X-ray (2 keV) luminosity of the clumped model (red squares) and the H13 model (blue squares), plotted against monochromatic luminosity at 2500 Å. The points are labeled according to inclination; angles $> 70^\circ$ correspond to BALs in this scheme (see Fig. 5.7). Also plotted are measurements from the COMBI-7 AGN and the BQS samples (Steffen et al. 2006) and the Saez et al. (2012) sample of BALQSOs. The dotted line shows the best fit relation for non-BALQSOs from Steffen et al. (2006).

Despite a number of successes, there are some properties of the synthetic spectra that are at odds with the observations. First, the ratios of the EW of the Ly α and Mg II 2800 Å lines to the EW of C IV 1550 Å are much lower than in the composite spectra. Similar problems have also been seen in simpler photoionization models for the BLR (Netzer 1990). It may be that a larger region of very dense ($n_e \sim 10^{10} \text{ cm}^{-3}$) material is needed, which could correspond to a disc atmosphere or ‘transition region’ (see e.g. Murray et al. 1995; Knigge et al. 1998a). While modest changes to geometry may permit this, the initial grid search did not find a parameter space in which the Ly α or Mg II EWs were significantly higher (see section 5.4.1). Second, EWs increase with inclination (see Fig. 5.6 and Fig. 5.8; also Fig. 5.10). This is discussed further in section 5.4.2.

5.3.3 X-ray Properties

The main motivation for adding clumping to the model was to avoid over-ionization of the wind in the presence of strong X-rays. Having verified that strong BALs appear in

the synthetic spectra, it is also important to assess whether the X-ray properties of this fiducial model agree well with quasar and BALQSO samples for the relevant inclinations.

Fig. 5.9 shows the emergent monochromatic luminosity (L_ν) at 2 keV and plotted against L_ν at 2500 Å for a number of different viewing angles in the model. The monochromatic luminosities are calculated from the synthetic spectra and thus include the effects of wind reprocessing and attenuation. In addition to model outputs, I also show the BALQSO sample of Saez et al. (2012) and luminous AGN and quasar samples from Steffen et al. (2006). The best fit relation from Steffen et al. (2006) is also shown. For low inclination, ‘quasar-like’ viewing angles, the model properties are in excellent agreement with AGN samples. The slight gradient from 20° to 60° in the models is caused by a combination of disc foreshortening and limb-darkening (resulting in a lower L_{2500} for higher inclinations), and the fact that the disk is opaque, and thus the X-ray source subtends a smaller solid angle at high inclinations (resulting in a lower L_{2keV} for higher inclinations).

The high inclination, ‘BALQSO-like’ viewing angles show moderate agreement with the data, and are X-ray weak due to bound-free absorption and electron scattering in the wind. Typically, BALQSOs show strong X-ray absorption with columns of $N_H \sim 10^{23} \text{ cm}^{-2}$ (Green & Mathur 1996; Mathur et al. 2000; Green et al. 2001; Grupe et al. 2003b). This is often cited as evidence that the BAL outflow is shielded from the X-ray source, especially as sources with strong X-ray absorption tend to exhibit deep BAL troughs and high outflow velocities (Brandt et al. 2000; Laor & Brandt 2002; Gallagher et al. 2006). These results imply that the clumpy BAL outflow itself can be responsible for the strong X-ray absorption, and supports the suggestion of Hamann et al. (2013) that geometric effects explain the weaker X-ray absorption in mini-BALs compared to BALQSOs.

5.3.4 LoBALs and Ionization Stratification

At high inclinations, the synthetic spectra exhibit blue-shifted BALs in Al III and Mg II – the absorption lines seen in LoBALQSOs – and even show absorption in Fe II at the highest inclinations. Line profiles in velocity space for C IV, Al III and Mg II, are shown in Fig. 5.10 for a range of BALQSO viewing angles. Ionization stratification of the wind causes lower ionization material to have a smaller covering factor, as demonstrated by

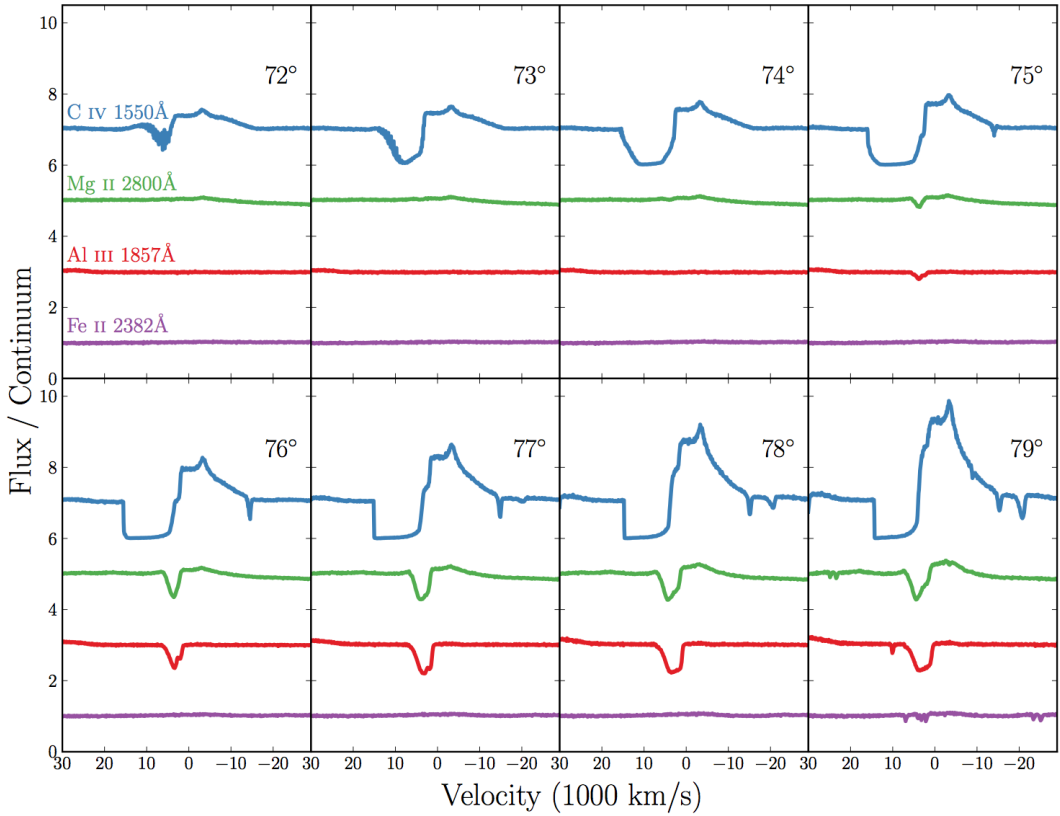


FIGURE 5.10: C IV, Mg II, Al III and Fe II line profiles for viewing angles from 72° – 79° . The profiles are plotted relative to the local continuum with an offset applied for clarity. Lower ionization profiles appear at a subset of high inclinations, compared to the ubiquitous C IV profile.

figures 5.4 and 5.10. This confirms the behaviour expected from a unification model such as Elvis (2000). LoBALs are only present at viewing angles close to edge-on ($i > 75^{\circ}$), as predicted by polarisation results (Brotherton et al. 1997). As observed in a BALQSO sample by Filiz Ak et al. (2014), the model BAL troughs are wider and deeper when low ionization absorption features are present, and high ionization lines have higher blue-edge velocities than the low ionization species. There is also a correlation between the strength of LoBAL features and the amount of continuum attenuation at that sightline, particularly blueward of the Lyman edge as the low ionization base intersects the line-of-sight. A model such as this therefore predicts that LoBALQSOs and FeLoBALQSOs have stronger Lyman edge absorption and are more Compton-thick than HiBALQSOs and Type 1 quasars. An edge-on scenario also offers a potential explanation for the rarity of LoBAL and FeLoBAL quasars, due to a foreshortened and attenuated continuum, although BAL fraction inferences are fraught with complex selection effects (Goodrich 1997; Krolik & Voit 1998).

5.4 Discussion

5.4.1 Parameter Sensitivity

Having selected an individual fiducial model from the simulation grid, it is important to briefly explore how specialised this model is, and how small parameter changes can affect the synthetic spectra. Fig. 5.11 shows the EW of Ly α , C IV 1550 Å and Mg II 2800 Å for a representative low inclination, and the BI for a representative high inclination, as produced by the models in the simulation grid. A few conclusions can be drawn from this plot straight away. First, almost all the models with $f_V = 0.1$ are over-ionized and fail to produce strong C IV BALs or emission lines. Second, it is difficult to significantly increase line emission while keeping the luminosity and mass-loss rate of the system fixed. I show an additional point on Fig. 5.11 corresponding to a model with an order of magnitude higher X-ray luminosity and double the mass loss rate. As expected, this results in far higher line EWs, but fails to produce BALs, because the collisionally excited emission swamps the BAL profile. In addition, this model would lie well above the expected $L_{2kev} - L_{2500}$ relation in Fig. 5.9. Such a high X-ray luminosity could therefore not be the cause of the strong line emission seen in *all* Type 1 quasars.

The parameter search presented here is by no means exhaustive, and conclusions may be limited by the specific parameterisation of the outflow kinematics used. For example, varying the mass-loss rate across the disc (see equation 2.14) may allow a denser emission region to exist closer to the continuum source. This could cause stronger emission lines to emerge at low inclination, as that region of the flow would be strongly irradiated but potentially dense enough to avoid over-ionization, possibly producing emission from lines such as C IV and Ly α . Nevertheless, I suggest that the angular distribution of both the line and continuum emission is perhaps the crucial aspect to understand. With this in mind, obtaining reliable orientation indicators appears to be an important observational task if we are to further our understanding of BAL outflows and their connection, or lack thereof, to the broad line region.

5.4.2 Inclination Trends: FWHM and EW

Broad line EWs increase with inclination in the fiducial model. This trend means that even though models with significantly denser and more strongly irradiated winds can

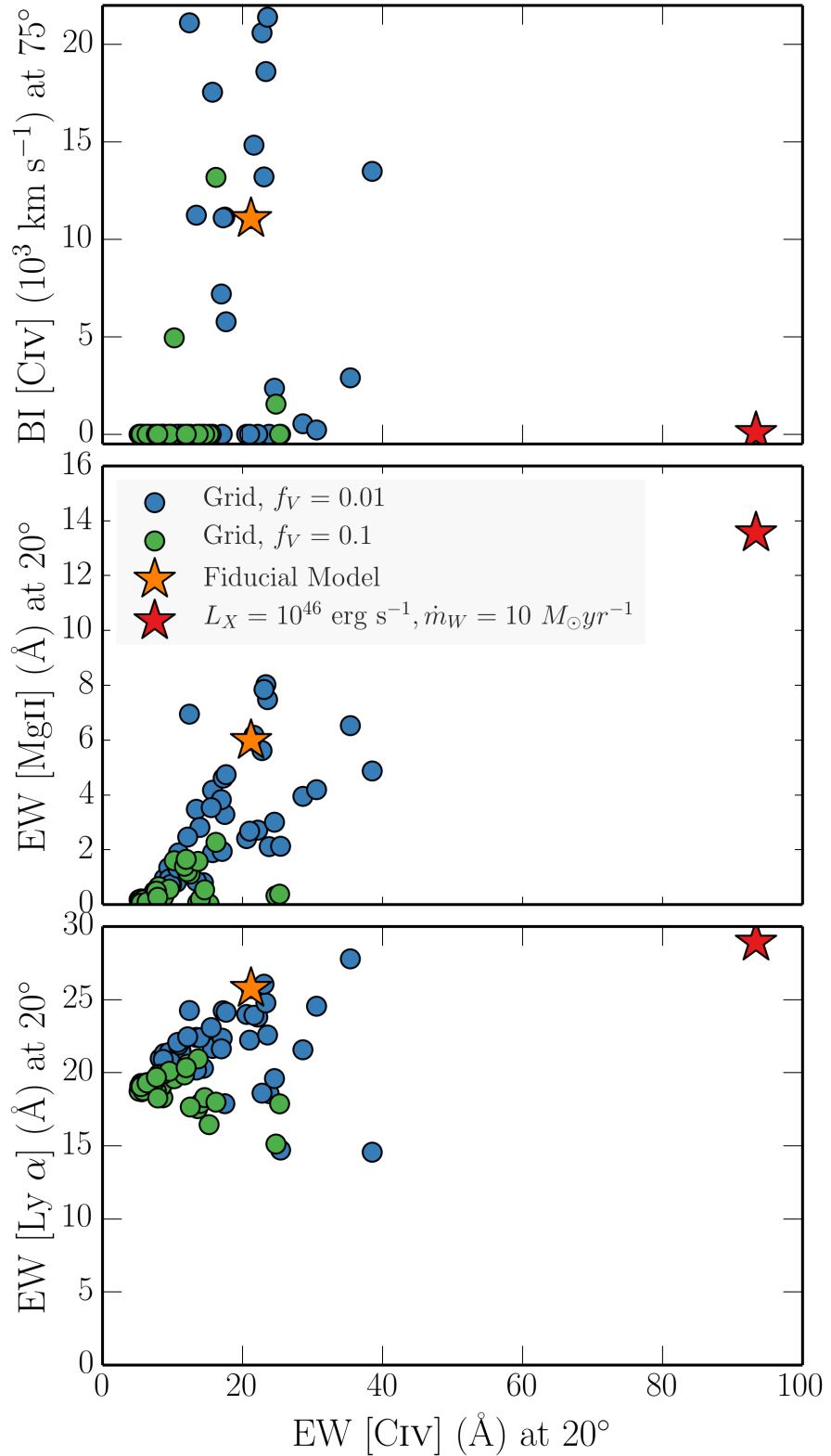


FIGURE 5.11: The EW of the C IV 1550 Å line at 20° plotted against a) the BI of C IV 1550 Å at 75°, b) the EW of the Mg II 2800 Å line at 20° and c) the EW of Ly α at 20°. The circles correspond to the simulation grid for two different values of f_V , and the fiducial model is marked with an orange star. I also show a higher X-ray luminosity model and a higher mass loss rate with a red star.

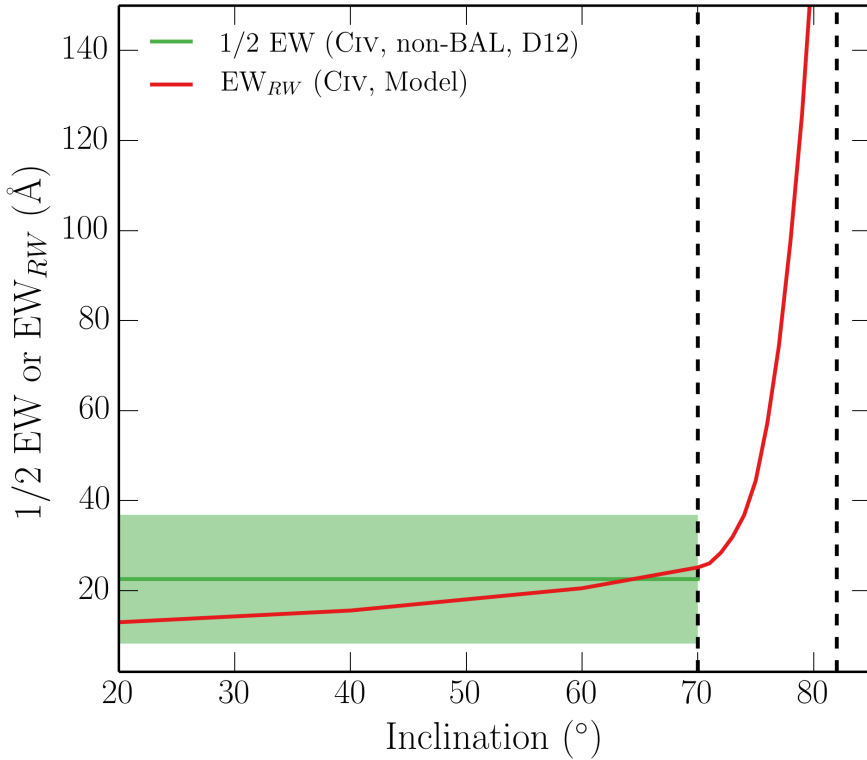


FIGURE 5.12: EW_{RW} as a function of inclination in the fiducial model, compared to $1/2 \text{ EW}$ from the quasar sample of Di Pompeo et al. (2012; D12). The shaded region corresponds to the standard deviation of the D12 sample.

match the line EWs fairly well at low inclinations, they also produce overly strong red wings to the BAL P-Cygni profiles at high inclinations. This trend with inclination is directly related to limb-darkening and foreshortening of the model continuum. However, it appears to contradict observations, which show remarkably uniform emission line properties in quasars and BALQSOs (Weymann et al. 1991; DiPompeo et al. 2012a).

In order to quantitatively assess how emission lines change with inclination when blue-shifted absorption may affect the line profile, I define the ‘red wing equivalent width’ (EW_{RW}) as

$$\text{EW}_{RW} = \int_{\lambda_0}^{\lambda'} \left(1 - \frac{F_\lambda}{F_0} \right) d\lambda, \quad (5.5)$$

where F_0 is the continuum flux, and the integral is calculated from λ_0 , line centre, to a wavelength λ' where the flux has returned to the continuum level. This quantity is shown as a function of inclination in Fig. 5.12 for the C IV UV line. I also show $1/2$ the EW value, together with the standard deviation, from DiPompeo et al. (2012a).

The variation of EW with inclination is significantly larger than the variation across the quasar population. The angular distribution of the disc continuum and line emission is

clearly crucially important in determining the emergent broad line EWs, as suggested by, e.g., the analysis of [Risaliti et al. \(2011\)](#). I shall explore this question further in chapter 6.

5.4.2.1 FWHM and Black Hole Mass Estimates

In a recent study, ([Yong et al. 2016](#), hereafter Y16) used the SV93 wind prescription to assess the variation of full-width at half-maximum (FWHM) of H β (and resultant BH mass estimates) with inclination in a disc wind model. Although their model is fairly simple – it does not include, for example, full radiative transfer or ionization physics – this analysis still gives interesting insights into how emission lines from a disc wind might bias BH mass estimates.

If the BLR gas is virialised, as often assumed, then the black hole mass is related to the velocity dispersion, Δv , of the gas by

$$M_{BH} = f \frac{\Delta v^2 R_{BLR}}{G}, \quad (5.6)$$

where R_{BLR} is some appropriate emissivity-weighted radius and is often either assumed, estimated from ionization arguments or calculated from reverberation mapping. When using the FWHM of a broad emission line to estimate the velocity dispersion the above equation can be rewritten as

$$M_{BH} = f_{FWHM} \left[c \frac{(FWHM)}{\lambda_0} \right]^2 \frac{R_{BLR}}{G}, \quad (5.7)$$

where λ_0 is the central wavelength of the line in question and the FWHM is in the same wavelength units.

In our benchmark disc wind model, the BH mass is known, and determines the escape velocities and rotational motions of the outflow. Thus, using a typical radius for line formation in the model, it is trivial to estimate f_{FWHM} for each viewing angle. Fig. 5.13 shows f_{FWHM} as a function of inclination for the H α emission line in the fiducial model, assuming $R_{BLR} = 10^{17}$ cm. The results are compared to predicted values for five Seyfert I galaxies from dynamical modelling ([Pancoast et al. 2014b](#), hereafter P14), and the Y16 predictions. Y16 designed two models in order to mimic those proposed by MCGV95 and [Elvis \(2000\)](#), whose models are described in section 2.3. Note that I have used

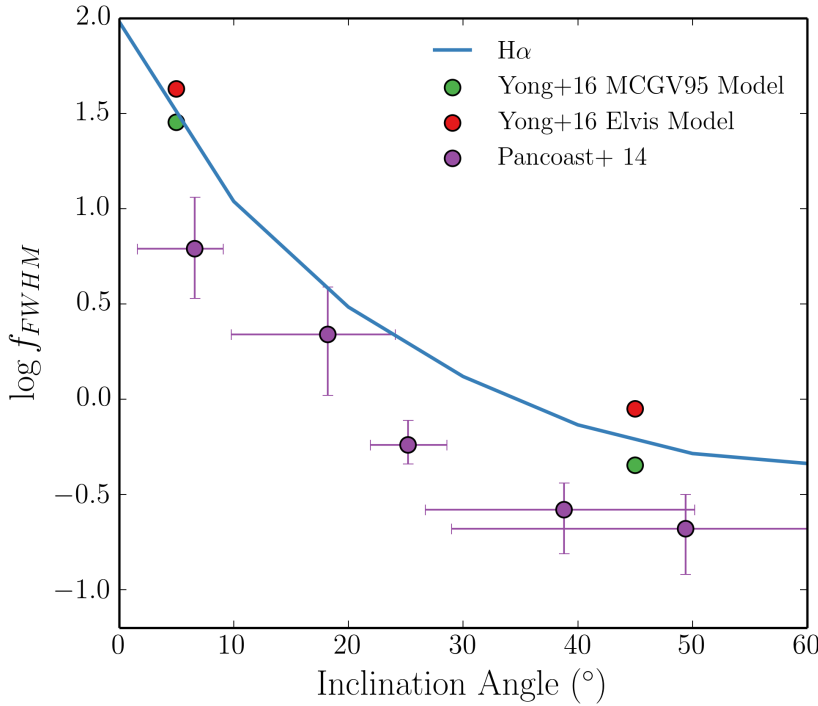


FIGURE 5.13: f_{FWHM} as a function of inclination from the fiducial model for three different lines. The Yong et al. (2016) predictions from two models, and the Pancoast et al. (2014) modelling results for five Seyfert I galaxies are also shown. At inclination angles $\gtrsim 70^\circ$ radiative transfer effects can become important as the sightline looks into the flow; here I show only moderate to low inclination angles where the system would be observed as a non-BAL quasar.

FWHM of $H\alpha$ rather than $H\beta$ due to the low $H\beta$ luminosity at some viewing angles. Nevertheless, this value should trace f_{FWHM} from $H\beta$ fairly well.

At ‘quasar-like’ angles ($0^\circ – 60^\circ$), the values from the model presented here agree fairly well with the predictions of Y16 from their simpler analysis, suggesting that, at least in this specific set-up, radiative transfer and ionization has a minimal role in determining the emergent FWHM at those angles. Instead, at low inclinations the effect is dominated by velocity projection effects. At inclinations looking into the wind radiative transfer and shielding effects become important, and the FWHM can actually decrease. The similarity in the shape of the curve to the P14 results suggest that the behaviour of FWHM is somewhat degenerate with the BLR geometry. P14 found a thick disc model for the BLR best reproduced the observations, but these results suggest that a wind model can mimic the behaviour of a disc-shaped BLR. Overall, the strong inclination dependence of f_{FWHM} strengthens the argument that viewing angle can introduce significant uncertainty into virial mass estimates, and that individual values for f_{FWHM}

should really be used for different objects (e.g. Decarli et al. 2008; Kollatschny & Zetzl 2011; Pancoast et al. 2014a,b; Shen & Ho 2014; Brotherton et al. 2015; Yong et al. 2016).

5.5 Summary And Conclusions

I have carried out MCRT simulations using a simple prescription for a biconical disc wind, with the aim of expanding on the work of H13. To do this, two main improvements were necessary: First, I included a simple treatment of clumping, and second, the modelling of recombination lines was improved by treating H and He as ‘macro-atoms’. Having selected a fiducial model from an initial simulation grid, I assessed the viability of such a model for geometric unification of quasars, and found the following main points:

1. Clumping moderates the ionization state sufficiently to allow for the formation of strong UV BALs while agreeing well with the X-ray properties of luminous AGN and quasars.
2. A clumpy outflow model naturally reproduces the range of ionization states expected in quasars, due to its stratified density and temperature structure. LoBAL line profiles are seen at a subset of viewing angles, and Fe II absorption is seen at particularly high inclinations.
3. The synthetic spectra show a strong Ly α line and weak He II 1640 Å emission line, as a result of the improved treatment of recombination using macro-atoms. Balmer emission lines and a Balmer recombination continuum are also seen in the optical spectrum, but this is only really significant at high inclination where the continuum is suppressed.
4. The higher X-ray luminosity causes a significant increase in the strength of the collisionally excited emission lines produced by the model. However, the equivalent-width ratios of the emission lines do not match observations, suggesting that a greater volume of dense ($n_e \sim 10^{10} \text{ cm}^{-3}$) material may be required.
5. The line EWs in the synthetic spectra increase with inclination. BAL and non-BAL quasar composites have comparable EWs, so the fiducial model fails to reproduce this behaviour. If the BLR emits fairly isotropically then for a foreshortened, limb-darkened accretion disc it is not possible to achieve line ratios at low inclinations

that are comparable to those at high inclinations. I suggest that understanding the angular distribution of line and continuum emission is a crucial question for theoretical models.

6. There is also a strong dependence on inclination in the FWHM of H α , as found in numerous other studies. The results add to the growing evidence that inclination introduces large uncertainties into virial BH mass estimates, and suggest that disc wind models might produce similar inclination-dependent behaviour in f_{FWHM} to disc-shaped BLR models.

This work confirms a number of expected outcomes from a geometric unification model, and suggests that a simple biconical geometry such as this can come close to explaining much of the phenomenology of quasars. However, these conclusions pose some challenges to a picture in which BALQSOs are explained by an *equatorial* wind rising from a classical thin disc, and suggest the angular distribution of emission is important to understand if this geometry is to be refuted or confirmed. I suggest that obtaining reliable observational orientation indicators and exploring a wider parameter space of outflow geometries in simulations are obvious avenues for future work.

Chapter 6

Quasar Emission Lines as Probes of Orientation and Unification

This chapter is based on a paper in preparation:

Matthews J. H., Knigge C., ‘Quasar Emission Lines as Probes of Orientation and Unification’, to be submitted to MNRAS.

6.1 Introduction

In the previous chapter, I presented tests of geometric unification models using MCRT and photoionization simulations. One of the key results from that analysis is that trends with inclination prohibit models with equatorial outflows matching observations, as the EWs of the broad emission lines tend to increase with inclination in the models. This suggests a fundamental issue with the simplest geometric unification models. There must be a problem with either the prescription for the continuum emission or the equatorial outflow geometry; otherwise, geometric disc wind unification models of BAL and non-BAL quasars simply cannot reproduce the observed spectra.

One way of constraining the outflow geometry is by understanding the orientations of BALQSOs, or, equivalently, the opening angles of their winds. The covering factor and opening angle of the outflow are also important quantities for estimating the feedback efficiency (e.g. [Borguet et al. 2012](#)), measuring the BAL fraction (e.g. [Krolik & Voit 1998](#)) and understanding the outflow physics (e.g. [Proga 2005](#)). The motivation to measure

orientations is not limited to disc wind models; the AM85 and UP95 unification schemes described in section 1.3.1 both attempt to explain the diverse behaviour of AGN merely as a function of viewing angle. Orientation indicators therefore also allow us to explore if these models adequately explain the type 1/type 2 dichotomy in AGN.

Unlike in galactic accretion disc systems, measuring inclinations for quasars and AGN is notoriously difficult (see e.g. Marin 2016). Obtaining reliable orientation indicators is thus an important observational goal for the community (see e.g. Marin 2016). Perhaps as a result of this problem, directly opposing geometries have been proposed for BAL outflows (see section 2.1.3.1). Attempts to constrain the inclinations of BALQSOs have been made previously with different diagnostics; for example, by considering radio measurements (Zhou et al. 2006; DiPompeo et al. 2012b) or polarisation (Brotherton et al. 2006).

Of course, if they depend on inclination, emission lines may themselves provide information about viewing angle. This is especially true if the line is roughly isotropic, as the continuum is expected to be strongly anisotropic if it is emitted from a geometrically thin, optically thick accretion disc. It follows that, if we can estimate the angular distribution of line and continuum emission, the EW of an emission line can act as an orientation indicator. Conversely, if the orientations of quasars can be measured via an independent method, then the emission line EW distribution can be used to test models for the origin of the UV and optical continuum. The variation of EW with inclination is demonstrated neatly by the behaviour of emission lines in high-state CVs, where inclinations are fairly well constrained. High-state CVs show a clear trend of increasing line EW with inclination (Hessman et al. 1984; Patterson 1984; Echevarria 1988; Noebauer et al. 2010, see also sections 1.2.2.2 and 4.2.2), a trend that is attributed to foreshortening and limb darkening of the disc continuum.

The ideal emission line to use for this method would be one that is completely isotropic, i.e. *optically thin*. The [O III] 5007 Å narrow emission line fulfils this criteria – at least in terms of its atomic physics – since it is a strong, forbidden line formed in the narrow-line region (NLR) of AGN. However, the ratio of [O III] 5007 Å to the infra-red [OIV] 28.59 μm line has been shown to vary between type 1 and type 2 AGN (Kraemer et al. 2011), potentially implying a degree of anisotropy. This is discussed further in section ???. If the line is isotropic, then any dispersion in the distribution of [O III] 5007 Å EW (EW[O III]) must therefore be driven by some combination of the intrinsic luminosity (Boroson &

(Green 1992), the covering factor/geometry of the NLR (Baskin & Laor 2005) and the inclination of the disc. In a recent study, Risaliti et al. (2011) showed that the EW[O III] distribution could be well-fitted by a simple model driven purely by disc inclination. In this chapter, I apply a similar method in order to provide a fundamental test of BAL and non-BAL quasar unification models in which the continuum source is a geometrically thin, optically thick accretion disc. This is motivated by the remarkably similar emission line properties of BAL and non-BAL quasars – a similarity that would not be expected from the simplest models in which BALQSOs are viewed from equatorial angles.

This chapter is structured as follows. First, I describe the data sample and selection criteria being used. I begin by simply examining the distributions of the EW of the [O III] 5007 Å emission line, EW[O III], and comparing the BAL and non-BAL quasar distributions. In section 6.3, I review the angular distribution of continuum emission one would expect from simple α -disc models, as well as exploring more advanced disc models computed with AGNSPEC. I then use these theoretical angular distributions applied to a simple toy model in section 6.4, and conduct MC simulations in an attempt to fit the observed LoBAL and non-BAL quasar distributions of EW[O III], using a similar approach to Risaliti et al. (2011). In section 6.5, I discuss the results in the context of radio and polarisation measurements of AGN, and explore the location of BAL quasars in ‘Eigenvector 1’ parameter space. I also consider the broad emission line distribution in HiBAL quasars in more detail. Finally, in section 6.6, I summarise the results.

6.2 Data Sample

The data sample used in this chapter is based on the Shen et al. (2011, hereafter S11) catalog of 105,783 quasars from the The Sloan Digital Sky Survey (SDSS) Data Release 7 (DR7). As I will use emission line diagnostics in this study, this sample must be further divided according to which emission lines are present in the SDSS wavelength range at a given redshift. Sample A contains all quasars within the redshift range $0.35 < z < 0.83$, such that the Mg II 2800 Å and [O III] 5007 Å line EWs are both measured, and Mg II LoBAL identification is possible. Sample B contains all quasars within the redshift range $1.45 < z < 2.28$, such that the EWs and presence of BAL in Mg II 2800 Å and C IV 1550 Å are both measurable. The BH mass estimates and Eddington fractions from S11 of the two sample are shown in Fig. 6.1, together with the same quantities for the

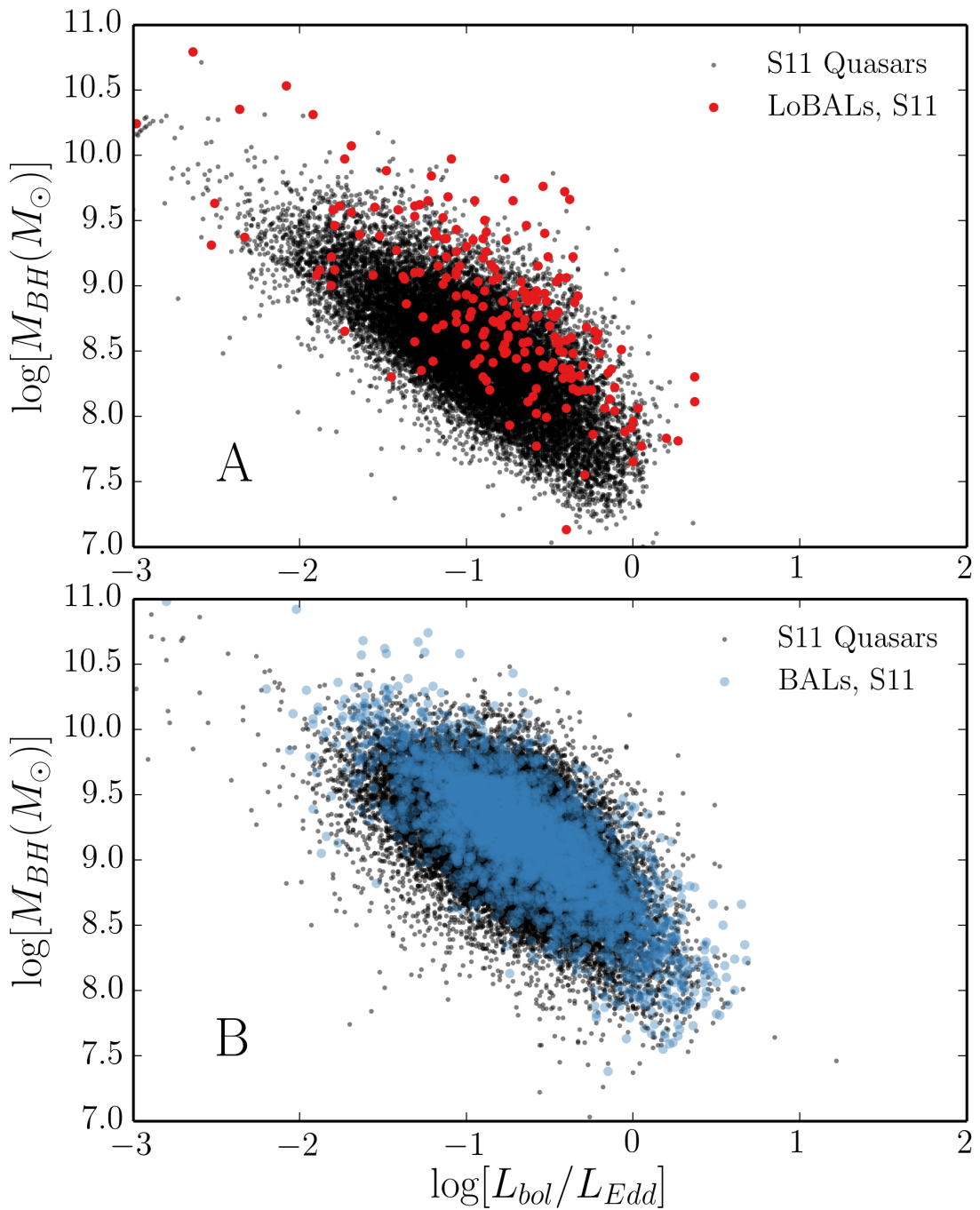


FIGURE 6.1: BH mass and Eddington fraction measurements from S11 for Sample A (top) and Sample B (bottom). The LoBALQSOs in sample A and BALQSOs in Sample B are also plotted in each case.

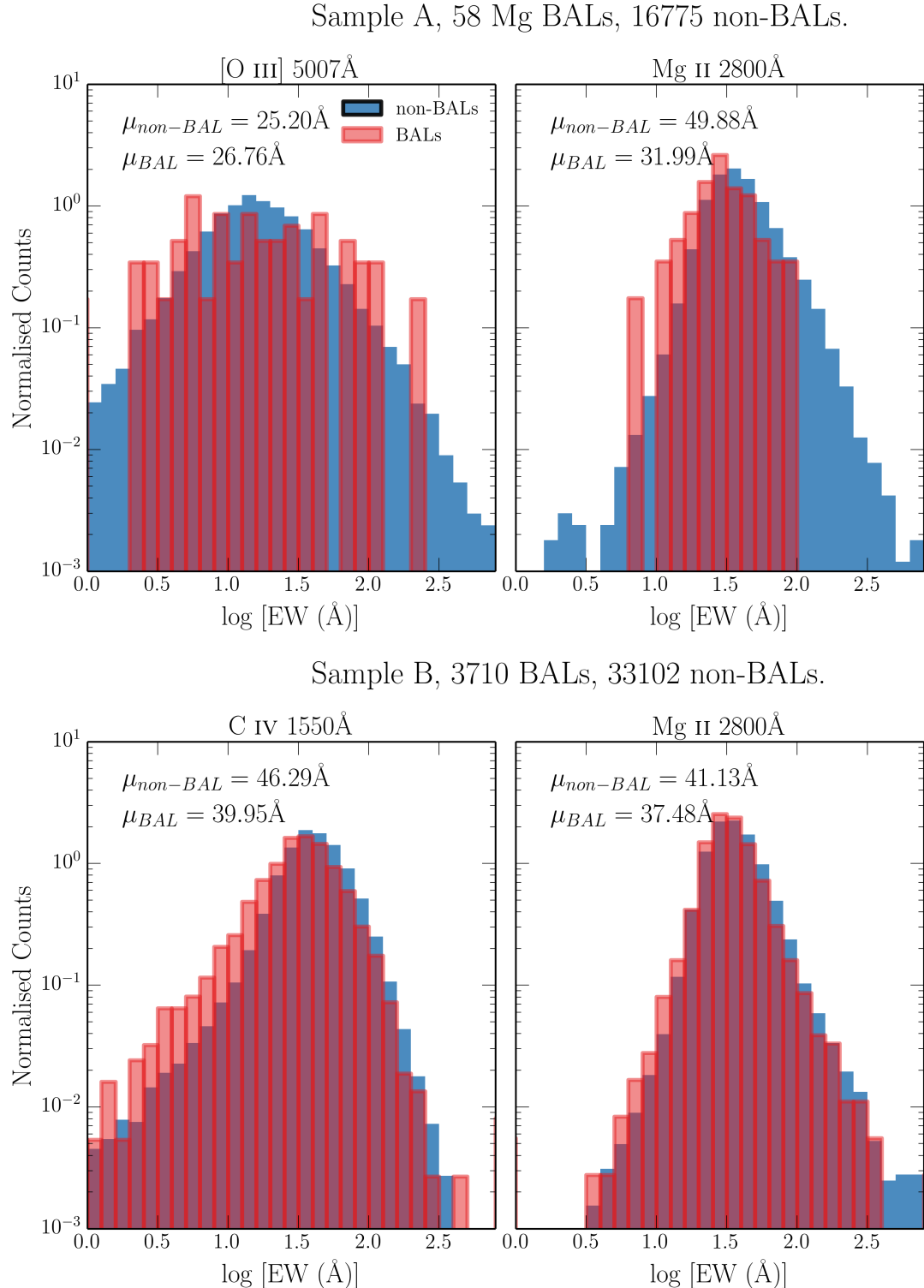


FIGURE 6.2: Histograms of equivalent widths for three emission lines from the two different samples. The mean of the BAL and non-BAL quasar distributions are labeled in each case, and the histograms are normalised.

LoBALQSOs in sample A and BALQSOs in sample B. The BH masses are the fiducial estimates from S11, who give a detailed discussion of their calibration.

S11 are careful to take into account traditional problems with quasar line fitting, such as narrow line or Fe pseudocontinuum contamination, in their fits to emission line profiles and resultant EW measurements. For Mg II 2800 Å this includes careful subtraction of the Fe emission using the [Vestergaard & Wilkes \(2001\)](#) templates. This subtraction is not included for C IV 1550 Å, as the Fe emission is less prominent and harder to model. This may lead to a systematic overestimate by ~ 0.05 dex in the C IV line EW. The [O III] 5007 Å line is fitted with a Gaussian. The flux ratio of this line with the sister component of the doublet, [O III] 4959 Å, is found to agree well with the theoretical expectation of around 3, implying a reliable subtraction of broad H β . In order to mask out the effects of e.g., absorption, on the C IV and Mg II lines, S11 ignore 3σ outliers in the fit to the profile. Based on these considerations, the S11 catalog makes for a reliable set of EW measurements. This is especially true when making inferences from multiple emission lines, as systematics inherent to individual lines or spectral windows are less likely to affect the analysis as a whole.

In attempting to draw broad conclusions about unification models as a whole, I would ideally also construct a large, homogeneous dataset of HiBAL and non-BAL quasars, both with [O III] 5007 Å EWs. Unfortunately, the wavelength limits of SDSS do not allow this; only LoBAL quasars have both BAL and EW[O III] measurements. One of the problems with using just LoBALQSOs in tests of unification is that there is evidence that they are drawn from a different population than normal quasars. Examples include anomalously high LoBAL fractions in dust-reddened quasar samples ([Urrutia et al. 2009](#)) and infra-red selected samples ([Dai et al. 2012](#)); although see also [Lazarova et al. \(2012\)](#).

Fig. 2 shows histograms of a number of different emission line properties for samples A and B. As discussed by previous authors (e.g. [Weymann et al. 1991](#)), I find that BAL and non-BAL quasars seem to possess very similar emission line properties. The EW is related to the intrinsic, ‘face-on’ equivalent width, EW_{*} by the equation

$$\text{EW} = \text{EW}_*/\epsilon(\theta) \quad (6.1)$$

where θ is the viewing angle with respect to the symmetry axis and $\epsilon(\theta)$ is the ‘angular emissivity function’, which describes how the continuum luminosity from the disc varies

as a function of viewing angle. For a foreshortened disc this is simply $\epsilon(\theta) = \cos \theta$. Note that this assumes isotropic line emission, which may not be accurate for optically thick permitted dipole transitions; the effect of line anisotropy is discussed further in section 6.5.4.

If BALQSOs are preferentially viewed from larger-than-average viewing angles, we would expect them to possess higher EWs. It is already apparent from Fig. 6.2 that the BALQSO distribution means are not significantly higher than the non-BAL quasar means – in fact, in many cases they are lower. This is not expected from a model in which the continuum comes from a foreshortened disc, and BAL outflows are at all equatorial. This problem is examined further in section 6.4. First, I will examine the motivations for different forms of $\epsilon(\theta)$ in AGN and quasars.

6.3 The Angular Distribution of Emission from an Accretion Disc

As introduced in chapter 1, the most widely-used theoretical model for accretion discs is the so-called ‘ α -disc’ model of SS73. There are a number of well-documented problems when fitting AGN SEDs with SS73 accretion disc models (see section 1.4). Despite these problems, Capellupo et al. (2015) succeeded fitting α -disc models to AGN spectra when the effects of GR, mass-loss and comptonisation were included. In this section, I start by discussing the angular distribution of emission from a classic SS73 disc, before exploring opacity and GR effects. In order to do so, I use AGNSPEC (Hubeny et al. 2000; Davis & Hubeny 2006; Davis et al. 2007). I stress that the discussion here is not limited to α -discs; the only real condition for the angular distributions derived here is that the disc is geometrically thin and optically thick.

6.3.1 Standard Thin Disc Models

Any geometrically thin, optically thick disc will appear foreshortened and limb darkened (if temperature decreases with height from the central disc plane). Foreshortening is a simple $\cos \theta$ geometric effect, where θ is the inclination with respect to the vertical z axis, which is perpendicular to the disc plane. Limb darkening, $\eta(\theta)$, is usually approximated

by a linear dependence of the emergent flux on $\cos \theta$, i.e.

$$\eta(\theta) = a(1 + b \cos \theta), \quad (6.2)$$

where a is a normalisation constant, and b governs the strength of the limb darkening. Setting $b = 3/2$, known as the Eddington approximation, tends to give good agreement with solar observations (e.g. [Mihalas 1978](#)). The two effects can be combined to give a net angular emissivity function of

$$\epsilon(\theta) = a \cos \theta \left(1 + \frac{3}{2} \cos \theta\right). \quad (6.3)$$

6.3.2 Including GR and Opacity Effects

In reality, limb darkening is not frequency independent and depends on the bound-free and bound-bound opacities in the disc. In addition, it has been shown that GR light bending can ‘isotropize’ the radiation field in XRBs ([Zhang et al. 1997](#); [Muñoz-Darias et al. 2013](#)), in some cases overcoming foreshortening effects. In order to assess the impact of GR and disc opacities on $\epsilon(\theta)$, I use AGNSPEC models, which conducts a stellar atmosphere calculation to obtain the SED from a series of annuli, before using the KERRTRANS code ([Agol 1997](#)) to calculate the emergent SED by ray-tracing along Kerr geodesics. Fig. 6.3 shows $\epsilon(\theta)$ as a function of θ for two AGNSPEC models for minimally and maximally spinning BHs. The models are characterised by $M_{BH} = 10^9 M_\odot$ and an Eddington fraction of 0.2. The angular distribution is fairly insensitive to these choices. For comparison, I also show foreshortened and limb-darkened predictions for SS73 models. Although the AGNSPEC continua are significantly more isotropic at 500 Å, there is very little effect redward of around 1000 Å, which is the relevant region of $\epsilon(\theta)$ for [O III] 5007 Å, C IV 1550 Å and Mg II 2800 Å. In fact, using the foreshortened estimate is the conservative (least anisotropic) prescription in these regimes. I will thus adopt $\epsilon(\theta) = \cos \theta$ for the remainder of this work.

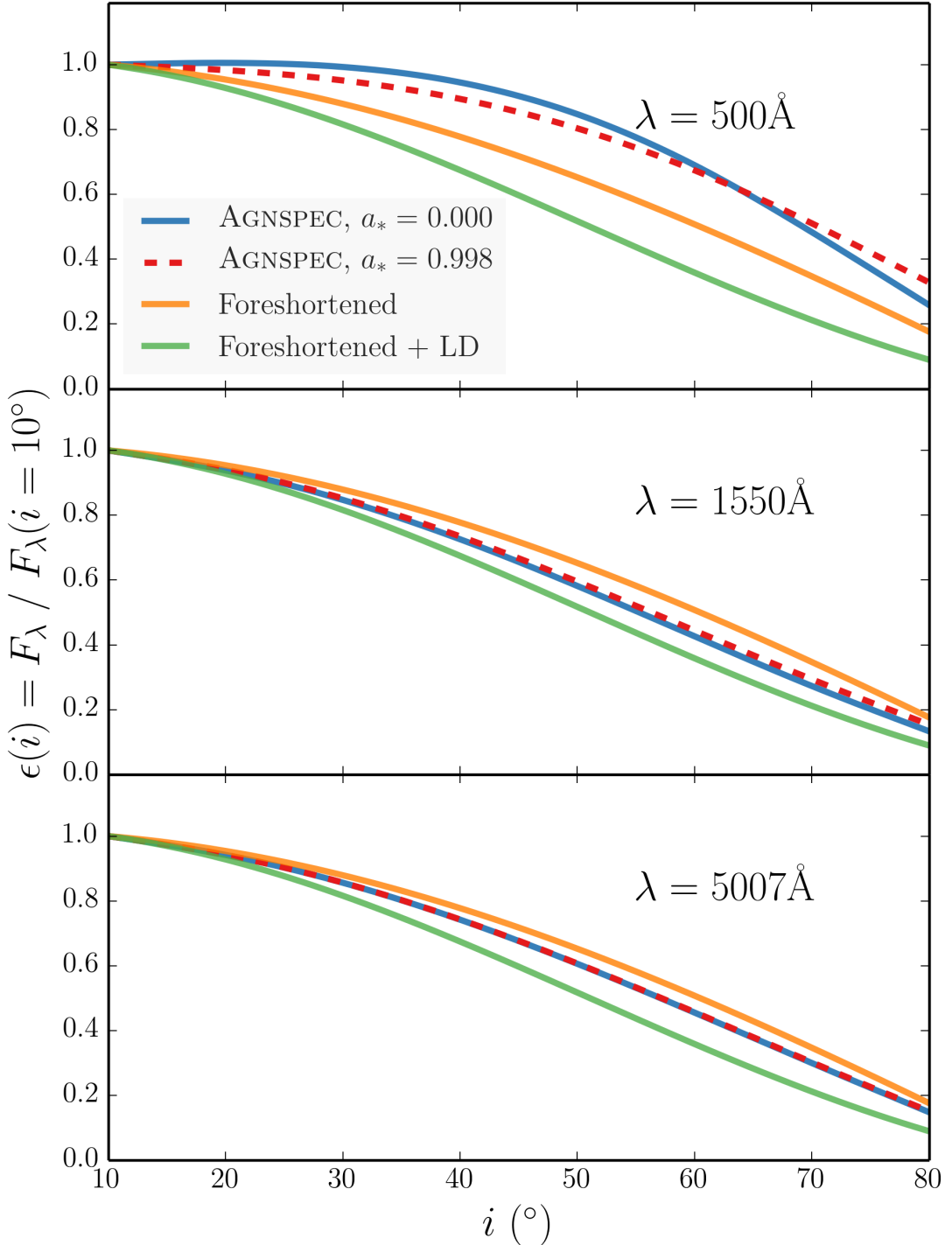


FIGURE 6.3: Angular variation of continuum luminosity from AGNSPEC and classical thin disc models. The monochromatic continuum luminosities is divided by the monochromatic continuum luminosity at 10° , from AGNSPEC and classical thin disc models, at three different wavelengths. The models are computed for an Eddington fraction of 0.2 and $M_{BH} = 10^9 M_\odot$. In each panel I show both Kerr and Schwarzschild AGNSPEC models, and the classical models are for both pure foreshortened discs and foreshortened and limb darkened (LD) discs.

6.4 Predicted EW Distributions Compared to Observations

6.4.1 Fitting the Quasar Distribution

Before comparing the EW[O III] distributions of BAL and non-BAL quasars, I will first examine whether the quasar sample can be fitted by a model in which the primary driver of EW[O III] is orientation. [Risaliti et al. \(2011\)](#), hereafter R11) analysed the EW[O III] distribution of 6029 quasars in SDSS DR5. They demonstrated that a foreshortened disc and isotropic [O III] 5007 Å line produces a high EW tail in the EW distribution, with a characteristic slope of $\Gamma_{EW} = -3.5$. In order to first reproduce their result and discuss its implications, I have created a sample according to their selection criteria. The criteria are that the object in question lies in the redshift range 0.01 to 0.8, have an absolute magnitude $M_i < -22.1$, an apparent magnitude $m_i < 19.1$, and signal to noise per pixel of greater than 5. Using the updated SDSS quasar sample of S11, this defines a sample of 14,424 quasars.

I carried out the following procedure to simulate the effect of inclination on the EW[O III] distribution, and used it to fit the observed EW[O III] distribution of quasars. This method is similar to the method used by R11 demonstrate that the power law tail in the distribution is expected.

1. An isotropic angle was chosen for the mock quasar. If $\theta < \theta_1$ then the mock quasar was designated as unobscured, and otherwise it is ignored.
2. In order to be included in the sample, the mock quasar also had to survive a selection test. This was done by drawing a random sample from the real quasar sample, and calculating a ‘doubly observed continuum flux’, F_O at 5100 Å (rest frame), such that $F_O = F_{5100} \epsilon(\theta)$. The flux limit is set at 5×10^{-13} erg s⁻¹ cm⁻¹ Å⁻¹, but the results are fairly insensitive to the limit chosen. This process simulates the distribution of angles in a flux-limited sample under the assumption that face-on objects dominate the intrinsic luminosity distribution, allowing easy comparison to R11.
3. For each mock sample, an EW_* was drawn from an intrinsic (i.e. ‘face-on’) EW distribution for quasars. This was assumed to be a Gaussian distribution. The

mean, μ_* , and width, σ_* , of this Gaussian can either be set arbitrarily – for example, to demonstrate trends in mock data – or obtained from a χ^2 fit to the observed EW distribution.

4. The EW for each mock quasar was estimated such that $\text{EW} = \text{EW}_*/\epsilon(\theta)$, and this process was repeated to build up a mock sample of 10^6 objects.

The result of this numerical experiment is, as found by R11, a distribution with a high EW tail. I can now vary the maximum angle, θ_1 , and examine how this tail changes. Mock data for a series of maximum angles is shown in Fig. 6.4, for two different intrinsic Gaussians. The power law behaviour is only seen when the maximum angle is sufficiently large, and a rapid decay in the distribution is observed at a characteristic EW related to both the width and mean of the intrinsic distribution, as well as the cosine of the maximum angle. The distribution shown in the top panel has μ_* and σ_* from R11 Model 1, whereas the bottom panel shows a narrower distribution to illustrate the earlier onset of the high EW cutoff.

Fig. 6.5 shows the result of a χ^2 minimization fit to the R11 sample. The best fit is achieved with a maximum angle of $\theta_1 = 83.5^\circ ({}^{+0.7}_{-0.2}, 3\sigma)$ and a narrower intrinsic distribution than model 1 of R11. The run of χ^2 with maximum angle is shown in Fig. 6.6, where the choice for μ_* and σ_* is left free in each case. Maximum angles below $\sim 80^\circ$ are strongly disfavoured by this model. I adopt linear binning to facilitate easy comparison with R11, and only fit up $\text{EW} = 100$ Å due to poor statistics above that limit. This makes inferring any information about a potential high EW cutoff difficult as a more complete sample at high EW is required.

6.4.2 Comparing non-BAL and LoBAL Distributions: Sample A

In order to compare the observed EW[O III] distributions to those expected for LoBALs and non-BALs I conducted a Monte Carlo simulation similar to that described in section 6.4.1, but with a few key differences. I once again assumed $\epsilon(\theta) = \cos \theta$. The geometry of the toy model used in this simulation is shown in Fig. 6.7. The aim is to test if this toy model can fit the non-BAL quasar distribution for reasonable outflow opening angles, whilst simultaneously predicting a LoBALQSO distribution that agrees well with the observed distributions.

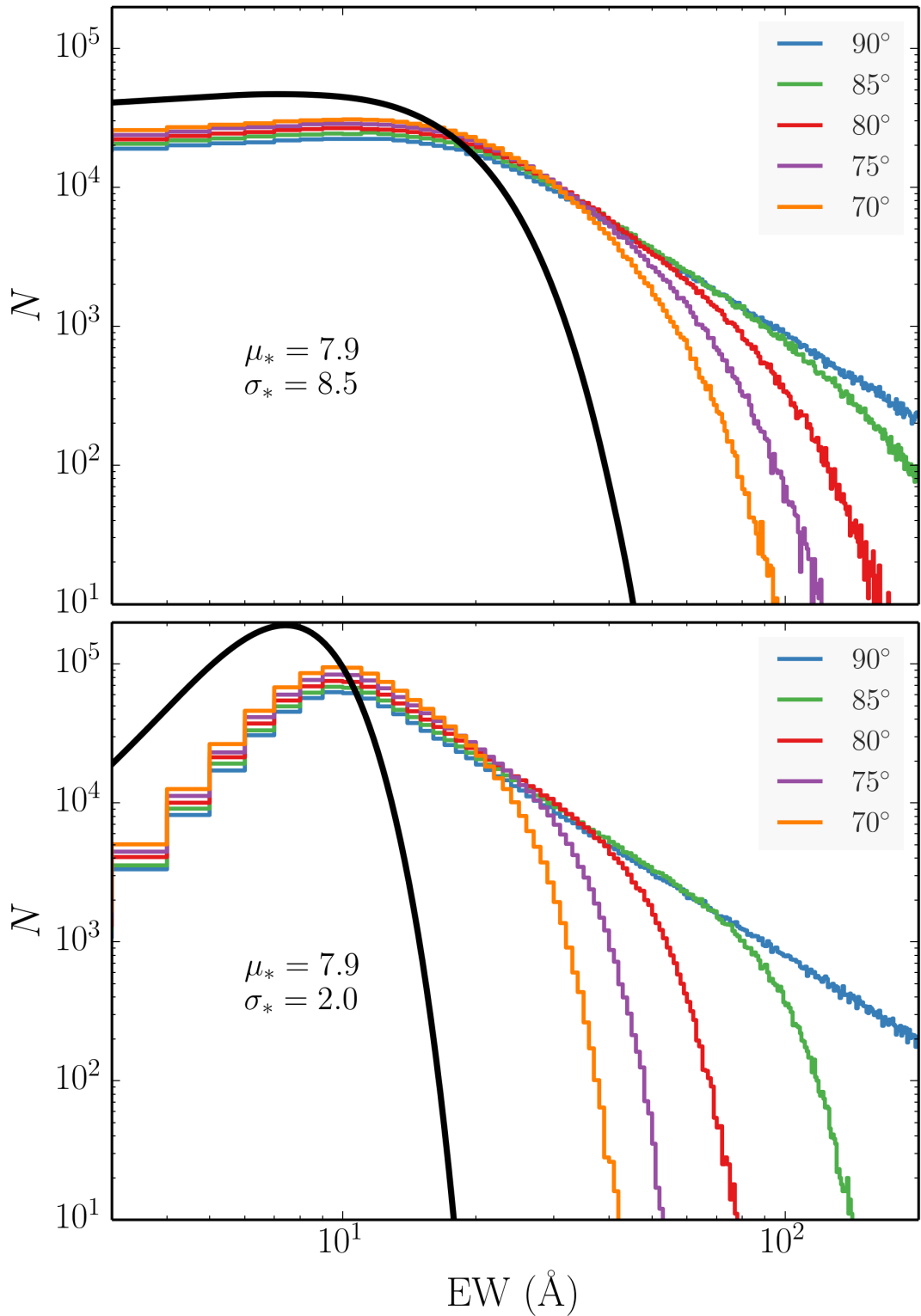


FIGURE 6.4: Theoretical EW distributions from the numerical experiment described in section 6.4.1 for a few different maximum angles. The results in the top panel use the same intrinsic distribution as Model 1 from R11 (shown in black), whereas the bottom panel shows the distributions obtained from a narrower intrinsic Gaussian. By the time the maximum angle is limited to around 70° the cutoff is clear even at moderate values of EW.

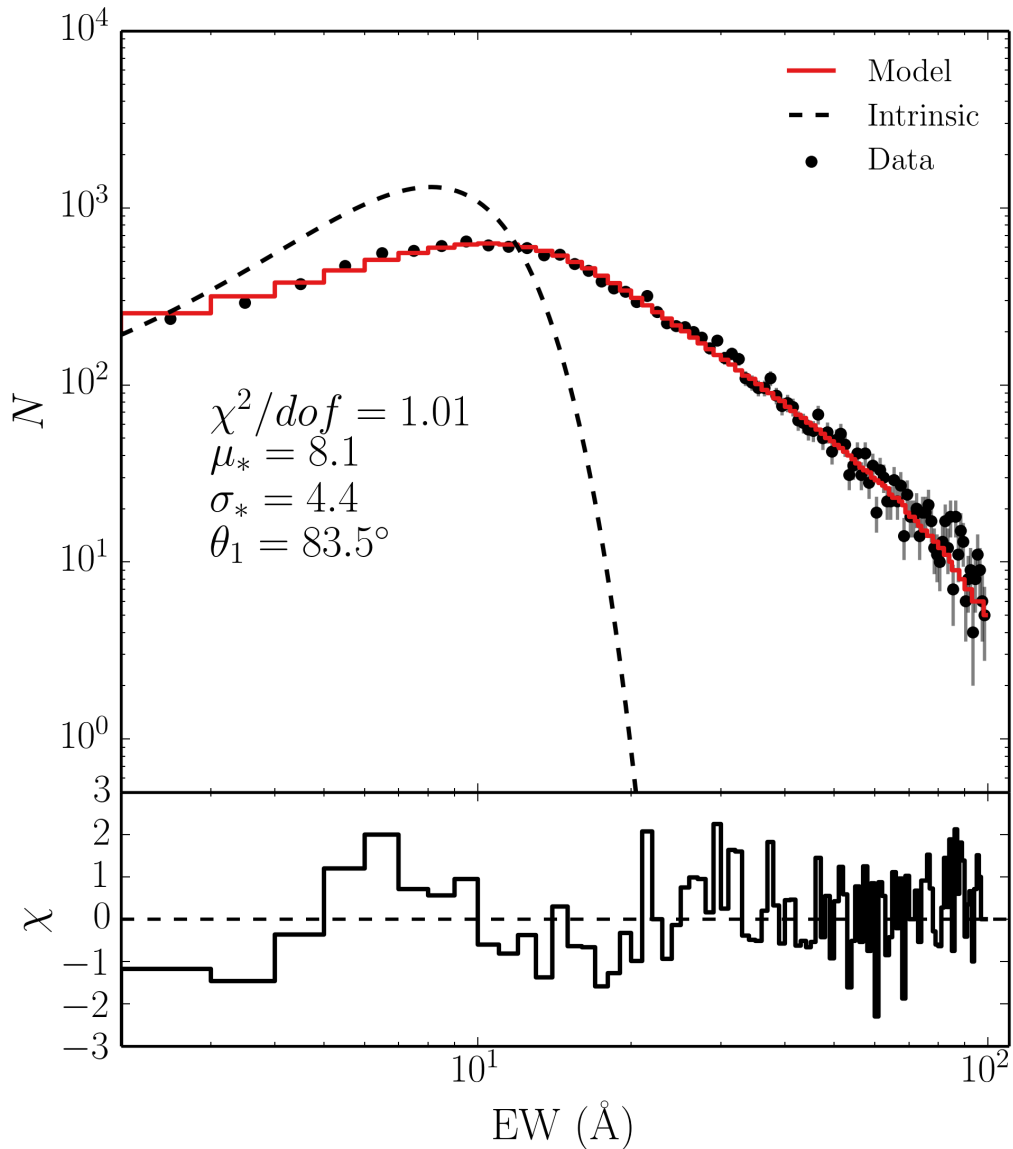


FIGURE 6.5: The EW[O III] distribution of quasars in the R11 sample (black points), with \sqrt{N} errorbars, and the best fit model with a maximum viewing angle of 84° . The intrinsic Gaussian distribution is shown with a dashed line. The plotted data is equivalent to the non-BAL histogram in the top left panel of Fig. 6.2, except that it uses linear binning and adopts the R11 sample criteria rather than using sample A.

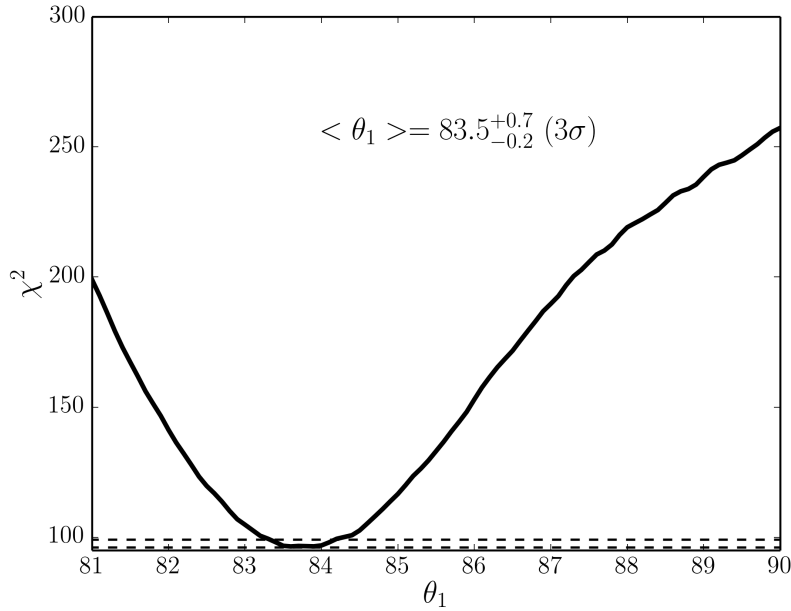


FIGURE 6.6: χ^2 as a function of maximum angle, θ_1 , calculated in steps of 0.1° . The choice for μ_* and σ_* is left free in each case. The dotted lines mark the minimum χ^2 and the 3σ confidence interval.

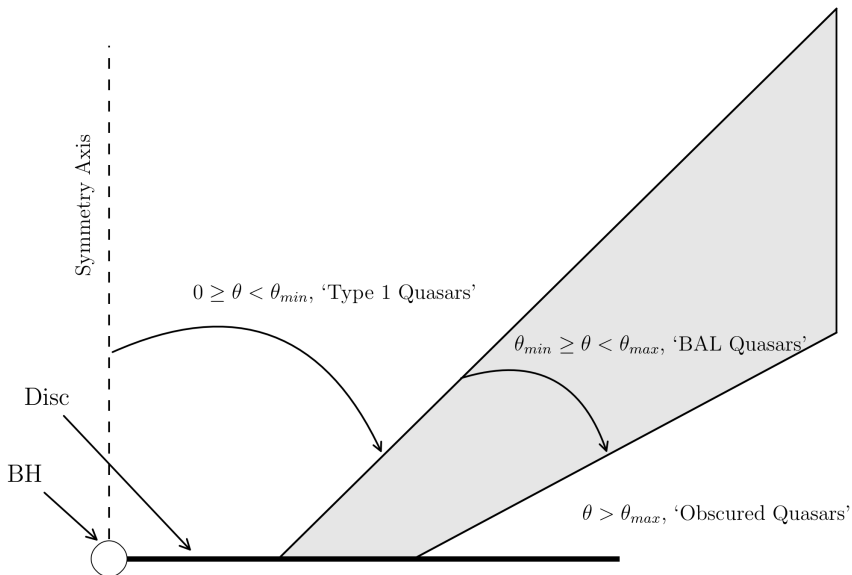


FIGURE 6.7: The geometry of the toy model used to carry out the Monte Carlo simulations.

First, a set of isotropic angles was generated. If $\theta_{\min} < \theta < \theta_{\max}$, the mock quasar was flagged as a BAL; if $\theta < \theta_{\min}$ it was designated a non-BAL, and otherwise the object was ignored. Once again, the object also had to survive a selection test based on a fixed flux limit. I then fitted the non-BAL distribution using the method described previously. For each mock sample, a EW_* was drawn from the intrinsic gaussian, and a mock EW was estimated such that $\text{EW} = \text{EW}_*/\epsilon(\theta)$. This process was repeated to build up a mock sample of objects and carried out for a series of pairs of θ_{\min} and θ_{\max} . This allows theoretical distributions for BAL and non-BAL quasars for a series of different outflow geometries to be derived.

The diagnostics recorded from the simulation are the following four quantities:

- The p -value associated with a two-tailed Kolgomorov-Smirnov (K-S) test statistic, p_{KS} , in which the mock BALQSO EW[O III] distribution is compared to the real LoBALQSO distribution. This is not an optimized fit parameter, but rather a measure of the difference between the predicted BALQSO data and the observed LoBALQSO data. A small p -value is associated with a larger difference between the two distributions, as the null hypothesis that the two distributions are the same can be rejected at a higher confidence level.
- The BAL fraction, f_{BAL} , calculated from the number of objects in the mock sample with $\theta_{\min} < \theta < \theta_{\max}$. This is the predicted observed BAL fraction with flux selection effects, so should be compared directly to the ‘intrinsic’ values of, e.g., [Knigge et al. \(2008\)](#) and [Allen et al. \(2011\)](#).
- The χ^2/dof from the fit to the non-BAL quasar distribution.
- $\Delta\mu_{EW}$, the difference between the mean value of the mock BAL distribution and the mean value of the mock non-BAL distribution. To mimic observations, this should be small.

The simulation results are shown in figure 6.8, in which the four diagnostics are plotted as a function of θ_{\min} and θ_{\max} .

As expected, equatorial viewing angles for LoBAL quasars are disfavoured, and furthermore, it is only possible to fit the tail to the EW[O III] distribution if non-BAL quasars are allowed to be viewed from high inclinations. There is no region of parameter space where a satisfactory fit is obtained to the quasar distribution without simultaneously

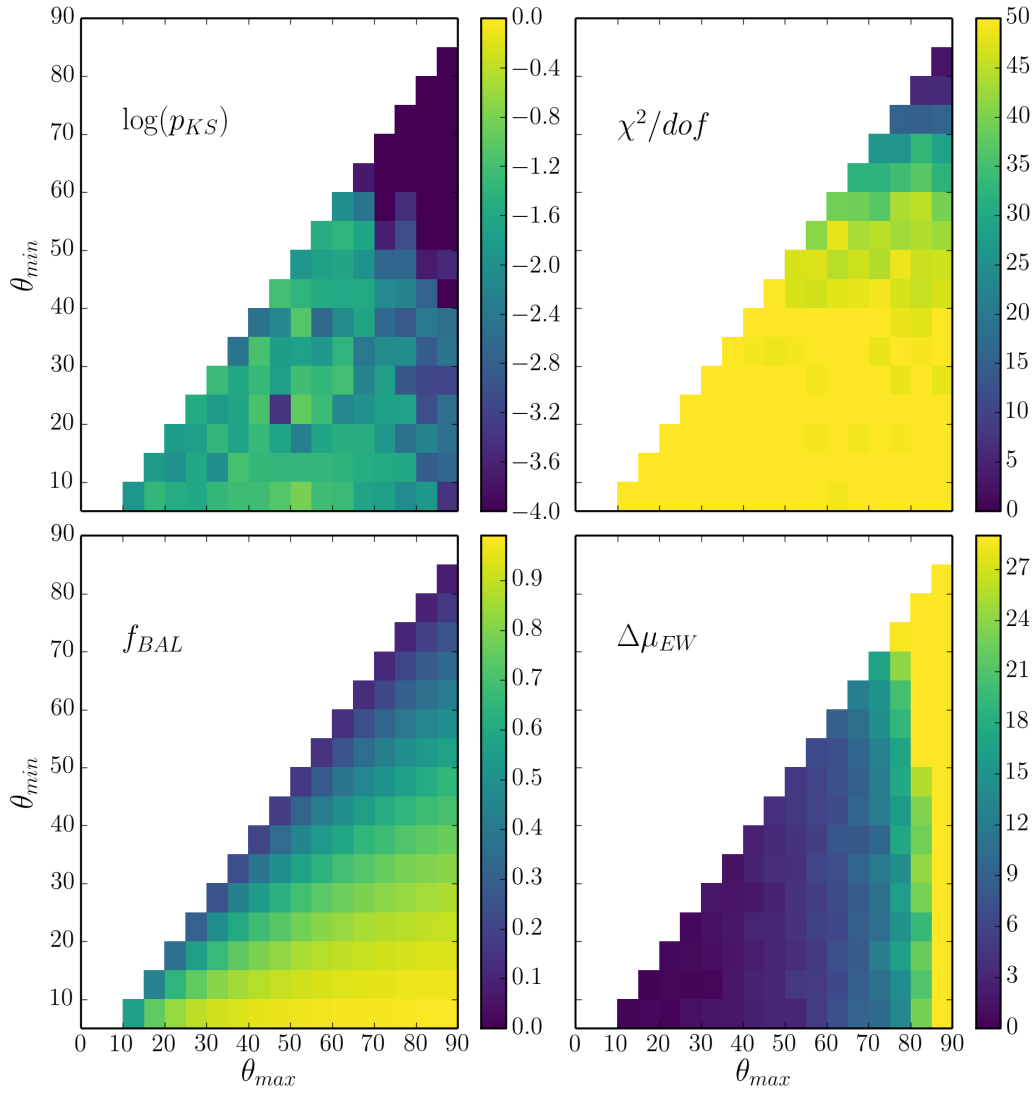


FIGURE 6.8: Heat map showing the results of the MC simulation described in section 6.4.2. The quantities shown are discussed further in the text, but correspond to (clockwise from top left): the p_{KS} value from a comparison between the mock BAL dataset and the observed BAL dataset, the reduced χ^2 from the fit to the non-BAL EW distribution, the difference in mean EW between the mock BAL and mock non-BAL datasets, and the BAL fraction expected for the geometry in question.

obtaining a large value of $\Delta\mu_{EW}$, or similarly, a very small value of p_{KS} . The simulations clearly favour a geometry in which BALQSOs are viewed from similar angles to non-BAL quasars.

One concern with the approach used here is that systematic differences between the non-BAL and LoBAL quasar populations in the *luminosity* of the [O III] 5007 Å line and continuum could mask the expected trends in EW[O III]. I have verified that this is a small effect; although Boroson & Meyers (1992) found weak [O III] 5007 Å emission in LoBALQSOs, the distributions of $L[\text{O III}]$ are very similar in sample A. The LoBALQSO

sample has continuum luminosities a factor ≈ 2 higher than the non-BAL quasar sample on average – this is not enough to permit high inclination models, although it does moderate the conclusions slightly. This also shows that host galaxy contamination is not significantly different in the LoBALQSO sample.

The conclusions here are limited by the lack of knowledge about the intrinsic face-on distribution of EW[O III], or equivalently, the orientations of the quasars themselves. If either of these quantities were known then the results of the K-S test and χ^2 minimization could be used to place more robust constraints on BAL and non-BAL viewing angles and the associated covering factor of the outflow. Furthermore, the distribution of C IV quasar EW cannot be fit by the same model as the EW[O III] distribution. Another key limitation is the SDSS wavelength coverage, which means that only LoBALs can be used when EW[O III] is present (sample A). I would suggest that future observational programs might look to build up a large sample of EW[O III] measurements for HiBAL quasars.

6.5 Discussion

I have demonstrated that the EW distributions of the [O III] 5007 Å emission line in LoBAL and non-BAL quasars is not consistent with a model in which LoBAL quasars are viewed from equatorial angles and the continuum emission originates from a foreshortened accretion disc. The EW distributions of C IV 1550 Å suggest that a similar conclusion applies to HiBAL quasars. This result would only be strengthened were I to include limb darkening. I will now explore how the above results compare to other observations of quasars that might probe system orientation, as well as the potential impact of obscuration and line anisotropy on the results.

6.5.1 Eigenvector 1

Eigenvector 1 (EV1) is a fundamental parameter space for AGN and quasars ([Boroson & Green 1992](#); [Sulentic et al. 2000](#); [Marziani et al. 2001](#); [Shen & Ho 2014](#)). It relates the FWHM of H β , the relative iron strength, R_{FeII} , and EW[O III]. Both EW[O III] and FWHM[H β] have been used as orientation indicators: FWHM[H β] should increase

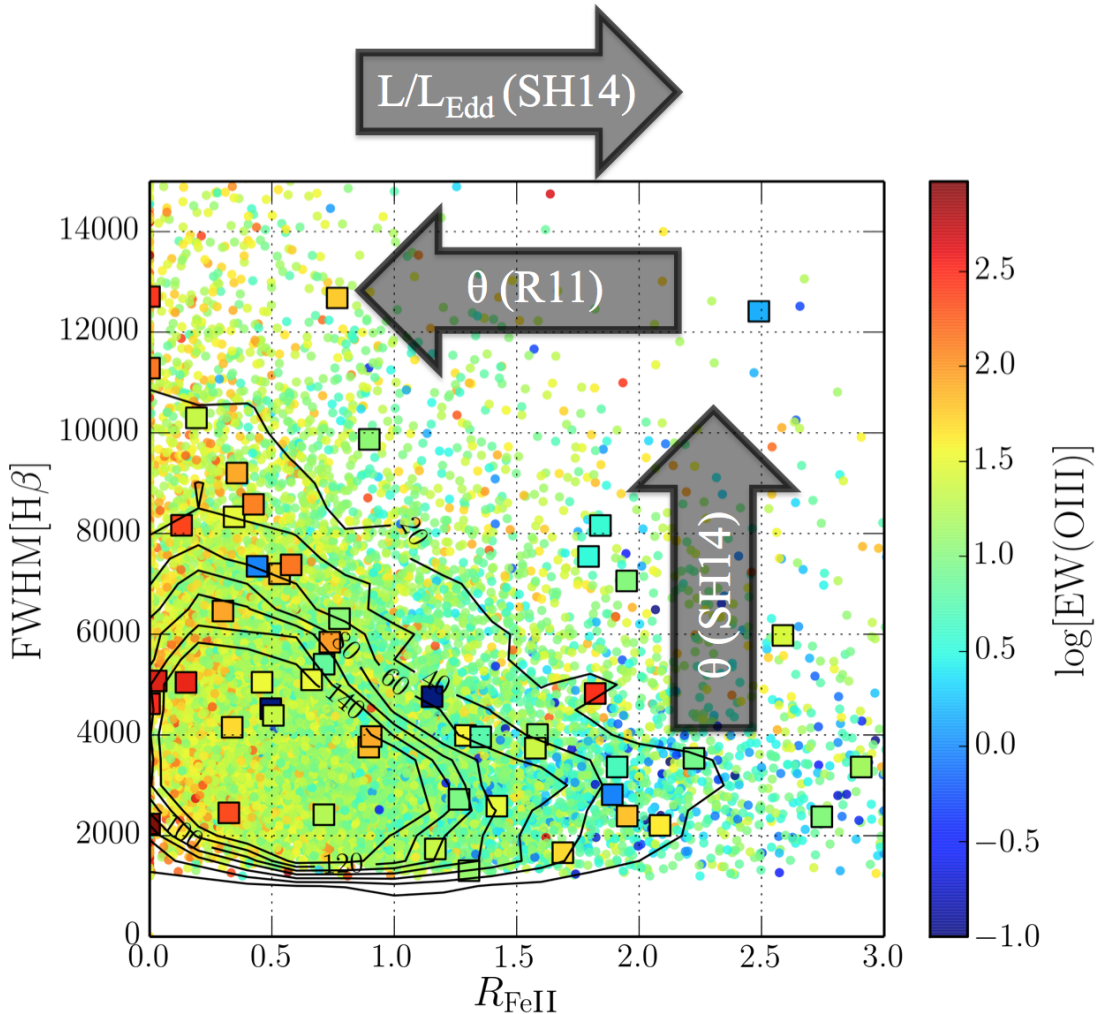


FIGURE 6.9: Eigenvector 1 for LoBAL and non-BAL quasars. FWHM of the $H\beta$ line plotted against the relative iron strength, R_{FeII} . The colour coding corresponds to the EW of OIII. The dots mark all quasars from sample A, while the squares mark those with Mg II LoBALs. A few of the Mg II LoBALQSOs are missing due to their lack of $FWHM[H\beta]$ measurements. The arrows show the approximate direction of the expected inclination (θ) trend under both the SH14 and R11 interpretations, and the expected trend in Eddington fraction (L/L_{Edd}) from SH14 only.

with inclination if the line formation region is at all disc-shaped due to velocity projection effects (see section 5.4.2.1). This means that comparing the LoBALQSO EV1 distribution to the non-BAL quasar EV1 distribution is particularly interesting. Once again, HiBALQSOs cannot be placed on this space due to the lack of rest-frame optical coverage.

Fig. 6.9 shows the quasar distribution from sample A in EV1 parameter space, with LoBAL quasars from sample A overplotted. Shen & Ho (2014, hereafter SH14) propose that the main inclination driver in this parameter space is $FWHM[H\beta]$, and that high inclination sources should thus cluster nearer to the top of the plot. In contrast, R11's

analysis predicts that high inclination sources should cluster around high EW OIII widths. As $\text{EW}[\text{O III}]$ and $\text{FWHM}[\text{H}\beta]$ are very weakly correlated (Spearman's rank coefficient of 0.14), this means they should lie to the left of the parameter space, due to the clear correlation between $\text{EW}[\text{O III}]$ and R_{FeII} . These expected trends are shown with arrows in Fig. 6.9; inspection of the figure clearly shows that BAL quasars are not only found in one region of the EV1 parameter space.

In order to assess this more quantitatively, I also show contours of quasar counts overlaid on the scatter plot. The contours correspond to the number of objects in each bin, where the bins are of size $\Delta R_{\text{FeII}} = 0.2$ and $\Delta \text{FWHM}[\text{H}\beta] = 500 \text{km s}^{-1}$. The percentage of quasars falling within the inner contour is 45%, whereas only 18% of LoBALQSOs fall in the space. Conversely, 24% of LoBALQSOs fall outside the outermost contour compared to 10% of non-BAL quasars. It would therefore appear that BAL quasars are slightly preferentially clustered towards the high-mass and high-inclination end of EV1 space (under the interpretation of SH14). This is further illustrated by Fig. 6.10, which shows the LoBAL fraction in larger bins, compared to the mean LoBAL fraction. This is again suggestive of an overdensity of LoBALQSOs towards the upper right of the parameter space. It is also clear that a unification picture in which BAL quasars are viewed exclusively from high inclinations is inconsistent both the R11 and SH14 interpretations of EV1 parameter space.

Larger datasets, preferably including HiBAL quasars with EV1 measurements, are needed in order to properly constrain the EV1 behaviour of BAL quasars. However, overall, the behaviour of EV1 in LoBALQSOs slightly strengthens the conclusion that BAL quasars are not always viewed from extreme inclinations, or alternatively, that we not yet understand the real drivers of EV1.

6.5.2 Polarisation

Spectropolarimetry of BAL quasars offers some of the best insights into the geometries of BAL outflows and tends to show a few key properties. The first is enhanced polarisation in the BAL troughs themselves (Schmidt & Hines 1999). This is readily explained by a scattering region unobscured by the BAL trough, with the higher polarisation percentage simply due to the decreased direct flux. This may also explain the non-black saturation in BAL troughs (see section 5.3.2.1).

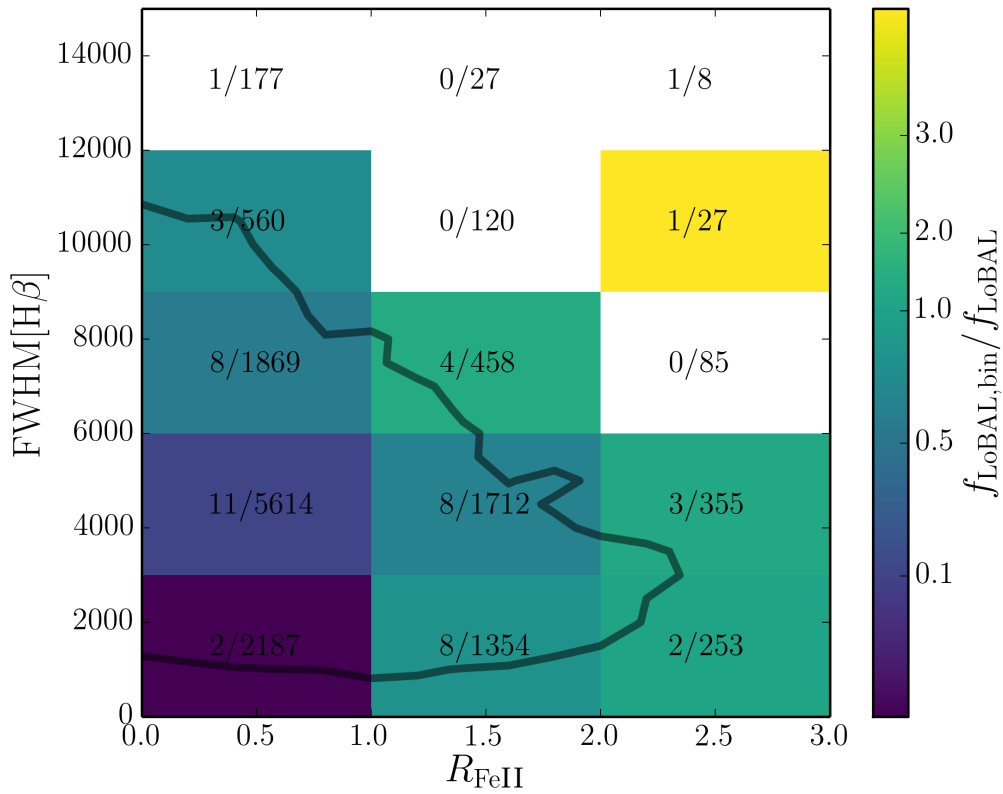


FIGURE 6.10: LoBAL fraction compared to global LoBAL fraction in Eigenvector 1 space, in bins of $\Delta R_{\text{FeII}} = 1$ and $\Delta \text{FWHM}[\text{H}\beta] = 3000 \text{ km s}^{-1}$. The contour shows the outermost contour from Fig. 6.9 for reference. The text shows $N_{\text{LoBAL}}/N_{\text{non-BAL}}$, where N_{LoBAL} is the number of LoBALQSOs in the bin and $N_{\text{non-BAL}}$ in the number of non-BAL quasars in the bin.

The second property is a continuum polarisation percentage that is around 2.4 times greater, on average, than seen in the non-BAL population (Schmidt & Hines 1999). A histogram of the continuum polarisation percentages of a sample of BAL quasars from Schmidt & Hines (1999) are compared to the Type I and Type II AGN populations from Marin (2014) in Fig. 6.11. The corresponding cumulative distribution function is shown in Fig. 6.12. These show that BAL polarisation percentages seem to lie between those of type 1 and type 2 AGN. If type 1 and type 2 objects are viewed from low and high inclinations, respectively, as expected from unified models and suggested by Marin (2014, 2016), this would imply an intermediate inclination for BALQSOs. This enhanced polarisation for BALQSOs, relative to non-BAL systems, is also well reproduced by intermediate inclination outflows in simple radiative transfer models (Marin & Goosmann 2013).

The third characteristic polarisation property of BALQSOs is a polarisation angle of $\gtrsim 60^\circ$ with respect to the radio jet axis in RL objects (Brotherton et al. 2006, and

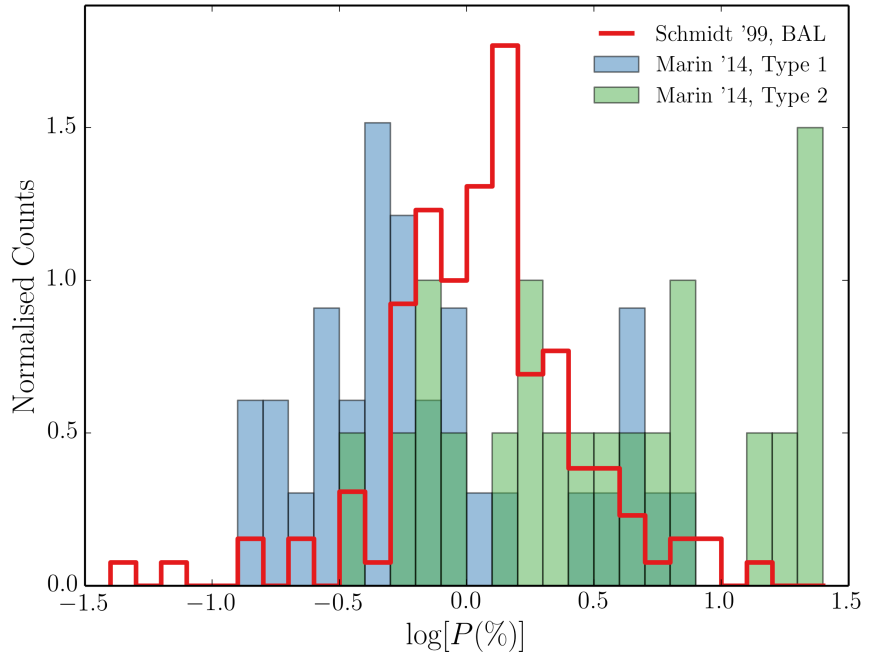


FIGURE 6.11: Histograms of polarisation percentages for BAL quasars from Schmidt et al. (1999) together with the Marin et al. (2014) AGN sample.

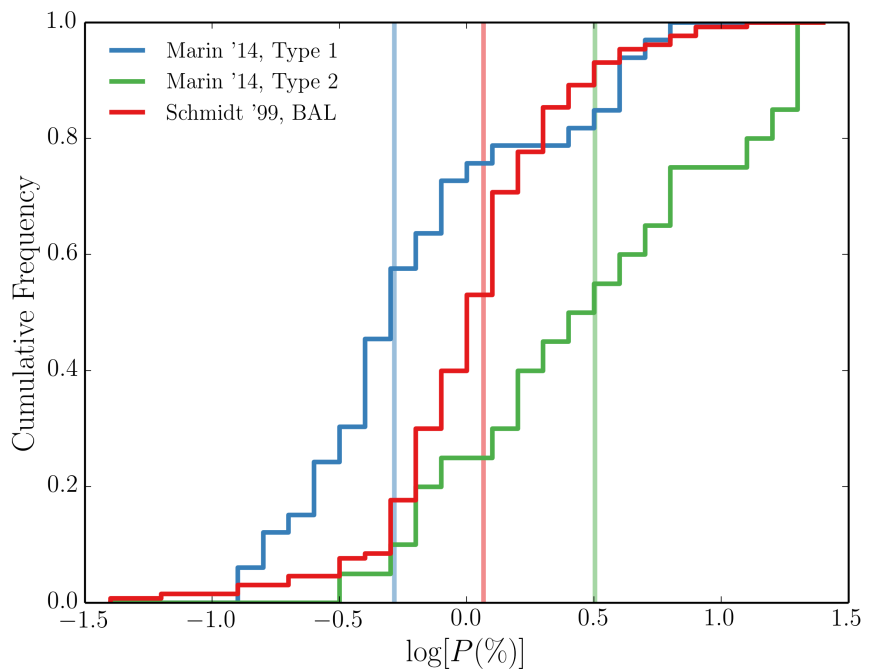


FIGURE 6.12: Cumulative distribution functions of the histograms shown in Fig. 6.11 for BAL quasars from Schmidt et al. (1999) together with the Marin et al. (2014) AGN sample. The colour-coding and x -axis scale are the same as Fig. 6.11. The translucent vertical lines mark the median value in each sample.

references therein). This suggests a higher inclination (compared to non-BAL quasars) viewing angle for BALQSOs under the interpretation of a geometric model. Indeed, early polarisation studies suggested that the observations could be explained by a model with a polar scattering region, distinct from the BLR and BAL regions, which was then viewed at an equatorial angle (e.g. [Goodrich & Miller 1995](#); [Cohen et al. 1995](#); [Lamy & Hutsemékers 2004](#)). Regardless of the true geometry, the reason for the difference must be understood. I would suggest that polarisation predictions are made from wind models such as the one I presented in chapter 5, using a similar approach to [Marin & Goosmann \(2013\)](#), but considering BALs in more detail. Overall, however, polarisation measurements seem to imply that BALQSOs are viewed from higher inclinations if geometric unification models are correct and are in slight tension with the idea that BAL quasars are viewed from the same range of angles as non-BAL quasars.

6.5.3 The Effect of Obscuration

[Caccianiga & Severgnini \(2011\)](#) (hereafter C11) showed that the distribution of EW[O III] can also be well fitted by an obscuration model. They modelled the EW[O III] distribution using absorption models for 169 objects with column density measurements from the *XMM Newton* Bright Serendipitous Source (XBS) sample. They find that AGN with column densities of $N_H \gtrsim 10^{22} \text{ cm}^{-2}$ can explain the high EW powerlaw tail.

The column density measurements for BAL quasars suggest that obscuration cannot explain the distribution of EW[O III] in quasars. As briefly discussed in chapter 5, BALs generally show strong X-ray absorption with column densities of $N_H \gtrsim 10^{23} \text{ cm}^{-2}$ ([Green & Mathur 1996](#); [Mathur et al. 2000](#); [Green et al. 2001](#); [Grupe et al. 2003b](#)). [Gallagher et al. \(1999\)](#) found all BAL quasars in a sample of 7 had $N_H > 10^{22} \text{ cm}^{-2}$, placing them firmly in the EW tail according to the C11 model. This is broadly consistent with the mean value of $3.5 \times 10^{22} \text{ cm}^{-2}$ from [Morabito et al. \(2013\)](#), and would imply that BALQSOs should have significantly higher EWs if obscuration governs the EW[O III] distribution. Of course, only LoBAL quasars had EW[O III] measurements in the sample used here – this actually strengthens the conclusion, as low ionization BALQSOs show even higher column densities, approaching Compton-thick values ([Morabito et al. 2011](#)). This argument holds regardless of the outflow geometry adopted. I therefore suggest that the obscuration model of C11 cannot explain the EW[O III] distribution of LoBALQSOs, and the similarity of the observed LoBAL and non-BAL distributions would

also suggest that obscuration is unlikely to drive the behaviour of EW[O III] overall. These conclusions are moderated if the line of sight to the X-ray source, which is used to measure N_H , experiences a different absorbing column to that of the optical continuum, and is also dependent on the particular reddening model used by C11. It is worth noting at this point that there is a degree of scatter in the N_H values measured from X-ray and optical observations (Maiolino et al. 2001b,a).

6.5.4 Line Anisotropy

Optically thin lines are isotropic – the *local* escape probabilities in each direction are equal due to the low optical depth. When lines are optically thick, the situation is more complex, as local velocity gradients then determine the line anisotropy. Indeed, Keplerian velocity shear has been shown to modify the shape of disc-formed emission lines (Horne & Marsh 1986), and an additional radial shear from a wind can cause double-peaked lines to become single-peaked (Murray & Chiang 1996, 1997; Flohic et al. 2012). Although there is a sub-population of AGN with double-peaked lines (REFs), AGN and quasars in general show broad, single-peaked lines (REFs).

R11 suggested that the broad emission lines trace the disc emission in terms of their anisotropy. If this was the case, we would not expect a difference in the BAL and non-BAL quasar EW distributions. However, an emission line would only be purely foreshortened if emitted by a disc with zero velocity shear. If the lines came from a region subject to Keplerian velocity shear then the surface brightness of an optically thick line is (Horne & Marsh 1986)

$$J_{\text{thick}}(\theta) \approx \cos \theta S_L \Delta\nu \sqrt{8 \ln \tau_0}, \quad (6.4)$$

where S_L is the line source function (assumed constant) and τ_0 is the line centre optical depth, given by

$$\tau_0 = \frac{\mathcal{W}}{\sqrt{2\pi}\Delta\nu \cos \theta}. \quad (6.5)$$

The parameter \mathcal{W} is given by

$$\mathcal{W} = \frac{\pi e^2}{m_e c} f N', \quad (6.6)$$

where f is the oscillator strength and N' is the number density integrated along the vertical height of the disc. The linewidth $\Delta\nu$ is enhanced from the thermal line width

by the velocity shear, such that

$$\Delta\nu = \Delta\nu_{th} \left[1 + \left(\frac{3}{4} \frac{v_k}{v_{th}} \frac{H}{R} \right)^2 Q(\theta, \phi) \right]^{1/2}, \quad (6.7)$$

where I have defined

$$Q(\theta, \phi) = \sin^2 \theta \tan^2 \theta \sin^2 2\phi. \quad (6.8)$$

Here, ϕ is the azimuthal angle in the disc, v_{th} and v_{th} are the thermal line widths in frequency and velocity units respectively, H is the scale height of the disc at radius R , and v_k is the Keplerian velocity. The outcome of the Horne & Marsh (1986) analysis is that optically thick lines formed in a Keplerian disc are strongly anisotropic, but they do not follow a simple $\cos \theta$ distribution. Instead, the line anisotropy is a function of the velocity shear in the disc, the atomic physics of the line in question, the location of the line formation region and the vertical disc structure.

To examine the form of this line anisotropy, we can now define the angular emissivity function for a line, $\epsilon_{line}(\theta)$. In the optically thick case with no additional velocity shear, $\epsilon_{0,line}(\theta) = \cos \theta$. In the presence of Keplerian velocity shear, and neglecting the weak $\sqrt{8 \ln \tau_0}$ term, we can write

$$\epsilon_{k,line}(\theta, \phi) = \cos \theta \left[1 + \left(\frac{3}{4} \frac{v_k}{v_{th}} \frac{H}{R} \right)^2 Q(\theta, \phi) \right]^{1/2}. \quad (6.9)$$

This quantity is compared to $\cos \theta$ in Fig. 6.13 as a function of for a few values of ϕ , using typical quasar parameters of $v_k = 10,000 \text{ km s}^{-1}$ and $v_{th} = 10 \text{ km s}^{-1}$, and assuming $H/R = 0.01$. I also show the azimuthally-averaged function, $\bar{\epsilon}_{k,line}$, which determines the integrated emergent flux as a function of θ . Fig. 6.14 also shows $\bar{\epsilon}_{k,line}$ for a few different model values of v_k , v_{th} and H/R ; the models are defined in table 6.1.

The results suggest that optically thick line emission from a disc-like BLR cannot readily explain the EW distributions of the broad emission lines, as proposed by R11, or the similarity of the distributions of C IV 1550 Å EW and Mg II 2800 Å EW in BAL and non-BAL quasars. This is because broad emission lines formed in a Keplerian disc do not simply trace the disc continuum emission in terms of their angular emissivity function. The presence of an equatorial wind would only serve to exacerbate the effect, as it would cause more line emission to escape along the poloidal velocity gradient towards high inclinations. I would therefore suggest that future efforts might include fully modelling

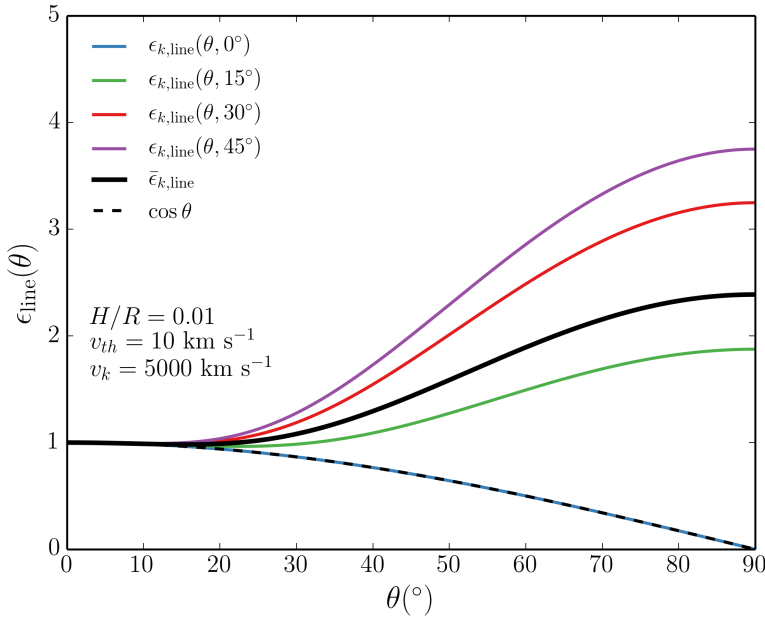


FIGURE 6.13: The line angular emissivity function from a Keplerian disc as a function of inclination angle, θ , for a few different azimuthal angles, ϕ . The azimuthally-averaged case, $\bar{\epsilon}_{k,\text{line}}$ (thick black line), and the zero Keplerian velocity shear case, $\epsilon_{0,\text{line}}(\theta) = \cos \theta$ (dotted line), are also shown.

Model	H/R	$v_k(\text{km s}^{-1})$	$v_{th}(\text{km s}^{-1})$
A	0.01	10,000	10
B	0.01	5,000	10
C	0.01	5,000	25
D	0.001	5,000	25

TABLE 6.1: The values of the Keplerian velocity, v_k , thermal velocity, v_{th} , and ratio of disc scale height to radius, H/R , for four models. These values are used as inputs to calculate $\bar{\epsilon}_{k,\text{line}}$ as shown in Fig. 6.14, and model B is also used in Fig. 6.13.

the line emission as a function of inclination to feed into the above analysis – it is certainly not sufficient to assume that a disc-shaped BLR should emit in the same way as a disc continuum.

6.6 Conclusions

I have explored the emission line properties of BAL and non-BAL quasars, particularly focusing on the EW distributions in two redshift ranges of the SDSS quasar catalog. My main conclusion is that the EW distributions of BAL and non-BAL quasars are remarkably similar and that this is *not* what one would expect from a unification model in which an equatorial BAL outflow rises from a foreshortened accretion disc. This

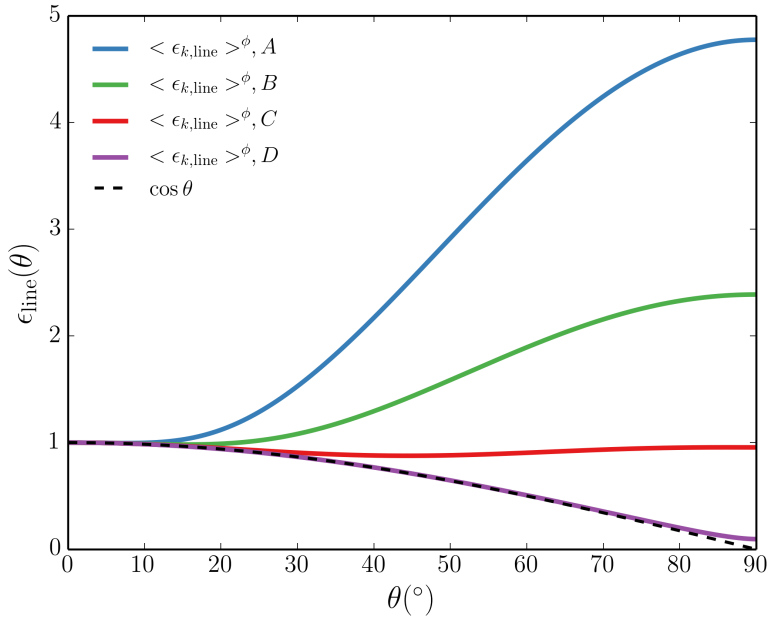


FIGURE 6.14: The azimuthally-averaged line angular emissivity function, $\bar{\epsilon}_{k,\text{line}}$, from a Keplerian disc as a function of inclination angle for the four models shown in table 6.1. The model parameters are the values of H/R , v_k and v_{th} . The zero Keplerian velocity shear case, $\epsilon_{0,\text{line}}(\theta) = \cos \theta$ (dotted line), is also shown. Unless the disc is very thin ($H/R \sim 0.001$), $\bar{\epsilon}_{k,\text{line}}$ shows large deviations from $\cos \theta$.

geometry has been used extensively in geometric unification and BAL outflow models in the past (e.g. Murray et al. 1995; Proga et al. 2000; Proga & Kallman 2004; Risaliti & Elvis 2010; Borguet & Hutsemékers 2010; Higginbottom et al. 2013; Nomura et al. 2013, 2016) and was even adopted earlier in this thesis. I then established that an angular emissivity function of $\epsilon(\theta) = \cos \theta$ is a fairly conservative estimate of the anisotropy expected from thin disc models, as GR or opacity effects in the disc do not cause the continuum to become more isotropic in the relevant wavelength regimes. I used this form of $\epsilon(\theta)$ to conduct a series of simulations similar to those described by Risaliti et al. (2011). As expected, these simulations confirmed the above finding..

There are three basic ways to explain these results (with the caveat that the conclusions drawn about LoBALQSOs are assumed to apply to BALQSOs in general):

- **Scenario 1:** The quasar continuum is much more isotropic than one would expect from a geometrically thin, optically thick accretion disc. I have demonstrated that general relativistic effects cannot account for this discrepancy in the UV. Reprocessing by surrounding dense plasma with a large covering factor or limb brightening in the disc may provide possible explanations which this analysis cannot yet confirm or refute.

- *Scenario 2:* Quasar discs are strongly anisotropic, as expected from a geometrically thin, optically thick accretion disc. In this case, BAL outflows cannot only emerge at extreme inclinations and should instead be seen from fairly low inclinations. Polarisation measurements need to be reconciled with this hypothesis. I recommend that future RT modelling efforts explore different outflow geometries and that detailed polarisation modelling is undertaken to constrain the outflow opening angles.
- *Scenario 3:* The geometric unification model does not explain the incidence of BALs in quasars, or requires an additional component which is *time-dependent*, such as an evolutionary or accretion state origin for BAL outflows. In this scenario, BAL quasars would be seen from very similar angles to non-BAL quasars. If this is the case, the covering factors and opening angles of the outflows still need to be constrained so that feedback efficiencies can be accurately estimated.

I have confirmed that obscuration cannot explain the EW distributions of all quasars due to the high column density observed in BAL (and particularly LoBAL) quasars. Line anisotropy from a disc-shaped BLR cannot explain the observed similarities between the broad emission line distributions if the disc is Keplerian, and it also cannot affect the quasar EW[O III] distributions, as [O III] 5007 Å is a forbidden, optically thin transition.

Regardless of the conclusions about BAL quasars and their outflow geometries, this analysis allows conclusions to be drawn about the *overall* quasar population. In scenario 1, the EW[O III] distribution of quasars cannot be driven by inclination as suggested by (Risaliti et al. 2011). This would imply that EW[O III] is a poor orientation indicator. The lack of correlation between EW[O III] and FWHM[H β] also suggests that it is not possible for them both to be strongly orientation dependent. Even if scenario 1 holds, the FWHM[H β] and EV1 measurements of LoBALs imply that they are seen from similar inclinations to type 1 quasars. If scenario 2 holds, then this would suggest that all quasars are viewed from fairly low inclinations, in which case the EW[O III] distribution cannot be dominated by inclination, and its shape must instead be governed by the intrinsic properties of the NLR.

The above three scenarios each pose a different challenge to the current understanding of, respectively, accretion physics, outflow models and our understanding of unification and

the BAL fraction. This work therefore adds to the growing evidence that our simplest models are not sufficient to describe quasars and that alternatives need to be sought.

Chapter 7

Conclusions and Future Work

“...and the credits rave as the critics roll.”

Mike Vennart, Silent/Transparent

I began this thesis with the statement that accreting systems and their associated outflows are astrophysically important. However, I also demonstrated that much of the diverse phenomenology associated with such systems, as well as the underlying *physics*, is not well understood. Having attempted to address some of the issues raised in the introductory chapters, I will provide some concluding remarks. First, I will summarise my findings, before commenting on how future research can help unveil the true nature of accretion discs and their winds.

A large portion of this PhD has been spent maintaining, testing and developing the MCRT and ionization code, PYTHON. The first step in this project was to understand the macro-atom scheme developed by [Lucy \(2002, 2003\)](#), and its specific integration into PYTHON. I described the scheme and the operation of PYTHON in detail in chapter 3, partly in the hope that it will prove a useful document for future efforts involving this powerful, but complex, piece of software. The latter parts of the same chapter focused on the series of tests I conducted to robustly verify that the code works as expected and is able to reproduce the expected analytical and computational results in certain physical limits. Near the start of the project many of these tests would fail, either because PYTHON did not possess the relevant atomic data, or because the necessary integration between the macro-atom and simple-atom portions of the code was not yet in place. Thus, while time consuming, progressing to the point where all the tests shown

in chapter 3 could be passed was an important milestone and enabled the techniques in question to be applied to astrophysical problems with confidence.

The first of these astrophysical problems involved CVs, and in particular those accreting at a relatively high rate, such as DNe in outburst and NLs. Having improved the radiative transfer techniques from previous CV modelling efforts involving PYTHON (LK02, [Noebauer et al. 2010](#)), it was now possible to see if the outflows that are responsible for the P-Cygni profiles seen in UV resonance lines could also affect the *optical* line and continuum emission. The results are unambiguous. By simply taking the SV93/LK02 models – designed to reproduce the UV spectra of high-state CVs – and ‘turning on’ the improved radiative transfer mode, the wind has a significant effect on the optical spectrum, producing strong H α , He II 4686 Å and He II 3202 Å lines, among others, at high inclinations.

I then conducted a small parameter search over just two kinematic parameters, to see if a model could produce *all* of the optical H and He lines observed in high-state CVs. Synthetic spectra from a model with a more slowly accelerating outflow show the full sequence of H and He recombination lines, with the observed trend from strong emission at high inclination to weaker lines at low inclination. Furthermore, the dense outflow now produces strong Balmer recombination emission that is sufficient to ‘fill in’ the Balmer absorption edge intrinsic to the disc atmosphere input spectrum. The optically optimised model is not without issues: the red wing to the C IV line is now overly strong, particularly at high inclinations, and He II emission is stronger than observed. Nevertheless, the synthetic spectra exhibit reasonable verisimilitude with observations of the high inclination NL RW Tri, and the results indicate that disc winds may have a much broader impact, especially in wavelength terms, than is traditionally expected. Furthermore, the large vertical extent of the line emitting region has implications for techniques that assume planar line emission, such as Doppler tomography (e.g. [Marsh & Horne 1988](#)) and eclipse mapping (e.g. [Horne et al. 1994](#)).

In chapter 5, I applied similar techniques to the question of quasar unification, but with one additional adaptation. In order to simultaneously increase the emission measure of the wind, as well as moderate the ionization state in the presence of strong X-rays, I incorporated a simple treatment of clumping into PYTHON. The technique – known as microclumping – is prevalent in the stellar wind community, but this is the first time it has been applied to quasar winds in this context. Although the motivation for including

clumping was in some sense empirical, in that H13 could not produce a model with strong C IV BALs without severely limiting the X-ray luminosity, the validity of this approach is strengthened by the theoretical and observational evidence for clumping in line-driven hot star winds (see sections 2.1.4.1 and 2.2.3).

Once again, I conducted a parameter search, this time in 5 dimensions. A broad family of models produce strong UV emission lines at low inclinations and UV BALs at high inclinations. Thus, the first success of the clumpy quasar wind model is that, for clumping factors comparable to those required in stellar wind modelling (Hamann et al. 2008), the ionization state of the wind matches well with observations even in the presence of strong X-ray radiation. Indeed, the X-ray properties of the model now agree well with observed X-ray luminosities of non-BAL and BAL quasars, suggesting that the partially self-shielding BAL outflow itself might be responsible for the observed X-ray weakness of BAL quasars. Perhaps the most compelling attribute of the wind model is that it naturally reproduces the broad range of ionization states observed in AGN, such that the wind emission has very similar characteristics to the observed BLR spectrum (see, e.g., Fig. 5.8). The primary limitation of the fiducial quasar model is a geometric one: it is not possible to produce comparable line EWs at low inclination to those at high inclination, due to the foreshortened, limb-darkened, and absorbed disc emission. Thus, even if the low inclination line emission could be matched to the observed quasar EWs, the model would then over-predict the line emission emerging at high inclination ‘BALQSO-like’ angles. This suggests an issue with an equatorial unification model, and provides the motivation for exploring the observational characteristics of emission lines in BAL and non-BAL quasars.

The final project in this PhD saw a switch in philosophy, as, informed by the radiative transfer modelling, I turned to observations and, in particular, the invaluable dataset that is the *Sloan Digital Sky Survey*. The aim of this exercise was to quantitatively assess the apparent similarity in emission line properties in BAL and non-BAL quasars, which is hard to understand in simple geometric wind-based unification models. I first reproduced the results of Risaliti et al. (2011) using the updated dataset. This was done by fitting the distribution of the EW of the [O III] 5007 Å narrow emission line with a simple geometric model. In this model I convolved an intrinsic Gaussian distribution with the expected angular distribution of quasars from a flux-limited sample. I then constructed a toy model for geometric unification and showed that predictions from the simplest

quasar wind models – those where an equatorial outflow rises from a geometrically thin, optically thick accretion disc – are not consistent with the observed EW distributions of quasar emission lines. The results also suggest that obscuration is not the key driver of the EW[O III] distribution – albeit under the assumption that LoBAL quasars are drawn from the same population as non-BAL quasars.

The overall conclusions of this final study are striking and extend beyond just constraining BAL outflow parameters. They suggest there is a fundamental problem with our simplest quasar models, with a few potential solutions. Perhaps quasar discs are much more isotropic than one might expect. If this is the case, how is it reconciled with accretion disc theory? Alternatively, BAL and non-BAL quasars may be viewed from a similar range of angles, in which case their differences in polarisation properties must be understood. The final possibility is, of course, that geometric unification does not explain the incidence of BALs in the UV spectra of quasars. This final scenario is not a solution to the problem, *per se*. After all, BAL outflows *must* emerge at some range of angles, and this range of angles is important to constrain in order to understand the outflow physics.

Perhaps unsurprisingly, the work presented in this thesis has raised many questions, some of which are fundamental to our understanding of CVs, quasars and accreting systems generally. I will therefore devote some time to discussing what I believe are the natural next steps in furthering our understanding of accretion and outflows on all scales.

7.1 Suggestions for Future Work

7.1.1 CVs as Accretion and Outflow Laboratories

CVs are the closest and best understood laboratories for studying accretion physics. In particular, the NL variables make excellent testbeds for the α -disc model, as they are one of the few accreting systems known to lie in a relatively constant accretion rate state – satisfying an implicit assumption of the SS73 prescription. I suggest that two observational programs relating to NLs are pursued. The first is to take broadband, simultaneous spectroscopy of a number of NL variables. This will allow the impact of winds on the spectrum to be assessed more carefully as modelling of the entire wavelength

range can be undertaken, including detailed fits to the observed spectra. It will also allow the broadband SED to be fitted with confidence and inferences to be made about the temperature profile of the disc. Our team recently submitted an HST proposal with this goal (PI: Long). The second is to take measurements of the depth of the Balmer jump in a relatively large sample of NLs, either through narrow band spectroscopy or two-band photometry. Together with inclination measurements the predictions of disc and outflow models can be tested directly by exploring how the depth of the Balmer absorption edge varies with viewing angle and accretion rate.

7.1.2 Improving the Treatment of Clumping

One of the limitations of the work presented in chapter 5 is that the treatment of clumping is simple, and probably does not adequately capture the physics of dense substructures in AGN outflows. Indeed, it is only intended as a ‘first step’ towards accurately including clumpiness in PYTHON. So, what is the next step? One fairly simple way of including some degree of porosity in the treatment would be to relax the assumption that the Sobolev length is larger than the clump size. The Sobolev optical depth can then be calculated either in or out of a clump, with probabilities proportional to the clump filling factor. This would mean that there is a chance that photons will not interact with clumps, possibly leading to the non-black saturation that is observed in BAL troughs ([Arav et al. 1999a,b](#), see also section 5.3.2.1). More generally, an approach similar to macroclumping, as used in stellar wind modelling (e.g. [Hamann et al. 2008](#); [Šurlan et al. 2012](#)), would allow a more realistic inclusion of porosity.

More complex approaches could also be considered, such as the ‘two-phase’ ideas used in clumpy torus models ([Stalevski et al. 2013](#)) and suggested for the BLR (e.g. [Netzer 1990](#); [de Kool & Begelman 1995](#); [Elvis 2000](#)). However, the general problem here is that, while introducing more freedom into the wind model would certainly allow one to fit quasar and CV spectra more effectively, the question is whether this provides useful physical insight. This is somewhat open to interpretation, as the filling factors and origins of clumps in BLR and outflow models are not well constrained. I would therefore suggest that some of the above techniques are implemented and experimented with, but would urge caution with regards to the interpretation of the overall results. As mentioned in chapter 4, including clumping in the CV modelling could prove particularly interesting with regards to the optical P-Cygni profiles observed in He I and H α in some

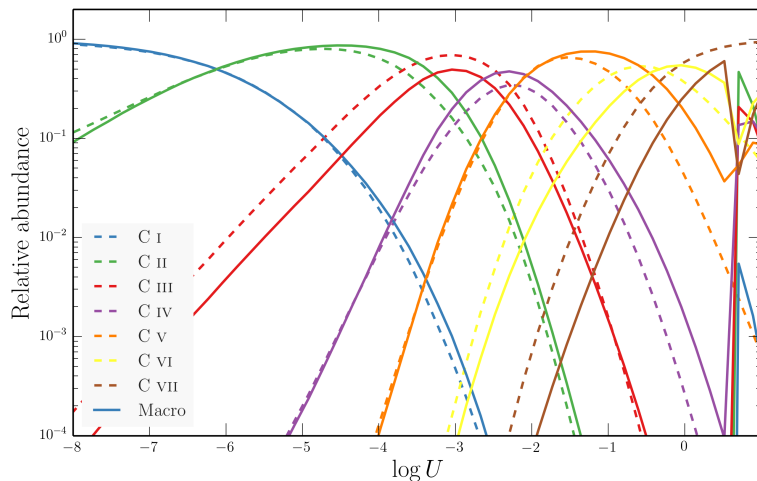


FIGURE 7.1: Ion fractions as a function of ionization parameter when Carbon is treated as a simple-atom (dotted lines) or macro-atom (solid lines). Although serious, as yet unsolved, numerical problems appear at high ionization parameters, the fundamental machinery for treating Carbon as a macro-atom is now in place.

CVs. Intriguingly, similar profiles were also seen during the recent outburst of V404 Cyg ([Muñoz-Darias et al. 2016](#)).

7.1.3 Improving Atomic Models

Although treating both hydrogen and helium as a macro-atom was a significant improvement over the previous two-level approaches, much can still be done to improve how PYTHON deals with atomic processes. One of the main limitations of the code is the current treatment of collisions, as discussed in chapter 4. One way to improve the accuracy of collision strengths between dipole transitions would be to use experimental data (e.g. [Gaetz & Salpeter 1983](#)). I have also recently begun an effort to incorporate macro-atom data for additional elements. The fundamental aim of this is to model a series of more complex atoms that cannot be described with the two-level atom approach, so that, for example, the density-dependent phosphorous doublets, or the semi-forbidden C III] 1909 Å, line could be accurately predicted. Fig. 7.1 shows how I have recently incorporated a carbon macro-atom into the code and produces reasonable results for moderate ionization stages, although there are still some problems at high ionization parameters.

7.1.4 Using Radiative Transfer to Make Reverberation and Microlensing Predictions

I described in the introduction how the ‘accretion disc size problem’ poses a profound challenge to the current best-bet model for the AGN continuum. I suggest that radiative transfer with PYTHON is used to predict the reverberation and microlensing signatures from wind models for AGN and quasars. The former has already been started by Sam Mangham as part of a PhD project, and an example transfer function from the fiducial quasar wind model is shown in Fig. 7.2. With the machinery now in place, the continuum lags from such a model can be computed and compared to observations. This will be particularly useful if it is possible to produce a reasonable wind model for NGC 5548, as comparisons can then be made to existing and ongoing long-term monitoring campaigns (e.g. [Edelson et al. 2015](#)) to assess if a wind can produce the observed lags, including the excess lag in the Balmer continuum that can now be modelled in PYTHON with the macro-atom scheme. MCRT can also be used to predict the microlensing signatures from wind and BLR models. If PYTHON is modified to produce spatially-resolved images, binned in frequency space, as a function of viewing angle, then these can be directly fed into the microlensing analysis. This will allow for an independent test of the microlensing models themselves, as well as making predictions for the sizes associated with line and continuum emission from outflows.

7.1.5 Placing BAL Quasars on the Eigenvector 1 Parameter Space

In chapter 6 we saw how LoBAL quasars are not specifically clustered in one region of parameter space in the so-called ‘Eigenvector 1’ diagram. Under the interpretation of [Shen & Ho \(2014\)](#), this implies no preferred inclination range for BALQSOs, although there is a suggestion of an overdensity towards the upper right quadrant of the parameter space (see Fig. 6.10). Ideally, I would have been able to also plot the HiBAL quasars in this parameter space, since LoBAL quasars may not be drawn from the same population as normal type 1 quasars (e.g. [Urrutia et al. 2009](#); [Dai et al. 2012](#)). I would thus advocate targeting an SDSS-selected sample of HiBAL quasars, in the redshift range $1.45 < z < 2.28$, with near infra-red telescopes in order to obtain rest-frame optical spectroscopy covering H β , [O III] 5007 Å and the broad Fe II emission underlying H β . This would allow HiBAL quasars to be placed in the EV1 parameter space, and in the

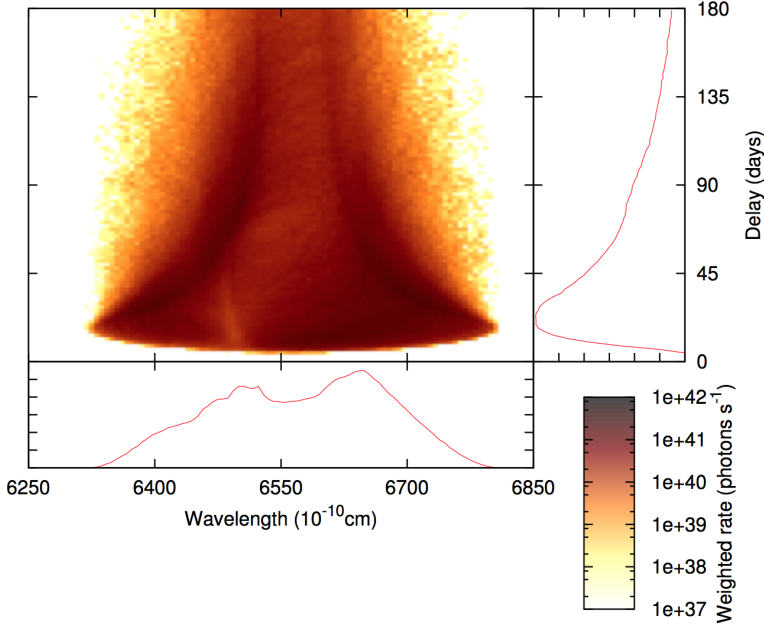


FIGURE 7.2: Credit: Sam Mangham. Velocity-resolved transfer function for H α from the fiducial quasar model presented in chapter 5. The transfer function is for a viewing angle of 40°.

process provide EW[O III] measurements. The fitting of the EW[O III] distribution I carried out in chapter 6 for LoBALs could then be repeated on this HiBAL sample.

7.2 Closing Remarks

Disc winds are ubiquitous in accreting systems and have a profound connection with the accretion process. I have demonstrated, through state-of-the-art MCRT simulations, that disc winds extend their influence beyond the blue-shifted BALs and P-Cygni profiles traditionally associated with outflows. They may produce the optical line and continuum emission in CVs, possibly even dominating the observed spectrum. Simple clumpy biconical wind models also naturally exhibit the range of ionization states and emission lines seen in type 1 AGN and quasars, and once again may significantly alter the continuum shape. Regardless of their true impact, the influence of disc winds on the spectra of accreting systems must be understood, and the outflow covering factors and opening angles accurately estimated, for three main reasons. First, so that the feedback efficiency of BAL outflows, and mass-loss rates in CVs, can be calculated. Second, so that the true intrinsic continuum can be unveiled, and the viability of the current ‘best-bet’ accretion disc models can be assessed. Third, so that the orientations of AGN and quasars can be properly constrained, allowing us to unify their diverse phenomenology.

These questions are still unanswered, but I hope that in this thesis I have demonstrated that *disc winds matter* and are fundamental to our understanding of accreting compact objects.

Bibliography

- Abbott D. C., 1982, ApJ 259, 282
- Abbott D. C., Lucy L. B., 1985, ApJ 288, 679
- Abramowicz M., Fragile P. C., 2013, Living Reviews in Relativity 16(1)
- Adams F. C., Graff D. S., Richstone D. O., 2001, ApJ Letters 551, L31
- Agol E., 1997, Ph.D. thesis, UNIVERSITY OF CALIFORNIA, SANTA BARBARA
- Alexander D. M., Bauer F. E., Brandt W. N., Daddi E. et al., 2011, ApJ 738, 44
- Allen J. T., Hewett P. C., Maddox N., Richards G. T., Belokurov V., 2011, MNRAS 410, 860
- Antonucci R., 1988, in M. Kafatos (ed.), Supermassive Black Holes, p. 26
- Antonucci R., 2013, Nature 495, 165
- Antonucci R., Geller R., Goodrich R. W., Miller J. S., 1996, ApJ 472, 502
- Antonucci R. R. J., Miller J. S., 1985, ApJ 297, 621
- Arav N., 1996, ApJ 465, 617
- Arav N., Becker R. H., Laurent-Muehleisen S. A., Gregg M. D. et al., 1999a, ApJ 524, 566
- Arav N., Korista K. T., Barlow T. A., Begelman, 1995, Nature 376, 576
- Arav N., Korista K. T., de Kool M., Junkkarinen V. T., Begelman M. C., 1999b, ApJ 516, 27
- Arévalo P., Uttley P., 2006, MNRAS 367, 801
- Badnell N. R., 2006, ApJs 167, 334
- Balbus S. A., Hawley J. F., 1991, ApJ 376, 214
- Baldi R. D., Capetti A., Robinson A., Laor A., Behar E., 2016, MNRAS
- Baldry I. K., Glazebrook K., Brinkmann J., Ivezić Ž. et al., 2004, ApJ 600, 681
- Baptista R., Silveira C., Steiner J. E., Horne K., 2000, MNRAS 314, 713
- Barnard R., Foulkes S. B., Haswell C. A., Kolb U. et al., 2006, MNRAS 366, 287
- Bartlett E., 2013, Ph.D. thesis, University of Southampton

- Baskin A., Laor A., 2005, MNRAS 358, 1043
- Becker R. H., White R. L., Gregg M. D., Brotherton M. S. et al., 2000, ApJ 538, 72
- Begelman M. C., McKee C. F., Shields G. A., 1983, ApJ 271, 70
- Bell E. F., McIntosh D. H., Katz N., Weinberg M. D., 2003, ApJs 149, 289
- Belloni T. (ed.), 2010, The Jet Paradigm, Vol. 794 of *Lecture Notes in Physics, Berlin Springer Verlag*
- Benz A. O., Fuerst E., Kiplinger A. L., 1983, Nature 302, 45
- Beuermann K., Stasiewski U., Schwope A. D., 1992, A&A 256, 433
- Beuermann K., Thomas H.-C., 1990, A&A 230, 326
- Bîrzan L., McNamara B. R., Nulsen P. E. J., Carilli C. L., Wise M. W., 2008, ApJ 686, 859
- Blandford R. D., Payne D. G., 1982, MNRAS 199, 883
- Blandford R. D., Znajek R. L., 1977, MNRAS 179, 433
- Bondi H., 1952, MNRAS 112, 195
- Bondi H., Hoyle F., 1944, MNRAS 104, 273
- Bongiorno A., Schulze A., Merloni A., Zamorani G. et al., 2016, A&A 588, A78
- Bonning E. W., Cheng L., Shields G. A., Salviander S., Gebhardt K., 2007, ApJ 659, 211
- Borguet B., Hutsemékers D., 2010, A&A 515, A22
- Borguet B. C. J., Arav N., Edmonds D., Chamberlain C., Benn C., 2013, ApJ 762, 49
- Borguet B. C. J., Edmonds D., Arav N., Dunn J., Kriss G. A., 2012, ApJ 751, 107
- Boroson T. A., Green R. F., 1992, ApJs 80, 109
- Boroson T. A., Meyers K. A., 1992, ApJ 397, 442
- Bowler R. A. A., Hewett P. C., Allen J. T., Ferland G. J., 2014, MNRAS 445, 359
- Braito V., Reeves J. N., Dewangan G. C., George I. et al., 2007, ApJ 670, 978
- Brandt W. N., Laor A., Wills B. J., 2000, ApJ 528, 637
- Brotherton M. S., De Breuck C., Schaefer J. J., 2006, MNRAS 372, L58
- Brotherton M. S., Singh V., Runnoe J., 2015, MNRAS 454, 3864
- Brotherton M. S., Tran H. D., van Breugel W., Dey A., Antonucci R., 1997, ApJ Letters 487, L113
- Brown J. C., Richardson L. L., Antokhin I., Robert C. et al., 1995, A&A 295, 725
- Burkert A., Silk J., 2001, ApJ Letters 554, L151
- Caccianiga A., Severgnini P., 2011, MNRAS 415, 1928
- Capellupo D. M., Hamann F., Barlow T. A., 2014, MNRAS 444, 1893

- Capellupo D. M., Hamann F., Shields J. C., Rodríguez Hidalgo P., Barlow T. A., 2011, MNRAS 413, 908
- Capellupo D. M., Hamann F., Shields J. C., Rodríguez Hidalgo P., Barlow T. A., 2012, MNRAS 422, 3249
- Capellupo D. M., Netzer H., Lira P., Trakhtenbrot B., Mejía-Restrepo J., 2015, MNRAS 446, 3427
- Cappi M., Mihara T., Matsuoka M., Hayashida K. et al., 1996, ApJ 458, 149
- Cassinelli J. P., 1979, ARAA 17, 275
- Castor J. I., Abbott D. C., Klein R. I., 1975, ApJ 195, 157
- Castor J. L., 1974, MNRAS 169, 279
- Cavagnolo K. W., McNamara B. R., Wise M. W., Nulsen P. E. J. et al., 2011, ApJ 732, 71
- Chamberlain C., Arav N., Benn C., 2015, MNRAS 450, 1085
- Chartas G., Kochanek C. S., Dai X., Poindexter S., Garmire G., 2009, ApJ 693, 174
- Chen B., Dai X., Baron E., 2013a, ApJ 762, 122
- Chen B., Dai X., Baron E., Kantowski R., 2013b, ApJ 769, 131
- Church M. J., Reed D., Dotani T., Bałucińska-Church M., Smale A. P., 2005, MNRAS 359, 1336
- Clavel J., Schartel N., Tomas L., 2006, A&A 446, 439
- Cohen M. H., Ogle P. M., Tran H. D., Vermeulen R. C. et al., 1995, ApJ Letters 448, L77
- Cohen R. D., Puetter R. C., Rudy R. J., Ake T. B., Foltz C. B., 1986, ApJ 311, 135
- Connolly S. D., McHardy I. M., Dwelly T., 2014, MNRAS 440, 3503
- Connolly S. D., McHardy I. M., Skipper C. J., Emmanoulopoulos D., 2016, MNRAS
- Coppejans D. L., Körding E. G., Miller-Jones J. C. A., Rupen M. P. et al., 2015, MNRAS 451, 3801
- Cordova F. A., Mason K. O., 1982, ApJ 260, 716
- Cottis C. E., Goad M. R., Knigge C., Scaringi S., 2010, MNRAS 406, 2094
- Crenshaw D. M., Kraemer S. B., 2012, ApJ 753, 75
- Crenshaw D. M., Kraemer S. B., Gabel J. R., Kaastra J. S. et al., 2003, ApJ 594, 116
- Crenshaw D. M., Rodriguez-Pascual P. M., Penton S. V., Edelson R. A. et al., 1996, ApJ 470, 322
- Croton D. J., Springel V., White S. D. M., De Lucia G. et al., 2006, MNRAS 365, 11
- Crummy J., Fabian A. C., Gallo L., Ross R. R., 2006, MNRAS 365, 1067

- Cunto W., Mendoza C., Ochsenbein F., Zeippen C. J., 1993, A&A 275, L5
- Dabrowski Y., Fabian A. C., Iwasawa K., Lasenby A. N., Reynolds C. S., 1997, MNRAS 288, L11
- Dai X., Kochanek C. S., Chartas G., Kozłowski S. et al., 2010, ApJ 709, 278
- Dai X., Shankar F., Sivakoff G. R., 2008, ApJ 672, 108
- Dai X., Shankar F., Sivakoff G. R., 2012, ApJ 757, 180
- Davis S. W., Hubeny I., 2006, ApJs 164, 530
- Davis S. W., Woo J.-H., Blaes O. M., 2007, ApJ 668, 682
- de Kool M., Begelman M. C., 1995, ApJ 455, 448
- Decarli R., Labita M., Treves A., Falomo R., 2008, MNRAS 387, 1237
- Denney K. D., De Rosa G., Croxall K., Gupta A. et al., 2014, ApJ 796, 134
- Dere K. P., Landi E., Mason H. E., Monsignori Fossi B. C., Young P. R., 1997, A&As 125, 149
- Dexter J., Agol E., 2011, ApJ Letters 727, L24
- Dhillon V. S., 1996, in A. Evans, J. H. Wood (eds.), IAU Colloq. 158: Cataclysmic Variables and Related Objects, Vol. 208 of *Astrophysics and Space Science Library*, 3
- Dhillon V. S., Rutten R. G. M., 1995, MNRAS 277, 777
- Díaz Trigo M., Boirin L., 2015, ArXiv e-prints
- DiPompeo M. A., Brotherton M. S., Cales S. L., Runnoe J. C., 2012a, MNRAS 427, 1135
- DiPompeo M. A., Brotherton M. S., De Breuck C., 2012b, ApJ 752, 6
- Done C., Davis S. W., Jin C., Blaes O., Ward M., 2012, MNRAS 420, 1848
- Done C., Jin C., 2015, ArXiv e-prints
- Drew J., Verbunt F., 1985, MNRAS 213, 191
- Echevarria J., 1988, MNRAS 233, 513
- Edelson R., Gelbord J. M., Horne K., McHardy I. M. et al., 2015, ApJ 806, 129
- Edge D. O., Shakeshaft J. R., McAdam W. B., Baldwin J. E., Archer S., 1959, MmRA 68, 37
- Eggleton P. P., 1983, ApJ 268, 368
- Ehman J. R., Dixon R. S., Kraus J. D., 1970, AJ 75, 351
- Ekers J. A., 1969, Australian Journal of Physics Astrophysical Supplement 7
- Elitzur M., 2012, ApJ Letters 747, L33
- Elitzur M., Ho L. C., Trump J. R., 2014, MNRAS 438, 3340

- Elvis M., 2000, ApJ 545, 63
- Elvis M., Wilkes B. J., McDowell J. C., Green R. F. et al., 1994, ApJs 95, 1
- Emmanoulopoulos D., Papadakis I. E., Dovčiak M., McHardy I. M., 2014, MNRAS 439, 3931
- Emmanoulopoulos D., Papadakis I. E., McHardy I. M., Arévalo P. et al., 2012, MNRAS 424, 1327
- Eracleous M., Halpern J. P., 1994, ApJs 90, 1
- Evans P. A., Hellier C., Ramsay G., Cropper M., 2004, MNRAS 349, 715
- Fabian A. C., 2012, ARAA 50, 455
- Fabian A. C., Kunieda H., Inoue S., Matsuoka M. et al., 1994, PASJ 46, L59
- Fabian A. C., Nandra K., Reynolds C. S., Brandt W. N. et al., 1995, MNRAS 277, L11
- Fath E. A., 1909, Lick Observatory Bulletin 5, 71
- Feldmeier A., 1995, A&A 299, 523
- Fender R. P., 2001, MNRAS 322, 31
- Fender R. P., Belloni T. M., Gallo E., 2004, MNRAS 355, 1105
- Fender R. P., Gallo E., Russell D., 2010, MNRAS 406, 1425
- Ferland G., 2002, ArXiv Astrophysics e-prints
- Ferland G. J., 2005, Hazy, A Brief Introduction to Cloudy 05.07
- Ferland G. J., Porter R. L., van Hoof P. A. M., Williams R. J. R. et al., 2013, RMXAA 49, 137
- Ferrarese L., Merritt D., 2000, ApJ Letters 539, L9
- Filiz Ak N., Brandt W. N., Hall P. B., Schneider D. P. et al., 2012, ApJ 757, 114
- Filiz Ak N., Brandt W. N., Hall P. B., Schneider D. P. et al., 2014, ApJ 791, 88
- Flohic H. M. L. G., Eracleous M., Bogdanović T., 2012, ApJ 753, 133
- Foltz C. B., Weymann R. J., Morris S. L., Turnshek D. A., 1987, ApJ 317, 450
- Frank J., King A., Raine D., 1992, Accretion power in astrophysics.
- Frank J., King A. R., 1981, MNRAS 195, 227
- Friend D. B., Abbott D. C., 1986, ApJ 311, 701
- Fukumura K., Tombesi F., Kazanas D., Shrader C. et al., 2015, ApJ 805, 17
- Gabriel E., Fagg G. E., Bosilca G., Angskun T. et al., 2004, in Proceedings, 11th European PVM/MPI Users' Group Meeting, Budapest, Hungary, p. 97
- Gaetz T. J., Salpeter E. E., 1983, ApJs 52, 155
- Gallagher S. C., Brandt W. N., Chartas G., Garmire G. P., 2002, ApJ 567, 37
- Gallagher S. C., Brandt W. N., Chartas G., Priddey R. et al., 2006, ApJ 644, 709

- Gallagher S. C., Brandt W. N., Sambruna R. M., Mathur S., Yamasaki N., 1999, ApJ 519, 549
- Gallo E., Fender R. P., Pooley G. G., 2003, MNRAS 344, 60
- Gandhi P., Hönig S. F., Kishimoto M., 2015, ApJ 812, 113
- Gandhi P., Terashima Y., Yamada S., Mushotzky R. F. et al., 2013, ApJ 773, 51
- Ganguly R., Bond N. A., Charlton J. C., Eracleous M. et al., 2001, ApJ 549, 133
- Ganguly R., Sembach K. R., Tripp T. M., Savage B. D., Wakker B. P., 2006, ApJ 645, 868
- Gardner E., Done C., 2016, ArXiv e-prints
- Gayet R., 1970, A&A 9, 312
- Gebhardt K., Bender R., Bower G., Dressler A. et al., 2000, ApJ Letters 539, L13
- Ghosh K. K., Punshy B., 2007, ApJ Letters 661, L139
- Gibson R. R., Jiang L., Brandt W. N., Hall P. B. et al., 2009, ApJ 692, 758
- Gierliński M., Done C., 2004, MNRAS 349, L7
- Gierliński M., Done C., 2006, MNRAS 371, L16
- Giustini M., Cappi M., Chartas G., Dadina M. et al., 2011, A&A 536, A49
- Gofford J., Reeves J. N., Braito V., Nardini E. et al., 2014, ApJ 784, 77
- Gofford J., Reeves J. N., McLaughlin D. E., Braito V. et al., 2015, MNRAS 451, 4169
- Gofford J., Reeves J. N., Tombesi F., Braito V. et al., 2013, MNRAS 430, 60
- Goodrich R. W., 1997, ApJ 474, 606
- Goodrich R. W., Miller J. S., 1995, ApJ Letters 448, L73
- Gough B., 2009, GNU Scientific Library Reference Manual - Third Edition, Network Theory Ltd., 3rd edition
- Green A. R., McHardy I. M., Lehto H. J., 1993, MNRAS 265, 664
- Green P. J., Aldcroft T. L., Mathur S., Wilkes B. J., Elvis M., 2001, ApJ 558, 109
- Green P. J., Mathur S., 1996, ApJ 462, 637
- Greenstein J. L., Oke J. B., 1982, ApJ 258, 209
- Groot P. J., Rutten R. G. M., van Paradijs J., 2004, A&A 417, 283
- Grupe D., Mathur S., Elvis M., 2003a, AJ 126, 1159
- Grupe D., Mathur S., Elvis M., 2003b, AJ 126, 1159
- Grupe D., Nousek J. A., 2015, AJ 149, 85
- Gu M., Cao X., 2009, MNRAS 399, 349
- Gültekin K., Richstone D. O., Gebhardt K., Lauer T. R. et al., 2009, ApJ 698, 198
- Hōshi R., 1979, Progress of Theoretical Physics 61, 1307

- Haardt F., Maraschi L., 1991, ApJ Letters 380, L51
- Hall P. B., Anderson S. F., Strauss M. A., York D. G. et al., 2002, ApJs 141, 267
- Hall P. B., Anosov K., White R. L., Brandt W. N. et al., 2011, MNRAS 411, 2653
- Halpern J. P., 1984, ApJ 281, 90
- Hamann F., Chartas G., McGraw S., Rodriguez Hidalgo P. et al., 2013, MNRAS 435, 133
- Hamann W.-R., Koesterke L., 1998, A&A 335, 1003
- Hamann W.-R., Leuenhagen U., Koesterke L., Wessolowski U., 1992, A&A 255, 200
- Hamann W.-R., Oskinova L. M., Feldmeier A., 2008, in W.-R. Hamann, A. Feldmeier, L. M. Oskinova (eds.), Clumping in Hot-Star Winds, 75
- Hamann W.-R., Wessolowski U., Koesterke L., 1994, A&A 281, 184
- Häring N., Rix H.-W., 2004, ApJ Letters 604, L89
- Harrop-Allin M. K., Warner B., 1996, MNRAS 279, 219
- Hartley L. E., Murray J. R., Drew J. E., Long K. S., 2005, MNRAS 363, 285
- Hassall B. J. M., 1985, MNRAS 216, 335
- Haug K., 1987, AP&SS 130, 91
- Hazard C., Mackey M. B., Shimmins A. J., 1963, Nature 197, 1037
- Hazard C., Morton D. C., Terlevich R., McMahon R., 1984, ApJ 282, 33
- Heap S. R., Boggess A., Holm A., Klinglesmith D. A. et al., 1978, Nature 275, 385
- Heil L. M., Vaughan S., Uttley P., 2012, MNRAS 422, 2620
- Hessman F. V., Robinson E. L., Nather R. E., Zhang E.-H., 1984, ApJ 286, 747
- Higginbottom N., Knigge C., Long K. S., Sim S. A., Matthews J. H., 2013, MNRAS 436, 1390
- Higginbottom N., Proga D., Knigge C., Long K. S. et al., 2014, ApJ 789, 19
- Hillier D. J., 1984, ApJ 280, 744
- Hillier D. J., 1991, A&A 247, 455
- Hillier D. J., Miller D. L., 1999, ApJ 519, 354
- Hoare M. G., Drew J. E., 1991, MNRAS 249, 452
- Hoare M. G., Drew J. E., 1993, MNRAS 260, 647
- Hogg J. D., Reynolds C., 2015, ArXiv e-prints
- Honeycutt R. K., Schlegel E. M., Kaitchuck R. H., 1986, ApJ 302, 388
- Hönig S. F., Kishimoto M., Tristram K. R. W., Prieto M. A. et al., 2013, ApJ 771, 87
- Horne K., 1993, Eclipse Mapping of Accretion Disks: The First Decade, 117
- Horne K., Marsh T. R., 1986, MNRAS 218, 761

- Horne K., Marsh T. R., Cheng F. H., Hubeny I., Lanz T., 1994, ApJ 426, 294
- Hoyle F., Lyttleton R. A., 1939, Proceedings of the Cambridge Philosophical Society 35, 405
- Hubeny I., 2001, in G. Ferland, D. W. Savin (eds.), Spectroscopic Challenges of Photoionized Plasmas, Vol. 247 of *Astronomical Society of the Pacific Conference Series*, 197
- Hubeny I., Agol E., Blaes O., Krolik J. H., 2000, ApJ 533, 710
- Hubeny I., Lanz T., 1995, ApJ 439, 875
- Humphrey A., Binette L., 2014, MNRAS 442, 753
- Idan I., Lasota J.-P., Hameury J.-M., Shaviv G., 2010, A&A 519, A117
- Ioannou Z., van Zyl L., Naylor T., Charles P. A. et al., 2003, A&A 399, 211
- Iwasawa K., Fabian A. C., Mushotzky R. F., Brandt W. N. et al., 1996a, MNRAS 279, 837
- Iwasawa K., Fabian A. C., Reynolds C. S., Nandra K. et al., 1996b, MNRAS 282, 1038
- Janiuk A., Czerny B., Madejski G. M., 2001, ApJ 557, 408
- Ju W., Stone J. M., Zhu Z., 2016, ArXiv e-prints
- Junkkarinen V. T., Burbidge E. M., Smith H. E., 1983, ApJ 265, 51
- Kaastra J. S., Kriss G. A., Cappi M., Mehdipour M. et al., 2014, Science 345, 64
- Kaastra J. S., Mewe R., Liedahl D. A., Komossa S., Brinkman A. C., 2000, A&A 354, L83
- Kafka S., Honeycutt R. K., 2004, AJ 128, 2420
- Kaspi S., Brandt W. N., Maoz D., Netzer H. et al., 2007, ApJ 659, 997
- Kerzendorf W. E., Sim S. A., 2014, MNRAS 440, 387
- King A., 2003, ApJ Letters 596, L27
- Klein O., Nishina T., 1929, Zeitschrift fur Physik 52, 853
- Knigge C., 1999, MNRAS 309, 409
- Knigge C., Baraffe I., Patterson J., 2011, ApJs 194, 28
- Knigge C., Drew J. E., 1997, ApJ 486, 445
- Knigge C., Long K. S., Blair W. P., Wade R. A., 1997, ApJ 476, 291
- Knigge C., Long K. S., Wade R. A., Baptista R. et al., 1998a, ApJ 499, 414
- Knigge C., Long K. S., Wade R. A., Baptista R. et al., 1998b, ApJ 499, 414
- Knigge C., Scaringi S., Goad M. R., Cottis C. E., 2008, MNRAS 386, 1426
- Knigge C., Woods J. A., Drew J. E., 1995, MNRAS 273, 225
- Kollatschny W., Zetzl M., 2011, Nature 470, 366

- Konigl A., Kartje J. F., 1994, ApJ 434, 446
- Koratkar A., Blaes O., 1999, PASP 111, 1
- Körding E., Rupen M., Knigge C., Fender R. et al., 2008, Science 320, 1318
- Körding E. G., Jester S., Fender R., 2006, MNRAS 372, 1366
- Kormendy J., Ho L. C., 2013, ARAA 51, 511
- Kotani T., Ebisawa K., Dotani T., Inoue H. et al., 2000, ApJ 539, 413
- Kotov O., Churazov E., Gilfanov M., 2001, MNRAS 327, 799
- Kraemer S. B., Schmitt H. R., Crenshaw D. M., Meléndez M. et al., 2011, ApJ 727, 130
- Kraft R. P., Mathews J., Greenstein J. L., 1962, ApJ 136, 312
- Kriss G. A., Krolik J. H., Otani C., Espey B. R. et al., 1996, ApJ 467, 629
- Krolik J. H., Begelman M. C., 1986, in Bulletin of the American Astronomical Society, Vol. 18 of *BAAS*, 903
- Krolik J. H., Kriss G. A., 2001, ApJ 561, 684
- Krolik J. H., Voit G. M., 1998, ApJ Letters 497, L5
- Kromer M., Sim S. A., 2009, MNRAS 398, 1809
- Kudoh T., Shibata K., 1997, ApJ 474, 362
- Kurosawa R., Proga D., 2009, ApJ 693, 1929
- Kurucz R. L., 1991, in L. Crivellari, I. Hubeny, D. G. Hummer (eds.), NATO ASIC Proc. 341: Stellar Atmospheres - Beyond Classical Models, 441
- Kurucz R. L., Bell B., 1995, Atomic line list
- Kusterer D.-J., Nagel T., Hartmann S., Werner K., Feldmeier A., 2014, A&A 561, A14
- Kuulkers E., Motta S., Kajava J., Homan J. et al., 2015, The Astronomer's Telegram 7647
- La Dous C., 1989a, MNRAS 238, 935
- La Dous C., 1989b, A&A 211, 131
- Lamy H., Hutsemékers D., 2000, A&A 356, L9
- Lamy H., Hutsemékers D., 2004, A&A 427, 107
- Landi E., Del Zanna G., Young P. R., Dere K. P., Mason H. E., 2012, ApJ 744, 99
- Laor A., 1991, ApJ 376, 90
- Laor A., Brandt W. N., 2002, ApJ 569, 641
- Laor A., Davis S. W., 2014, MNRAS 438, 3024
- Lasota J.-P., 2001, NAR 45, 449
- Lazarova M. S., Canalizo G., Lacy M., Sajina A., 2012, ApJ 755, 29
- Liebert J., Stockman H. S., 1985, in D. Q. Lamb, J. Patterson (eds.), Cataclysmic

- Variables and Low-Mass X-ray Binaries, Vol. 113 of *Astrophysics and Space Science Library*, p. 151
- Long K. S., Blair W. P., Davidsen A. F., Bowers C. W. et al., 1991, ApJ Letters 381, L25
- Long K. S., Knigge C., 2002, ApJ 579, 725
- Long K. S., Wade R. A., Blair W. P., Davidsen A. F., Hubeny I., 1994, ApJ 426, 704
- Longmore A. J., Lee T. J., Allen D. A., Adams D. J., 1981, MNRAS 195, 825
- Lucy L. B., 1999a, A&A 344, 282
- Lucy L. B., 1999b, A&A 345, 211
- Lucy L. B., 2002, A&A 384, 725
- Lucy L. B., 2003, A&A 403, 261
- Lucy L. B., Solomon P. M., 1970, ApJ 159, 879
- Lusso E., Worseck G., Hennawi J. F., Prochaska J. X. et al., 2015, MNRAS 449, 4204
- Lynden-Bell D., 1969, Nature 223, 690
- Lyubarskii Y. E., 1997, MNRAS 292, 679
- MacGregor K. B., Hartmann L., Raymond J. C., 1979, ApJ 231, 514
- Madau P., Ghisellini G., Fabian A. C., 1994, MNRAS 270, L17
- Magdziarz P., Blaes O. M., Zdziarski A. A., Johnson W. N., Smith D. A., 1998, MNRAS 301, 179
- Magorrian J., Tremaine S., Richstone D., Bender R. et al., 1998, AJ 115, 2285
- Maiolino R., Marconi A., Oliva E., 2001a, A&A 365, 37
- Maiolino R., Marconi A., Salvati M., Risaliti G. et al., 2001b, A&A 365, 28
- Mangham S. W., Knigge C., Matthews J. H., Long K. S. et al., 2016, in prep.
- Marin F., 2014, MNRAS 441, 551
- Marin F., 2016, ArXiv e-prints
- Marin F., Goosmann R. W., 2013, MNRAS 436, 2522
- Marinucci A., Bianchi S., Matt G., Alexander D. M. et al., 2016, MNRAS 456, L94
- Marscher A. P., 2006, in P. A. Hughes, J. N. Bregman (eds.), Relativistic Jets: The Common Physics of AGN, Microquasars, and Gamma-Ray Bursts, Vol. 856 of *American Institute of Physics Conference Series*, p. 1
- Marsh T. R., Horne K., 1988, MNRAS 235, 269
- Marsh T. R., Horne K., 1990, ApJ 349, 593
- Marziani P., Sulentic J. W., Zwitter T., Dultzin-Hacyan D., Calvani M., 2001, ApJ 558, 553

- Mathur S., Green P. J., Arav N., Brotherton M. et al., 2000, ApJ Letters 533, L79
- Matt G., Guainazzi M., Maiolino R., 2003, MNRAS 342, 422
- Matthews J. H., Knigge C., Long K. S., Sim S. A., Higginbottom N., 2015, MNRAS 450, 3331
- Matthews J. H., Knigge C., Long K. S., Sim S. A. et al., 2016, MNRAS 458, 293
- Matzeu G. A., Reeves J. N., Nardini E., Braito V. et al., 2016, MNRAS 458, 1311
- Mauche C. W., 1996, ArXiv Astrophysics e-prints
- Mauche C. W., Raymond J. C., 1987, ApJ 323, 690
- Mazzali P. A., Lucy L. B., 1993, A&A 279, 447
- McConnell N. J., Ma C.-P., 2013, ApJ 764, 184
- McHardy I. M., Koerding E., Knigge C., Uttley P., Fender R. P., 2006, Nature 444, 730
- McHardy I. M., Papadakis I. E., Uttley P., 1999, Nuclear Physics B Proceedings Supplements 69, 509
- Menzel D. H., Pekeris C. L., 1935, MNRAS 96, 77
- Merloni A., Heinz S., di Matteo T., 2003, MNRAS 345, 1057
- Meyer F., Meyer-Hofmeister E., 1981, A&A 104, L10
- Mihalas D., 1978, Stellar atmospheres /2nd edition/
- Miller L., Turner T. J., 2013, ApJ Letters 773, L5
- Miller L., Turner T. J., Reeves J. N., 2008, A&A 483, 437
- Misawa T., Charlton J. C., Eracleous M., Ganguly R. et al., 2007, ApJs 171, 1
- Misawa T., Eracleous M., Chartas G., Charlton J. C., 2008, ApJ 677, 863
- Misra R., Kembhavi A. K., 1998, ApJ 499, 205
- Mitsuda K., Inoue H., Nakamura N., Tanaka Y., 1989, PASJ 41, 97
- Morabito L. K., Dai X., Leighly K. M., Sivakoff G. R., Shankar F., 2011, ApJ 737, 46
- Morabito L. K., Dai X., Leighly K. M., Sivakoff G. R., Shankar F., 2013, ArXiv e-prints
- Morgan C. W., Kochanek C. S., Morgan N. D., Falco E. E., 2010, ApJ 712, 1129
- Motta S., Beardmore A., Oates S., Sanna N. P. M. K. A. et al., 2015, The Astronomer's Telegram 7665
- Muñoz-Darias T., Casares J., Mata Sánchez D., Fender R. P. et al., 2016, Nature
- Muñoz-Darias T., Coriat M., Plant D. S., Ponti G. et al., 2013, MNRAS 432, 1330
- Murray N., Chiang J., 1996, Nature 382, 789
- Murray N., Chiang J., 1997, ApJ 474, 91
- Murray N., Chiang J., Grossman S. A., Voit G. M., 1995, ApJ 451, 498
- Nandra K., Pounds K. A., 1994, MNRAS 268, 405

- Narayan R., McClintock J. E., 2012, MNRAS 419, L69
- Narayan R., McClintock J. E., Tchekhovskoy A., 2014, Energy Extraction from Spinning Black Holes Via Relativistic Jets, 523
- Narayan R., Yi I., 1994, ApJ Letters 428, L13
- Narayan R., Yi I., 1995, ApJ 452, 710
- Nardini E., Reeves J. N., Gofford J., Harrison F. A. et al., 2015, Science 347, 860
- Nestor D., Hamann F., Rodriguez Hidalgo P., 2008, MNRAS 386, 2055
- Netzer H., 1990, in R. D. Blandford, H. Netzer, L. Woltjer, T. J.-L. Courvoisier, M. Mayor (eds.), Active Galactic Nuclei, p. 57
- Neugebauer G., Oke J. B., Becklin E. E., Matthews K., 1979, ApJ 230, 79
- Neustroev V. V., Suleimanov V. F., Borisov N. V., Belyakov K. V., Shearer A., 2011, MNRAS 410, 963
- Noebauer U. M., Long K. S., Sim S. A., Knigge C., 2010, ApJ 719, 1932
- Nomura M., Ohsuga K., Takahashi H. R., Wada K., Yoshida T., 2016, PASJ 68, 16
- Nomura M., Ohsuga K., Wada K., Susa H., Misawa T., 2013, PASJ 65, 40
- North M., Knigge C., Goad M., 2006, MNRAS 365, 1057
- O'Dowd M. J., Bate N. F., Webster R. L., Labrie K., Rogers J., 2015, ArXiv e-prints
- Orr A., Molendi S., Fiore F., Grandi P. et al., 1997, A&A 324, L77
- Osaki Y., 1974, PASJ 26, 429
- Osterbrock D. E., 1989, Astrophysics of gaseous nebulae and active galactic nuclei
- Otani C., Kii T., Reynolds C. S., Fabian A. C. et al., 1996, PASJ 48, 211
- Ouyed R., Pudritz R. E., 1997, ApJ 482, 712
- Owocki S., 2014, ArXiv e-prints
- Owocki S. P., Castor J. I., Rybicki G. B., 1988, ApJ 335, 914
- Owocki S. P., Rybicki G. B., 1984, ApJ 284, 337
- Owocki S. P., Rybicki G. B., 1985, ApJ 299, 265
- Pancoast A., Brewer B. J., Treu T., 2014a, MNRAS 445, 3055
- Pancoast A., Brewer B. J., Treu T., Park D. et al., 2014b, MNRAS 445, 3073
- Parmar A. N., Oosterbroek T., Boirin L., Lumb D., 2002, A&A 386, 910
- Patterson J., 1984, ApJs 54, 443
- Patterson J., 1994, PASP 106, 209
- Patterson J., Patino R., Thorstensen J. R., Harvey D. et al., 1996, AJ 111, 2422
- Pauldrach A., Puls J., Kudritzki R. P., 1986, A&A 164, 86

- Pauldrach A. W. A., Kudritzki R. P., Puls J., Butler K., Hunsinger J., 1994, A&A 283, 525
- Pelletier G., Pudritz R. E., 1992, ApJ 394, 117
- Penrose R., Floyd R. M., 1971, Nature Physical Science 229, 177
- Pereyra N. A., Kallman T. R., Blondin J. M., 1997, ApJ 477, 368
- Perley R. A., Dreher J. W., Cowan J. J., 1984, ApJ Letters 285, L35
- Ponti G., Fender R. P., Begelman M. C., Dunn R. J. H. et al., 2012, MNRAS 422, L11
- Potash R. I., Wardle J. F. C., 1980, ApJ 239, 42
- Pounds K., Lobban A., Reeves J., Vaughan S., 2016, MNRAS 457, 2951
- Pounds K. A., Nandra K., Stewart G. C., Leighly K., 1989, MNRAS 240, 769
- Pounds K. A., Reeves J. N., 2009, MNRAS 397, 249
- Pringle J. E., 1981, ARAA 19, 137
- Prinja R. K., Ringwald F. A., Wade R. A., Knigge C., 2000, MNRAS 312, 316
- Prinja R. K., Smith L. J., 1992, A&A 266, 377
- Proga D., 2003, ApJ 585, 406
- Proga D., 2005, in J.-M. Hameury, J.-P. Lasota (eds.), *The Astrophysics of Cataclysmic Variables and Related Objects*, Vol. 330 of *Astronomical Society of the Pacific Conference Series*, 103
- Proga D., Kallman T. R., 2004, ApJ 616, 688
- Proga D., Kallman T. R., Drew J. E., Hartley L. E., 2002a, ApJ 572, 382
- Proga D., Kallman T. R., Drew J. E., Hartley L. E., 2002b, ApJ 572, 382
- Proga D., Stone J. M., Drew J. E., 1998, MNRAS 295, 595
- Proga D., Stone J. M., Kallman T. R., 2000, ApJ 543, 686
- Puccetti S., Fiore F., Risaliti G., Capalbi M. et al., 2007, MNRAS 377, 607
- Puebla R. E., Diaz M. P., Hillier D. J., Hubeny I., 2011, ApJ 736, 17
- Randall S. W., Forman W. R., Giacintucci S., Nulsen P. E. J. et al., 2011, ApJ 726, 86
- Read J. I., Trentham N., 2005, Philosophical Transactions of the Royal Society of London Series A 363
- Reeves J. N., O'Brien P. T., Ward M. J., 2003, ApJ Letters 593, L65
- Reeves J. N., Wynn G., O'Brien P. T., Pounds K. A., 2002, MNRAS 336, L56
- Reichard T. A., Richards G. T., Hall P. B., Schneider D. P. et al., 2003, AJ 126, 2594
- Reynolds C. S., 1999, in J. Poutanen, R. Svensson (eds.), *High Energy Processes in Accreting Black Holes*, Vol. 161 of *Astronomical Society of the Pacific Conference Series*, 178

- Reynolds C. S., Fabian A. C., 1995, MNRAS 273, 1167
- Ringwald F. A., Naylor T., 1998, AJ 115, 286
- Risaliti G., Elvis M., 2010, A&A 516, A89
- Risaliti G., Elvis M., Fabbiano G., Baldi A. et al., 2007, ApJ Letters 659, L111
- Risaliti G., Elvis M., Nicastro F., 2002, ApJ 571, 234
- Risaliti G., Salvati M., Marconi A., 2011, MNRAS 411, 2223
- Romanova M. M., Ustyugova G. V., Koldoba A. V., Chechetkin V. M., Lovelace R. V. E., 1997, ApJ 482, 708
- Ross R. R., Fabian A. C., 2005, MNRAS 358, 211
- Rottenberg J. A., 1952, MNRAS 112, 125
- Rupke D. S. N., Veilleux S., 2011, ApJ Letters 729, L27
- Rutten R. G. M., van Paradijs J., Tinbergen J., 1992, A&A 260, 213
- Rybicki G., 1970, in H. G. Groth, P. Wellmann (eds.), IAU Colloq. 2: Spectrum Formation in Stars with Steady-State Extended Atmospheres, 87
- Rybicki G. B., Hummer D. G., 1978, ApJ 219, 654
- Sabra B. M., Hamann F., 2001, ApJ 563, 555
- Scaringi S., Körding E., Uttley P., Knigge C. et al., 2012, MNRAS 421, 2854
- Scaringi S., Maccarone T. J., Koerding E., Knigge C. et al., 2015, ArXiv e-prints
- Schechter P., 1976, ApJ 203, 297
- Schmidt G. D., Hines D. C., 1999, ApJ 512, 125
- Schmidt M., 1963, Nature 197, 1040
- Schmidt M., 1965a, ApJ 141, 1295
- Schmidt M., 1965b, ApJ 141, 1
- Schmutz W., 1997, A&A 321, 268
- Seaton M. J., 1959, MNRAS 119, 90
- Setti G., Woltjer L., 1989, A&A 224, L21
- Seyfert C. K., 1943, ApJ 97, 28
- Shakura N. I., Sunyaev R. A., 1973, A&A 24, 337
- Shankar F., Calderone G., Knigge C., Matthews J. et al., 2016, ApJ Letters 818, L1
- Shaviv G., Wehrse R., 1991, A&A 251, 117
- Shaw A. W., Charles P. A., Bird A. J., Cornelisse R. et al., 2013, MNRAS 433, 740
- Shaw A. W., Gandhi P., Altamirano D., Uttley P. et al., 2016, MNRAS 458, 1636
- Shen Y., Ho L. C., 2014, Nature 513, 210
- Shen Y., Richards G. T., Strauss M. A., Hall P. B. et al., 2011, ApJs 194, 45

- Shi Y., Rieke G. H., Smith P., Rigby J. et al., 2010, ApJ 714, 115
- Shlosman I., Vitello P., 1993, ApJ 409, 372
- Silk J., Rees M. J., 1998, A&A 331, L1
- Silva C., Uttley P., Costantini E., 2015, in The Extremes of Black Hole Accretion, 63
- Sim S. A., 2004, MNRAS 349, 899
- Sim S. A., Drew J. E., Long K. S., 2005, MNRAS 363, 615
- Sim S. A., Long K. S., Miller L., Turner T. J., 2008, MNRAS 388, 611
- Sim S. A., Miller L., Long K. S., Turner T. J., Reeves J. N., 2010a, MNRAS 404, 1369
- Sim S. A., Proga D., Kurosawa R., Long K. S. et al., 2012, MNRAS 426, 2859
- Sim S. A., Proga D., Miller L., Long K. S., Turner T. J., 2010b, MNRAS 408, 1396
- Simon L. E., Hamann F., 2010, MNRAS 409, 269
- Sluse D., Hutsemékers D., Anguita T., Braibant L., Riaud P., 2015, ArXiv e-prints
- Smak J., 1981, ACTAA 31, 395
- Smak J., 1995, ACTAA 45, 259
- Sobolev V. V., 1957, SvA 1, 678
- Sobolev V. V., 1960, Moving envelopes of stars
- Sobolewska M. A., Siemiginowska A., Gierliński M., 2011, MNRAS 413, 2259
- Soleri P., Muñoz-Darias T., Motta S., Belloni T. et al., 2013, MNRAS 429, 1244
- Somerville R. S., Primack J. R., Faber S. M., 2001, MNRAS 320, 504
- Springel V., Di Matteo T., Hernquist L., 2005, ApJ Letters 620, L79
- Spruit H. C., 1996, in R. A. M. J. Wijers, M. B. Davies, C. A. Tout (eds.), NATO Advanced Science Institutes (ASI) Series C, Vol. 477 of *NATO Advanced Science Institutes (ASI) Series C*, p. 249
- Stalevski M., Fritz J., Baes M., Popovic L. C., 2013, ArXiv e-prints
- Stalin C. S., Srianand R., Petitjean P., 2011, MNRAS 413, 1013
- Stockman H. S., Angel J. R. P., Miley G. K., 1979, ApJ Letters 227, L55
- Strateva I., Ivezić Ž., Knapp G. R., Narayanan V. K. et al., 2001, AJ 122, 1861
- Struve O., 1935, ApJ 81, 66
- Suleimanov V., Hertfelder M., Werner K., Kley W., 2014, ArXiv e-prints
- Sulentic J. W., Zwitter T., Marziani P., Dultzin-Hacyan D., 2000, ApJ Letters 536, L5
- Surdej J., Hutsemekers D., 1987, A&A 177, 42
- Sutherland R. S., 1998, MNRAS 300, 321
- Tanaka Y., Ueda Y., Boller T., 2003, MNRAS 338, L1
- Tatum M. M., Turner T. J., Sim S. A., Miller L. et al., 2012, ApJ 752, 94

- Thorne K. S., 1974, ApJ 191, 507
- Tohline J. E., Osterbrock D. E., 1976, ApJ Letters 210, L117
- Tombesi F., Cappi M., Reeves J. N., Palumbo G. G. C. et al., 2010, A&A 521, A57
- Tombesi F., Meléndez M., Veilleux S., Reeves J. N. et al., 2015, Nature 519, 436
- Tran H. D., 2001, ApJ Letters 554, L19
- Trump J. R., Hall P. B., Reichard T. A., Richards G. T. et al., 2006, ApJs 165, 1
- Turing A. M., 1948, QJMAM 1(1), 287
- Ueda Y., Inoue H., Tanaka Y., Ebisawa K. et al., 1998, ApJ 492, 782
- Urrutia T., Becker R. H., White R. L., Glikman E. et al., 2009, ApJ 698, 1095
- Urry C. M., Padovani P., 1995, PASP 107, 803
- Ustyugova G. V., Koldoba A. V., Romanova M. M., Chechetkin V. M., Lovelace R. V. E., 1999, ApJ 516, 221
- Uttley P., Cackett E. M., Fabian A. C., Kara E., Wilkins D. R., 2014, AAPR 22, 72
- Uttley P., McHardy I. M., 2001, MNRAS 323, L26
- Uttley P., McHardy I. M., Vaughan S., 2005, MNRAS 359, 345
- Šurlan B., Hamann W.-R., Kubát J., Osokinova L. M., Feldmeier A., 2012, A&A 541, A37
- Van de Sande M., Scaringi S., Knigge C., 2015, MNRAS 448, 2430
- van der Hooft F., Heemskerk M. H. M., Alberts F., van Paradijs J., 1998, A&A 329, 538
- van Regemorter H., 1962, ApJ 136, 906
- Verner D. A., Barthel P. D., Tytler D., 1994, A&As 108, 287
- Verner D. A., Ferland G. J., Korista K. T., Yakovlev D. G., 1996a, ApJ 465, 487
- Verner D. A., Verner E. M., Ferland G. J., 1996b, Atomic Data and Nuclear Data Tables 64, 1
- Vestergaard M., Wilkes B. J., 2001, ApJs 134, 1
- Voit G. M., Weymann R. J., Korista K. T., 1993, ApJ 413, 95
- Wade R. A., 1984, MNRAS 208, 381
- Wade R. A., 1988, ApJ 335, 394
- Walker M. F., 1963, ApJ 137, 485
- Walton D. J., Miller J. M., Harrison F. A., Fabian A. C. et al., 2013, ApJ Letters 773, L9
- Wang B., Han Z., 2012, NAR 56, 122
- Warner B., 2003, Cataclysmic Variable Stars

- Weymann R. J., Morris S. L., Foltz C. B., Hewett P. C., 1991, ApJ 373, 23
- Weymann R. J., Turnshek D. A., Christiansen W. A., 1985, in J. S. Miller (ed.), Astrophysics of Active Galaxies and Quasi-Stellar Objects, p. 333
- White N. E., Stella L., Parmar A. N., 1988, ApJ 324, 363
- Woltjer L., 1959, ApJ 130, 38
- Woods D. T., Klein R. I., Castor J. I., McKee C. F., Bell J. B., 1996, ApJ 461, 767
- Woods J. A., 1991, Ph.D. thesis, D. Phil thesis, Univ. Oxford , (1991)
- Yong S. Y., Webster R. L., King A. L., 2016, PASA 33, e009
- Zakamska N. L., Strauss M. A., Krolik J. H., Collinge M. J. et al., 2003, AJ 126, 2125
- Zanstra H., 1929, Publications of the Dominion Astrophysical Observatory Victoria 4, 209
- Zhang S. N., Cui W., Chen W., 1997, ApJ Letters 482, L155
- Zhou H., Wang T., Wang H., Wang J. et al., 2006, ApJ 639, 716
- Zubovas K., King A., 2013, ApJ 769, 51